

Imperial College London

Department of Earth Science and Engineering

Quantifying the effects of mass transport in the curing and
leaching of agglomerated ores using
X-ray Microtomography

Luis Eduardo Salinas-Farran

Supervisor: Prof. Stephen J. Neethling

Submitted in part fulfilment of the requirements for the degree of Doctor of Philosophy in Earth
Science and Engineering of Imperial College London and the Diploma of Imperial College London

London

March 2022

Abstract

Agglomeration and subsequent curing are widely used as pre-treatments for ore prior to heap leaching as they both improve the permeability of the heap and bring leaching solution into close contact with the ore, initializing the leaching reactions. In this thesis, a low-grade copper sulphide ore was used for the experiments and two different agglomeration/leaching solutions were tested, namely a more standard sulphuric acid solution including ferric/ferrous ions, and a solution which also contained chloride ions. A novel image processing methodology was developed to track grains over both the curing and leaching process, taking into account the anisometric changes experienced by the agglomerates and the formation and depletion of species. A combination of XMT and SEM/EDX was used to characterise the chemical and mineralogical changes occurring over both processes.

The formation and depletion of mineral components were quantified and tracked beyond the typical time scales used industrially, highlighting that the presence of chloride ions makes a substantial difference to the chemical and structural evolution of the agglomerates. Over the curing process, at least 20 days are required to perceive a significant degree of dissolution. Reprecipitation of metal containing species was observed, especially near the agglomerate surfaces. These precipitates are water-soluble species, and 50% of the initial sulphides were extracted from the agglomerates containing chloride ions, but only 20% from the other agglomerates after curing and water washing.

A model of the agglomerate behaviour over the curing process is proposed based on the results observed from the XMT measurements. This model considers both the metal dissolution extent, as well as the reprecipitation of species due to water evaporation. The mathematical model is explained together with the computational approach used to solve it, and the simulation results are compared with the experimental results. This model is able to successfully predict the trends seen in the experiments, with the relative reaction and evaporation rates being a controlling factor.

The leach performance was assessed for agglomerates leached using the same recipes used for the agglomeration stage. The compaction and changes in microporosity in the sample were quantified, showing that these changes do not significantly influence the leaching performance. By taking advantage of the more selective leaching that takes place when chloride ions are added to the leach solution, the leaching variability in the system was assessed. SEM/EDX measurements were then used to calibrate the XMT quantifications, isolating the dissolution of copper-containing grains from the pyrite dissolution. It was, thus, possible to quantify the surface kinetics of the hundreds of thousands of grains in the sample, with these kinetics being represented by a family of bi-modal curves.

It was shown that the mass transport and mineralogical changes occurring throughout the curing and leaching processes could be quantified both at the grain-scale and the macro-scale by using the developed methodology for combining SEM/EDX measurements with XMT. By incorporating this data into particle scale and, ultimately, heap scale leach models, improved predictions and optimisation of leach performance can be made.

Declaration of Originality

I hereby declare that this work is original research carried out by me and that no part of this thesis has been submitted for consideration towards another degree at this or any other institution. Any work in this thesis which is not my own work has been properly referenced.

Luis Eduardo Salinas-Farran

March 24th, 2022

Copyright Declaration

The copyright of this thesis rests with the author. Unless otherwise indicated, its contents are licensed under a Creative Commons Attribution Non-Commercial 4.0 International Licence (CC BY-NC).

Under this licence, you may copy and redistribute the material in any medium or format. You may also create and distribute modified versions of the work. This is on the condition that: you credit the author and do not use it, or any derivative works, for a commercial purpose.

When reusing or sharing this work, ensure you make the licence terms clear to others by naming the licence and linking to the licence text. Where a work has been adapted, you should indicate that the work has been changed and describe those changes.

Please seek permission from the copyright holder for uses of this work that are not included in this licence or permitted under UK Copyright Law.

Acknowledgements

I would like to thank my supervisor, Professor Stephen Neethling for his constant support and valuable advice throughout the course of my PhD, and for always keeping his door open to share his immeasurable knowledge, it has been an amazing journey. I would also like to thank my co-supervisor Professor Peter Lee for his support and help. I am most grateful to Professor Paul Shearing, Dr Francesco Iacoviello, and the Electrochemical Innovation Lab at University College London for letting me use their XMT machines and for sharing their research experience. Many thanks to Dr Andrew Batchelor from the University of Nottingham and Dr William Brownscombe from the Natural History Museum for their help with the characterisation of the mineral samples and constructive comments on my research.

I am deeply grateful to Dr Francisco “Pancho” Reyes. It would not have been possible to do this PhD without his help, I cannot thank him enough. Also special thanks to Dr Pablo Brito-Parada for his support when it was most needed. Many many thanks to all my friends, pichanga friends, life friends, gym buddies, band mates, and colleagues who have made this an extraordinary experience. I am referring to (alphabetically, not in order of importance) Becky, Camilo, David, Dennis, Diego, Joaquín, Jorge, Juanito, Julito, Marquito, Miguel, Nico, Pablo, Pau, Pipe, Rubén,... (I beg your pardon if I missed anyone). Thanks very much to all those who I shared a pint with (will avoid naming them to keep this on one page). And a big thanks (much obliged) to music and the bands I have had the chance to play with. It has helped me keeping it together.

I am also so grateful to my family, especially to Mayerlic, Richard, Esperanza, and my partner Belén. Oh boy, it would have been impossible without you. Thanks for your support, infinite love, and advice during the last 4.5 years! A mis padres y hermana, gracias por visitarme siempre que han podido, por estar siempre conmigo; los he sentido como si estuvieran junto a mí todo este tiempo y eso es impagable. A mi pareja, muchas gracias por todo, por el apoyo y amor en esos días difíciles, así como por hacer cada día un día especial. A todos, gracias por ser lo más lindo e importante de mis días.

Lastly, thanks to London (especially NW8, W14, and W4). What an amazing city! Even during COVID times...

London, SW7. March 2022

*

(Still)

Happiness

is

only

real

when

shared...

Index

List of Figures.....	12
List of Tables.....	17
Chapter 1. Introduction.....	18
1.1. Motivation	18
1.2. Objectives	19
Chapter 2. Literature review	20
2.1. Hydrometallurgy.....	20
2.1.1. Introduction.....	20
2.1.2. Fundamentals of hydrometallurgy	21
2.2. Leaching process	22
2.2.1. Leaching of oxide ores.....	24
2.2.1.1. Leaching of copper oxides.....	26
2.2.2. Leaching of sulphide ores.....	26
2.2.2.1. Leaching of copper sulphides.....	27
2.2.2.1.1. Leaching of chalcopyrite.....	31
2.2.3. Bioleaching	32
2.2.4. Chloride leaching.....	33
2.2.5. Particle scale effects in leaching.....	34
2.2.5.1. Particle size effects.....	34
2.2.5.2. Multi size systems	34
2.2.5.3. Particle porosity	35
2.2.5.4. Gangue content.....	35
2.2.6. Leaching techniques.....	36
2.2.6.1. In-situ Leaching.....	37
2.2.6.2. Heap leaching	37
2.2.6.2.1. Chemistry of the heap leaching process	39
2.2.6.2.2. Industrial Heap leaching.....	39
2.2.6.3. Dump leaching.....	46
2.2.6.4. Vat leaching	46
2.2.6.5. Agitation leaching.....	47
2.2.6.6. Pressure leaching	47
2.3. Leaching simulation.....	48
2.4. X-ray micro tomography	50
2.4.1. Use of XMT in the mining industry	50

2.4.2. Fundamentals of XMT	51
2.4.2.1. Brief history	51
2.4.2.2. XMT system	51
2.4.2.3. X-ray source	54
2.4.2.4. Basic physical principles	54
2.4.2.5. Reconstruction	56
2.4.2.5.1. Image artifacts	57
2.4.2.5.2. Beam Hardening Effect	57
2.4.2.5.3. Ring Artifacts	59
2.4.2.5.4. Partial volume effects	60
2.4.2.6. Image processing	60
2.4.2.6.1. Image filtering	61
2.4.2.6.2. Segmentation and classification	62
2.4.2.6.3. Segmentation - Thresholding method	62
2.4.2.6.4. Separation - Watershed-based method	63
2.4.2.6.5. Labelling and tracking of features	63
2.5. Summary	64
Chapter 3. Experimental Methods	66
3.1. Introduction	66
3.2. Mineral ores	66
3.3. Collaboration with Industry	67
3.3.1. Agglomeration process at the pilot plant	68
3.4. Experimental setup	70
3.4.1. Particle size distribution	70
3.4.2. Chemical composition of the solution	71
3.4.3. Curing experiments	72
3.4.3.1. Agglomeration tests	72
3.4.3.1.1. Tumbling drum agglomeration	72
3.4.3.1.2. Tumbling reactor filling level	73
3.4.3.1.3. Rolling speed	73
3.4.3.1.4. PSD of the feed material used for agglomeration	73
3.4.3.1.5. Agglomeration time	74
3.4.3.2. Curing conditions	74
3.4.3.2.1. Glass columns	74
3.4.3.2.2. Temperature controlled Incubator	75
3.4.3.2.3. Curing period	77

3.4.3.2.3. Peristaltic pump	77
3.4.4. Leaching process conditions.....	78
3.4.4.1. Leaching flowrate	78
3.4.4.2. Pregnant Leach Solution.....	78
3.5. Summary	79
Chapter 4. Automated XMT-based assessments of agglomerated ores.....	80
4.1. Introduction.....	80
4.2. X-ray microtomography	80
4.2.1. XMT system	80
4.2.2. Scanning conditions.....	82
4.3. Particle tracking methodology	84
4.3.1. Global thresholding	84
4.3.2. Agglomerate segmentation.....	85
4.3.3. Agglomerate relabelling	86
4.3.4. Mineral grain and precipitates thresholding.....	87
4.3.5. Mineral grain labelling.....	89
4.3.6. Sulphide grain registration and tracking	90
4.3.6.1. Image registration	90
4.3.6.2. Grain tracking	91
4.4. Minimising errors	93
4.4.1. Calibrating the quantification methodology to address random errors.....	94
4.5. Summary	96
Chapter 5. XMT-based assessments of the curing process of agglomerated ores	98
5.1. Introduction.....	98
5.2. Structural changes.....	99
5.3. Energy-dispersive X-rays analysis with Scanning Electron Microscope for mineral identification.	102
5.4. Sulphide distribution over the curing process	104
5.5. Leaching extent over the curing process.....	105
5.6. Summary	109
Chapter 6. Modelling the curing of agglomerated ores.....	110
6.1. Introduction.....	110
6.2. Mathematical Model.....	110
6.2.1. Considerations.....	111
6.2.2. Fluid Motion	111
6.2.3. Copper motion	113

6.2.4. Summary of equations	115
6.2.5. Numerical methods	117
6.2.6. Discretization of the equations	119
6.3. Validation of the model.....	120
6.4. Sensitivity analysis	124
6.4.1. Diffusion limited case	124
6.4.2. Reaction limited case	125
6.5. Variations in the agglomeration and curing conditions.....	126
6.5.1. Influence of the evaporation rate	126
6.5.2. Influence of the agglomerate size	128
6.6. Final remarks	130
Chapter 7. XMT-based assessments of the leaching of agglomerated ores	132
7.1. Introduction.....	132
7.2. Relationship between image measurement and chemical analysis	133
7.2.1. Recovery calculations from ICP measurements	133
7.2.2. Recovery calculations from XMT imaging	135
7.2.3. Relationship between image measurement and chemical analysis	137
7.3. Leaching results at the column scale.....	138
7.3.1. Different column scales.....	138
7.3.2. Relationship between the agglomerate-scale results and the characteristics of the ore.	139
7.4. Structural changes.....	140
7.5. Sub-particle level analysis	143
7.5.1. Leaching performance by size-distance category	144
7.5.2. Calibration of the XMT results using SEM/EDX and mineral mapping.....	145
7.5.3. Calibration process.....	149
7.5.4. Distribution of kinetics	151
7.5.4.1. Mathematical description	152
7.5.4.2. Results	153
7.6. Summary	158
Chapter 8. Conclusions.....	159
Bibliography.....	163
Appendix A	176
Publications	176
Appendix B	177

List of Figures

Figure 2.1. Decrease in copper grade over the last century (Energy and Capital, 2016).....	20
Figure 2.2. Eh-pH stability diagram for the system Cu-O at ambient conditions and ion activity of 1M. .	23
Figure 2.3. Schematic of the geological occurrence of copper minerals.	25
Figure 2.4. Eh-pH stability diagram for the Cu-Fe-S-O system at ambient conditions and ion activity of 1M.	29
Figure 2.5. Schematic of the formation of secondary reaction products and/or passivation layer on a chalcopyrite grain. Adapted from (Zhao et al., 2019).	30
Figure 2.6. Typical relationship between copper grade and ore particle size for different methods of atmospheric leaching. Adapted from (Davenport et al., 2000)	36
Figure 2.7. Basic scheme of a typical hydrometallurgical processing route.	38
Figure 2.8. Schematic of a permanent heap, indicating very basically the standard components and conditions.	40
Figure 2.9. Schematic of an on/off (dynamic) heap, indicating very basically the standard components and conditions.	41
Figure 2.10. Schematic of a leaching pad. A single-composite liner system is presented on top, and a double-composite liner system on the bottom. Adapted from (Lupo, 2010).....	42
Figure 2.11. Schematic of a tumbling drum agglomerator and very basic description of the standard operational conditions. Adapted from (Bouffard, 2005)	43
Figure 2.12. Schematic of a typical vat leaching reactor. Adapted from (María and Ruiz, 2013).....	47
Figure 2.13. Schematic of a typical XMT system, showing its essential components and how the final tomographic reconstruction is produced. Adapted from (Mao et al., 2019).	52
Figure 2.14. Schematic of a scan acquired from a set of packed spherical samples placed at different relative positions w.r.t the source and the detector.	53
Figure 2.15. Linear attenuation coefficient of some of some minerals, such as pyrite, the most common copper sulphides, and most common gangue components. Adapted from (Berger et al. 2010).....	56
Figure 2.16. Beam hardening effect, the passing ray becomes artificially more penetrating as it loses low energy components of its spectrum. Adapted from (Stauber and Müller, 2008).	58
Figure 2.17. Uncorrected image and corresponding propagation path length in the segmented materials. (a) Uncorrected image, (b) two components segmentation image (corrected image) (Zhao et al., 2018).	59
Figure 2.18. Strong ring artifact on a reconstructed slice of a mineral sample (a) Original image, (b) Artifact removed after multiple filtering steps. Adapted from (Stampanoni et al., 2009).	59

Figure 2.19. Example of the partial volume effects that occur for a coin-shaped object of different sizes. The edges of smaller objects become more difficult to define.....	60
Figure 3.1. Fresh agglomerates packed into gabions of 2x2x10m and left to cure at ambient conditions.	69
Figure 3.2. Examples of agglomerates of different quality, agglomerates in the centre being of the aimed quality. (a) low moisture content (below 8%), leading to dry agglomerates; (b) good quality agglomerates with 8-12% of moisture content; (c) high moisture content (above 12%), leading to wet agglomerates.....	70
Figure 3.3. Motor Speed Berco Mill and stainless-steel drum used for agglomeration.	72
Figure 3.4. Particle size distribution of the feed material used for agglomeration.	74
Figure 3.5. Columns filled with agglomerates used to carry out curing and leaching experiments.	75
Figure 3.6. Experimental rig used to perform the curing and leaching experiments. A: Incubator with temperature controller, and B: Schematic description of the experimental rig.....	76
Figure 3.7. Temperature controller used to control the conditions inside the incubator.	76
Figure 3.8. Multichannel peristaltic pump used for the leaching experiments.	77
Figure 4.1. X-ray Microtomography machine used to scan the columns of agglomerates.	81
Figure 4.2. Scanned sections of the columns.	82
Figure 4.3. Cross section of an XMT image acquired from an agglomerate at day 65 of curing, pointing the main components in the sample.....	83
Figure 4.4. Histogram of scans acquired at early and late stages of the curing process. (a) scan of early stages of curing pointing both the peak corresponding to the rock phase, and the peak corresponding to the sulphide phase, (b) scan of advanced stages of curing pointing the peak corresponding to the rock phase and the peaks corresponding to the sulphide grains and precipitates.	84
Figure 4.5. Agglomerates and glass column segmented from the background using the Otsu algorithm (Otsu, 1979). (A) grayscale image of the glass column where agglomerates were packed, (B) binary image of the agglomerates and glass column segmented from the background.....	85
Figure 4.6. The agglomerates are segmented using a connectivity analysis for subsequent assignment of a unique label. (A) the glass column is removed from the image, (B) segmented agglomerates, where each sample is assigned a unique label (represented by a different colour).....	86
Figure 4.7. Example of the agglomerate relabelling process performed using a combination of a centroid tracking algorithm together with a relabelling algorithm.....	87
Figure 4.8. Sulphide grain thresholding performed using both the Maximum entropy and the Moments algorithms for scans of different stages of the curing process. (A) shows the grayscale image, (B) shows	

the results obtained using the Maximum entropy algorithm; (b) shows the results obtained using the Moments algorithm.....	88
Figure 4.9. Two-step methodology for segmenting precipitates and mineral grains using a combination of the Maximum entropy and the Moments thresholding algorithms. (a) All metal-containing species are segmented jointly from the rock matrix using the Moments algorithm (presented in opaque yellow), (b) the sulphide grains are segmented using the Maximum Entropy algorithm (presented in metallic orange), (c) the sulphide-grain phase (in orange) is subtracted from the joint phase and precipitates (presented in bright yellow) are segmented as a single phase.....	88
Figure 4.10. Sulphide grains of the reference image are assigned a unique label. (A) sulphide grains of an agglomerate at day 0 of the curing process (presented in bright yellow), (B) a unique label is assigned to each sulphide grain in the agglomerate (each colour represents a unique label).....	90
Figure 4.11. Graphical scheme of the registration and grain tracking methodology. For this example, the sulphide grains of recipe D at day 14 are successfully tracked using days 4, 1, and 0 as reference.	93
Figure 4.12. Standard deviation of the relative error in volume measurement for a sample scanned twice. The sulphide grains were tracked using the grain tracking methodology explained in section 4.3.	95
Figure 4.13. Cumulative fraction by volume and particle size distribution (PSD) of the sulphide grains corresponding to curing agglomerates of recipes A and B.	96
Figure 5.1. Cross-sections of the XMT images obtained for columns of agglomerates of recipes A and B (with and without NaCl, respectively). On top, agglomerates of recipe A at days 0, 32 and 65 of curing and after washing (AW). On the bottom, agglomerates of recipe B at days 0, 30 and 65 of curing and after washing (AW)The XMT data can also be used to assess the evolution of the porosity distribution within the agglomerates. This is important for subsequent leach behaviour as this macroscopic internal porosity provides a path for reactants to enter the agglomerates and dissolved metal species to leave. 3D images of this internal porosity can be obtained using the methodology explained in section 5.2. .	100
Figure 5.2. 3D rendering of a single agglomerate of recipes A and B at different curing timesteps. The internal porosity of the agglomerates is presented in light blue, whereas the rock matrix in translucent grey.....	101
Figure 5.3. MLA results for two agglomerates of recipe A (containing 150 g/t of NaCl) after 65 days of curing. A: Agglomerate with high formation of the Cu – Cl – Kaolinite compound. The BSE image obtained from SEM is shown on the left, whereas the MLA is shown in the middle with a blue box, which is a close-up view of the precipitated material on the agglomerate surface. B: Agglomerate with high formation of the Cu – S – Cl – O complex. The BSE image obtained from SEM is shown on the left,	

whereas the MLA is shown in the middle with a red box, which is a close-up view of this compound precipitated in the internal pores and close to the agglomerate surface.	103
Figure 5.4. Copper-sulphide grain leached and reprecipitated after 65 days of curing. A: grayscale image; and B: elemental composition of the needle-shaped crystals that form as a product of the curing process.	104
Figure 5.5. Net change in grain volume as a function of distance to the grain surface at different curing times. AW represents the change in grain volume after water washing. All changes are relative to day 0.	105
Figure 5.6. Normalised concentration of species at different stages of the curing process, and after water washing the samples.	106
Figure 5.7. Dimensionless concentration of sulphide grains as a function of distance to the nearest surface.	107
Figure 5.8. Dimensionless concentration of precipitates as a function of distance to the nearest surface.	107
Figure 5.9. Precipitation ratio (PR) as a function of distance to the nearest surface.	109
Figure 6.1. Schematic of the transport and evaporation processes occurring over the curing or agglomerated ores.	112
Figure 6.2. Gamma distribution with standard values of $\alpha = 1.8$ and $\beta = 0.4$	122
Figure 6.3. Average concentration values of Mineral Grains (blue) and Precipitated Species (orange) for both XMT experiments and Simulations at day 20 of curing.	123
Figure 6.4. Precipitation ratio (ratio between precipitated species and the remaining mineral grains) obtained at day 20 of curing for A: XMT experiments, and B: Simulations.	123
Figure 6.5. Precipitation Ratio as a function of distance to the nearest surface for day 20 of curing obtained from simulations carried out considering Da values from $10 - 6$ to $10 - 1$	125
Figure 6.6. Precipitation Ratio as a function of distance to the nearest surface for day 20 of curing obtained from simulations carried out considering Da values from 10^4 to 10^8	126
Figure 6.7. Leaching extent for different rates of evaporation at day 20 of curing.	127
Figure 6.8. Precipitation Ratio at different curing times for different evaporation rates.	128
Figure 6.9. Leaching extent for different sizes of agglomerate at day 20 of curing.	129
Figure 6.10. Precipitation ratio at different curing times for different agglomerate sizes.	130
Figure 7.1. Copper recovery obtained from ICP-MS measurements.	134
Figure 7.2. Iron recovery obtained from ICP-MS measurements.	135
Figure 7.3. Metal sulphide recovery obtained from the XMT image measurements.	137

Figure 7.4. Relationship of recovery between image measurement and chemistry measurement from ICP-MS.	138
Figure 7.5. Average recovery for the entire column, for the three scanned volumes (top, middle and bottom) within each column and for the individual agglomerates.	139
Figure 7.6. Overall recovery for each agglomerate plotted as a function of its initial mineral content. (A) samples of type A with a coefficient of determination of $r = -0.051$, and (B) samples of type B with a coefficient of determination of $r = 0.036$	139
Figure 7.7. Overall recovery for each agglomerate plotted as a function of its initial size. (A) samples of type A with a coefficient of determination of $r = -0.137$, and (B) samples of type B with a coefficient of determination of $r = 0.207$	140
Figure 7.8. Internal porosity distribution as a function of distance to the nearest surface for two randomly selected agglomerates of each recipe type. (A) porosity distribution for agglomerates of recipe A, and (B) porosity distribution for samples of type B.	142
Figure 7.9. Cumulative fraction by volume and particle size distribution (PSD) of the sulphide grains corresponding to leaching agglomerates of samples A and B.	144
Figure 7.10. Overall change in grain volume for each size-distance category at different leaching times. (A) results obtained for agglomerates of recipe A, and (B) results obtained for agglomerates of recipe B.	145
Figure 7.11. EDX/SEM images and mineral map obtained for the five column sections analysed. (A) corresponds to the bottom section of column A, (B) corresponds to the medium section of column A, (C) corresponds to the top section of column A, (D) corresponds to the bottom section of column B, and (E) corresponds to the medium section of column B.	147
Figure 7.12. Pyrite grade of each column, section, and agglomerate at different stages of the process.	150
Figure 7.13. Copper-containing species grade of the full column, each section, and each agglomerate at different stages of the process for agglomerates of recipe A.	151
Figure 7.14. Cumulative distribution function of the rate constants for the different size categories and different distance to surface categories. Results obtained for days 1, 4, and 15.	155
Figure 7.15. Cumulative distribution function of the rate constants for the different size categories and different distance to surface categories. Results obtained for days 20, 25, and 32.	156
Figure 7.16. Cumulative distribution function of the rate constants for the different size categories and different distance to surface categories. Results obtained for days 39 and 46.	157

List of Tables

Table 3.1. Main mineral species within the ore feed used for the agglomeration tests. Bold indicates the totals for a category of mineral, with the individual minerals listed below.	67
Table 3.2. Particle size distribution of the ore sample.	71
Table 3.3. Chemical composition of solution used for agglomeration and leaching experiments.	71
Table 3.4. Composition of pulp used for agglomeration experiments.	73
Table 3.5. Rotational speed of tumbling drum used for agglomeration (described in section 3.3.1).	73
Table 3.6. Flowrate obtained at different rotatory speed values with four tubing cassette connections.	78
Table 3.7. Sampling intervals for collecting the PLS from the leaching experiments.	79
Table 4.1. Scanning intervals for the curing experiments.	82
Table 4.2. Scanning intervals for the leaching experiments.	82
Table 4.3. Scanning conditions and settings.	83
Table 5.1. Composition of the copper-chloride complexes formed at day 65 of curing. The fraction by weight of the sample that each of them represents is also presented (this information corresponds to the mineral map presented in Figure 5.3).	104
Table 6.1. Set of non-dimensional equations used to describe the curing of agglomerated ores.	116
Table 6.2. Set of non-dimensional equations used to describe the curing of agglomerated ores expressed in terms of the non-dimensional groups (6.17) to (6.21).	117
Table 6.3. Parameters used for solving the model. All quantities are in standard SI units.	121
Table 7.1. Main mineral species remaining at the end of the leaching process for agglomerates of recipe A and B. Bold indicates the totals for a category of mineral.	148

Chapter 1. Introduction

1.1. Motivation

Heap leaching is a hydrometallurgical method commonly used to process low-grade sulphide and oxide deposits. The continuous decrease in ore grades is one of the main reasons why processes such as heap leaching have gained popularity in recent years. It is a low-cost/low-impact process which involves crushing the ore, piling it into heaps, and then irrigating the mineral particles with a leaching solution in order to dissolve the metals. The solution percolates through the particle bed to be collected at the base of the heap, and this pregnant solution is processed to recover the dissolved metals. Heap permeability is one of the main issues of this process. Low percolation can be caused by high amounts of fine particles and clays. In order to improve heap permeability, agglomeration can be performed as an intermediate step between crushing and stacking. The agglomeration process is usually performed in rolling drums by the addition of binders and acid to form bridges between fines and coarse particles. After agglomeration, it is common to leave agglomerates to cure for periods from a few hours up to several weeks. Agglomeration and subsequent curing are widely used as pre-treatment for the ore prior to heap leaching as it both improve the permeability of the heap and brings leaching solution into close contact with the ore, initializing the leaching reactions.

Mineral exposure and permeability should be balanced in order to obtain the highest recovery. This could be accomplished with an optimum specification of the particle size distribution (PSD) for the heap. The effective particle size will determine the available void space for air and the percolating solution. Furthermore, the agglomerate size determines the maximum amount of moisture that the bed can retain. Some relevant parameters for heap leaching are mineral exposure/liberation, flow behaviour and particle interaction. However, these factors are difficult to examine using conventional methods in the mineral processing operations.

Agglomerate structure is typically analysed by testing electrical conductivity, permeability, and soaking. These are macroscopic tests and there is very little information that can be obtained about the agglomerate's internal structure. Although conventional methods such as microscopic techniques, SEM and MLA are used to obtain mineralogical information, these are destructive techniques that require the sample to be sliced in order to be analysed. This makes it impossible to track the agglomerate's behaviour over time. Consequently, advanced characterization tools such as X-ray micro tomography (XMT) could play an important role in understanding the factors in the performance of the ore agglomeration process and its subsequent curing and leaching. Since XMT is a non-destructive method for imaging the internal structure of objects in 3D, it is one of the most appropriate techniques to analyse the agglomerate

structure. Understanding the factors that influence the microstructure of the agglomerates and how these, in turn, affect the macroscopic properties is the first aim of this project.

One of the key factors in the leach performance are the apparent leaching kinetics. These apparent kinetics are a complex function of the mass transfer within the particle and the reaction kinetics at the mineral surfaces, with this relationship being strongly influenced by the mineralogical texture of the ore and the structure of the agglomerate. The second aim of this project is thus to experimentally track this behaviour using XMT with this data being used to develop and calibrate improved models for the curing and leaching process. This will require the development of techniques to analyse the series of 3D data in order to extract the time evolution of all the individual sulphide grains. This data will allow both the mass transfer and surface kinetic influences on the leach behaviour to be assessed, with this forming the basis for the development of an agglomerate scale simulator. This combination of XMT data and simulation methodology will be used to assess the likely impact of changes in the agglomerate structure on leach performance. These assessments are currently done experimentally, with the performance evaluation for each new agglomerate requiring experiments that take many months to carry out. For that reason, this study would also increase the industrial relevance and usefulness of the work, leading to improvements in process design and economical estimations for mineral processing projects.

1.2. Objectives

The main aim of this project is to experimentally track the behaviour of agglomerated ores during the curing and leaching processes. This will be performed using XMT in order to both improve our understanding of the internal processes, as well as to produce better models for the apparent kinetics.

Research questions:

- How is the agglomerate structure influenced by the parameters chosen for the agglomeration process?
- How much leaching occurs during the curing process and how is this influenced by the agglomeration recipe?
- What are the key factors that impact agglomerate performance during the leaching process?
- Can leach and curing performance be accurately modelled and simulated?

Chapter 2. Literature review

2.1. Hydrometallurgy

2.1.1. Introduction

Hydrometallurgy (HM) is the field of metallurgy that involves metal recovery from mineral ores using organic or aqueous media. Though it is a typical practice that these processes are operated at comparatively low temperatures, and in order to allow higher temperatures to be used in aqueous media, pressure can vary from a few bar up to very high pressures depending on the process requirements (Davenport *et al.*, 2000).

About 20% of the copper-from-ore is produced by hydrometallurgical methods (Davenport *et al.*, 1996). Lately it has gained popularity due to the continuous decrease in mineral grade (e.g. the average copper ore grade was of 1.13% in 2002, while only 0.84% in 2016 (Energy and Capital, 2016)) (Figure 2.1) and the high processing costs of conventional processing routes. Furthermore, HM processes require much less water compared to flotation and its operational controls are lower than in pyrometallurgical processes¹ (Ghorbani, Franzidis and Petersen, 2016). This has encouraged an explosive development in technologies for hydrometallurgical processes.

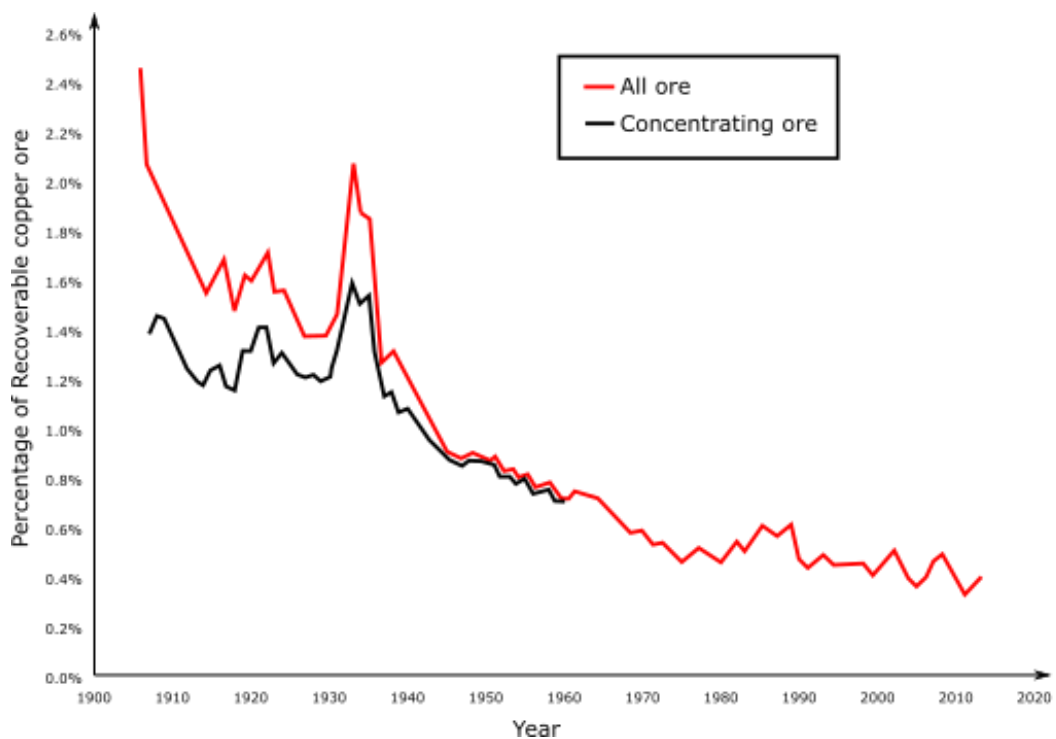


Figure 2.1. Decrease in copper grade over the last century (Energy and Capital, 2016)

¹ This can be both an advantage and a disadvantage.

2.1.2. Fundamentals of hydrometallurgy

There are three main processing stages in hydrometallurgy: leaching, concentration and purification of solutions, and final product recovery. All of them are usually performed in a successive series of stages, with the number of steps required to process each mineral depending on the type of ore and the metals treated. In minerals processing operations, the most typical processes are chemical leaching (LIX), solvent extraction (SX) and electrowinning (EW). This processing sequence is also known as LIX-SX-EW, and a brief description of each stage can be given as follows:

i) Chemical leaching: Chemical leaching is a dissolution process in which an aqueous solution is contacted with a valuable material (i.e. a compound to be extracted and/or concentrated) that is generally associated with gangue materials. Since the chemical reactions occurring in the leaching process are normally redox reactions, it is important to control the Eh-pH conditions of the system. Thus, the aqueous medium and its conditions are selected such that the valuable material can be dissolved by the leach solution and so it can be extracted from its containing body. It is also desired that the leaching of the gangue is minimised to reduce reagent consumption. Once the loaded solution (named Pregnant Leach Solution or PLS), reaches a certain concentration value (defined by the operation conditions), it is commonly replaced by fresh unloaded solution in order to maximize extraction. This can be a continuous or discontinuous process depending mainly on the economical limitations and the grade of the treated material.

ii) Solvent Extraction: The main aim of the Solvent Extraction process is both to exchange and concentrate ions, as well as to purify the solution. Since the conditions of the leaching process can produce the dissolution of undesired materials, several unwanted elements can also be present in the PLS. For this reason, a cleaning step is performed before obtaining the final product by Electrowinning.

In metallurgical operations, PLS is typically contacted with an Organic Extractant (OE) due to their difference in polarity, the PLS typically being polar and the OE non-polar, and for the high selectivity to ion exchange of some organic solvents. The contact process is a highly exothermic process, and it is usually performed in mixer-settler tanks. Even though the two solutions are immiscible, an intense mixing container is used to enhance contact between solutions. This is generally a multi-stage process, as the loading capacity of the OE is limited, and it is commonly performed as a counter current flow process in order to maximize extraction. Once the concentration of valuable material in the OE reaches a desired value, the depleted PLS can be recycled to the leaching stage and the loaded OE is contacted with fresh acid solution (also known as Electrolyte). This step is performed in order to exchange ions, unloading the OE and enriching the Electrolyte with the valuable material. The unloaded OE can be reused for solvent extraction processes and the electrolyte is sent to Electrowinning to obtain the final product.

iii) Electrowinning: The electrolyte is treated in a process called Electrowinning, the main aim being to obtain a final product of high purity. Solution is constantly pumped into through flow cells. A set of cathodes and anodes, which are connected to an electricity source, are submerged in solution and electricity flows through the electrolyte. Using the electrochemical properties of the solution, the electrical intensity can be controlled in order to deposit only the desired material and leave the unwanted components in solution. The obtained cathodes are of a typical purity level of over 99.9%, which is only achievable by a strict control of the overall process. Moreover, the depleted solution can be recycled to the Solvent Extraction stage, in which it can be loaded again.

Since the main objective of this thesis is to describe the leaching of agglomerated ores, the leaching processes that are unrelated to mining are out of the scope of this thesis. Thus, only chemical leaching will be described, being subsequently referred to as leaching.

2.2. Leaching process

Leaching is a process of selective dissolution of the constituents of an ore or a mineral concentrate. An aqueous solution containing the valuable metal is obtained, as well as an insoluble residue that contains the gangue material. This is mainly a mass-transfer process between a solid and a liquid phase, which may take place either at ambient conditions or at high pressure/temperature. In this section, the general physical and chemical processes associated to the leaching process will be described, while particular examples of leaching processes carried out at the industrial scale will be discussed in further detail in section 2.2.6.

Different types of solution can be used to leach mineral ores. Water-soluble compounds, such as sulphates and chlorides, can be easily dissolved with pure water. For the leaching of more complex ores, the addition of chemical reagents is generally necessary. Reagents such as acids, bases, complexing agents, oxidizing agents, and reducing agents, are commonly added to adjust solution conditions. These conditions vary essentially due to the characteristic dissolution mechanism of a specific mineral, which can be physical, chemical, electrochemical, or electrolytic. Thus, several reagents may be required to accomplish an appropriate dissolution.

A method for assessing the stability of minerals in solution is by analysing Eh-pH diagrams, also known as Pourbaix diagrams. These diagrams are constructed with the available thermodynamic information for the formation of different compounds. Using the Nernst equation, the Gibbs free energy of formation for a given compound can be transformed into a set of line equations where the pH and Eh are the independent and dependent variables, respectively. Since metals can occur in several mineralogical forms, in order to construct a Pourbaix diagram it is convenient to consider as many compounds as possible. This, though, may result in very confusing information due to mixed stability

zones and the presence of compounds that are unlikely to form in relatively short periods of time (i.e. compounds with very slow formation kinetics).

Metallurgical operations normally process oxides and sulphides separately² and only the most common minerals must be considered in order to assess an approximate behaviour of a mineral group in solution. For instance, considering the Cu – O – H system at ambient conditions and ion activity of 1 M, the stability zones for the main copper oxide minerals can be obtained (shown in Figure 2.2). The two black-dotted lines in the diagram represent the water stability zone, which changes with the system conditions (e.g. pressure and temperature). It is the area between these two parallel dotted lines which is the zone of interest for most hydrometallurgical processes.

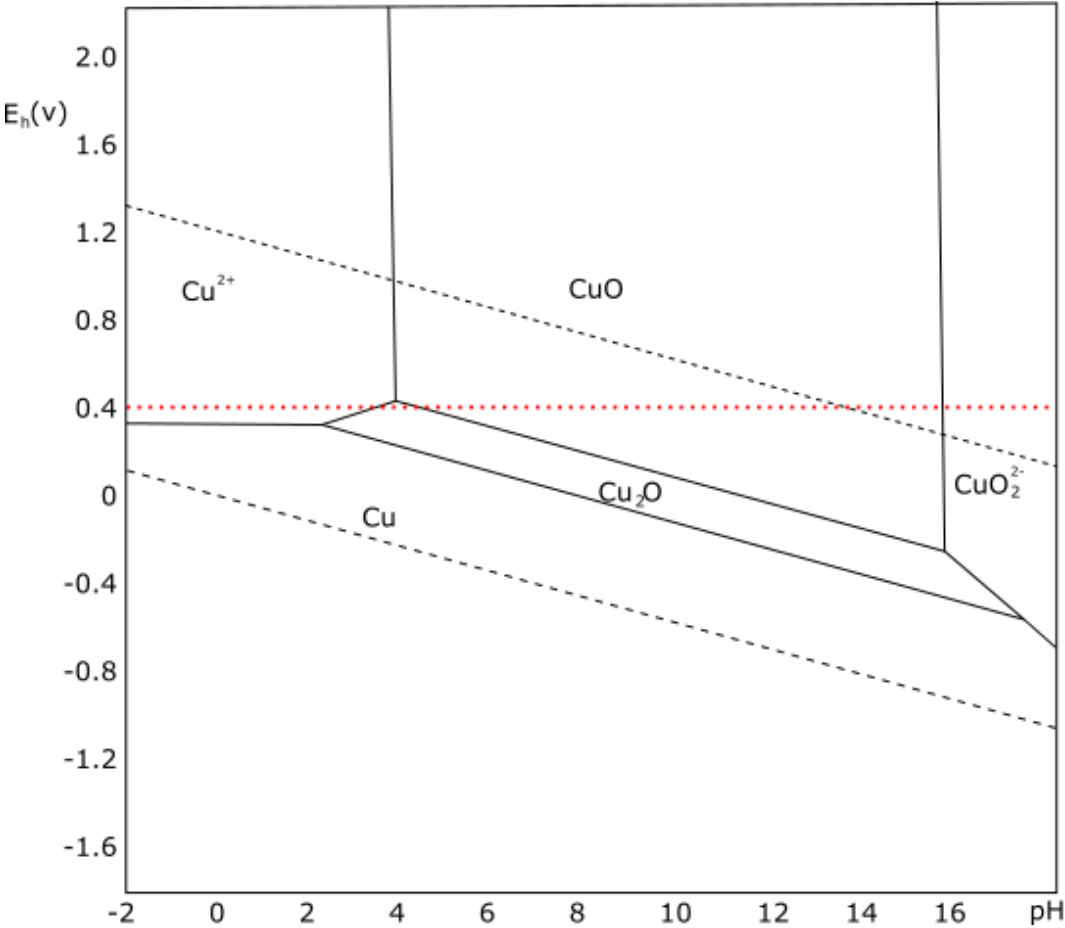


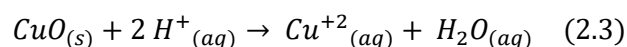
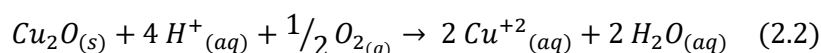
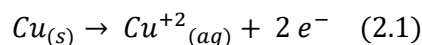
Figure 2.2. Eh-pH stability diagram for the system Cu-O at ambient conditions and ion activity of 1M.

The easiest way to analyse the diagram in Figure 2.2 is by fixing one of the variables (e.g. Eh or pH) and drawing a straight line that crosses the axis orthogonally on a selected value. As an example, if the Eh value is fixed at 0.4 V, a horizontal line that splits the diagram into two sections can be drawn. This red-

² Due to their natural occurrence, oxides and sulphides are commonly separated and treated in distinct stages. Although, at industrial scale, there will always be a certain degree of combination of both mineral types within leaching operations, especially in sulphide processing. It is thus convenient to consider both oxides and sulphides when assessing the leaching of sulphur-containing species.

dotted line in Figure 2.2 can be interpreted as a stability line for copper oxides at different pH values, with Eh fixed at 0.4 V. Following this blue-dotted line, it is easy to see that at high pH values (i.e. pH above 16), a copper oxide anion (namely CuO_2^{-2}) is the predominant phase. Whereas when pH is reduced, CuO is the most stable compound between pH values of 5 and 16; while below 5 and above 3, Cu_2O will be the predominant species. Lastly, for a pH lower than 3, the copper (II) ion is stable and will be the predominant copper compound in solution. Thus, a solution whose Eh = 0.4 V and pH < 3 can be used to dissolve copper from copper-oxide minerals, obtaining a PLS loaded with Cu^{+2} ions as the copper species at higher pH values are solids.

Another interesting piece of information that can be extracted from a Pourbaix diagram is the dissolution reactions of a specific mineral³. There are several chemical reactions considered for a single diagram, and the lines that divide the stability zone of the metallic ions and their forming compounds corresponding to the dissolution reactions. For instance, the lines that divide the stability zone of Cu^{+2} (top left corner) and $\text{Cu}_{(s)}$, Cu_2O , and CuO in Figure 2.2 correspond to the following dissolution reactions:



Pourbaix Diagrams can be built for almost any system. Several commercial programs include these diagrams or permit an easy selection of the specific data and conditions necessary to develop the diagrams. The only limitation, though, is the availability of reliable thermodynamic data. These diagrams also only give the thermodynamically feasible conditions and further experimental tests will be necessary in order to assess if the kinetics are fast enough to allow for economically feasible extraction rates.

2.2.1. Leaching of oxide ores

Oxide ores are minerals whose main component is oxygen. However, there are minerals that present similar behaviour (i.e. halides) and are commonly considered as part of the same group. Due to their geological occurrence and easier accessibility when compared to sulphide ores, these minerals are typically treated in the early stages of production (Figure 2.3).

³ This is the case for when the diagram has already been produced, as for producing a new diagram from the scratch, one may need to know all dissolution and formation chemical reactions.

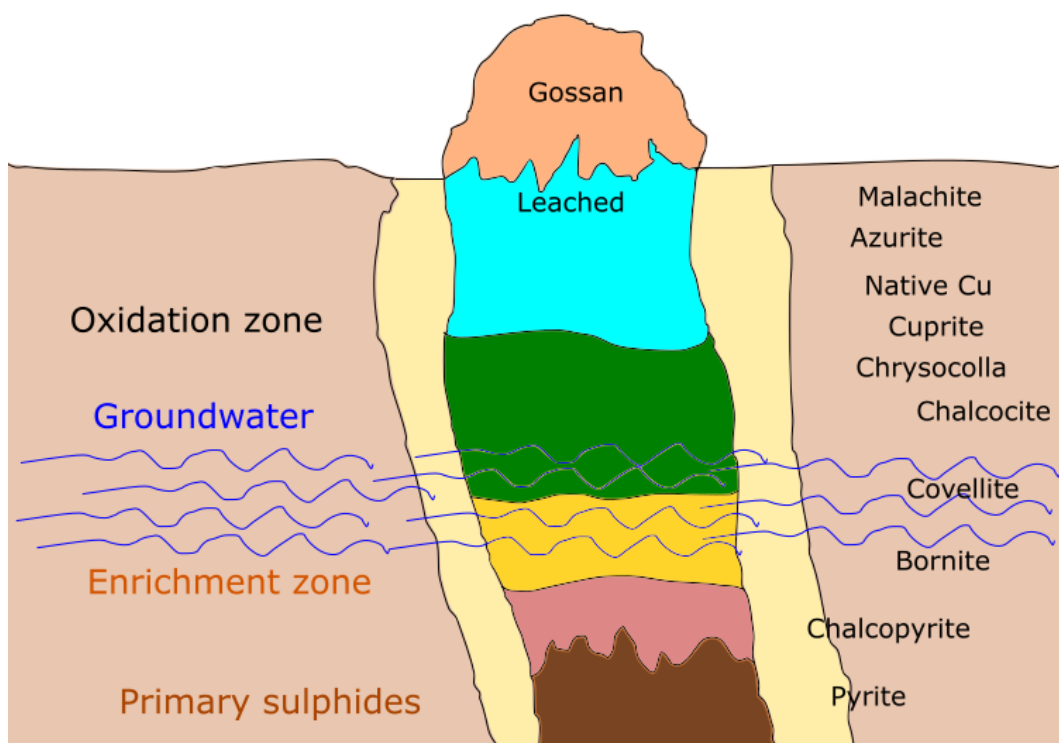
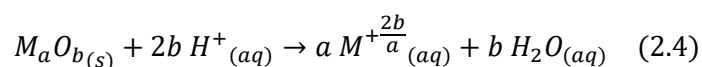


Figure 2.3. Schematic of the geological occurrence of copper minerals.

Leaching of oxide ores is commonly performed in an acidic medium, though there are a few oxide minerals that require the presence of an oxidizing agent (e.g. UO_2), or a reducing agent (e.g. MnO_2). Sulphuric acid is the most widely used reagent due to its abundance and relatively low cost. For certain minerals, leaching is also possible using basic media. An example is the leaching of bauxite (the main source of aluminium, consisting of various aluminium oxides with different degrees of hydration) in a NaOH medium. Bauxite can be leached in acid and basic media, though the product that is obtained from acid leaching is very difficult to filter and to wash/clean, whereas in basic medium (i.e. NaOH) controlled cooling is used to obtain a crystalline and clean aluminium precipitate, which is industrially implemented in the Bayer Process (developed in 1887).

For the case of chemical dissolution of oxides in acidic media, the process can be described by the following reaction:



Where a and b are integer numbers.

While equation (2.4) is only valid for minerals of the type $M_aO_{b(s)}$ (which is an association of two elements: a metal and oxygen), this equation is extremely useful to describe the main dissolution mechanism of the vast majority of oxides in acidic media. As the oxide mineral is contacted with a solution containing only H^+ ions, the metal M is extracted directly, and no other reagent is needed to adjust

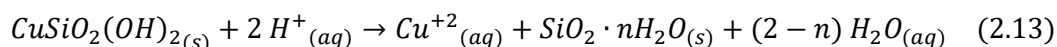
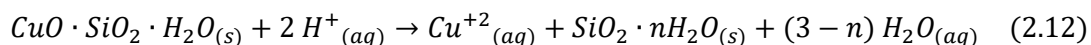
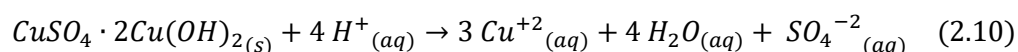
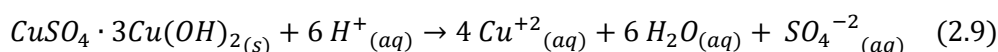
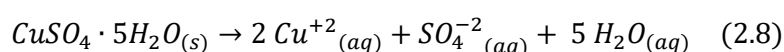
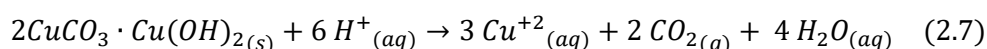
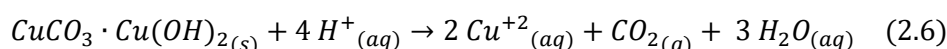
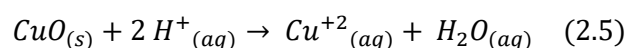
solution conditions. However, other chemicals will be present in most systems, which will influence the direction/equilibrium of this reaction by affecting the Eh and pH of the solution.

Mineral processing operations conventionally deal with more complex oxide minerals, such as carbonates, hydroxides, and silicates. These generally occur in the same geological deposits and are regularly leached with solutions of similar chemical conditions. Thus, most of these more complex oxide minerals are chemically dissolved and there is no requirement of a Redox pair to leach them. A suitable example are Copper-oxide minerals, as only chemical dissolution reactions are reported when leaching in acid media.

2.2.1.1. Leaching of copper oxides

Copper is commonly extracted from oxides by chemical dissolution, though an exception is the dissolution of Cu_2O which requires a redox pair. Leaching is commonly performed with a dilute sulphuric acid solution applied via a range of different operational methods, which mainly depend on the scale and type of mineral being treated. These operational methods will be further described in section 2.2.6

The chemical dissolution of the main copper oxides in acid can be described by the following reactions (María and Ruiz, 2013):



As described previously, $\text{Cu}_2\text{O}_{(s)}$ needs a redox pair in order to be fully dissolved and obtain copper (II) in solution. Thus, the reaction that describes the electrochemical dissolution of Cu_2O in acid is reaction (2.2), where the presence of oxygen permits a complete dissolution of copper (II) oxide. When there is a lack of oxygen, cuprite is only partially dissolved into Cu^{2+} and solid copper.

2.2.2. Leaching of sulphide ores

The leaching of sulphide ores is more complex than that of oxide ores, which are commonly extracted first because of their easier hydrometallurgical processing and accessibility (section 2.2.1). The importance of sulphide minerals is, though, increasing due to the depletion of oxides and the constantly

decreasing copper grades found in sulphide repositories⁴. Thus, as pits deepen, sulphides are found in a greater extent within the mineral deposit.

Sulphides are traditionally processed in a concentration plant, followed by a series of pyrometallurgical stages, finally obtaining a purified copper cathode by electrorefining. Since valuable metals are highly diluted in the ore, comminution and concentration are carried out to increase metal content in the feed to the fusion-conversion process (i.e. a pyrometallurgical smelting phase), with the main intention of decreasing energy consumption and maximizing equipment availability. Yet there is a metal-grade threshold below which it is not economically feasible to process a mineral ore in a concentration-smelter-electrorefining circuit.

Hydrometallurgical methods are the preferred option when it comes to processing low-grade sulphide ores due to their low cost and comparatively lower environmental regulations. Leaching can be performed both in tanks and by piling the material into heaps, the latter being the most common for processing low-grade sulphides. This is mainly because these processes involve virtually no milling (i.e. ROM material is directly packed into piles or is crushed before stacking) and are less energy intensive than pyrometallurgical processes. However, heap leaching has historically been reported as a poor alternative to process medium-to-high grade ores. This is mainly because of two reasons, namely the longer processing periods when it comes to achieving metal extraction extents that can be considered competitive, and the comparatively low recoveries, especially for primary sulphides such as chalcopyrite.

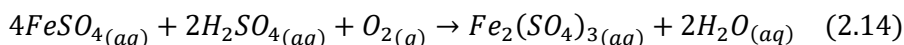
This disadvantage is reducing as more efficient HM techniques have been developed to process both high- and low-grade minerals. Processes such as high-pressure concentrate leaching has been developed to process the high-grade concentrate that was commonly processed using pyrometallurgical methods; and multi-stage leaching and leaching with addition of unconventional reagents are used to process lower grade minerals of coarser sizes. Still the bottleneck is that there is a shortage of knowledge on the decomposition chemistry of several minerals, which restricts the competitiveness of HM processes (Peters, 1976).

2.2.2.1. Leaching of copper sulphides

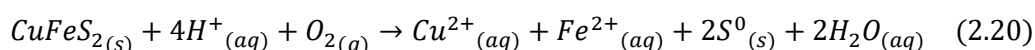
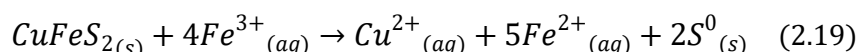
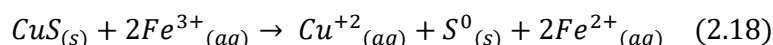
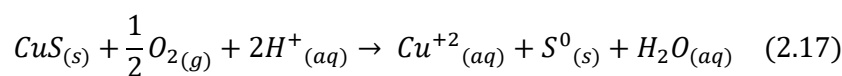
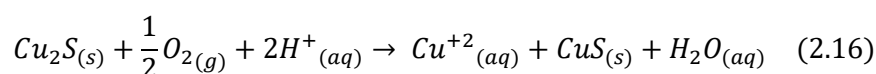
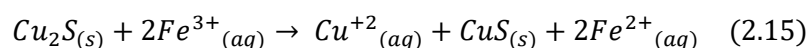
Copper sulphides are commonly refractory minerals with slow leaching kinetics. Their dissolution is typically electrochemical, and an oxidizing agent is thus necessary to maintain the appropriate redox conditions required to accomplish metal dissolution. Oxygen and ferric ions are commonly used as the oxidizing agent, the latter being typically responsible for oxidising copper sulphide and oxygen for re-oxidising ferric ions to ferrous (Davenport *et al.*, 2000) following reaction (2.14).

⁴ The cost of processing lower-grade ores via processes such as concentration may be even higher than the revenues.

At industrial scale, leaching is commonly performed by packing the ores into piles (i.e. heap or dump leaching), where the presence of bacteria within the ore bed aids sulphide leaching by transforming Fe^{2+} into Fe^{3+} (section 2.2.6.2) maintaining the appropriate redox conditions for metal dissolution. Another option is adding $Fe(III)$ ions directly to the leach solution, while maintaining a consistent oxygen concentration is extremely difficult. Most leaching methods require oxygen distribution pipes and inlets, though keeping a homogeneous oxygen flow is still a challenge.



Some examples of overall dissolution reactions in acidic media for the main copper sulphides can be summarized as follows:



Copper sulphides generally occur in poly-sulphide deposits, with the ore typically bearing more than one mineral type (e.g. primary and secondary sulphides together). It is thus common to leach these minerals together, having a combination of multiple reactions occurring simultaneously. Consequently, it is convenient to produce a Pourbaix diagram for the Cu-Fe-O-S system to gain an understanding on the processes occurring in leaching operations. For this purpose, reactions (2.5) to (2.20), as well as the formation reactions of iron sulphides and oxides that are most typically found in copper sulphide deposits (i.e. pyrite, pyrrhotite, magnetite, and hematite) must be considered. (Figure 2.4) shows this Eh-pH diagram, where it can be seen that primary copper sulphides, such as chalcopyrite (Cpy) and bornite, show a very refractory behaviour, meaning that typical leaching conditions will be insufficient. Meanwhile, secondary copper sulphides present a simpler dissolution mechanism and acidic oxidising conditions are sufficient to leach them out.

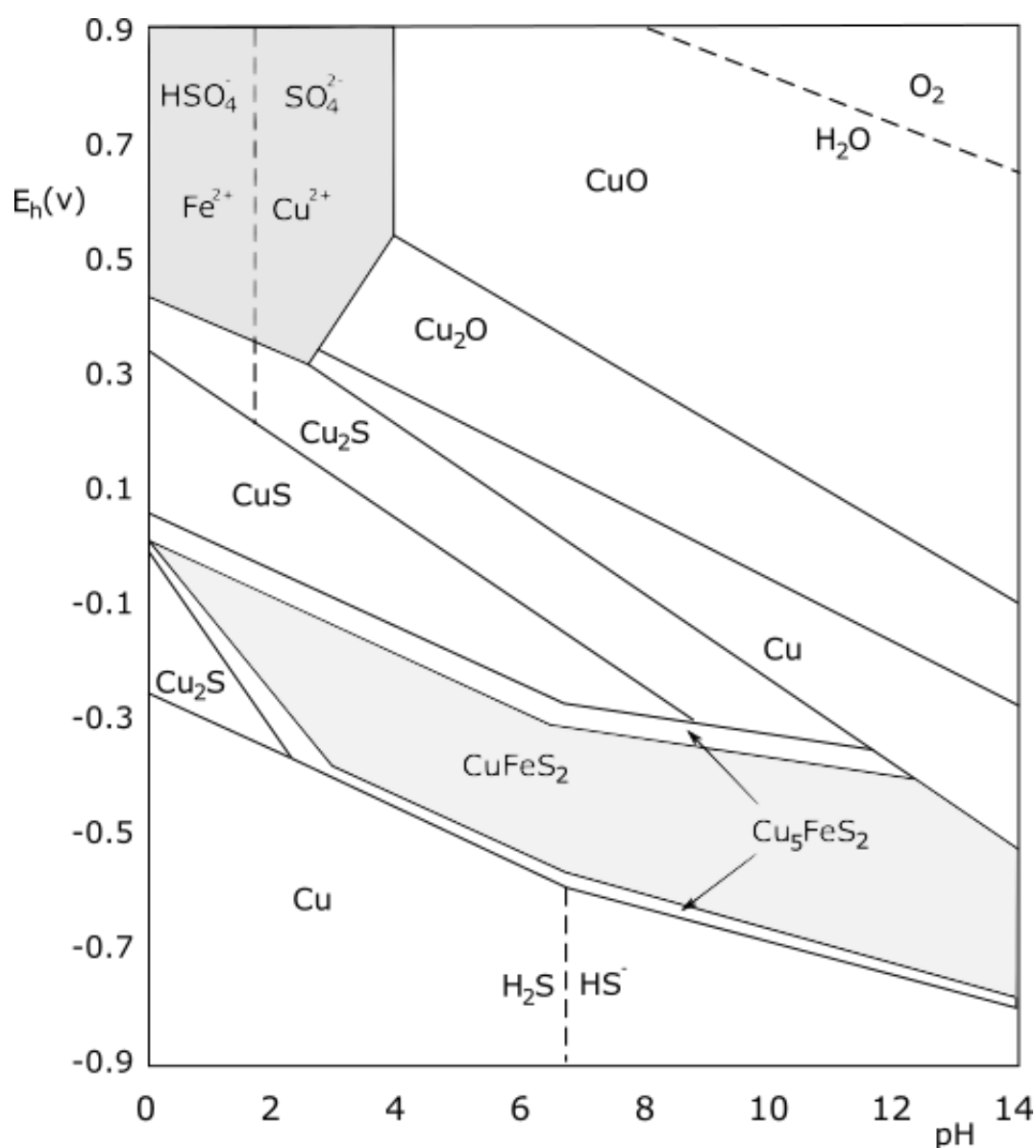


Figure 2.4. Eh-pH stability diagram for the Cu-Fe-S-O system at ambient conditions and ion activity of 1M.

While the leaching of copper sulphides has been studied for decades and, with this, the dissolution reactions of copper in various media are reasonably well known (e.g. equations 2.14 to 2.20), a critical limitation remains the formation of secondary reaction products or passivation layers (Figure 2.5). These layers are typically composed of a mixture of elemental sulphur, complex sulphides or polysulphides, iron oxides or hydroxides, and/or jarosite (Linge, 1976; Warren, Wadsworth and El-Raghy, 1982; Hackl *et al.*, 1995; Gómez *et al.*, 1996; Parker *et al.*, 2003; Sandström, Shchukarev and Paul, 2005; Córdoba *et al.*, 2008a, 2008b; Fu *et al.*, 2012), though recent results have suggested that sulphur and jarosite may be the primary cause of passivation (Klauber, 2008). Passivation is the result of the diffusion of reagents to and from the mineral surface being hindered due to the non-conductive nature of the

forming layer (Watling, 2013), turning the diffusion stage into a “bottleneck” that severely slows down the leaching process.

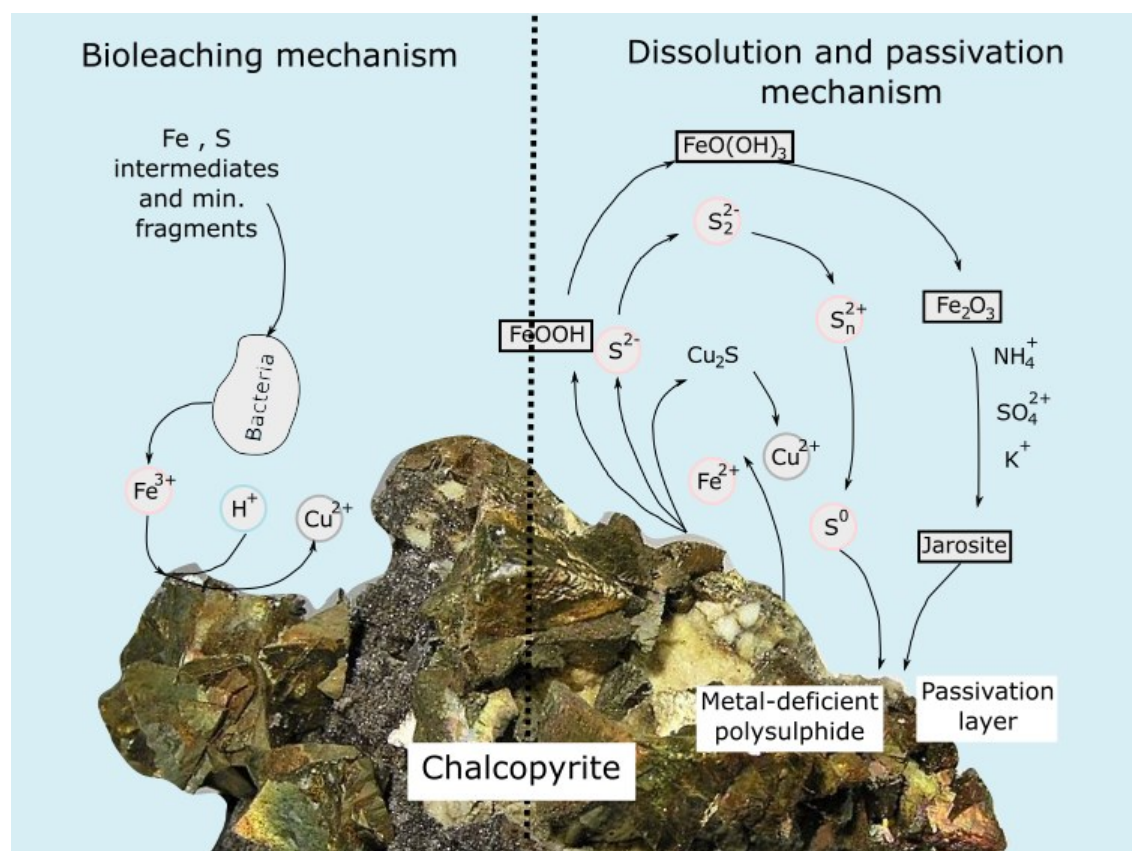


Figure 2.5. Schematic of the formation of secondary reaction products and/or passivation layer on a chalcopyrite grain. Adapted from (Zhao *et al.*, 2019).

Leaching performance can be enhanced by controlling the microorganism population (i.e. bioleaching), adding supplementary chemical reagents to the agglomeration and leach solutions, leaching sulphides under high temperature/high pressure conditions, and/or by fine grinding to increase reactivity and overcome passivation (Batty and Rorke, 2006; Harvey and Bath, 2007; Dixon, Mayne and Baxter, 2008). Important efforts have been put into combining these processes to achieve even superior results, though the main limitation as yet is that the operational conditions of each practice may affect the performance of the others. Bioleaching, Chloride leaching (as a type of leaching with addition of supplementary reagents), and Pressure leaching⁵ will be further discussed in sections 2.2.4, 2.2.5, and 2.2.6, respectively; while fine grinding will not be further revised due to the economical limitations of the most common leaching techniques (e.g. heap or dump leaching).

⁵ Unlike bioleaching and leaching with addition of supplementary reagents, high-pressure/high-temperature leaching is commonly a unit operation on its own.

2.2.2.1.1. Leaching of chalcopyrite

Chalcopyrite is the most abundant copper mineral (Parker *et al.*, 2003), accounting for approximately 70% of the world's copper reserves (Córdoba *et al.*, 2008b). As with most primary copper sulphides, chalcopyrite is a highly refractory mineral even in acidic ferric sulphate solutions. To improve their copper leaching rate, high leaching temperatures and high concentration of strong oxidants are required to increase the oxidation kinetics (Córdoba *et al.*, 2008c). Under High-temperature/high-pressure conditions, the redox couple Fe(II)/Fe(III) acts in a catalytic manner and the sulphur layer (section 2.2.2.1) is oxidised to sulphate, which is soluble in the aqueous leach solution (Davenport *et al.*, 2000). However, while chalcopyrite can be oxidized effectively in less than an hour at high pressures and temperatures above 180 °C, the process has a very high oxygen demand for the oxidation of sulphide to sulphate, and the oxidation of some associated sulphide minerals (e.g. pyrite) will generate sulfuric acid (Dreisinger, 2006).

Several researchers have pointed out that high redox potentials can also promote passivation of chalcopyrite during leaching (Córdoba *et al.*, 2009). (Córdoba *et al.*, 2008b) suggested that the passivation of chalcopyrite is related to high potential values (typically caused by a high $\text{Fe}^{3+}/\text{Fe}^{2+}$ ratio), and when the redox potential is initially very high, the tendency to the equilibrium of the ferric/ferrous pair favours the fast precipitation of ferric ions as jarosite and, thus, the passivation of chalcopyrite. Despite the evidence indicating that the passivation layer is the key reason for the slow leaching kinetics of chalcopyrite, there are researchers who argue that the refractory nature of chalcopyrite is a product of its semi-conductor properties (O'Connor and Eksteen, 2020). This property would be responsible for the slow dissolution rates under deficient redox conditions.

Environmental, technical, and economical limitations of pyrometallurgical processes have paved the way for competitive hydrometallurgical processing. The most common HM methods to process chalcopyrite are stirred tank leaching (section 2.2.6.5), pressure leaching (section 2.2.6.6), and heap (and dump) leaching (section 2.2.6.2 and 2.2.6.3). While extraction efficiencies of the former two are significantly higher, heap leaching is a more attractive option for ore deposits of low copper grade (i.e. Cu-grade below about 0.5%) as it can take place economically with lower technological requirements and no requirement for energy intensive milling or pre-concentration. However, heaps are more difficult to aerate efficiently and the undesirable formation of gradients of pH and nutrient levels, as well as liquor channelling are difficult to manage (Pradhan *et al.*, 2008). Moreover, the transfer rates of oxygen and carbon dioxide that can be obtained are low, and extended periods of operation are required in order to achieve sufficient conversions (Acevedo and Gentina, 1989).

Historically, heap leaching of secondary sulphides has been carried out by controlling the microorganism population within the ore bed (i.e. Bioleaching) (section 2.2.3), and while chalcopyrite bio-heap leaching has been implemented at the industrial scale, extractions are low and often only justified in dump leach applications where the material would otherwise be classified as waste through its low grade. A hybrid technology has been successfully implemented as an alternative in processing plants (Watling, 2013). This process combines the high recoveries associated with reactor bioleaching of chalcopyrite concentrate with the lower capital cost of heap leaching (e.g. The Geocoat process).

The addition of unconventional chemical reagents to the leach solution has also been shown to be a competitive option for the processing of primary copper sulphides (section 2.2.4). For instance, chloride leaching has been extensively proven to extract >95% of copper from CuFeS_2 at temperatures around the boiling point and at atmospheric pressure (Winand, 1991). This process offers significant advantages for hydrometallurgical processing, in supporting high metal solubility, enhanced redox behaviour, and increased rates of leaching (Liddicoat and Dreisinger, 2007). Chloride leaching processes have been implemented at the industrial scale, presenting relatively high extraction efficiencies, and providing a viable alternative to standard bioleaching.

2.2.3. Bioleaching

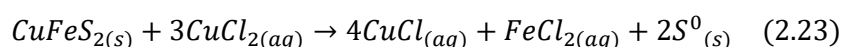
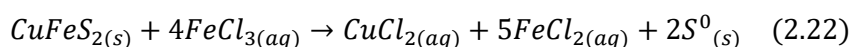
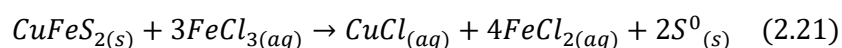
Bioleaching is a process in which the use of microorganisms facilitates the leaching of mineral ores, especially in the presence of sulphide minerals. These bacteria can occur naturally in sulphide-mineral heaps, but the supplementary addition of cultured bacteria has an important effect on the establishment of appropriate populations of biological organisms. Some bacteria live at ambient temperatures, while others need higher temperatures to thrive. Thus, specific microorganisms are cultured such that their vital energy is obtained either by oxidising metal sulphides, ferrous ions and/or elemental sulphur. Preliminary attempts to explain possible mechanisms for bioleaching were named as “Direct” and “Indirect” mechanisms and were later on replaced with mechanisms called “Contact”, “Non-contact” and “Co-operative” bioleaching (Gericke, Govender and Pinches, 2010; Schippers *et al.*, 2010). It is now recognized that bioleaching is inherently chemical where the role of microorganisms is to produce the necessary chemical reagents, like Fe (III) and protons, for the leaching of metal sulphides, thus maintaining the conditions for the reactions to occur. Bioleaching can thus be considered as a chemical system catalysed by microorganisms (Watling, 2013).

Approximately 15% of the world's copper production is currently recovered by bacteria-assisted leaching processes (considering both heap and dump leaching processes). Acidophilic bacteria are the most typically used due to the acidic conditions of copper sulphide leaching. In oxidative bioleaching processes, these bacteria oxidize ferrous ions to ferric ions, which oxidize copper, and the continual regeneration of ferric ions improves the copper-leaching rate (Norris and Owen, 1993; Clark and

Norris, 1996; Antonijević and Bogdanović, 2004). A remaining restriction and technical challenge for biomining is the leaching of chalcopyrite mainly due to its highly refractory behaviour and the development of an efficient bioleaching process for the recovery of copper from chalcopyrite is still a challenge. This process is expected to have applications not only in the treatment of low-grade ore, but also in the processing of mine tailings generated worldwide by the mining industry.

2.2.4. Chloride leaching

Chloride leaching⁶ is an attractive alternative to conventional bio-leaching methods as chalcopyrite dissolution at ambient temperature has been shown to have a higher reaction rate in a chloride/chloride-sulphuric media than that achieved using only a sulphuric media. The reason for this is that in the presence of chloride ions, the passivation layer formed by elemental sulphur (e.g. in reactions (2.15) to (2.20)) and other secondary products (section 2.2.2.1) becomes more porous and crystalline, permitting reactions to proceed (Lu, Jeffrey and Lawson, 2000b, 2000a; Carneiro and Leão, 2007; Ghorbani, Franzidis and Petersen, 2016). Furthermore, Cu⁺ is stable in chloride media, allowing the use of both Cu²⁺ and Fe³⁺ as oxidant ions for the dissolution reactions (Velásquez-Yévenes, Nicol and Miki, 2010) as shown by reactions (2.21), (2.22), and (2.23).



(Lu and Dreisinger, 2013) highlight that some of the main advantages of leaching chalcopyrite concentrates with a sulphate-chloride media are an enhanced redox behaviour, increased rates of leaching, pyrite is generally not attacked during leaching, and that the solution supports high metal solubility. The reaction mechanism depends on the chemistry and leaching conditions. Mixed-potential electrochemical models are commonly used to describe the dissolution of chalcopyrite in both chloride and sulphate media, although experimental data has shown that an extended reaction model in which chalcopyrite partially dissolves non-oxidatively provides a more consistent alternative (Nicol, Miki and Velásquez-Yévenes, 2010). The exact mechanisms and reaction pathways are, though, still a matter for debate (Liddicoat and Dreisinger, 2007; Yoo *et al.*, 2010; Veloso *et al.*, 2016; Bobadilla-Fazzini *et al.*, 2017).

High concentrations of chloride ions also allow stronger bridging between particles over the curing process and enhance leaching kinetics (Yévenes, Miki and Nicol, 2010). At the same time, though, chloride ions are extremely corrosive and common equipment is not sufficiently resistant. High

⁶ In this study the term “chloride leaching” refers to any leaching method which involve the addition of Cl⁻ ions.

concentrations of Cl^- may also cause several problems at the Electrowinning stage. Hence, one or more wash stages must be performed as a prior step to electrowinning the metal in order to maintain the electrolyte chloride concentration below 15-30 ppm (Burkhardt, 2003).

Combining bio and chloride leaching has been attempted with virtually no success. Even though small quantities of sodium chloride enhance leaching kinetics (100 mM or 0.35 g/L NaCl) (Yoo *et al.*, 2010), bacteria are not resistant to concentrations higher than 5 g/L. This situation limits the combination of both techniques, leading to further investigation in the field of bioengineering.

2.2.5. Particle scale effects in leaching

Leaching processes are carried out for particulate systems, which involve multi-size material. Leaching can occur with a wide size distribution and very different average sizes, which depends on whether tank or heap leaching is to be used. Typically, only a crushing stage is required prior to starting the chemical attack, although there also are processes in which material should be milled to a finer size (will be discussed in further detail in section 2.2.6). For this reason, there will be a broad distribution of sizes involved in leaching. Fines are of particular interest, as these will more likely be metal-rich particles and an agglomeration stage is typically performed to avoid metal losses (section 2.2.6.2.2). Thus, it is critical to thoroughly understand both the particle-scale effects of the multi-sized material involved in leaching, as well as their different hydraulic and physicochemical properties.

2.2.5.1. Particle size effects

Leaching kinetics are directly affected by particle size. Whether the process is diffusion-controlled or chemically controlled, the kinetics dependency will be proportional to $1/r$ and $1/r^2$, respectively. Thus, the volume-to-surface ratio is a key variable in the process, commonly obtaining higher leaching rates for finer particles due to their larger relative surface area. At the same time, it has been proven that leaching outer-shell mineral grains produces a less penetrable outer layer. After the depletion of surface minerals, the leaching solution must irrigate through the porous network or cracks to subsequently return the dissolved species to the surface (Ogbonna, Petersen and Laurie, 2006; Ghorbani, Becker, Petersen, *et al.*, 2011). This directly affects reagent diffusion, slowing down leaching kinetics at the long term (rim effect) (Ghorbani, Becker, Mainza, *et al.*, 2011), effect that can be typically negligible for very fine particles as the diffusion distance is much shorter.

2.2.5.2. Multi size systems

Leaching is a process that naturally involves particles of multiple sizes and while there may be processes that involve a certain degree of classification of particles by their dimensions, most will include a wide range of sizes. This makes the modelling of the process more difficult since not only one size of

particles need to be considered, but a distribution of sizes. Thus, more complex strategies are required to accurately represent the system.

Modelling the leaching of multi-size particulate systems where the reaction is controlled either by product-layer diffusion film transfer or by mass transfer through the pores/fracture spaces (which are the most common cases in leaching processes) is commonly carried out by considering all particles to be of a single size, commonly represented by the d50 or d90 of the system; or by solving the population balance equation. The latter is a much superior option as it considers the effective size distribution of the system and not only an approximation. By solving this equation, the various controlling mechanisms can be determined for each size fraction in the system. This may be combined with the material and energy balances in order to produce a better representation of the processes occurring within the system.

To obtain the most accurate results, the particulate system must also be appropriately characterised in terms of composition and morphology. This means that not only should the particle size be analysed, but also that extensive experimental work must be carried out to quantify the mass transport processes taking place in the system. A particularly important aspect to analyse is the grain distribution and accessibility to leaching solution within the particles since the leaching solution comes into contact with minerals by penetration through the unreacted gangue via pores and cracks, or partially reacted gangue, before reaching the target minerals (Rossi, 1990). This is a key factor that affects the leaching process, and its analysis and further understanding is a major aim of this study.

2.2.5.3. Particle porosity

Particle porosity is a critical variable for the performance of leaching processes, as it is through these pores that the leach solution flows and reaches the mineral grains to extract the valuable metals. Different types of porosity can be found throughout a particulate system, such as pores between the particles (inter-particle voids), pores within the particles (intra-particle voids), and microcracks that develop due to either chemical attack or previous comminution processes. All of these pore types play a critical role in enabling the contact between solution and the mineral grains and must be considered for the appropriate planning of the process. This will be further studied in section 7.4, where the link between changes in porosity over the leaching process and the leaching performance are analysed.

2.2.5.4. Gangue content

Valuable minerals are typically contained within a gangue matrix of no economic value, which in some cases can represent more than 99% of the sample's composition (as is the case with copper minerals). Plants must either concentrate the valuable mineral or ensure that the mineral grains are accessible to a selective leaching reagent. The selectivity of the leaching reagents is thus critical, as gangue minerals can potentially be highly reactive, causing an excessive consumption of leach solution and, worse

still, the dissolution of undesired elements from the gangue. Hence, an adequate characterisation of the ore, and more importantly of the gangue, is vital for an appropriate processing operation.

2.2.6. Leaching techniques

There are six main methods used for the leaching of copper minerals (Davenport *et al.*, 2000; María and Ruiz, 2013):

- In-situ leaching
- Heap leaching
- Dump leaching
- Vat leaching
- Agitation leaching
- Pressure leaching

Variables that affect the selection of the most appropriate leaching technique are the natural occurrence of the ore body, the topography of the mine site (including its climatic conditions), mineralogy of the copper-bearing ore, the copper grade, the ability to preconcentrate, and particle size (Davenport *et al.*, 2000), but it will mainly be determined by the prevailing economic conditions. The typical relationship between copper grade and ore particle size for different methods of atmospheric leaching is shown in Figure 2.6. It can be seen that heap and dump leaching are commonly performed using coarser ore particle sizes, meaning that a simple crushing stage will often suffice and the energy expenditure in the comminution process will be much lower than that of other leaching techniques.

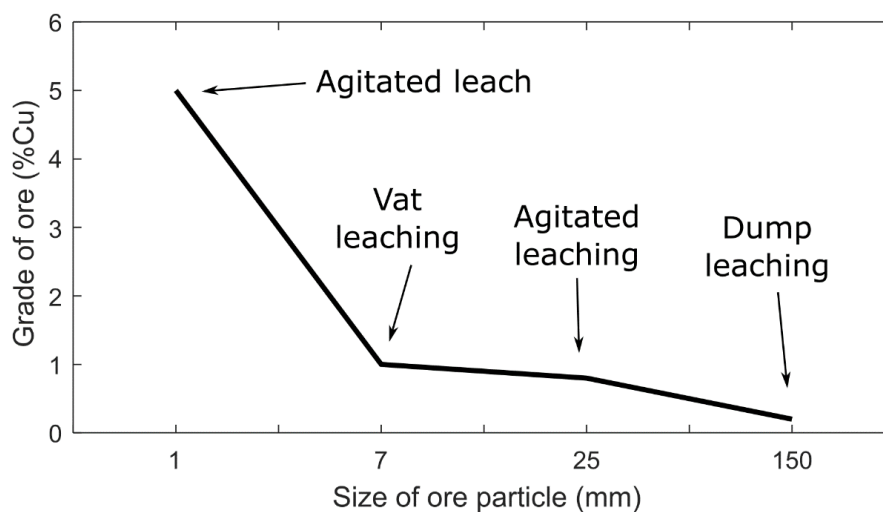


Figure 2.6. Typical relationship between copper grade and ore particle size for different methods of atmospheric leaching. Adapted from (Davenport *et al.*, 2000)

2.2.6.1. In-situ Leaching

In-situ leaching is a technique in which the leach solution is injected directly into the mineral deposit, thus avoiding with this both the extraction and comminution processes. This leaching method is commonly applied for underground deposits that are nearing completion of mining, or for extremely low-grade deposits (María and Ruiz, 2013), though there are important environmental concerns with potential contamination of groundwater and aquifers (Davenport *et al.*, 2000). The bearing ore is first fractured by using in-situ explosives (i.e. explosives directly placed within the ore deposit), and a drainage tubing system or pond is installed to collect and subsequently pump the metal-loaded solution to the surface.

This method has been used to leach low-grade copper and uranium ores, commonly lasting for several years and obtaining loaded solutions with a metal content of less than 1 g/L (María and Ruiz, 2013). The main difficulty comes from uneven irrigation due to channelling and lack of permeability. In-situ leaching can be classified into two main types, namely gravitational in-situ leaching and forced or pressure in-situ leaching. Gravitational in-situ leaching, which is the most widely used, is performed for deposits above groundwater levels, meaning that solutions move mainly by gravity and can be recollected from lower levels (María and Ruiz, 2013). While forced or pressure in-situ leaching is performed for deposits below groundwater levels, taking advantage of both the natural permeability of the ore and the high pressure/temperature conditions (María and Ruiz, 2013). In this process, solution is pumped under pressure within the rocks to force metal dissolution, which also pushes the PLS out of the ores.

2.2.6.2. Heap leaching

Heap leaching (HL) is the primary method for treating oxides and lower-grade secondary sulphide ores containing up to 0.5% Cu (Davenport *et al.*, 2000), though recent developments in the field of primary sulphides leaching have also enabled heap leaching of chalcopyrite on an industrial scale. It requires good planning to optimize solution percolation and metal recovery. HL involves crushing ore, piling it into heaps and then irrigating the top of the heap with a leaching solution, with the metal being leached out from the ore as solution percolates through the bed (Petersen, 2016a). The PLS collected at the base of the heap is then purified in an SX stage, to lastly obtain the final product by EW (Ghorbani, Franzidis and Petersen, 2016; Petersen, 2016). Figure 2.7 shows a basic schematic of this processing route.

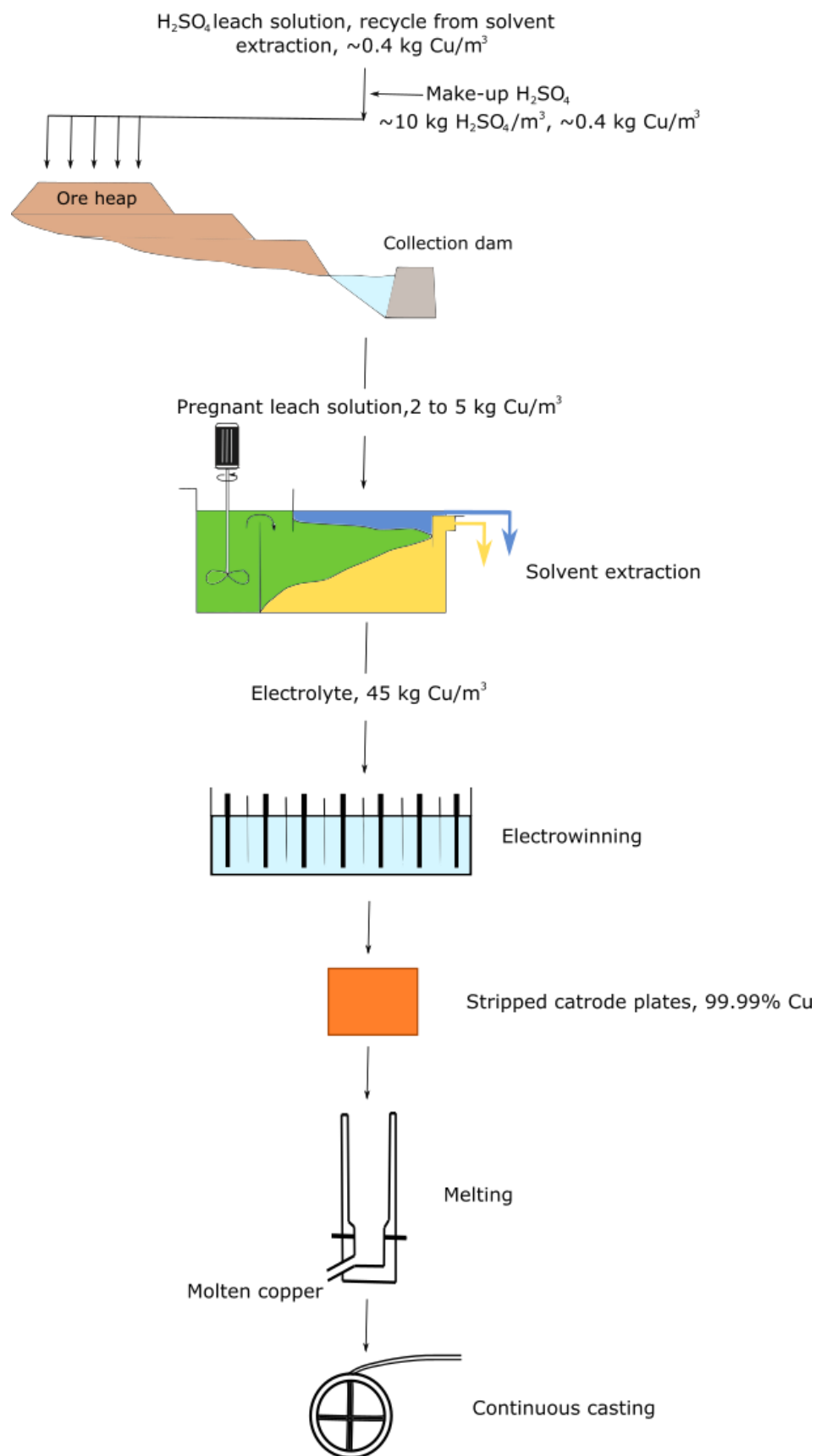


Figure 2.7. Basic scheme of a typical hydrometallurgical processing route.

Leaching processes may be affected by numerous factors, such as physicochemical, microbiological, intrinsic properties of the minerals and/or by the processing methods (Brandl, 2001). Moreover, depending on each particular heap leaching operation, more complex hydrodynamic and mechanical problems may arise. Therefore, the best results are commonly obtained when an appropriate compromise of advantages and disadvantages is achieved, and macro and microscale processes are deeply understood.

2.2.6.2.1. Chemistry of the heap leaching process

The dissolution chemistry of oxide ores is simpler than that of sulphides. An acidic medium will be sufficient to accomplish metal dissolution with reactions being those summarized in Eq. 2.5 to 2.13. Copper oxides tend to leach rapidly under heap leaching conditions (Davenport *et al.*, 2000), which is not the case of Cu sulphides. As explained in section 2.2.1.1, leaching of copper sulphide requires an oxidising agent as well as sulphuric acid (Eq. 2.14 to 2.19). These reactions are commonly assisted by micro-organisms (i.e. bacteria), which may occur naturally or be supplemented artificially (section 2.2.3). While chalcocite may leach readily under typical heap leaching conditions, the dissolution of bornite and covellite may take from 90 days to three years (Davenport *et al.*, 2000). Chalcopyrite rarely reacts more than 50% due to the passivation layer that forms on its surface, and a suitable option to promote Cpy dissolution is the addition of supplementary reagents to the leach solution; in particular, as it is the case study for this thesis, the use of chloride ions in heap leaching (section 2.2.4). These unconventional reagents improve sulphide dissolution by enhancing the diffusion stage, which is always the controlling process in heap leaching.

Long processing times in heap leaching are due to changes in the diffusion rate, a major cause being the presence of clays and micas in the gangue (Davenport *et al.*, 2000)(section 2.2.5.4). However, the complete heap leaching system is complex and multiscale, with many interacting mechanisms at work. Other processes that are also important include the transport of fluid through the packed bed, the mass transport within the ore particles and reactions such as the dissolution of metals and other species taking place at the mineral grain surfaces (Ferrier *et al.*, 2016).

2.2.6.2.2. Industrial Heap leaching

Key parameters in heap leaching include permeability, mechanical stability, and mass transport. To achieve an adequate performance, optimum specification of the PSD is one of the main parameters to control (Ulrich, Andrade and Gardner, 2003; Kodali *et al.*, 2011; Dhawan *et al.*, 2013). The effective particle size will determine the available void space for air and the percolating solution. The most critical percolation problems are ponding and irregular flow of solution. The latter occurs when preferential flow occur and the leach solution cannot reach all the particles in the heap, with a direct effect on the ultimate

metal recovery. Ponding occurs when the solution accumulates in a zone from where it cannot flow, causing mechanical problems and even structural failures of the heap (Velarde, 2005).

Heap height is a compromise to maximize copper recovery at the lowest possible cost (Fagan, 2013; Petersen, 2016a). Lower heaps have greater area under leach (i.e. greater area on the top per volume of heap), increasing pumping requirements, extra drainage piping, and highly diluted PLS (due to the larger volumes of leach solution required) (Davenport *et al.*, 2000). Though advantages of lower heaps are a better overall copper recovery, the fact that may not require forced aeration, and permeability problems are less common at the base of the heap.

Construction of the heap

Leach heaps can be either multi-lift permanent heaps (Figure 2.8) or on/off (dynamic) heaps (Figure 2.9) (Davenport *et al.*, 2000). Multi-lift heaps consist of multiple 5-8 m lifts built on top of each other, where each new lift is built once the previous level has been leached. Heaps can reach a total height of up to 200 m (Petersen, 2016a). The main advantages are that the ore needs to be moved only once (on top of the heap), and that lixiviant can flow through all the lifts permitting additional recovery of copper from slower-leaching minerals in lower lifts (Davenport *et al.*, 2000). The disadvantages, though, are that construction of a heap requires strong impermeable base and versatile heap-building equipment, and good planning is essential as the initial base area must be large enough to hold all of the ore that will be treated during the life of the operation (Davenport *et al.*, 2000).

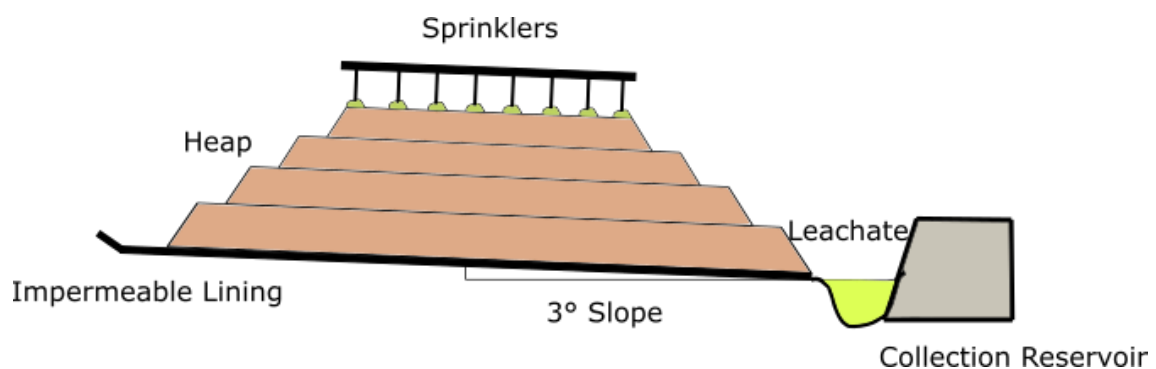


Figure 2.8. Schematic of a permanent heap, indicating very basically the standard components and conditions.

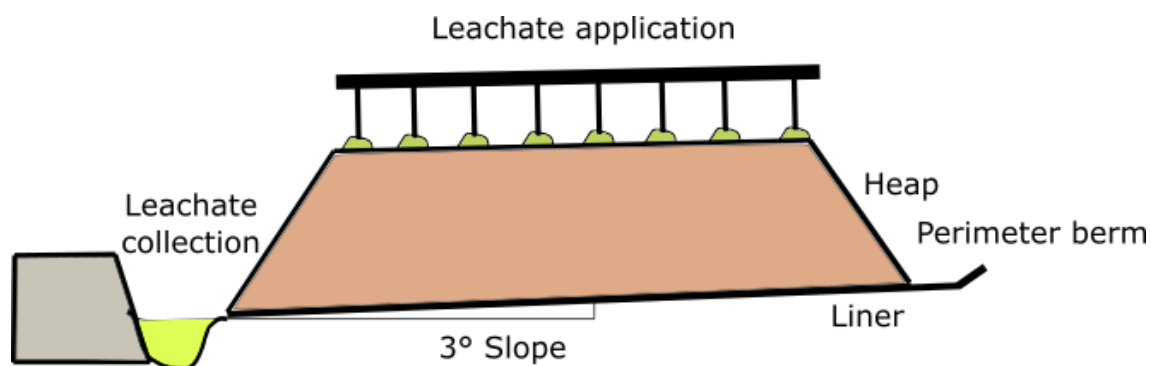


Figure 2.9. Schematic of an on/off (dynamic) heap, indicating very basically the standard components and conditions.

On the other hand, dynamic heaps consist of a single 7-12 m high pile built on an impermeable liner. The leached material is removed after leaching and replaced by a fresh pile of material. The greatest advantages of on/off heaps are that they are simple to construct, it is easier to control leaching at optimum conditions, the impermeable base need not be as strong as those needed for multi-lift heaps, and the aeration and PLS pipework can be maintained when the ore is removed from the pad (Davenport *et al.*, 2000). While the main disadvantages are that ore must be moved twice (on and off the pad) and the associated costs of residue disposal (Davenport *et al.*, 2000).

Impermeable base

Heaps are commonly built on an impermeable base. This base, also called a leach pad, consists of a plastic lined facility or geomembrane sheet commonly made of high or low-density polyethylene (HDPE or LDPE), polyvinyl chloride (PVC), or chlorinated PVC (Davenport *et al.*, 2000), yet the most popular materials used in modern leach pads are HDPE and LLDPE (Lupo, 2010) (both HDPE and LLDPE geomembranes are suitable for containment of acidic solutions and metal leaching products for periods of over 50 years (Renken, Mchaina and Yanful, 2005). This pad is essential for heap construction, however the liner system also involves some other design elements, such as foundation, liner bedding soil (rolled clay or earth is placed beneath this pad), a geomembrane liner, a protection layer directly over the geomembrane (e.g. a layer of finely crushed rock), a drainage or solution collection layer, solution collection pipes, air injection layers, and an air injection piping system (Lupo, 2010) (Figure 2.10). The ore is placed on top of this liner system, and PLS is collected at the base of the ore heap using a solution collection system, with the leach solutions eventually routed to a process plant for processing (Lupo, 2010). If permeability of lower lifts becomes a serious problem, it is possible to install intermediate liners. Although, there are two problems with their installation, namely that the heap below the liner is compressed as the upper lift is placed, and the ore below the liner cannot be washed with water, which is sometimes required as a part of final heap closure (Kappes, 2002).

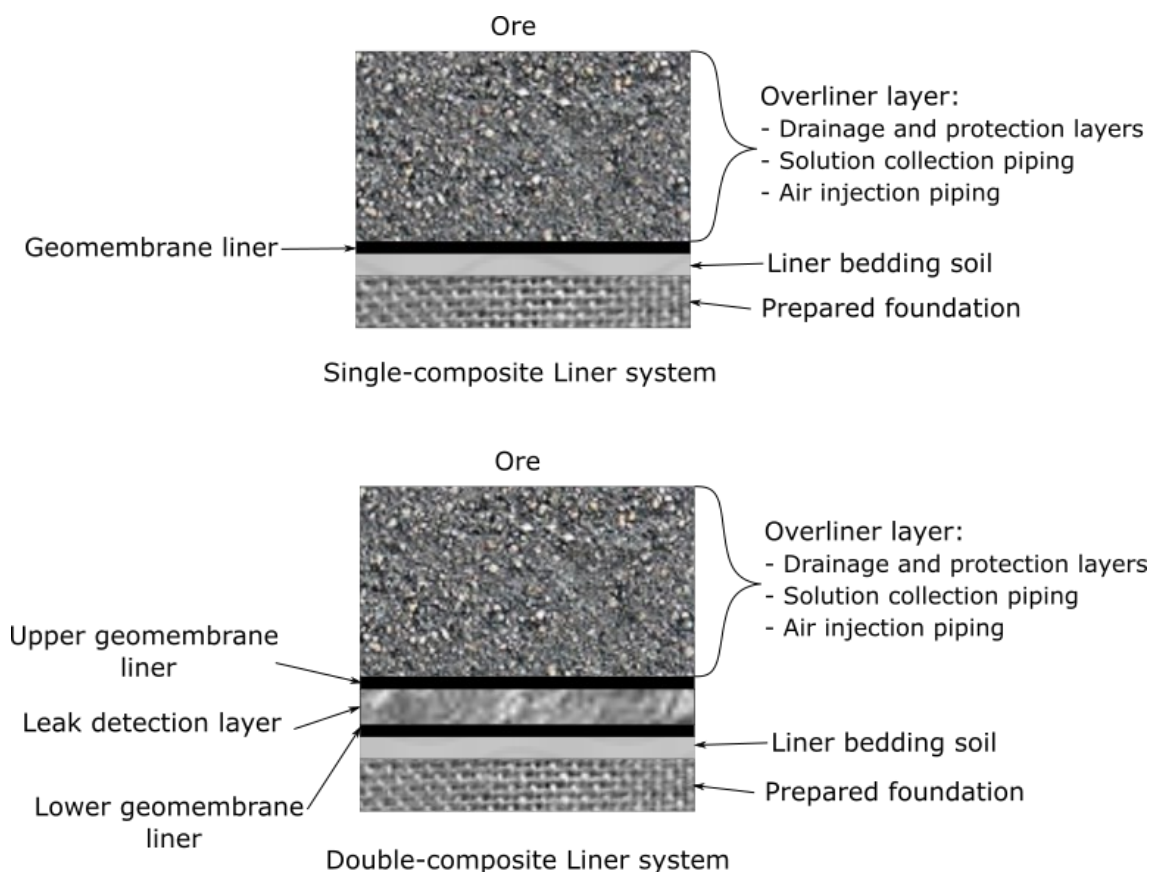


Figure 2.10. Schematic of a leaching pad. A single-composite liner system is presented on top, and a double-composite liner system on the bottom. Adapted from (Lupo, 2010).

Pre-treatment of the ore

A method for avoiding both low hydraulic conductivity and mechanical problems in a heap is to perform agglomeration as an intermediate step between crushing and stacking the ores into heaps. Agglomeration is frequently carried out when the fraction of fines⁷ is more than 50%. After contacting the ore with an agglomeration solution and producing agglomerates using a pan or drum agglomerator, a subsequent curing period is often carried out prior to irrigating the pile with the leach solution. While the primary purpose of curing is to develop mechanical strength in the agglomerate, it is also during this process that a first chemical attack on the minerals occurs, kickstarting the leaching reactions. It is thus essential to understand the impact of both the chemical composition of the agglomeration solution and the length of the curing process on the overall leaching performance.

Industrial-scale agglomeration is carried out using tumbling drums, belt conveyors, disc agglomerators or plug mills (Bouffard, 2005). In the copper ore industry, drum agglomeration is the most common practice. Crushed mineral and agglomeration solution are fed together to an inclined rotating

⁷ In the case of heap leaching, as typically ROM material is used, particles below 6 – 10 mm are considered to be fines.

drum. Agglomerate's moisture content, shape, and mechanical strength will depend directly on the parameters used for the process. Therefore, rotatory speed and inclination angle are monitored and manipulated to produce agglomerates of the desired quality (Figure 2.11). (Bouffard, 2005) summarises the three steps for a correct selection of the drum specifications, which are the calculation of the drum critical and normal rotation speed, the residence time, and the mass of mineral to be processed.

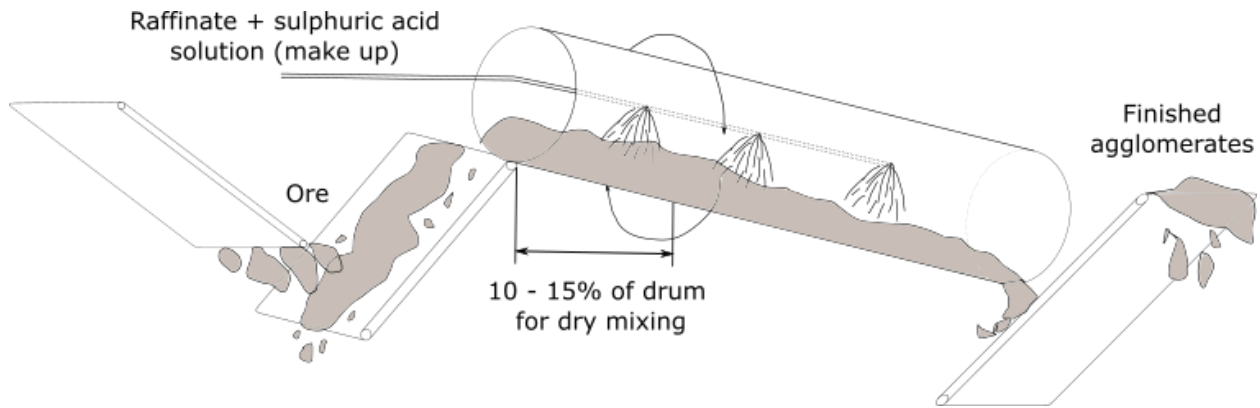


Figure 2.11. Schematic of a tumbling drum agglomerator and very basic description of the standard operational conditions. Adapted from (Bouffard, 2005)

Commercial drums are rarely more than 15m long and the rotation speed is commonly kept at 30 to 50% of the critical speed. For a rolling drum, the speed at which the centrifugal forces equal gravitational forces at the drum shell is called the critical speed and is defined as:

$$C = \sqrt{\frac{g \sin \theta}{2\pi^2 D}} \approx \frac{42.3}{\sqrt{D}} \quad (2.24)$$

where C is the critical speed (measured in rpm), D is the drum diameter (in m), g is the gravitational acceleration (m/min^2) and θ is the angle of the drum from the vertical (usually between 80 and 90°). In order to keep a correct agglomeration pattern, less than 20% of the available volume is used by the crushed ore and the binding agents (Bouffard, 2005).

While most of the heap leaching literature has focused on the active leaching stage, there is evidence that promoting leaching reactions during the agglomeration and curing stage can enhance the overall performance of the heap leaching process (Lu, Dreisinger and West-Sells, 2017). It is thus common to use a mixture of acidic solution or raffinate, bacterial cultures and its nutrients (Davenport *et al.*, 2000), and other chemical reagents as the agglomeration solution in order to enhance metal dissolution during the curing process.

During the curing stage agglomerates dry out, and cementation reactions occur. Part of the solution contained within the agglomerates will also be metal dissolution products, and much of the dissolved

metals will reprecipitate due to saturation of the solution brought about by evaporation of moisture (Purkiss and Anthony, 2002). These precipitates are generally acid and water soluble and will be readily removed in the following leaching stage.

The length of the curing process is a critical variable to control, though the optimum curing time will depend on both the mineralogical characteristics of the ore, as well as on the reagents added to the agglomeration solution. A number of researchers have demonstrated that an extended curing period will enhance metal recovery (Quezada *et al.*, 2018; Velásquez-Yévenes, Torres and Toro, 2018; Hernández *et al.*, 2019). Although, there is very little literature on the structural evolution of agglomerates over the curing process. Furthermore, assessing agglomerate quality is extremely difficult. This is mainly due to both the multiple definitions of “good quality agglomerates” that can be found, and due to the lack of standardized testing techniques. Generally, high standard agglomerates must be mechanically resistant, chemically compatible with the process conditions, curable at low temperature, and highly porous (Bouffard, 2005; Lewandowski and Kawatra, 2009; Kodali *et al.*, 2011). Common testing techniques usually only provide macroscopic information, being unable to characterize the internal structure of the agglomerate. Additionally, the sample preparation procedure of common imaging techniques, such as SEM/EDX (e.g. MLA, TIMA or QEMSCAN), involves destroying the sample. This makes it impossible to track structural changes over time. This work will thus extend existing knowledge by investigating the agglomerate and grain scale processes occurring during the curing process, assessing with this macro and micro-structural changes and their impact on the subsequent leaching process.

Stacking of ore on a heap

The ore (or agglomerated ore) is stacked into piles by two different methods, which depend on the leaching operation extent (tonnage). In operations of less than 2000 tpd (tonne per day), material is usually dumped from trucks or conveyor belts; while for larger operations, which may treat up to 20,000 tpd, ore is stacked using a wheel loader or mobile conveyor (grasshoppers) (María and Ruiz, 2013). Trucks have the advantage of simplicity but tend to compact the heap as they run over it, reducing permeability of the heap, decreasing leach kinetics, and limiting oxygen circulation in the heap (Davenport *et al.*, 2000). These problems are commonly avoided using conveyors, which makes them the preferred option today (Davenport *et al.*, 2000).

Aeration of the heap

The leaching of sulphides is dependant of both the presence of an oxidant and low pH conditions (section 2.2.2.1), and the reaction rate depends on mass transfer processes, specifically oxygen supply in many cases (Leahy, Philip Schwarz and Davidson, 2006). Oxygen also enhances bacterial activity (Watling,

2013). Without the use of sparging, oxygen supply to the heap depends on natural convection, which only occurs when temperatures inside the heap are greater than outside (Leahy, Philip Schwarz and Davidson, 2006). Furthermore, heaps with height larger than 10 m that does not have forced aeration are ineffective in terms of copper recovery due to lack of air flow (Aroca, Backit and Jacob, 2012). Therefore, air sparging (forced aeration) is common in leach heaps in order to ensure an appropriate operation.

Air injectors are placed within the heap right on top of the liner system (as previously shown in Figure 2.10) to provide a uniform air flow (i.e. oxygen flow) upwards through the pile. The additional cost of providing oxygen to the heap is more than offset by the increase in recovery and enhanced kinetics that result (Kappes, 2002; Bouffard, 2005). Forced air supply is also typically used when pyrite oxidation is the main source of solution heating in colder climates (Davenport *et al.*, 2000).

Irrigation

The lixiviant used is the copper-depleted raffinate returning from SX (Davenport *et al.*, 2000). The acid concentration of standard leach solutions can range from 3 to 16 gpl (equivalent to a pH of 0.5 - 2) (María and Ruiz, 2013), with the acid content depending directly on ore mineralogy. When the reactive gangue represents a high fraction of the ore, the acid requirement is commonly also high and make-up solutions are generally added to the recycled raffinate to increase its acid content. Water may also be added if evaporation is high or to replace ore hold-up losses (Davenport *et al.*, 2000). The lixiviant is added via an equi-spaced network of plastic pipes and drip emitters, wobblers, or sprinklers laid on top of the heap (Davenport *et al.*, 2000). Sprinklers and wobblers have the advantage that they distribute solution evenly over large areas, whereas drip emitters avoid excessive evaporation and cooling losses, though they need more maintenance. However, due to environmental concerns from dispersion of acidic droplets when wind blows, sprinklers and wobblers are out of favour.

The irrigation rate is typically of 10 L/h per m² of heap surface. Such a low rate prevents hydraulic and percolation problems in the heap and reduces solution accumulation on the surface (Petersen, 2016b). The leach solution is commonly added at ambient temperature, though it might be heated in cold regions to increase reaction kinetics (Bouffard, 2005). While dissolution reactions are exothermic, which will slightly increase the heap temperature, there will be heat losses due to evaporation. A well-balanced equilibrium of the irrigation pattern, acid content in solution, and the aeration rate will ensure that heap temperature is optimum (excessively high temperatures may kill bacteria, while cold slows down the leaching rate).

Optimum leach conditions

(Davenport *et al.*, 2000) summarizes the conditions that promote leaching as:

- Uniform heaps of optimally sized, cured, and agglomerated ore.
- Leaching conditions that maximize bacterial activity (30 °C, pH 1.5 – 2.5, 5 – 10 g/L sulphuric acid, limited organics).
- Uniform irrigation rate (approximately 10 L/h per m² of heap surface).
- Well-designed impervious heap base.
- Adequate heap temperature, depending on the mining site location.
- A controlled and uniform air supply.
- Heap height that is appropriate to the geo-mechanical characteristics and mineralogy of the ore.

Collection of PLS

The PLS collected at the base of a heap typically contains 1 - 6 g/L of Cu²⁺ (Davenport *et al.*, 2000). Heaps are commonly constructed in terrains with a slope of 3 - 5° (María and Ruiz, 2013), and PLS flows by gravity through drainpipes (~10 cm diameter). The pipes, which are spaced 2-4 m apart, have slits 2 mm wide, 20 mm long through which the PLS enters (Davenport *et al.*, 2000). The PLS flows in the collection trench to a PLS pond, to be later sent to the SX circuit. After the solution purification stage, the depleted acidic solution is returned to leaching and reused for both agglomeration and leaching.

2.2.6.3. Dump leaching

The dump leaching technique is very similar to heap leaching, but it is commonly used to treat extremely low-grade minerals (María and Ruiz, 2013). The chemistry, optimum conditions, and hydraulic issues are the same as for heap leaching, although to minimise costs, agglomeration is not performed as a pre-treatment. Dumps are built with run of mine (ROM) material or gravel recycled from previous leaching processes and may be as high as 200 m (Davenport *et al.*, 2000), and 80 m wide on the top and 250 m on the bottom (María and Ruiz, 2013). Metal recoveries are commonly low, ranging between 30 to 75% for processes that may take several years (Davenport *et al.*, 2000).

2.2.6.4. Vat leaching

Vat leaching is applied to high-grade oxide minerals of a size between 5 and 20 mm. The leach solution flows in a counter-current manner between a series of vessels that contain the ore to be processed (Figure 2.12). The solution containing the higher concentration of acid enters the last vat, so it is contacted with the lower-grade ore; and as acid concentration decreases, the leach solution is contacted with higher-grade ores (María and Ruiz, 2013). Each vat is equipped with a draining system that permits the PLS to be filtered and sent to the next vessel. The remaining ore is contacted with fresh liquor once the contact time has been reached. This cycle is repeated until the desired metal extraction extent is reached, with the number of cycles depending directly on the solubility of the leached minerals.

Once the leaching process has finished, the ores are water washed in counter current style to recover any remaining solution held in the ore bed (which can represent up to a 30% of the total leached copper) (María and Ruiz, 2013).

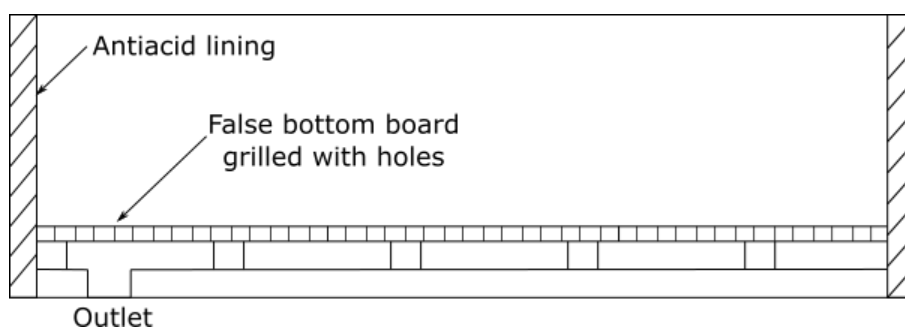


Figure 2.12. Schematic of a typical vat leaching reactor. Adapted from (María and Ruiz, 2013).

The overall efficiency of the process is as high as 90 to 100%, and the full cycle only takes 6 to 12 days (María and Ruiz, 2013). Nowadays, vat leaching is not as common as in the early 20th century, and it has been widely replaced by heap and dump leaching. In 2010, the only copper vat leaching operation in the world was Mantos Blancos in northern Chile, where the operation involved 12 vats to produce 40,000 t/a of copper cathodes (Davenport *et al.*, 2000).

2.2.6.5. Agitation leaching

Agitation leaching may be used both for oxides and sulphides of relatively high-metal grade (0.8 – 5 % Cu for oxides, and >6 % Cu for sulphides) (Davenport *et al.*, 2000). The ore is crushed and finely ground, reaching particle sizes below 3 mm. The ore is then mixed with water to obtain a pulp containing 40 – 70% by weight of solids, with the leach solution being subsequently added (Ntakamutshi *et al.*, 2017). Agitation makes it possible to avoid the sedimentation of the particles, promoting leaching kinetics through improved mass transport around the particles (Chong, Hawker and Vaughan, 2013). This process leads to better solubilisation efficiencies for metals, and it is common to obtain concentrations of copper as high as 2 – 12 g/L for oxide leaching, and 12 – 25 g/L for sulphides. Overall copper extraction values can range between 95 – 98 % (with the lowest values achieved in sulphide leaching), though reactor maintenance and energy consumption are higher, especially from the required milling, and thus the investment required is larger (Ghorbani, Franzidis and Petersen, 2016; Oxley, Smith and Caceres, 2016; van Staden *et al.*, 2017).

2.2.6.6. Pressure leaching

Pressure leaching is a process performed above atmospheric pressure, which permits aqueous systems to remain stable at higher temperatures than their usual boiling temperature (María and Ruiz, 2013). This process is commonly carried out in autoclave reactors, in which it is possible to reach temperatures of up to 250 °C and pressures of 30 atm. Higher pressures allow higher concentrations of

gas reagents, which commonly increases reaction kinetics. The material to be leached is commonly ground to a very fine size, $< 10\ \mu\text{m}$, for maximum exposure of the lixiviant to the mineral surfaces (Davenport *et al.*, 2000).

Pressure leaching has gained popularity due to the refractory nature of chalcopyrite that makes it hard to obtain economically viable leaching rates under typical heap leaching conditions⁸, while it is feasible to leach both chalcopyrite ores and concentrates under high-temperature conditions. Concentrate leaching is a highly competitive option to smelting, with a large number of advantages but it is currently in the early stages of development at the industrial scale. There are two main processes being used in minerals processing operations, which are the medium-temperature/medium-pressure (MT-MP) process, and the high-temperature/high-pressure (HT-HP) process. Both processes use oxygen as the main oxidizing agent, and the operating conditions can range from 200 – 300 °C and ~3000 kPa for the HT-HP process, and 140 – 150 °C and 1000 – 1200 kPa for the MT-MP process. Should the reader be interested in learning more about these two processes, they are referred to (Davenport *et al.*, 2000; María and Ruiz, 2013).

2.3. Leaching simulation

Simulation is a widely used tool to predict process behaviour, minimizing the experimental resources required (Jämsä-Jounela and Cziprián, 1998). Every simulation needs a model to be developed. These models consider the fundamental variables and physicochemical processes of the system, with this information being used as an input to predict the performance of the system. One of the key factors in the leach performance is the apparent leach kinetics. This is the relationship between the leach rate of the metal in the individual particles and the concentration of reagents in the fluid surrounding the particles. These apparent kinetics are a complex function of the mass transfer within the particle and the reaction kinetics at the mineral surfaces, with this relationship being strongly influenced by the mineralogical texture of the ore (or agglomerate).

In order to predict apparent leach kinetics, mass transport, and reactions; this process needs to be modelled at the particle scale. The reason for this is that mass transport and the distribution of concentrations within particles are closely related. Since the leaching process involves both diffusive and convective processes (typically dominant at the intra and inter particle scales, respectively), it is thus critical to take into consideration the influence of both flux components.

⁸ This is compared to regular acid leaching, whereas both bioleaching and chloride leaching have been shown to be viable alternatives to pressure leaching.

On the one hand, the diffusive flux, J_{diff} , is commonly related to the concentration of species in the fluid, C , by Fick's first law:

$$J_{diff} = -D\nabla C \quad (2.25)$$

where D is the characteristic diffusion coefficient, which is a solution property. In order to also consider the medium characteristics and pore effects, such as porosity and tortuosity, the apparent diffusion coefficient, D_{eff} , is commonly used.

On the other hand, the convective flux, J_{conv} , which is produced by the mean fluid flow, is related to C by the equation

$$J_{conv} = \vec{v}C \quad (2.26)$$

where \vec{v} is the velocity vector field of the fluid. Considering mass conservation, the continuity equation for C is:

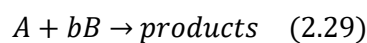
$$\frac{\partial C}{\partial t} + \nabla \cdot J = R \quad (2.27)$$

where R is a source/sink term of reactant species due to reaction. Combining the above equations, one obtains the Convection-Diffusion equation as follows

$$\frac{\partial C}{\partial t} = \nabla \cdot (D\nabla C - \vec{v}C) + R \quad (2.28)$$

Within the particles, the convection term can often be ignored. In this study, this is not the case since there will be evaporation occurring over the curing of agglomerates, which will be one of the main controlling factors of the process.

As the above equations are complex to solve, especially in 2 or 3D, simplified models are used to describe the influence of particle size on the apparent leach kinetics. One of the most commonly used models is the Shrinking Core Model (SCM), first introduced by (Yagi and Kunii, 1955, 1961) and further developed by (Levenspiel, 1972). For this model, it is assumed that particles are spherical and the same size. Porosity and mineral distribution are also both assumed to be uniform throughout the particle, and that the interface between the leached/unleached portion is extremely thin. The three main mechanisms that are potentially rate-controlling for SCM are: (a) mass transfer from the external fluid through the fluid film covering the particle, (b) reactant diffusion through the reacted layer and (c) chemical reaction at the surface of the shrinking unreacted core. In heap leaching, mechanism (a) has limited impact. If we consider the reaction



Then the governing equation for SCM may be written as

$$\frac{\partial C}{\partial t^*} = \frac{1}{\xi^2} \frac{\partial}{\partial \xi} \left(\xi^2 \frac{\partial C}{\partial \xi} \right) \quad (2.30)$$

here $C = C_A/C_{A_0}$, which considers C_{A_0} as the reference concentration of reagent A; $t^* = t/t_D$, with t_D the characteristic diffusion time; and $\xi = r/r_0$; where r_0 is the initial particle radius.

Even though the SCM is widely used, it is not the best approach in most cases as the assumption that particles are all spherical, that valuable elements are homogeneously distributed throughout the particle, and that there is a sharp reaction front are seldom representative of real particles. For this reason, it is important to develop techniques to track the dissolution rate at the individual particle scale. A better understanding of the process can be thus achieved by taking into consideration important variables such as position and size of the leachable species. This approach has only been attempted at the coarse ore particle level, with the behaviour of agglomerates yet to be investigated at this scale (Lin *et al.*, 2015; Ferrier *et al.*, 2016; Lin, Barker, *et al.*, 2016; Reyes *et al.*, 2017).

2.4. X-ray micro tomography

X-ray Microtomography (XMT) is an attractive complementary technique for sample characterization due to its non-destructive/non-invasive nature. XMT allows the same sample to be periodically scanned, producing a time series of 3D representations of the scanned object. The differences in X-ray attenuation values permit the discrimination between the sample components. Thus, the 3D XMT images can form the basis for both a qualitative and quantitative analysis of the agglomerate evolution, including both structural evolution and leaching behaviour.

2.4.1. Use of XMT in the mining industry

XMT based assessments have been widely used to quantify liberation (Miller *et al.*, 2009; Reyes *et al.*, 2018), structural changes (Kareh *et al.*, 2014), preferential breakage (Garcia, Lin and Miller, 2009), and leaching extent (Lin, 2015; Lin, Barker, *et al.*, 2016; Dobson *et al.*, 2017; Yang *et al.*, 2019) in mineral samples. A disadvantage of using XMT, though, is that different sulphides will present similar attenuation values when exposed to an X-ray beam. This means that for a typical mineral sample containing more than one type of metal sulphide (e.g. primary and secondary copper sulphides), it is very hard to differentiate between sample components and, thus, to quantify the dissolution rate of each component separately. This issue has been addressed before by calibrating the XMT measurements with two dimensional SEM/EDX images containing more detailed mineralogical data (Gay and Morrison, 2006; Reyes *et al.*, 2017). The ability of the SEM/EDX measurements to identify different mineral phases can then be combined with 3D time resolved XMT measurements to produce superior results to those achievable using either of the modalities on their own. This will be further discussed in Chapters 5 and

Chapter 7, where 2D mineralogical maps are used to characterize the distribution of each mineral type in the sample over the curing and leaching processes.

2.4.2. Fundamentals of XMT

2.4.2.1. Brief history

At least ten independent scientists invented tomography between 1921 and 1934, with none of them being aware of each other's accomplishment (Webb, 1995). Over the following decades, multiple tomography devices were patented, and the technique was refined up to the development of Computerized Tomography (CT) by Sir Godfrey Hounsfield and his research team in 1971. They proposed the idea of acquiring a set of tomography images from an object by simultaneously rotating the source and detector around an object to subsequently reconstruct a virtual representation of its internal structure aided by a computer. Sir G. Hounsfield was awarded the Nobel Prize in Physiology or Medicine in 1979 for this discovery, with the prize co-awarded to Allan M. Cormack for his development of the theoretical mathematics behind the CT scanner.

This laid the foundations for a new research field, which has produced countless novel techniques and devices both for medical and industrial uses. These scanning machines can be used in practically all fields of engineering, depending mostly on the type of material to be analysed and the resolution scale required (i.e. the size of the sample components). In this chapter, only industrial CT scanners are described. Thus, for further information about medical CT, the reader is referred to the following sources (Garvey and Hanlon, 2002; Rubin, 2014).

2.4.2.2. XMT system

An XMT system consists of three basic components: An X-ray source, a detector, and the sample. The sample is located between the X-ray source and the detector, and it is rotated axially, while a set of radiographs are obtained by the detector, which records the beam intensity after it passes through the sample. A grayscale 3D representation can be then produced by tomographic reconstruction, obtaining a voxelised rendering of the sample's internal structure. Figure 2.13 shows a schematic of a typical XMT system, showing its essential components and how the final tomographic reconstruction is produced.

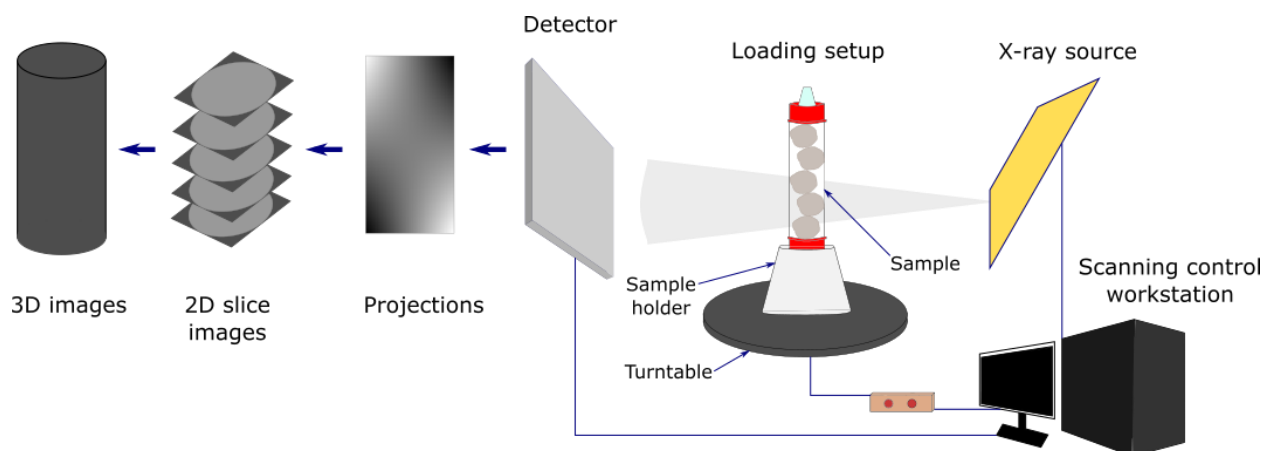


Figure 2.13. Schematic of a typical XMT system, showing its essential components and how the final tomographic reconstruction is produced. Adapted from (Mao *et al.*, 2019).

Image quality is a crucial parameter, as it will reflect the visual attributes of an image. It depends on both image resolution and quality of the data acquired, with these variables depending on a series of parameters such as the scanning time, the energy level, the object size, number of projections, and the machine's technical specifications. Commonly, the first step to assess the viability of scanning a particular sample involves an exploratory stage, with the time frame normally being the main limitation. In these cases, both resolution or contrast between components may not be the principal variables to consider and lower quality scans will suffice. Although, when accuracy and precision are primary (e.g. for feature quantification or classification), it is essential to understand the impact of the scanning conditions. Therefore, depending on the applications and the level of accuracy expected, these parameters must be combined in such a way that the acquired images meet the main requirements for each individual case.

Higher-energy X-rays penetrate more effectively than lower-energy rays, but these are less sensitive to changes in material density and composition (i.e. different components in the sample). While this makes the characterization process more complex, the scanning time can be substantially reduced. However, intensity directly affects the signal-to-noise ratio and thus image clarity. Consequently, longer radiation exposure periods are required for low-energy scans, as it is harder for the X-rays to go through an object (which is the case for mineral samples).

At the same time, image resolution is limited both by the detector type and the object size and its proximity to the X-ray source, as well as by the image artifacts present in the reconstructed image (section 2.4.2.5.1). This is because the detector type (or counts) will set the dimensions of the acquired image (i.e. the number of pixels in the image), while the sample proportion and closeness to the beam source will determine the pixel size and the number of projections required (directly linked to the field of view). As a rule of thumb, the best results are achieved when a larger number of projections are acquired at the

highest resolution possible. Although, this will limit the section of the object that can be recorded, and the scanning period required will be much longer.

Linear resolution can be determined by dividing the physical size of the field of view, which represents the transversal section scanned (i.e. $H \times W$), by the total number of counts (or pixels) in the detector (i.e. $N \times M$). This results in a linear resolution of $(H \times W) / (N \times M)$. However, when the number of projections is low, the reconstruction process will be poor and thus the results. Figure 2.14 shows a graphical example of this situation for a set of packed spherical samples and placed at different relative positions w.r.t the source and detector. It is worth mentioning that this only refers to Linear resolution and not to Spatial resolution. The latter directly relates to the minimum object size that can be quantified or assessed in an image, and it also affects image quality. Spatial resolution is the result of the contrast between materials, the signal-to-noise ratio, the size of the X-ray source (spot size) and the added effect of other artefacts like partial volume effects (Judy, 1976).

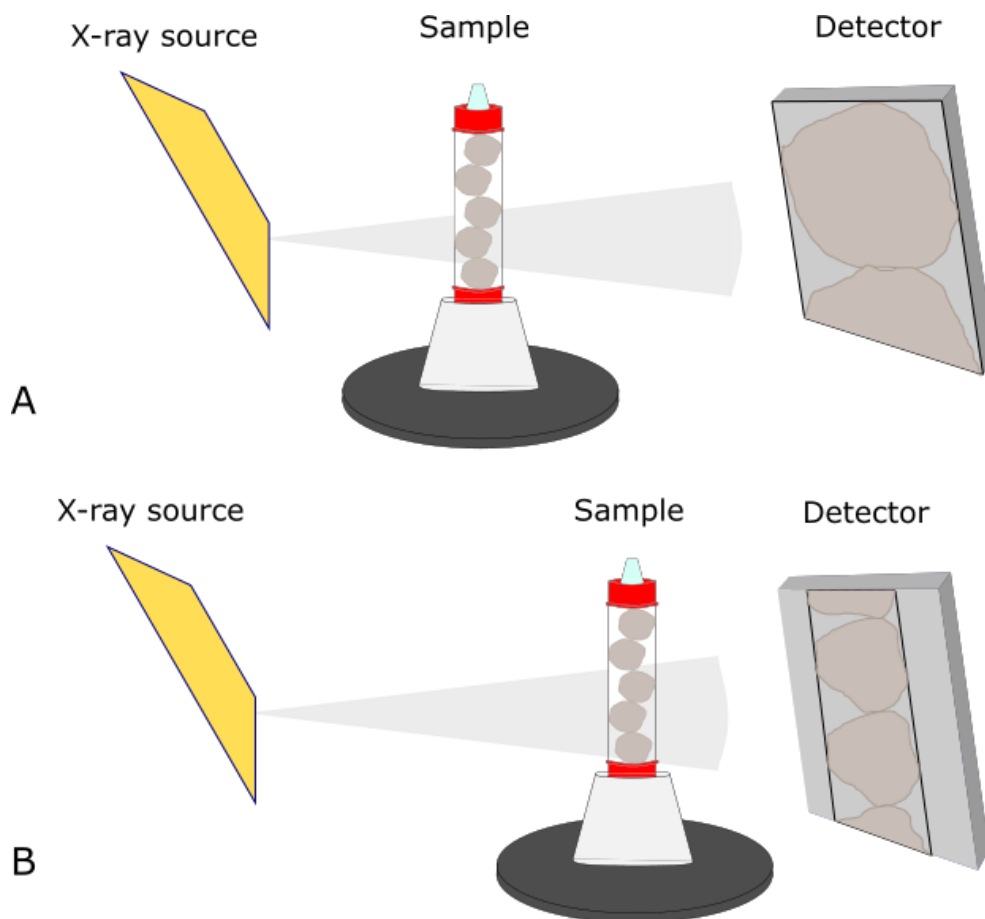


Figure 2.14. Schematic of a scan acquired from a set of packed spherical samples placed at different relative positions w.r.t the source and the detector.

An important improvement made to typical lab-scale XMT machines was the addition of an optical system that expands the range covered by the cone beam. This means that classic X-ray cone beam

magnification is combined with optical lenses to gain additional magnification of the sample, allowing for the acquisition of higher resolution images by augmenting the section of the object covered by the field of view. An example of this type of machines is the Zeiss XRadia family of X-ray scanners, which uses a combination of geometric and optical magnification lenses.

2.4.2.3. X-ray source

The two most common types of X-ray sources can be classified by the type of beam they produce. These are Cone-beam sources and Synchrotron radiation. In the case of the former, X-rays are produced by a beam of electrons produced by a filament and directed toward an anode, which re-emits the energy as characteristic X-ray emission, commonly as a cone-shaped beam. The size and shape of the source play an important role, as more accurate images are produced from smaller focal spot, whereas bigger spots are commonly used when a short exposure time is the priority, producing lower quality images.

Synchrotron radiation is emitted when light charged particles (electrons or positrons) moving with relativistic velocities undergo radial acceleration (Lehmann and Solomon, 2010). A magnetic field under vacuum guides this powerful electromagnetic wave in a direction tangential to the synchrotron orbit, producing radiation in the region from hard to soft X-rays. Unlike cone-beam sources, it takes the form of a parallel beam of finite cross section (Donath, 2007), where the emitted light is many orders of magnitude greater in brightness than a conventional X-ray source (Lin, 2015). This leads to much higher image contrast, with the typical exposure time required to record a synchrotron radiation image being a fraction of a second (Donath, 2007). It is therefore possible to assess the time-resolved structural changes of evolving phenomena occurring for a wide range of physical and chemical processes. Although, its main limitation is that there are only a handful of Synchrotron radiation sources worldwide, with equipment access thus being a limiting factor.⁷

2.4.2.4. Basic physical principles

XMT images are based on variations in the X-ray attenuation of the material resulting in a range of grayscale values. As an X-ray beam penetrates an object, the signal is exponentially attenuated according to the material along its path by scattering and absorption (Ketcham and Carlson, 2001). This attenuation can be related to the composition and density of the material (Stock, 1999). For a homogeneous material, the intensity (I) of the attenuated transmitted X-ray beam can be expressed by the Lambert-Beer's Law:

$$I = I_0 \exp(-\mu x) \quad (2.31)$$

where I_0 is the initial intensity of the X-ray beam, x is the thickness of the object material, and μ is the linear attenuation coefficient with units of inverse distance. This attenuation coefficient is a measure of

the extent to which the intensity is reduced by absorption and/or scattering, and it represents the total contribution of both types of processes (Dyson and Smith, 1998).

For a sample composed of more than one material, the equation becomes (Ketcham and Carlson, 2001):

$$I = I_0 \exp\left(\sum_i -\mu_i x_i\right) \quad (2.32)$$

where each increment i reflects a single material μ_i over a linear extent x_i . Since most XMT scanner beams are composed of a range of the X-ray spectrum, this equation must be solved by adding the increments of attenuations along the X-ray beam (Swinehart, 1962; Ketcham and Carlson, 2001). Thus, considering that the attenuation coefficient is a strong function of the X-ray energy (E):

$$I = \int I_0(E) \exp\left(\sum_i -\mu_i x_i\right) dE \quad (2.33)$$

However, assessing the precise form of the X-ray spectrum and its variations at off-centre angles in a cone beam is challenging, and it is commonly only estimated (section 2.4.2.3). For this reason, reconstruction is often performed by assigning a single value to each pixel or voxel (which is the 3D equivalent of a pixel) rather than some energy-dependent range (section 2.4.2.5) (Ketcham and Carlson, 2001).

A relationship between the attenuation coefficient and the energy of the passing ray can be given as (Dyson and Smith, 1998):

$$\mu(x, E) = \rho \left(a + b \frac{Z^{3.8}}{E^{3.2}} \right) \quad (2.34)$$

with ρ the mass density, a and b energy dependant coefficients, and Z the atomic number. This equation only considers Compton Scattering and the Photoelectric Effect as these are the most relevant at the energy levels of interest in XMT applications (Lin, 2015). There is a third physical process responsible for signal attenuation, pair production, though this effect is only significant at very high relative energy levels (above 10 MeV) (Ketcham and Carlson, 2001).

A convenient way of assessing the feasibility of distinguishing different components when scanning a mineral sample (or any other multi-component sample) is to compare their linear attenuation coefficients at different energy levels. This linear attenuation coefficient, μ , can be calculated by multiplying the mass density, ρ , by the mass attenuation coefficient, μ/ρ (Berger et al. 2010). As an example, Figure 2.15 shows how linear attenuation coefficients vary with the energy level for a set of

mineral samples, including the minerals of interest for this research project (i.e. chalcopyrite, pyrite, primary and secondary copper sulphides, and other typical rock matrix components).

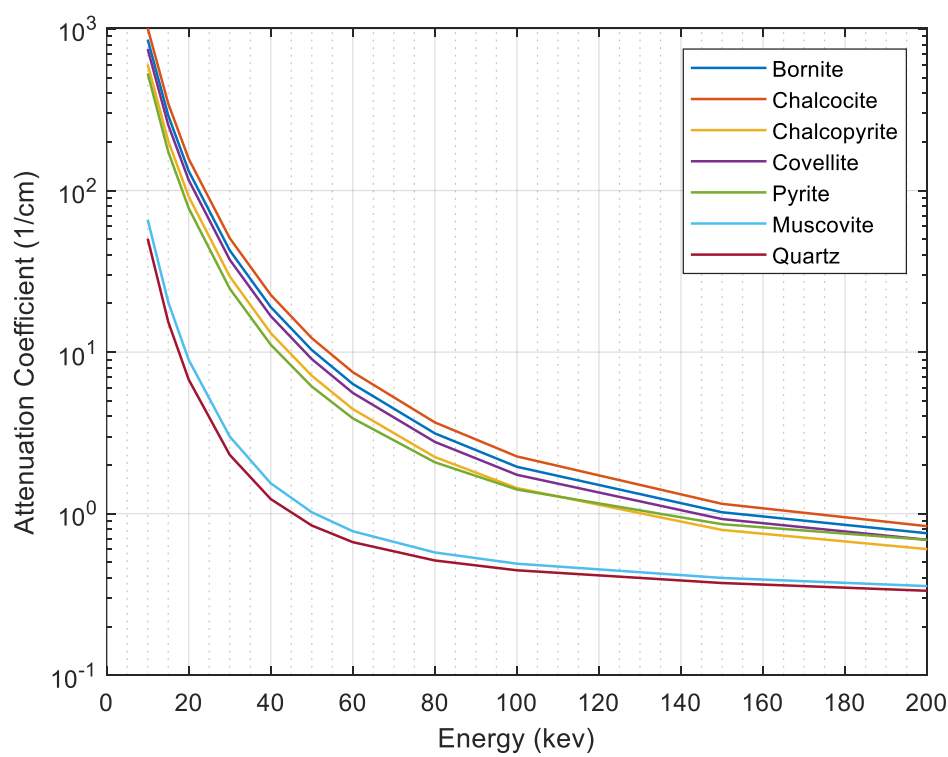


Figure 2.15. Linear attenuation coefficient of some of some minerals, such as pyrite, the most common copper sulphides, and most common gangue components. Adapted from (Berger et al. 2010).

2.4.2.5. Reconstruction

Reconstruction is the process of creating XMT image slices from the projections obtained by scanning an object. This process is achieved mainly by solving equation (2.32) for all angles and positions using appropriate mathematical transformations (or tomographic reconstruction). Two types of reconstruction algorithms are the most widely used, namely back projection (BP) and iterative reconstruction (IR). These algorithms use numerical approximations to find the solution (i.e. the tomographs) due to the complications of obtaining the exact result (section 2.4.2.4). IR generally produces fewer image artefacts, though it is more computationally demanding, and the BP-type algorithms are the preferred option in most cases.

An improved version of BP is the filtered back projection (FBP) algorithm, which was designed to overcome the limitations of conventional BP. FBP uses a stabilized and discretized version of the inverse Radon transform. It applies a convolution filter to remove blurring and it was, up till recently, the primary method in cross-sectional imaging reconstruction. However, it presents two characteristic limitations, namely noise and streak artifacts. Therefore, the advancement in computer technology is making it

possible for iterative algorithms to gradually gain popularity due to their ability to overcome noise without increasing radiation dose.

2.4.2.5.1. Image artifacts

An image artifact (IA) is any feature which appears in an image which is not present in the original imaged object (Hornak, 1996). Artifacts can originate from the physical interaction between the materials and the X-ray beam, or from the scanning process (detectors) (Moreno-Atanasio, Williams and Jia, 2010). Thus, these depend both on the scanner specifications and the sample. The occurrence of IA can be minimised by refining the sample preparation process, performing calibrations, and developing a good understanding of the influence of each process. Image pre-processing is also commonly performed as a middle step between acquiring the data and the subsequent image reconstruction and analysis in order to minimise the effect of these artifacts.

For images acquired with industrial XMT machines, the most common IA are beam hardening and ring artefacts, as well as partial volume effects. It is worth noting that while only these artifacts are described in this chapter, there are a large number of different kinds of artifacts and effects that have been thoroughly discussed by other authors. Thus, the reader is referred to these sources for more information (Hornak, 1996; Davies, 2018).

2.4.2.5.2. Beam Hardening Effect

Beam hardening (BH) occurs when an X-ray beam comprised of polychromatic energies passes through an object, resulting in selective attenuation of lower energy photons. Higher energy photons are more difficult to absorb than low energy photons, and lower energy components of the X-ray spectrum are more easily attenuated or even completely adsorbed when it goes through a dense material. The actual attenuation coefficient of any material reduces and makes short ray paths relatively more attenuating than long X-ray paths (Ketcham and Carlson, 2001). This results in a shift to higher values of both the mean energy, as well as of the shape of the spectrum, while the peak energy remains constant (Figure 2.16) (Stauber and Müller, 2008).

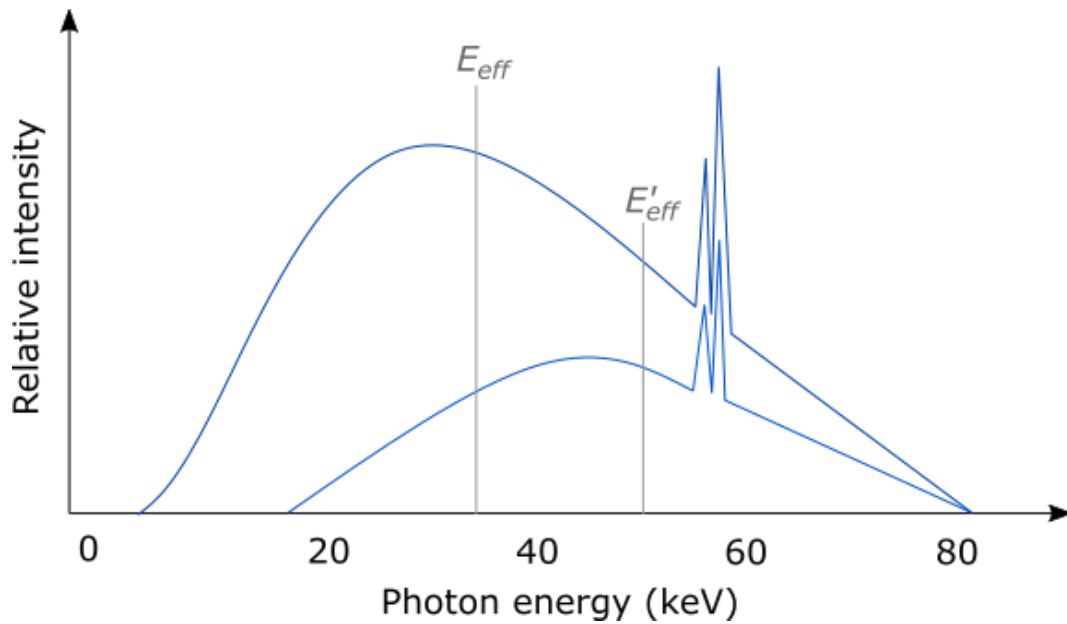


Figure 2.16. Beam hardening effect, the passing ray becomes artificially more penetrating as it loses low energy components of its spectrum. Adapted from (Stauber and Müller, 2008).

Beam hardening causes the edges of an object to appear brighter than the centre, even if the material is the same throughout (Figure 2.17) (Ketcham and Carlson, 2001). It is rather straightforward to differentiate between BH artifacts and actual material variations when imaging objects with roughly circular cross sections, but in irregular objects this is extremely difficult. Although, this problem can be addressed by refining both sample and scanning preparation, or by performing an adequate data processing, the simplest solution is to use a high-energy beam so that BH is negligible (Ketcham and Carlson, 2001). This is not possible when scanning mineral samples as only a low energy spectrum will permit the differentiation of the constituent features. Therefore, in these cases the strategy must be different. A possible option is to use an attenuating filter in order to pre-harden (or post-harden) the beam. This is commonly achieved by placing the filter either before or after the X-ray beam passes through the object. Although, by filtering the beam not only will the low-energy band be affected, but all energy levels will be degraded to some degree, and greater image noise will be added (unless longer acquisition times are used) (Ketcham and Carlson, 2001). Another approach is to use a wedge calibration as a reference material. This wedge is typically cylindrical and of similar characteristics of attenuation, so that calibration can be achieved by image processing techniques (Ketcham and Carlson, 2001).

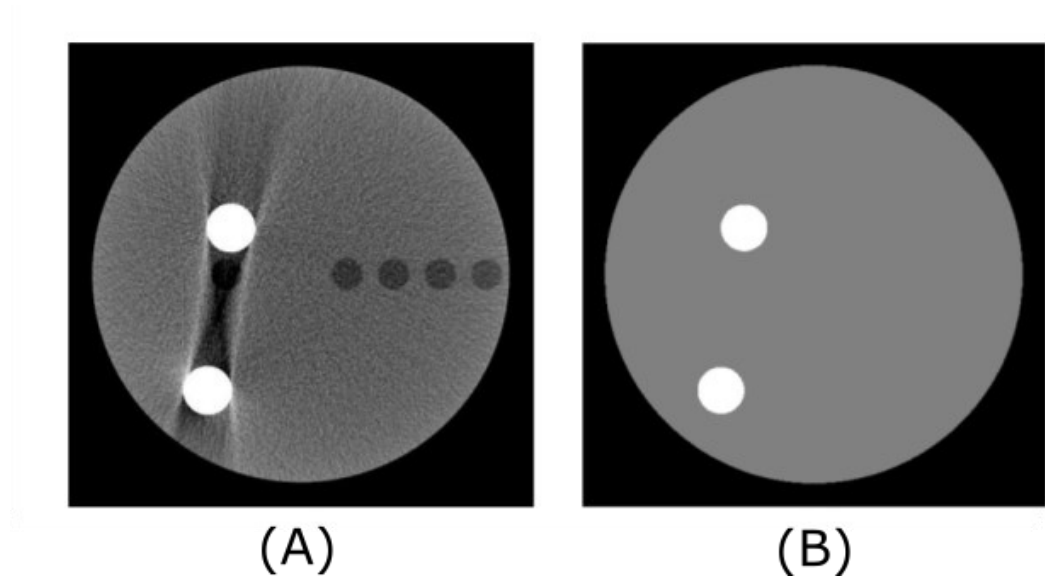


Figure 2.17. Uncorrected image and corresponding propagation path length in the segmented materials. (a) Uncorrected image, (b) two components segmentation image (corrected image) (Zhao *et al.*, 2018).

2.4.2.5.3. Ring Artifacts

Ring Artifacts (RA) appear when one or more of the acquired pixels is recorded brighter or darker than the others, and due to the rotation of the sample, it creates a ring-shaped figure which is not part of the original object. These are commonly present as bright or dark circles (rings) centred on the centre of rotation (Figure 2.18). The main cause of RA can be a malfunction of the detector, miscalibration, changes in the scanning conditions, or simply because of a piece of dust on the detector system (Stauber and Müller, 2008).

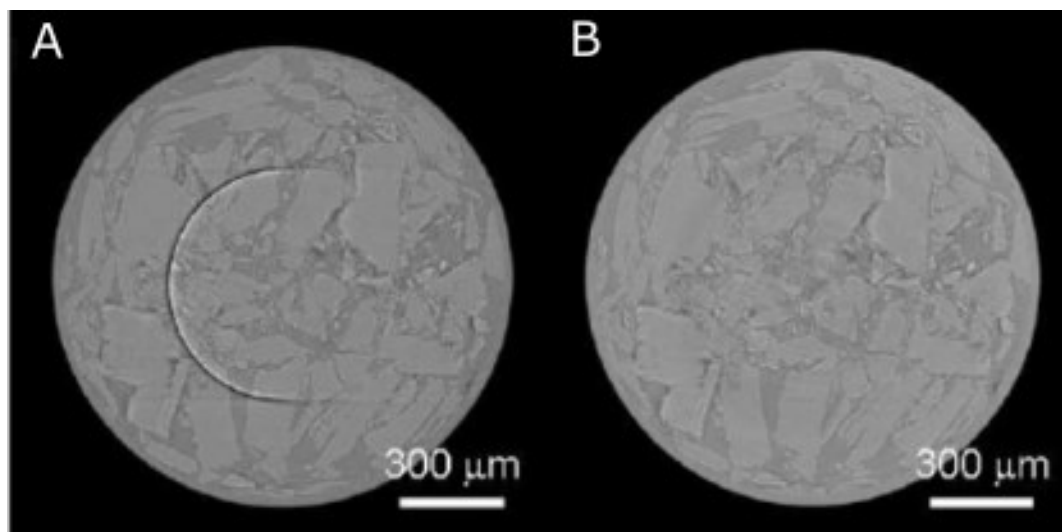


Figure 2.18. Strong ring artifact on a reconstructed slice of a mineral sample (a) Original image, (b) Artifact removed after multiple filtering steps. Adapted from (Stampanoni *et al.*, 2009).

Remedying this artifact is possible by electronical replacement of the information acquired by the defective pixel. This is usually performed by averaging its neighbouring pixels, yielding rather good results (Stauber and Müller, 2008). Another way to digitally remove this artifact is by converting the reconstructed image to polar coordinates, deleting all straight lines, and subsequently convert it back, obtaining excellent results in most cases (Ketcham and Carlson, 2001). Lastly, if the source of RA is linked to beam hardening, ring artifacts can be addressed at the scanning stage with many of the same methods used to reduce BH effects (i.e. using a high-energy beam, or by wedge calibration using a material of similar attenuating properties).

2.4.2.5.4. Partial volume effects

Due to the finite spatial resolution and the 3D nature of the XMT technique, each voxel in the image represents an average attenuation of a certain sub volume in the sample (Reyes-Leiva, 2018). Thus, edges between phases commonly become blurry, and the original shape is virtually impossible to define (Figure 2.19).

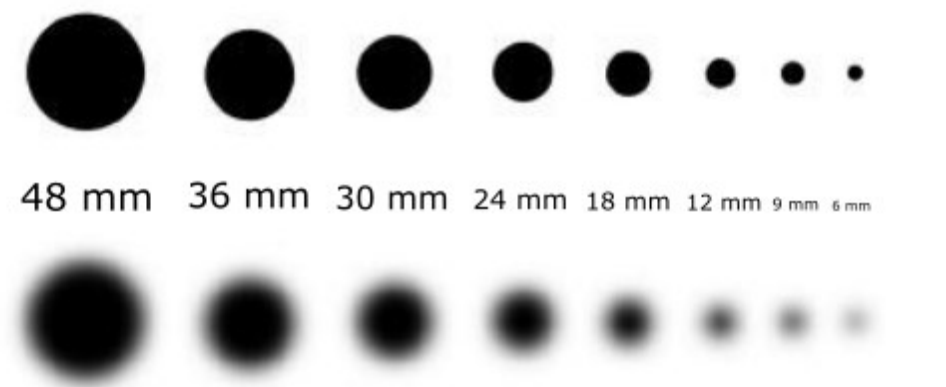


Figure 2.19. Example of the partial volume effects that occur for a coin-shaped object of different sizes. The edges of smaller objects become more difficult to define.

2.4.2.6. Image processing

Image processing is the manipulation of images to process the information recorded (da Silva and Mendonca, 2005). It is a critical process that allows features of the recorded images to be extracted for analysis. Since imaging has become standard for the characterisation of multiple processes in different fields, such as medicine, biology, geology, several fields of engineering, just to name a few; image processing has increasingly gained popularity over the last decades. Therefore, more advanced processing techniques are ever developed to address different complexities encountered.

Images are commonly processed in a series of successive steps. The number of operations that may be required mostly depend on the type of information that needs to be extracted and the image quality,

which is a combination of the signal-to-noise ratio, resolution, contrast, and the presence of image artefacts (see section 2.4.2.5.1). Images can contain large quantities of information, which makes it practically impossible for humans to carry out the necessary calculations (da Silva and Mendonca, 2005). Consequently, the use of algorithms to perform these operations is rather conventional.

For the purposes of this thesis, only the main image processing techniques that will be used will be revised and discussed. However, there is a large number of operations that will not be covered and in case the reader is interested in learning more about image processing and its multiple operations, please refer to (Serra, 1983; Haralick, Sternberg and Zhuang, 1987; Zitová and Flusser, 2003; Preim and Botha, 2014).

2.4.2.6.1. Image filtering

Image filtering involves the application of window operations that perform useful functions, such as noise removal and image enhancement (Davies, 2018). Images may be corrupted by variations in intensity, poor contrast, or any other undesirable characteristics. In such cases, it is convenient to deal with these aspects in the early stages of image processing to avoid accumulation of errors in later stages. Filtering can also be used to improve segmentation and refine edge detection, aiding feature quantification and characterization.

Most filtering algorithms fall into one of four categories: Gaussian smoothing (GS), median filters (MF), mode filters (MoF), and general rank order filters (GROF). Gaussian smoothing is typically used for elimination of the high frequency components of the signal (Davies, 2018). This is achieved by using a low-pass filter for convolution of the image in the spatial frequency domain. While it is commonly used for noise suppression, a side effect of denoising an image with GS is that details are also suppressed. Consequently, GS algorithms are not very useful for the applications of this study, as detail is a key requirement for minerals quantification.

Median and mode filters are used to remove pixels which have extreme and therefore highly improbable intensities. These pixels are replaced by a more suitable value, which is commonly selected by finding either the median, for MF, or the mode, for MoF, value of a certain pixel neighbourhood (the mean value can also be used, in which case it is called a “mean filter”). Although, the accuracy of MoF algorithms depends directly on the neighbourhood size, as multimodal distributions are typically found when the number of pixels considered is excessively small, meaning that the filtering value may not be the most appropriate. Still, both MF and MOF produce a blur that is small when compared to Gaussian smoothing. Despite a slight loss of fine details being also common, which may result in images that look softened, median and mode filters are the most widely used, with MF being the preferred option.

Lastly, the principle behind general rank order filters is the same as MF or MOF, meaning that the filter value is selected from a specific neighbourhood of pixels. However, for GROF, the n pixel intensities are sorted in ascending order, with the r th value of that sequence being the filter value (r will be a number between 1 and n). The minimum and maximum filters (which occur when r is equals to 1 or n , respectively) are often classed as morphological filters, and MF is a particular case of GROF for $r = n/2$, when n is even. Considering the vast number of filtering methods available, the selected technique will always depend on the applications and final purpose of the processed image.

2.4.2.6.2. Segmentation and classification

Segmentation is a method to extract regions of interest from an image by partitioning the original image into homogeneous regions (objects). It is an essential image processing step for quantification and image analysis, as its main purpose is to simplify an image to obtain data that is more meaningful and easier to analyse. Conventionally, image segmentation is grouped into five main categories: Edge-based, threshold-based, region-based, watershed-based, and clustering-based segmentation. In this thesis, only the thresholding and the watershed-based methods will be explained, the former being used for the initial segmentation of different phases and the latter for the separation and subsequent labelling of objects for a more detailed quantification of properties. The reader may refer to ((da Silva and Mendonca, 2005; Preim and Botha, 2014; Pashminehazar *et al.*, 2016)) for information on the other segmentation categories.

2.4.2.6.3. Segmentation - Thresholding method

Thresholding is the simplest segmentation process, as it has low computational cost when compared to other algorithms. Thresholding divides an image into segments depending upon the pixel attributes. It compares each pixel's intensity to a threshold value, T , and decides whether it belongs to an object (setting its value to 1) or to the background (giving it a value of 0). This binarization process can be either bi-level or multi-level. For bi-level thresholding, the image is segmented into two different regions depending on whether the pixel intensity is higher or lower than T . Whereas for multi-level thresholding, multiple threshold values are considered, obtaining an image with more than one object type. An important point to stress is that the accuracy of this binarization process depends directly on the threshold value selected, as it may directly affect subsequent quantification processes.

Thresholding can be categorized into global and local-adaptive. Global thresholding is based on the assumption that the image has a bimodal histogram. Therefore, objects can be extracted from the background by a simple operation that compares image values with a single threshold value T , obtaining a binary image with black background and white objects (i.e. bi-level binarization). Most global

thresholding algorithms use statistical data from the image histogram, such as the mean, median, entropy, etc. A common example of a global thresholding algorithm is the Otsu algorithm (Otsu, 1979), which is one of most widely used due to its simplicity and effectiveness. This algorithm minimizes the intra-class variance by summing the weighted variances of the two classes. This is equivalent to maximising the inter-class variance, from which the value of T is found.

Local-adaptive thresholding techniques make use of unique threshold values for partitioned sub images obtained from the whole image (pixel neighbourhood). The threshold value, T , is adapted to the local image characteristics, allowing images with varying contrast levels to be segmented. It is worth noting that for the applications of this project, global threshold algorithms meet the requirements most adequately.

2.4.2.6.4. Separation - Watershed-based method

Separation is the process of isolating different objects contained in an image with the main intention of quantifying and analysing the properties of each of these objects on their own. An accurate and fast separation technique is the watershed-based method. It is a region-based method that has its origins in mathematical morphology (Serra, 1983; Preim and Botha, 2014) and has been widely applied to a variety of image segmentation tasks.

In watershed segmentation the image is regarded as a topographic landscape with ridges and valleys (Hahn *et al.*, 2005). The elevation values of the landscape are typically defined by the gradients in the grey values of the respective pixels or by the values of a distance map generated for the binary (segmented) image. The watershed transform decomposes an image into catchment basins corresponding to all those points whose path of steepest descent terminates at this minimum (da Silva and Mendonca, 2005). Then, the basins are separated from each other. A new image is obtained in which each pixel is assigned either to a region or a watershed (Preim and Botha, 2014). This image can then be used for the analysis and characterisation of the properties of the different objects in the image.

2.4.2.6.5. Labelling and tracking of features

Image labelling is a type of data labelling that focuses on identifying and tagging specific details or objects in an image. It is commonly performed using automated algorithms (Trucco, 1995) and its main aim is to assign a unique label to each object so that the characteristics of that object can be easily compared at two different stages of the process. It is essential and of vital importance for the successful tracking of the changes experienced by the objects contained in a time series of images acquired for a given process (Zitová and Flusser, 2003; Preim and Botha, 2014).

Object tracking has a multitude of real-life applications, including traffic monitoring, robotics, medical imaging, autonomous vehicle tracking, and more. Object tracking refers to the ability to estimate or predict the position of a target object in each consecutive image once the initial position of the target object is defined (Thennammai *et al.*, 2015). It is probably one of the most challenging image processing operations. While it may be reasonably simple to successfully label the objects in each image in the time series⁹, finding the same object at two different stages is not so straightforward. This process requires taking into account the physical changes of the objects, such as compaction, expansion, rotation, translation, cracking, etc; which is not a trivial task.

Tracking accounts for three main successive steps, namely taking an initial set of object detections and creating a unique ID for each of the initial detections (i.e. labelling objects), and then tracking each of the objects as they move, maintaining the assignment of unique IDs (relabelling). There are several algorithms available for the relabelling step, the most commonly used being centroid tracking (Thennammai *et al.*, 2015), kernel-based (da Silva and Mendonca, 2005; Preim and Botha, 2014), and correlation-based tracking algorithms (Kishore and Rao, 2001). For this thesis, only centroid tracking algorithms (section 4.3.3) and correlation-based algorithms (section 4.3.6) will be used.

2.5. Summary

In this chapter, the principles of hydrometallurgy and, particularly, the leaching process were reviewed. The most common leaching techniques used at the industrial scale were described with special emphasis on the heap leaching process. The latest advances in the process were discussed and the gap in knowledge in certain quantification methodologies was identified. It was shown that a common practice when modelling the process is to consider the input and output of different sets of experiments. However, this only describes the overall behaviour of the system. Considering that the leaching process takes place at various scales, internal changes occurring within the samples and grain-scale processes will most likely affect the performance of the leaching process and must be taken into consideration for an appropriate planning of the process.

A novel alternative to characterise mineral samples is X-ray microtomography. This is a non-destructive and non-invasive imaging technique which -permits the acquisition of 3D grayscale images of samples. By periodically scanning the sample at different stages of the process combined with image processing algorithms, the structural changes in the sample can be quantified and linked to the overall leaching performance. The 3D XMT representations of the sample can also be used as the domain for

⁹ The main difference between labelling and tracking is that the former is the process of detecting a target object in an image. This can be performed for a series of images, but it does not imply that the same object is given the very same unique label at two stages or the process (i.e. different images). While tracking needs to use spatio-temporal features to locate the same object in two different images and assign it the same label used in the reference image.

resolving models and performing simulations of the process. The true geometry of the sample can be used to obtain more accurate results since the grain location and pore network of the sample is taken into account.

The basics of X-ray microtomography were reviewed and the main complexities that are introduced by using this technique were described and discussed. Among the most critical is that different sulphides present similar attenuation values when exposed to an x-ray beam. Thus, it will be virtually impossible to distinguish them from one another by only analysing the XMT image. Different methods for calibrating these XMT images are available, the use of 2D mineralogical maps as a complementary technique for mineral identification being the preferred option. Lastly, some of the main image processing techniques available were introduced and discussed, revealing the importance of each step on the successful quantification and tracking of the changes in properties for any set of objects throughout a process.

Chapter 3. Experimental Methods

3.1. Introduction

In order to understand the curing and leaching processes of agglomerated ores by using XMT-based assessments, two different recipes were used to agglomerate and leach chalcopyrite-containing mineral ores. Agglomerates were packed into columns to perform curing and leaching experiments inside an incubator where temperature was controlled. The length of the curing experiments was 65 days, and the leaching experiments were performed for 46 days. The columns were scanned periodically with an XMT machine in order to track both the curing and the leaching processes. These images were processed for further quantification of the sample's structural changes. It is important to note that the curing and leaching experiments were not performed using the same samples, but only the same mineral feed and chemical recipe¹⁰.

3.2. Mineral ores

The ore used for this study was obtained from the Escondida mine, northern Chile. It corresponds to a chalcopyrite porphyry ore with an average copper grade of 0.4% and an overall metal sulphide grade of 3.7%. The sample also contains minor quantities of secondary copper sulphides and pyrite as the main metal sulphide, with the main gangue minerals being clays and quartz. The detailed mineral composition of the sample is summarized in Table 3.1.

¹⁰ The curing experiments were firstly performed to assess the most appropriate curing length, which was used in the subsequent leaching experiments.

Table 3.1. Main mineral species within the ore feed used for the agglomeration tests. Bold indicates the totals for a category of mineral, with the individual minerals listed below.

Mineral type	Weight (%)
Copper containing species	0.83
Chalcopyrite	0.67
Chalcocite	0.11
Covellite	0.05
Pyrite	2.82
Gangue minerals	90.15
Quartz	19.81
Kaolinite	34.82
Illite	12.32
Muscovite	11.00
Montmorillonite	6.82
Alunite	5.21
Svanvergite	0.17
Other gangue minerals	6.2

3.3. Collaboration with Industry

It is usual to find that there is a gap between theoretical knowledge and industrial practices (Appleyard, 2017). This is due to the different focus that both sides have about new technologies. One of the main aims of this project is to have an impact on industrial scale processes. For that reason, developing collaboration with industry is one of the most important steps. Furthermore, the information that can be obtained is critical to focus research on the actual practices and to calibrate experimental data.

Collaborative work was established with BHP and, in particular, with the people involved in the CPY project. Useful information about the process was provided by them, such as agglomeration recipes, and samples of both good and bad agglomerates were received. BHP also supported the project with continuous feedback about the information that was generated. With the intention of having a better understanding on how the agglomerating process is performed, two mine visits were arranged with the company. The first one in May 2018 to the Spence mine, located in Sierra Gorda; and a second visit in September 2019 to the Escondida mine, located in Antofagasta; both mine sites located in northern Chile. The main mineral ore deposits are a low-grade porphyry copper ore containing both oxide and sulphide minerals, with Cpy representing a high fraction of the total copper sulphide content. Both mines are

currently processing low-grade copper sulphides (primary and secondary) by an agglomeration-heap leaching process, using oxygen as the main oxidising reagent and with the particularity of adding high quantities of NaCl to the sulphuric acid solution.

The chemical behaviour of Cpy makes the process challenging. As discussed in section 2.2.2.1.1, chalcopyrite is a highly refractory mineral and a wide range of techniques to treat it have been tested over the previous decades. The main problems when leaching Cpy is that a sulphur layer forms, passivating further reactions between the leach solution and the valuable particles. The study of how bacteria may affect the process is a common practice. These organisms consume sulphur and ferrous ions giving as by products sulphate and ferric ions, maintaining favourable conditions in the system for chalcopyrite dissolution. However, bioleaching is mostly used for the leaching of secondary copper sulphides and the leaching of Cpy does not present economically feasible bioleaching processes at the moment. An alternative to bioleaching is sulphate-chloride leaching. Chloride ions enhance leaching rates and keep the biological component out of the process. Furthermore, the addition of NaCl is highly beneficial for the mechanical strength of the agglomerates.

The CPY project was at the pilot plant stage when this project started in 2017 and their findings have been put into practice in 2020. Although, the pilot plant at Escondida and Spence are still developing new processes for the next 5 to 10 years. The main aim of this project is to design a competitive process to obtain copper from low-grade porphyry sulphur minerals, whose main copper containing component is chalcopyrite. In order to perform this, there are two major pilot plants in Antofagasta, one at each of the previously mentioned mine sites. The agglomeration process performed at the pilot plant at Spence will be further explained.

3.3.1. Agglomeration process at the pilot plant

The ore agglomeration is performed in a 1 m diameter, 6 m long drum agglomerator. The rotation speed is controlled depending on the residence time that the process needs, which at the same time depends on the mineralogy of the ore. The drum is tilted no more than 5 degrees from the horizontal, and the mineral, the raffinate solution, and the sodium chloride are fed from the highest side. The rotating drum discharges the agglomerates to a mobile hopper, which is used to transport the material to a 10 m height gabion. The gabion used is a 2 m by 2 m cross-section container, which emulates the behaviour of a small portion of a heap. The dimensions of this reactor allow the feeding of up to 12 tons of agglomerated ore and its main advantage is that wall effects can be avoided during the process. Agglomerates are cured for different periods of time (Figure 3.1). And after this, the leaching solution is irrigated from the top. The PLS solution is collected at the gabion bottom in a plastic drum and then transferred to a Solvent Extraction (SX) plant. Special attention is paid to parameters such as the

agglomeration times, the reagent quantities added, the correct moisture of the samples, the average copper extraction and the leaching times. This process is performed several times under different conditions in order to assess the influence of each variable. Figure 3.2 shows three different agglomerate qualities, in which the main difference is the moisture content.



Figure 3.1. Fresh agglomerates packed into gabions of 2x2x10m and left to cure at ambient conditions.



Figure 3.2. Examples of agglomerates of different quality, agglomerates in the centre being of the aimed quality. (a) low moisture content (below 8%), leading to dry agglomerates; (b) good quality agglomerates with 8-12% of moisture content; (c) high moisture content (above 12%), leading to wet agglomerates.

3.4. Experimental setup

Laboratory scale experiments were carried out with the main intention of mimicking the pilot plant conditions. The experiments were carried out in small batches, which are representative of larger scale processes by continuously comparing the evolution of the samples with the agglomerates obtained at pilot and industrial scale operations.

3.4.1. Particle size distribution

With the intention of characterizing the samples, an analysis of the PSD of the material to be agglomerated was performed. For this purpose, representative samples of approximately 730 g were separated into 10 different size categories using Endecotts Laboratory Test sieves. Each size fraction was weighted, and the average results obtained are summarized in Table 3.2.

Table 3.2. Particle size distribution of the ore sample.

Mesh size (μm)	Fraction of undersize (%)	Cumulative undersize (%)
50800	0.8	100
25400	10.3	99.2
19050	26.6	88.9
12700	26.2	62.3
6350	17.9	36.1
1651	5.7	18.2
425	2.9	12.5
147	0.7	9.6
106	0.8	8.9
75	1.0	8.1
45	7.1	7.1

3.4.2. Chemical composition of the solution

Assessing the influence of chloride ions in both the curing and leaching processes was one of the main aims of this project. For this reason, two different chemical recipes that emulate typical raffinate solutions from leach operations were studied. To maximize copper extraction, the same solution recipe was used both for curing and leaching each agglomerate set. Recipes A and B consisted of diluted sulphuric acid, ferric and ferrous, copper ions, traces of other metals; the ratio of $\text{Fe}^{2+}/\text{Fe}^{3+}$ being the primary factor in the redox potential. Additionally, different amounts of chloride ions were added in the form of sodium chloride. The chemical composition of both recipes is further described in Table 3.3.

Table 3.3. Chemical composition of solution used for agglomeration and leaching experiments.

	Cu (II)	Fe (II)	Fe (III)	H	Cl	Mn	Mg	Na	K	Al	SO ₄
Recipe A (g/L)	0.5	1.6	1.8	0.082	150	0.12	3	97.2	0.46	7	62
Recipe B (g/L)	0.5	1.6	1.8	0.082	-	0.12	3	-	0.46	7	62

The chemical reagents used for the agglomeration solution were Sulphuric acid ($\geq 98\%$ AnalaR NORMAPUR analytical reagent), Iron(III) sulphate pentahydrate ($\geq 97\%$), Iron (II) sulphate heptahydrate (AnalaR), Copper sulphate Anhydrous (99% AnalaR), Aluminium sulphate anhydrous (99.99%), Potassium sulphate Anhydrous (ACS grade), and Sodium chloride ($\geq 99\%$ GPR RECTAPUR); all obtained from VWR International. Deionized water was used to dilute the acid.

Eh and pH of the leach solution were measured periodically using a digital SevenGo Duo Mettler Toledo Eh-pH sensor. The Eh values for recipe A were 540-580 mV (with a target of 550 mV), and 670-710 mV for recipe B (with a target of 700 mV), both against a saturated calomel electrode. pH values varied from 1.05-1.21 and 1.12-1.35 for solutions A and B, respectively.

3.4.3. Curing experiments

3.4.3.1. Agglomeration tests

3.4.3.1.1. Tumbling drum agglomeration

Agglomeration is usually performed in a tumbling drum by feeding the mineral ore jointly with the solution. For this project, a Motor Speed Berco Mill, with dimensions of 174 mm height and 127 mm diameter, was used as a laboratory-scale tumbling drum (Figure 3.3). In order to reproduce industrial quality agglomerates, the rolling speed was set to 16% of the maximum power and the volume filling used was 16%.



Figure 3.3. Motor Speed Berco Mill and stainless-steel drum used for agglomeration.

3.4.3.1.2. Tumbling reactor filling level

Agglomeration is recommended to be performed with a drum filling of approximately 16%, with a moisture content of between 8-12 %. The amount of agglomeration solution (which composition is described in Table 3.3) and mineral required for the agglomeration tests were determined for the lab-scale reactor, which has a volume of 2,204 cm³. These results are summarized in Table 3.4.

Table 3.4. Composition of pulp used for agglomeration experiments.

Volume of pulp (mL)	Mass of mineral (g)	Moisture content (%)	Agglomeration solution (mL)
352.7	728.5	10	77.8

3.4.3.1.3. Rolling speed

The rolling speed is typically 30% of the critical speed, thus for this equipment it was set at 36 RPM ($0.30 \times 42.4 / 0.127^{1/2} = 35.6$ RPM). For the tumbling drum machine used, it was only possible to select the speed as a fraction of the maximum tumbling power. Although the rolling speed depends on the drum load. For this reason, it was necessary to replicate the agglomeration load and assess the tumbling speed at different power fraction values. The results of these assessments are summarized in Table 3.5, showing that 16% of the maximum power gives the desired rolling speed (i.e. 36 RPM).

Table 3.5. Rotational speed of tumbling drum used for agglomeration (described in section 3.3.1).

Fraction of max power (%)	Rotational speed (RPM)
10	18
15	33
16	36
20	46

3.4.3.1.4. PSD of the feed material used for agglomeration

In order to produce agglomerates of industrial quality, the particle fraction above 25.4 mm was removed, as their characteristic size was above the column diameter (discussed in section 3.4.3.2.1). Besides, the amount of material of each remaining size fraction was selected in such a way that the particle size of the feed used for agglomeration follows the PSD suggested by the company (see section 3.3.1). Figure 3.4 shows the PSD of the material used for agglomeration.

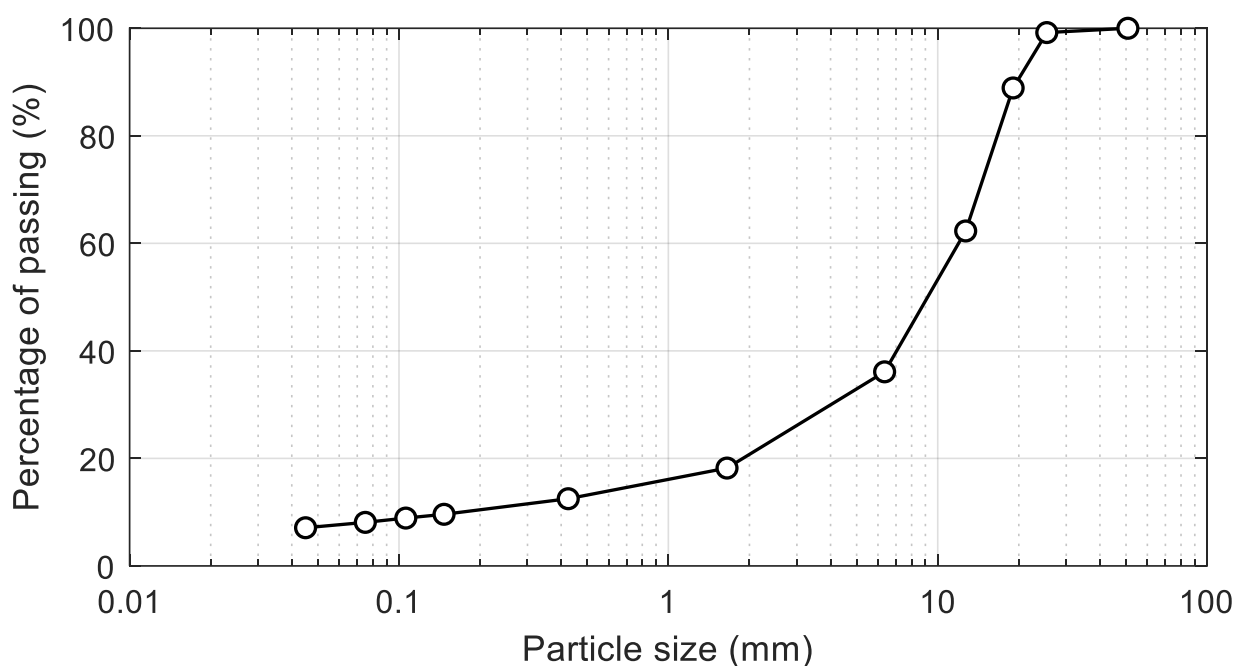


Figure 3.4. Particle size distribution of the feed material used for agglomeration.

3.4.3.1.5. Agglomeration time

In order to produce agglomerates with a D80 of approximately 25 mm, different residence times were tested by adding the mineral ores jointly with the reagents to a tumbling drum. An agglomeration time of 1.5 min was the appropriate residence time to obtain the desired agglomerates.

3.4.3.2. Curing conditions

3.4.3.2.1. Glass columns

Glass columns of 28 mm diameter and 190 mm height were used for packing the agglomerates after agglomeration (Figure 3.5). The material used to construct the columns is resistant to the acidic conditions at which the experiments were carried out. A set of 500 microns aperture size polypropylene meshes were used on both ends to filter fines and any precipitation which may block tubes.



Figure 3.5. Columns filled with agglomerates used to carry out curing and leaching experiments.

3.4.3.2.2. Temperature controlled Incubator

As a high concentration of chloride ions diluted in sulphuric acid was used for this set of experiments, various types of chloride containing gases could form at relatively low temperature (i.e. over 60°C). Furthermore, at a temperature lower than 20°C, rapid recrystallization of chloride salts is highly probable. For this reason, it was critical to perform the experiments inside an incubator where temperature can be controlled. A Perspex incubator with heater, designed for the experiments carried out by (Lin, 2015) was used for the experiments (Figure 3.6). Temperature was fixed at $35 \pm 0.5^\circ\text{C}$ on the temperature controller (Figure 3.7).

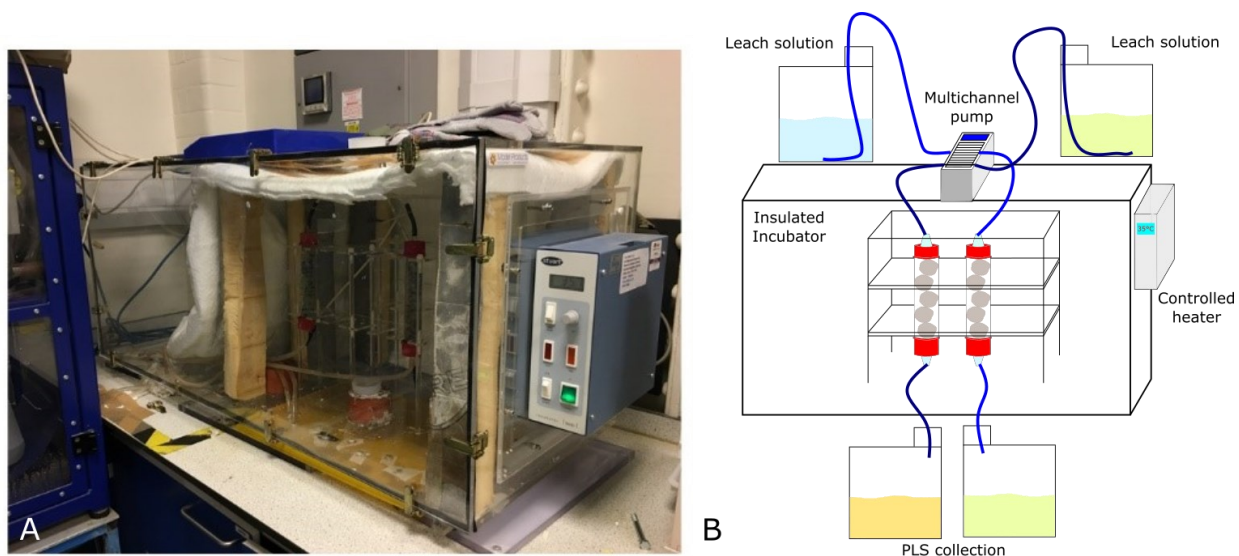


Figure 3.6. Experimental rig used to perform the curing and leaching experiments. A: Incubator with temperature controller, and B: Schematic description of the experimental rig.



Figure 3.7. Temperature controller used to control the conditions inside the incubator.

3.4.3.2.3. Curing period

After agglomeration, the columns were filled with approximately 130 g of agglomerated ores and were subsequently deposited in the incubator at 35°C. An extended curing time of 65 days was studied in order to better understand the evolution of the agglomerates. After the curing period, the two columns were water-washed for 5 days in order to extract soluble species that had been leached during the curing process.

3.4.3.2.3. Peristaltic pump

The curing stage is mainly a drying process which is commonly performed under natural air flow conditions rather than injecting air. Hence, the incubator was partially open to aerate the agglomerate surroundings and avoid a saturated atmosphere. On the other hand, for the leaching experiments a controlled flowrate and a solution collection system were necessary. Thus, the experimental rig also contained an on/off system of tubing connections and spill containers. Flowrate was controlled by a multi-channel Watson Marlow 205U peristaltic pump (Figure 3.8) and the leachate solution from each column was stored in a separate collection container. The leachate was not recycled, and new solution was irrigated over the samples in these experiments.



Figure 3.8. Multichannel peristaltic pump used for the leaching experiments.

3.4.4. Leaching process conditions

After curing, the agglomerates were leached. Leaching experiments were carried using the same leachate recipe used for agglomeration. Two different sets of samples were agglomerated using conditions described in Table 3.3 and packed into columns (described in section 3.4.3.2.1). Curing was performed for 25 days as curing experiments showed that 20 days was the minimum curing time required to observe a significant impact on the samples (this will be discussed in Chapter 5). Samples were water washed for 5 days prior to starting the irrigation with the leach solution. The main intention being to remove species that had been leached out during curing and isolating the dissolution produced by the leaching stage. Leaching was subsequently carried out for 46 days and both curing and leaching were performed inside an insulated incubator (section 3.4.3.2.2), which was used to maintain experiments at 35°C.

3.4.4.1. Leaching flowrate

As the leaching experiments required solution to be irrigated at a constant rate, a multichannel peristaltic pump was used (section 3.4.3.2.3). A suitable flowrate is $10 \text{ Lm}^{-2}\text{h}^{-1}$ (equivalent to approximately $100 \mu\text{Lmin}^{-1}$ in the column system) which is a typical flowrate value in industry. For this reason, four tubing cassettes were connected to the pump and different rotatory speed values were tested. In order to estimate the flow rate, four beakers of 20 mL were filled with solution from a different tubing connection. Time was recorded with a chronometer in order to estimate the flow rate. Table 3.6 summarizes the experiment results, showing that 2.2 RPM gives approximately 100 $\mu\text{L}/\text{min}$ for each connection.

Table 3.6. Flowrate obtained at different rotatory speed values with four tubing cassette connections.

Rotatory Speed (RPM)	2.1	2.2	2.3	2.5	3	5	10	20	30
Time to fill beaker (min)	277.8	200.2	142.9	140.4	101.6	19.75	8.1	4.1	3.1
Flow rate (μL)	72	99.9	140	142.5	196.9	1013	2466	4841	6493

3.4.4.2. Pregnant Leach Solution

The leaching experiments were carried out for 46 days, although columns were periodically disconnected from the leach solution in order to obtain XMT images of the agglomerates following the collection schedule summarized in Table 3.7. PLS was collected in a separate container for each leaching period and each batch was labelled with the starting and finishing date. Thus, each PLS containing bottle represents the leaching extraction between subsequent scanning points. Chemical analyses of the PLS

were carried out by an external laboratory using an ICP-MS machine for mass reconciliation and as a calibration for the XMT results.

Table 3.7. Sampling intervals for collecting the PLS from the leaching experiments.

	Sampling days									
Recipe A										
Recipe B	0	1	4	7	15	20	25	32	39	46

3.5. Summary

In order to quantify the leaching extent over the curing and leaching of agglomerated ores, glass columns were filled with agglomerates. Curing and leaching experiments were performed within an incubator with temperature control. Four different agglomeration recipes were used to assess the impact of chloride ions and pH on the leach performance. The agglomeration and leaching solutions were made up to simulate raffinate solution of typically values in minerals processing operations. Samples were scanned periodically and PLS was collected at each scanning point. Metal concentration was measured by ICP-MS for mass reconciliation.

Chapter 4. Automated XMT-based assessments of agglomerated ores

4.1. Introduction

Analysing the evolution of the internal structure of agglomerates can provide extremely valuable information for understanding the impact of the agglomeration, curing, and leaching conditions used. For this purpose, different imaging techniques are combined in order to better understand this process. The main technique used for this study is X-ray microtomography (section 2.4). The advantage of the XMT is that it is non-destructive, meaning that the same sample can be imaged multiple times over the course of the experiment, and produces 3D images, but is limited by the fact that these images are of X-ray attenuation values, which need to be independently assigned to different mineral classifications based on, for instance, corresponding SEM/EDX images.

In order to obtain statistically meaningful results, it was necessary to develop an automated image processing methodology. This 4D quantification methodology includes the tracking of each mineral grain, to assess the leaching extent at the particle scale; as well as the quantification of structural changes, to assess their impact on the overall performance of agglomerated ores over the curing and leaching processes. Thus, a more detailed and accurate description of the leaching process is possible using the developed methodology.

In this chapter, the XMT system and the conditions used to scan the samples are described (section 4.2). Then, the main image processing techniques and the grain tracking algorithm used to successfully separate, track, and quantify structural changes are listed and explained step by step (section 4.3). Lastly, the consistency of the results was assessed, showing that the presented methodology could be successfully used for automatic XMT-based assessment of agglomerated ores (section 4.4). Part of the methodology presented in this chapter was published in the journal *Hydrometallurgy* (Salinas-Farran, Batchelor and Neethling, 2022).

4.2. X-ray microtomography

4.2.1. XMT system

In order to track structural changes, columns filled with agglomerated ores were scanned periodically over a curing period of 65 days and over a leaching period of 46 days. The machine was selected so that the columns could be easily placed inside the scanner, permitting the stage to move safely to automate the scanning process. A Nikon 225H XT was used to scan the samples, which has a proprietary 225 kV microfocus X-ray source with 3 μm focal spot size. There are scanning machines that can reach higher pixel resolution, though these are not suitable for scanning the columns as they can only scan

samples of smaller size (up to about 15 cm in height). Figure 4.1 shows the scanning machine with one of the columns attached to the scanner stage.



Figure 4.1. X-ray Microtomography machine used to scan the columns of agglomerates.

Scanning the full column was virtually impossible due to image quality limitations. If the full column were to be represented by an image acquired on a single scan, the image resolution would be comparatively low and small features in the sample will most probably not be accurately represented (section 2.4.2.5) (for this system, any object of a size below $100\text{ }\mu\text{m}$ can be considered to be a small object, which may represent a great fraction of the objects of interest). Thus, three sections of each column were selected so that each one would represent the chemical and mechanical processes occurring at a given location in the column. Since the field of view (FOV) of each acquired image only records a smaller section of the sample, the image quality is significantly higher (this is further discussed in section 2.4.2.3). Figure 4.2 shows the scanned section of each column, while the scanning points for the curing and leaching experiments are described in Table 4.1 and Table 4.2, respectively. The scanning points correspond to the curing and leaching sampling points described in section 3.4.

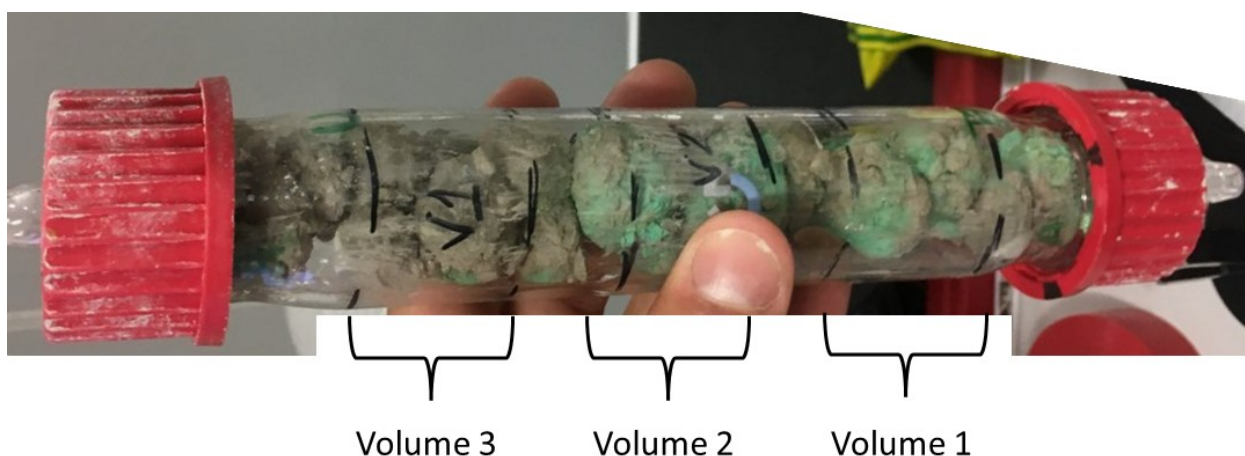


Figure 4.2. Scanned sections of the columns.

Table 4.1. Scanning intervals for the curing experiments.

Recipe A	0		3	10	20	32	65	70*
Recipe B	0	1	4	14	20	30	65	70*

*: Samples were washed for five days after a curing period of 65 days. The columns were subsequently scanned.

Table 4.2. Scanning intervals for the leaching experiments.

Recipe A	0*	1	4	7	15	20	25	32	39	46
Recipe B	0*	1	4	7	15	20	25	32	39	46

*: A curing period of 25 days was performed prior starting the leaching experiments. Samples were washed for five days, and columns were subsequently scanned.

4.2.2. Scanning conditions

Samples were scanned at an energy level of 89 kV, intensity of 165 μ A, exposure time of 2 s and 3185 angular projections. The linear resolution of the image was approximately 17 μ m, which allowed for the differentiation between pores, grains, and the rock matrix. Each scan took approximately 1 hour, with the scanning conditions being summarized in Table 4.3. Figure 4.3 shows a cross-section of one of the columns highlighting the main sample components¹¹, which present different grey-scale values in the image due to their different attenuation coefficients section 2.4.2.4.

An important point to stress is that under the scanning conditions used in this study, different metal-containing compounds can present similar attenuation values (further discussed in section 2.4). It can thus be hard to discriminate between them based only on the XMT scans. Much of the quantitative analysis thus concentrates on the overall sulphide dissolution, rather than copper dissolution, and on the formation/precipitation of metal-containing compounds.

¹¹ It is important to mention that an extremely important component are the precipitating species. Though these are only discernible at late curing stages and mostly for samples of type A.

Table 4.3. Scanning conditions and settings.

Filament	Tungsten
Energy level (kV)	89
Intensity (μA)	165
Exposure time (s)	2
Number of angular projections	3185
Linear resolution (μm)	17

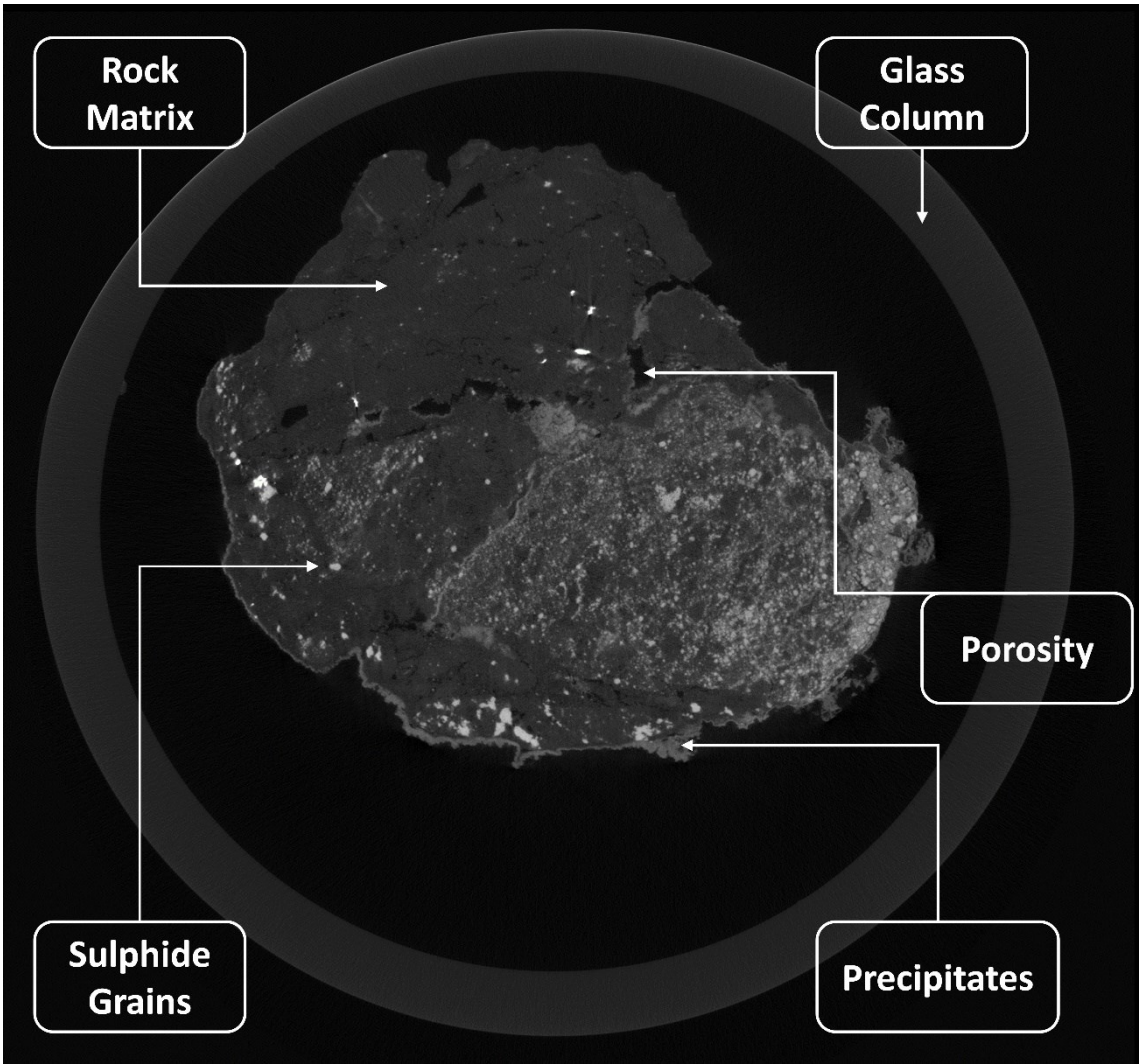


Figure 4.3. Cross section of an XMT image acquired from an agglomerate at day 65 of curing, pointing the main components in the sample.

4.3. Particle tracking methodology

4.3.1. Global thresholding

Finding the thresholding value that permits the differentiation of the sample's component is possible by analysing the shape of the curve. Although, for this study two types of histograms were typically found, namely a first type in which only the rock matrix, the background and noise, and the sulphide grains were identified (characteristic of the leaching process or very early stages of curing); and a second type in which precipitating compounds are also present (characteristic of medium-to-late stages of the curing process).

For instance, Figure 4.4A presents the histogram of one of the scanned volumes at early stages of the curing process (i.e. first type of histogram described previously) Figure 4.4B presents the histogram of a sample at late stages of the curing process (i.e. second type of histogram). Both figures have the threshold value for the glass column and the rock matrix indicated, as well as the approximate threshold value of the sulphide grains and the forming precipitates. It can be seen from both figures that even though global thresholding methods can be used to separate both the glass column and the agglomerates from the background, it is more challenging to do this for sulphide grains and precipitates as they present very similar peaks in the histogram counts and, thus, more complex thresholding methods are required.

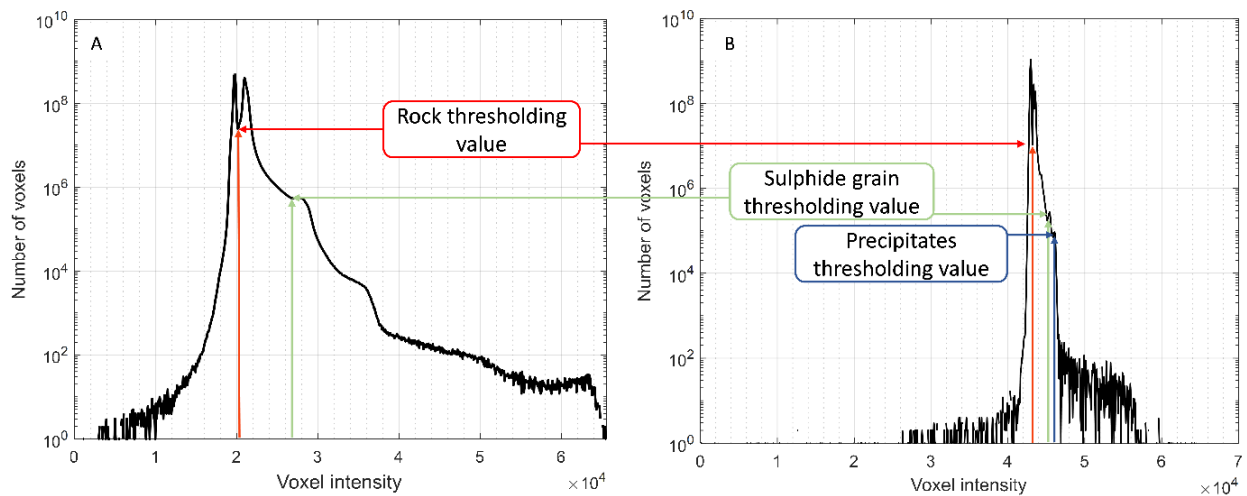


Figure 4.4. Histogram of scans acquired at early and late stages of the curing process. (a) scan of early stages of curing pointing both the peak corresponding to the rock phase, and the peak corresponding to the sulphide phase, (b) scan of advanced stages of curing pointing the peak corresponding to the rock phase and the peaks corresponding to the sulphide grains and precipitates.

Agglomerates were segmented from the background using the Otsu algorithm (Otsu, 1979). This algorithm was used mainly for its efficiency and simplicity. Figure 4.5 shows that the Otsu algorithm successfully finds the thresholding value to segment the column of agglomerates from the image background. It was also possible to distinguish between internal and external voids by using this

thresholding method. Therefore, porosity was classified into two categories, namely internal porosity, which corresponds to the pores within agglomerates; and external porosity, which is the inter-agglomerate porosity. This is important since the leach solution, which flows mainly through the inter-agglomerate voids, will penetrate the agglomerates through the internal pores that are connected to the external voids. This information can be used as a proxy to estimate factors such as the compaction occurring over the leaching process, which will be further discussed in Chapter 7.

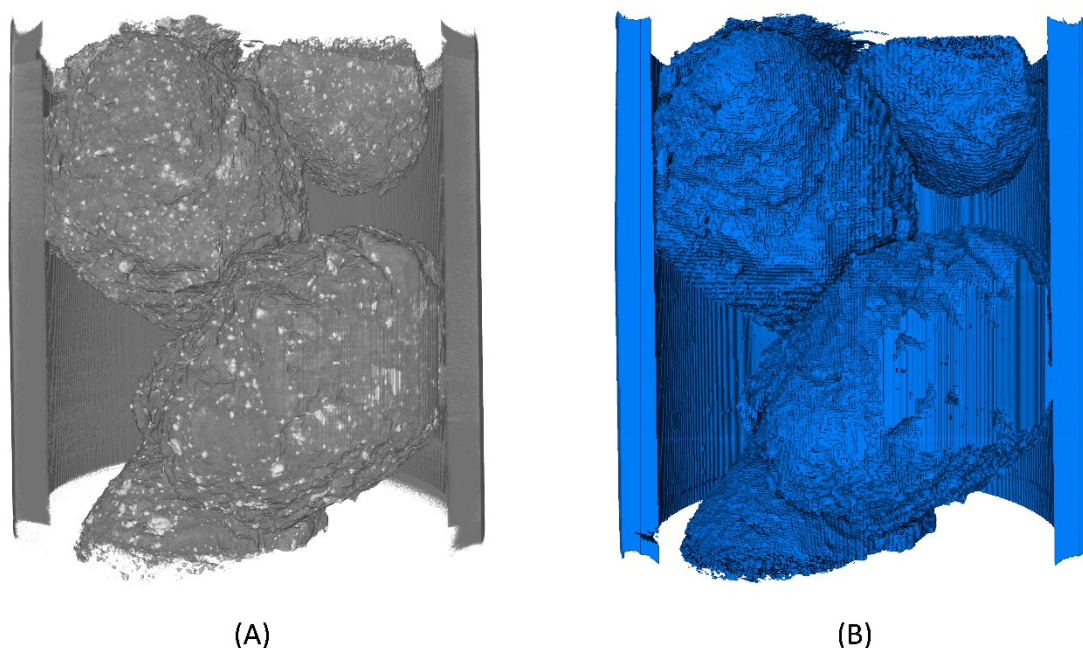


Figure 4.5. Agglomerates and glass column segmented from the background using the Otsu algorithm (Otsu, 1979). (A) grayscale image of the glass column where agglomerates were packed, (B) binary image of the agglomerates and glass column segmented from the background.

4.3.2. Agglomerate segmentation

Even though the data can be classified into four categories (as shown in Figure 4.3), tracking these objects in subsequent scans is not straightforward as the agglomerates move and change size and shape as they cure. After subtracting the image background, the glass column was also removed from the image (Figure 4.6A). Since agglomerates are packed with a high moisture content (about 10%), it is difficult to identify a clear interface between the different agglomerates. Thus, it was necessary to perform a connectivity analysis to correctly separate and label the agglomerates. This step was performed using a 3D watershed algorithm together with a flood-filling algorithm, both included in the toolset of the software Avizo. Figure 4.6B shows the segmented agglomerates, where each individual agglomerate is assigned a unique label (represented by the different colours in the figure).

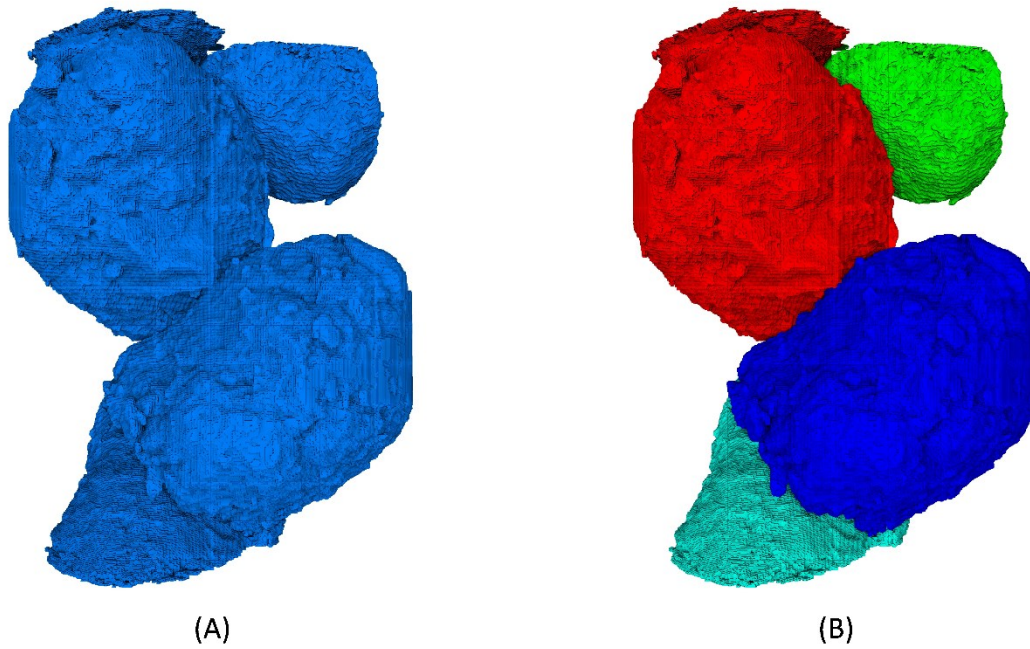


Figure 4.6. The agglomerates are segmented using a connectivity analysis for subsequent assignment of a unique label. (A) the glass column is removed from the image, (B) segmented agglomerates, where each sample is assigned a unique label (represented by a different colour).

4.3.3. Agglomerate relabelling

As the same column was repeatedly scanned at different time steps, tracking the same objects in different scans was critical to successfully quantify structural changes and leaching extent. Thus, the scan of day 0 of each process (i.e. the start of the curing and the start of the leaching processes) was used as reference and agglomerates of subsequent days were relabelled w.r.t day 0.

The agglomerate relabelling process was performed using a centroid tracking algorithm based on the work of (Lin *et al.*, 2015), and extended to overcome the particular issues that agglomerates presented. The mass centroid of each agglomerate was determined in order to find the same object in subsequent scans. Due to the pronounced deformations that agglomerates undergo over the process, a pre-alignment stage was essential. This process was performed by finding the transformation matrix that relates each scan to the reference image. A masking image was produced for each scan, which only contains the location of each agglomerate's centroid. The transformation matrix was applied to each subsequent masking image in order to match each centroid with its corresponding location at the reference day. Lastly, agglomerates were relabelled to the reference labels from day 0. Figure 4.7 shows an example of the agglomerate relabelling process, where it can be seen that all samples were successfully tracked and relabelled.

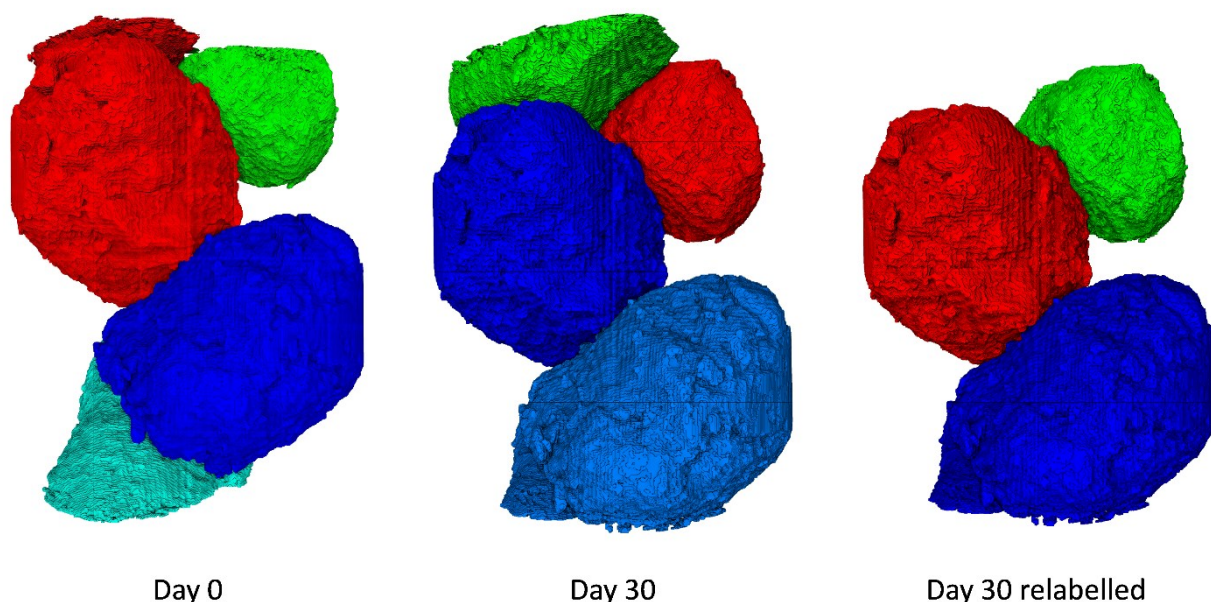


Figure 4.7. Example of the agglomerate relabelling process performed using a combination of a centroid tracking algorithm together with a relabelling algorithm.

4.3.4. Mineral grain and precipitates thresholding

Finding the thresholding value for both the mineral grains and the precipitates was considerably more complex than that for the glass column and the matrix. Global thresholding methods were the logical thresholding option since these have a relatively low computational cost compared to local thresholding methods, especially considering that the average image size is approximately 15-17 GB. As there is no clear peak in the histogram that represents the sulphide grains or the precipitates, relatively complex global thresholding methods were necessary.

Unlike previous steps (i.e. thresholding, segmentation and relabelling), which can be commonly found on previous studies in which micro CT was used to characterised mineral samples, this and the following steps were developed specifically for this study. Considering the extremely similar grayscale values that precipitates present when compared to the former sulphide grains, the segmentation of the two phases required a more complex approach. This routine involves a combination of Avizo and Matlab algorithms, which includes a series of thresholding and segmentation stages performed successively. The codes “maxent_th_values.m”, th_entropy_lesf.m”, and “moments_threshold.hx” (which are the core of this segmentation routine) can be accessed using the OneDrive link provided in Appendix B.

Different global thresholding approaches were tested using the software Avizo, which includes various thresholding algorithms. The “moments” and the “entropy” modules were the preferred option from all those assessed (further explained and discussed in section 2.4), which use a moment-preserving

algorithm (Tsai, 1985) and an entropy-based algorithm (Kapur, Sahoo and Wong, 1985), respectively. Figure 4.8 shows an example of the results obtained using the above-mentioned algorithms, where it can be seen that the Maximum Entropy algorithm (Figure 4.8B) presents the most robust results when segmenting mineral grains only. This is consistent with the findings of (Lin *et al.*, 2015), who found that algorithms based on the measurement of entropy were the most suitable for segmenting sulphide grains from XMT scans. The Moments algorithm (Figure 4.8C) is less selective, and all sulphides are segmented together.

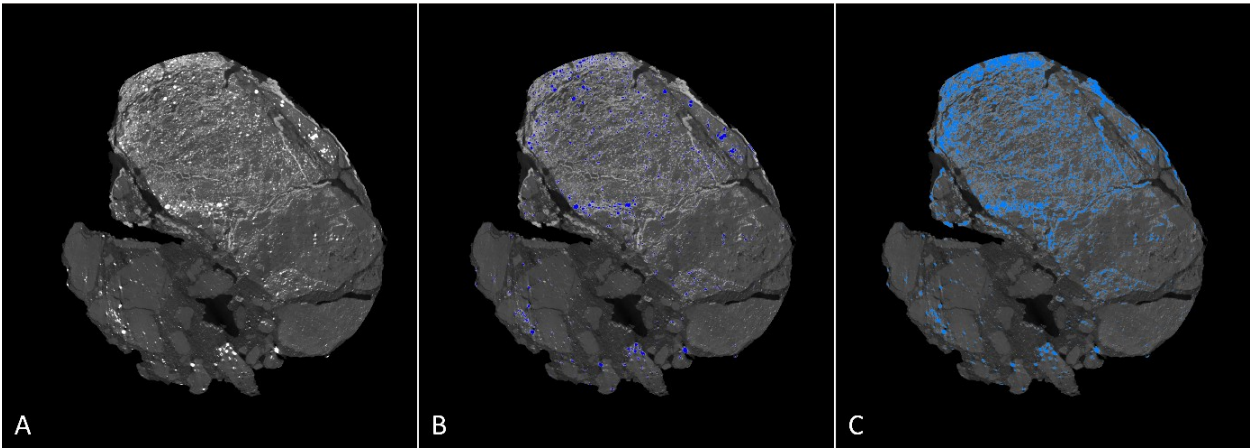


Figure 4.8. Sulphide grain thresholding performed using both the Maximum entropy and the Moments algorithms for scans of different stages of the curing process. (A) shows the grayscale image, (B) shows the results obtained using the Maximum entropy algorithm; (b) shows the results obtained using the Moments algorithm.

Precipitates are then successfully segmented by carrying out a series of steps. A first step involved the joint segmentation of mineral grains and precipitates using the Moments algorithm, and a following step in which the grains phase is subtracted to obtain solely the precipitates. An example of this process is shown in Figure 4.9, where it can be seen that both mineral grains and precipitates were successfully segmented from the rock matrix and are discernible from one another.

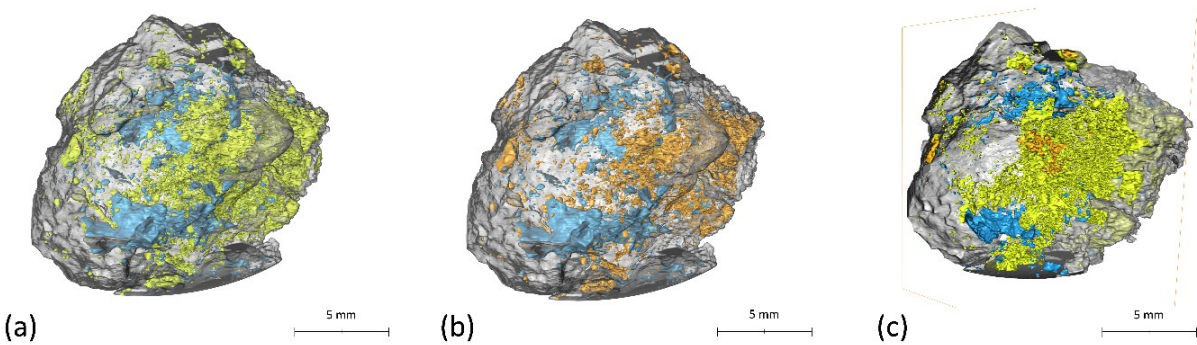


Figure 4.9. Two-step methodology for segmenting precipitates and mineral grains using a combination of the Maximum entropy and the Moments thresholding algorithms. (a) All metal-containing species are segmented jointly from the rock matrix using the Moments algorithm (presented in opaque yellow), (b) the sulphide grains are segmented using the Maximum Entropy algorithm (presented in metallic orange),

(c) the sulphide-grain phase (in orange) is subtracted from the joint phase and precipitates (presented in bright yellow) are segmented as a single phase.

4.3.5. Mineral grain labelling

Tracking the leaching extent over the curing and leaching of agglomerated ores is one of the main aims of this project. Yet, a major complication is the reprecipitation of species that occurs over the curing process. Thus, in order to accurately quantify the volume change of every single grain over the course of the experiments it is necessary to perform a successful labelling of the sulphide grains¹².

Labelling was achieved by developing a MATLAB routine (link to access “rock_quantification_agglomerates.m” code in Appendix B) that performs a connectivity analysis and assigns a unique label to each grain. This code is based on the work of Lin (2015) and was extended substantially to also consider the extreme morphological changes that agglomerates undergo over the curing process. The methodology used is different to the one used for agglomerate segmentation, as in this case there are a number of depleted grains that will only be present on the reference image and missing from some or all of the subsequent images. Thus, it will not be possible to find the mass centroid of these depleted grains in scans of later days. For this reason, only grains from the reference image are labelled (Figure 4.10) and a more complex grain tracking algorithm was developed in order to find the same grains on subsequent scans.

¹² It is important to note that the grain labelling was performed only for the mineral grains and not for the forming precipitates, for which particle tracking was not carried out.

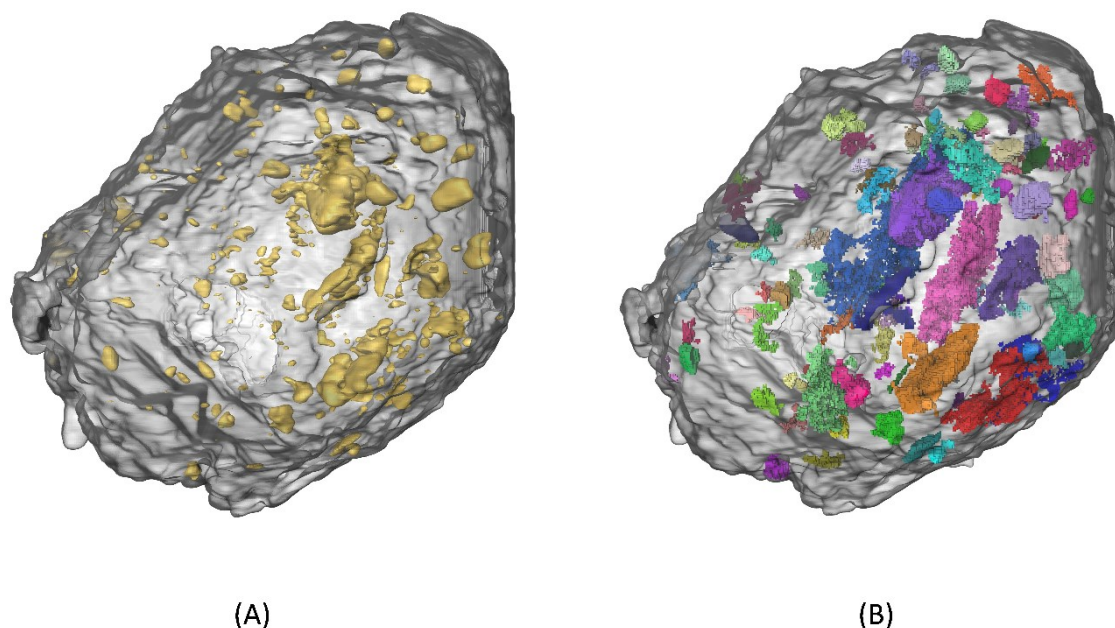


Figure 4.10. Sulphide grains of the reference image are assigned a unique label. (A) sulphide grains of an agglomerate at day 0 of the curing process (presented in bright yellow), (B) a unique label is assigned to each sulphide grain in the agglomerate (each colour represents a unique label).

4.3.6. Sulphide grain registration and tracking

4.3.6.1. Image registration

Image registration is the process of overlaying images to be analysed (Fox, Crocker and Treatment, 2008). It is commonly used to compare information from several images of the same object recorded at different conditions, time points or machines (Zitová and Flusser, 2003). As the main aim of this project is to track the agglomerate's structural and mineralogical changes, it was necessary to develop an innovative registration methodology to take into account the extensive morphological changes that agglomerates undergo and, thus, find the transformation matrix¹³ that relates images of advanced stages of the process with images from earlier stages.

Previous studies have only considered isometric or affine transformations, meaning that all parts of the object are stretched, rotated and/or sheared equally. Such is the case for rocks or more compact objects, which structure does not present considerable anisometric transformation during a specific process. This is not the case of agglomerated ores, though, as they can not only rotate and translate, but can also shrink, deform, and break over the curing process. Therefore, both isometric (rigid) and non-

¹³ This transformation matrix is a 4x4 matrix that relates two images so that a reference image can be compared to a model image.

isometric transformations (which consider unsymmetrical transformations, meaning that the sample can experience different degrees of deformation in each direction) were considered for this methodology.

Rigid transformations consider 3 translations and 3 rotations, whereas anisometric transformations are slightly more complicated. These consider non-symmetric object deformations, such as linear stretching and shrinking, as well as linear shearing; with a total of 9 transformations being optimized. Registration was hence performed using an iterative optimization algorithm (Avizo built-in module Register Images). Overall, the way this algorithm works is by optimizing the rigid transformation parameters as much as possible, followed by further optimization of the 9 non-isometric transformations. Or in other words, the agglomerates are first rotated and translated to match the original as closely as possible before additional stretch/shrinking and shearing is applied to improve the match. A link to access the “Registration_column (pre alignment).txt”¹⁴ and “Registration_agglomerates_per_day.txt” codes is provided in Appendix B.

4.3.6.2. Grain tracking

Up to this point, only the transformation matrix that relates two images has been found, but grains have not been tracked yet. The process of tracking grains is much more complex and requires that each of the millions of grains is identified and assigned a unique label, so it can be followed over the full process and its behaviour quantified at different stages of curing and leaching. This quantification at the grain scale will be then used to understand macroscale performance and to analyse the leaching variability within the system.

An algorithm to track sulphide grains in subsequent scans was then developed (link to access the “grain_quantification_agglomerates.m” code is available in Appendix B). For this grain tracking algorithm to work appropriately, both location and orientation of the later scan need to be accurately matched with the reference scan. This can be achieved either by placing the column in the same orientation at each scan, or by pre-aligning the columns using a more basic rigid transformation prior to carrying out the more advanced registration for each agglomerate on its own.

Grain tracking is further improved by performing a series of steps to find the transformation matrix for each scan w.r.t all previous days. It is important to note that a mask is produced based on the reference image. The interpolation required to project grains from later times back onto a grid corresponding to earlier stages of the process will make grain boundaries diffuse. Thus, an error associated with the measured grain volume could be introduced by the interpolation of the translated images onto the new grid. This error is mitigated by projecting a binary mask onto the appropriate grid in order to identify the

¹⁴ Avizo codes were developed in Tcl language, which the software reads from files with “.hx” extension. Although, for the purpose of making these codes available, they were transferred to text files (.txt extension).

relevant grains. The transformation matrix is then applied to this mask and not to the data itself, as rotating the data would influence the measured volume of the grains.

As it is assumed that there is no creation of grains during the process, only grains found at the reference scan can be tracked in later scans. Thus, labels assigned to grains of day 0 of each process are used as reference. There are, though, two main considerations that are made for the grain tracking algorithm. First, due to grain dissolution occurring over both the curing and the leaching stages, there will be grains that disappear and will not be found on later scans. These grains are considered to be fully leached and are assigned a label only for quantification purposes, whereas they are not physically present on the image mask produced for the relabelling process. At the same time, there will also be a few grains that may appear in later images that are not in the reference image. However, as these are all close to the image resolution, they are not assigned a label (this will be further discussed in section 4.4.1).

As an example, in order to track grains of recipe B (no NaCl added) at day 14 of the curing process (see Table 4.1), a set of transformation matrices that relate day 14 to days 4, 1, and 0, are found. A mask based on the reference day is used to relabel grains of subsequent days in ascending order, assuming that structural changes between subsequent scans are less significant than the structural changes that accumulate over a larger number of imaging intervals. Thus, grains of day 1 are first relabelled to day 0; then grains of day 4 are relabelled to day 1 and day 0; and lastly, grains of day 14 are relabelled to days 4, 1, and 0. Figure 4.11 shows a schematic representation of this example, which represents the registration and relabelling algorithms used for sulphide-grain tracking. It should be stressed that even though only 2D images are presented in the figure, these are simply illustrating the grain tracking process, which is in fact performed with 3D images.

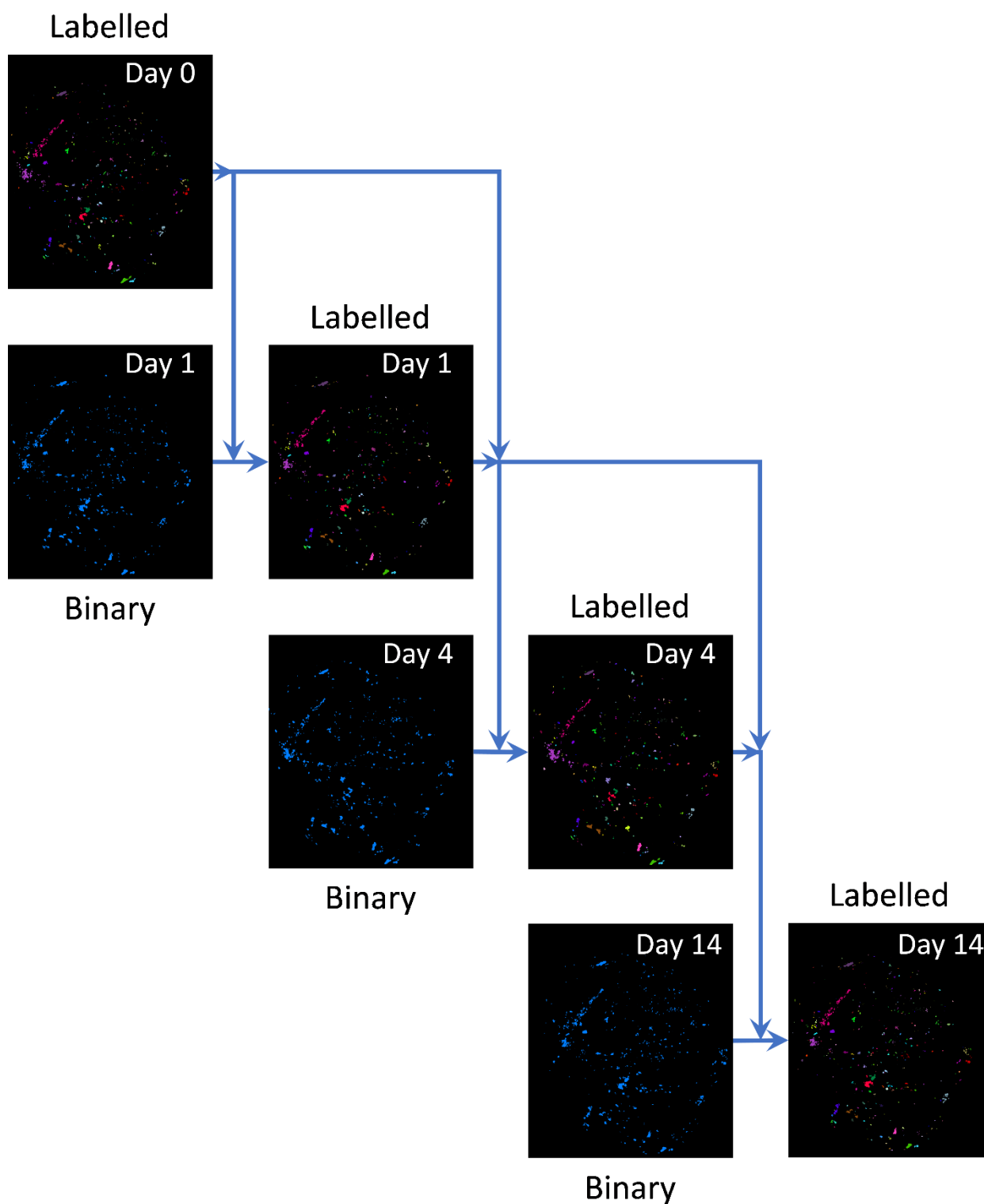


Figure 4.11. Graphical scheme of the registration and grain tracking methodology. For this example, the sulphide grains of recipe D at day 14 are successfully tracked using days 4, 1, and 0 as reference.

4.4. Minimising errors

It is important to assess the quality of the data obtained in order to correctly describe the chemical reactions taking place over the experiments. As this methodology creates a 4D library that represents the

leaching extent over the curing and leaching processes, it is essential to quantify and minimize errors that might be introduced in the different steps of the presented methodology.

Measurement errors can be divided into two categories, namely random errors, and systematic errors. Random errors occur due to variability in the samples and experimental conditions. These are largely unavoidable and will be present in any experiment. While random errors cause variability in the results, they do not influence the mean result and their effect can be reduced by combining multiple results. On the other hand, systematic errors are mostly produced by the machine used or by inaccurate observation and/or measurement methods. They cause a shift in the mean result and are not improved by performing more experiments. In this case, the error can be reduced by calibrating the machine or standardizing the quantification techniques.

When performing XMT-based assessments, the random error will be mainly related to the partial volume effects introduced by the different locations of each object relative to the voxel grid from scan to scan, whereas systematic errors will be introduced by the sensitivity of the thresholding method used to segment sulphide grains (Lin, 2015). For this reason, both random and systematic errors were quantified, with these analyses being presented in this section.

4.4.1. Calibrating the quantification methodology to address random errors

Image artefacts will affect the measurement of particle volume, producing a larger relative error for objects of smaller sizes (further discussed in section 2.4.2.5.2). Since the mineral ore used for the agglomeration experiments is a porphyry copper ore, a large number of fine grains will be present in the sample. Hence, analysing the accuracy of the volume measurements is critical, and the PSD of the sulphide grains will provide valuable information to estimate the random error in volume quantification.

Typically, to reduce uncertainty in measurements, the same experiment is performed multiple times using the same conditions. For XMT imaging, though, it is a common practice to use objects of known volume and linear attenuation as standards (Ketcham and Carlson, 2001). Another option is scanning the same sample multiple times, which will provide enough data to estimate and reduce the random error, whereas the systematic errors can be addressed using consistent image processing techniques (Lin *et al.*, 2015).

In order to determine the random component of the error, two consecutive scans of the same column were acquired on day 14 of the curing process, assuming that no significant extent of leaching would occur between scans. The column was placed in the sample holder attached to the XMT stage and scanned, then it was removed and placed approximately in the same position to be scanned once again. Using the grain tracking methodology explained in section 4.3. sulphide grains were individually labelled,

recording their volume and position. The relative error in volume measurement for sets of 500 grains was calculated and the standard deviation of this relative error was plotted against the grain volume (Figure 4.12).

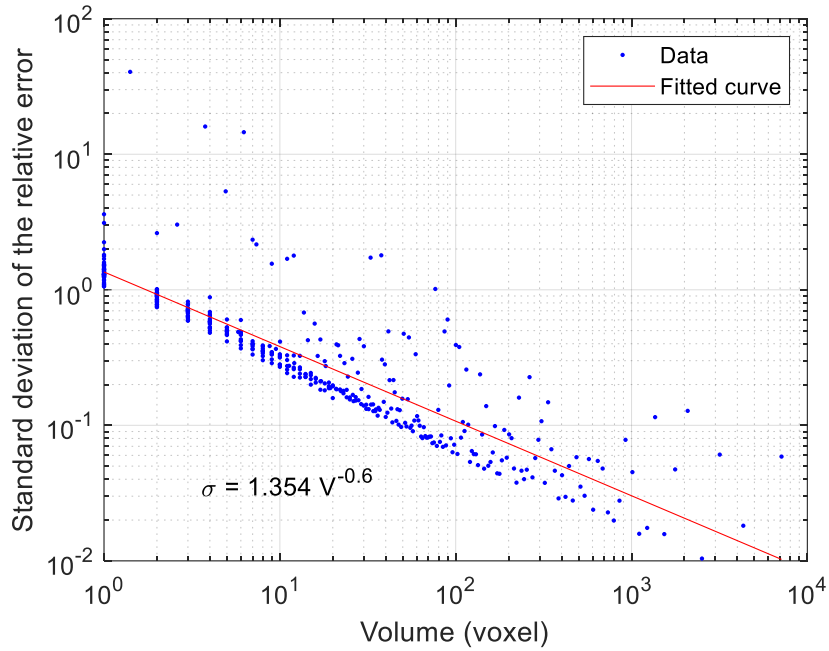


Figure 4.12. Standard deviation of the relative error in volume measurement for a sample scanned twice. The sulphide grains were tracked using the grain tracking methodology explained in section 4.3.

As expected, the standard deviation of the relative error depends strongly on the grain size. Its dependency on the size of the object follows a power law equation of the type:

$$\sigma = kV^b \quad (4.1)$$

With $k = 1.354$ and $b = -0.6$. A value of 0.6 is close to $2/3$, which is what would be expected if the volume error was associated with the surface area of the grains. This equation is consistent with the findings of (Lin *et al.*, 2015). They also proposed that in order to obtain less than a certain error in measurement, it was not necessary to scan the same volume numerous times, but a set of grains of the same size category could be combined to obtain the same level of accuracy. The number of grains from each size category that are necessary can be computed using the following the equation:

$$N = \frac{(kV^b)^2}{\varepsilon^2} \quad (4.2)$$

which relates the selected error in the measurement, ε , with the standard deviation distribution of the volume measurement for a scanned sample. For instance, if it is necessary to reach an error level of less than 5%, approximately 46 grains of 10 voxels must be combined, 3 grains of 100 voxels, or only one of 244 or more voxels. This is useful for having confidence in, e.g., the average change in volume of a grain

category. Since the sample contains hundreds of thousands of grains of each size, and the tracking algorithm allows every single grain to be quantified, the random component of the error is easily decreased by appropriately subdividing the sulphide grain PSD.

For this purpose, images of the reference day of the two columns were processed using the grain tracking algorithm, and the sulphide grains were labelled and measured. The number of grains of each size, as well as their volume in voxels were quantified. The resultant sulphide grains PSD is presented in Figure 4.13. From the figure it can be seen that although more than 85% of the grains are of a size below 100 voxels, they represent less than the 5% of the sample by volume. This is even more significant for smaller grains, as 60% of the grains are of a size below 10 voxels, and they represent less than 1% of the volume.

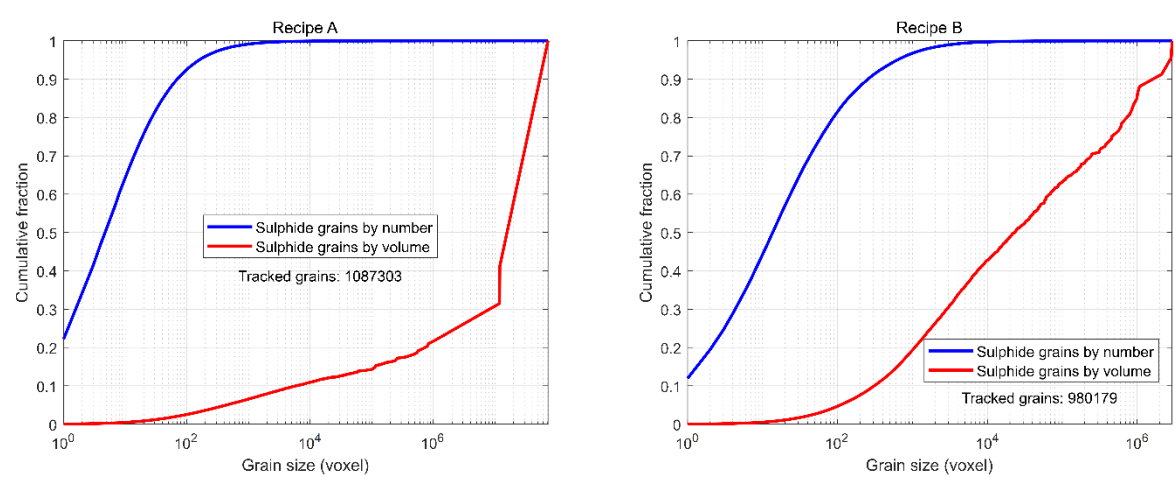


Figure 4.13. Cumulative fraction by volume and particle size distribution (PSD) of the sulphide grains corresponding to curing agglomerates of recipes A and B.

4.5. Summary

A methodology for automatic quantifications from XMT images was presented and the main image processing techniques were explained. The agglomerates were segmented from the background using the Otsu algorithm, whereas the sulphide grains were segmented using the Maximum Entropy algorithm. Due to the significant changes in the structure of the agglomerates, the most challenging process was tracking the sulphide grains in subsequent images. This was overcome by a registration and grain tracking methodology that considered a series of registration steps w.r.t all previous days. Thus, grains can be tracked over the full length of the curing and leaching experiments. This is an important improvement required as existing algorithms do not work well with agglomerates as they do not only move and rotate, but also deform.

The measurement errors were classified into systematic and random errors. Random errors were assessed by scanning a sample twice in a row to obtain the standard deviation distribution of the relative

error in the volume measurement. The required number of objects of a given size that needed to be combined to achieve specified accuracy was computed using the equation proposed by (Lin *et al.*, 2015), finding that in order to reduce the uncertainty in volume change measurements to less than 5%, approximately 46 grains of 10 voxels must be combined, 3 grains of 100 voxels, or only one of 244 or more voxels. Furthermore, by assessing the sample's PSD, more than 60% of the grains are of a size below 10 voxels, and they represent less than 1% of the volume. Systematic errors were addressed by finding a consistent thresholding method, which results in the selection of the Maximum Entropy algorithm as the most stable for segmenting sulphide grains and the Moments algorithm for segmenting the precipitates, process that involves two consecutive steps.

Chapter 5. XMT-based assessments of the curing process of agglomerated ores

5.1. Introduction

Key parameters in heap leaching include permeability, mechanical stability, and mass transport. All of these properties can be manipulated by performing agglomeration as an intermediate step between crushing and stacking the ores into heaps. After contacting the ore with an agglomeration solution and producing agglomerates using a pan or drum agglomerator, a subsequent curing period is often carried out prior to irrigating the pile with the leach solution. While the primary purpose of curing is usually to develop the mechanical strength of the agglomerate, it is also during this process that a first chemical attack on the minerals occurs, kickstarting the leaching reactions. It is thus essential to understand the impact of both the chemical composition of the agglomeration solution and the length of the curing process on the overall leaching performance.

In order to assess the performance of agglomerates over the curing process, a set of curing experiments were carried out for 65 days. The behaviour of ores agglomerated using a combination of sulphuric acid and ferric sulphate were compared with ones in which chloride ions are added in different proportions to the agglomeration recipe, as chloride leaching is gaining popularity as a chemical alternative to bioleaching for sulphide ores.

The curing process beyond the typical curing time scales was imaged using XMT, and quantifications were performed using the tracking methodology described in Chapter 4. During curing, the solution does not leave the agglomerates other than via evaporation and reprecipitation of metal containing mineral species is expected to occur. Energy-dispersive X-rays (EDX) analysis with Scanning Electron Microscope (SEM) quantifications were used as a complementary technique to identify the compounds and precipitates that formed in the presence of NaCl. Immediately after the 65 days of curing, the samples were water washed for 5 days to remove soluble species. This water wash was collected from each column and analysed for copper concentration using ICP to estimate the overall leaching extent that was achieved by the curing stage.

In this chapter, the effect of the duration of the curing process is assessed while structural changes in the sample are analysed with the ultimate aim of determining the most appropriate curing length to use for enhancing the subsequent leaching stage. Section 5.2 describes the structural changes occurring over the process, section 5.3 describes the mineralogical composition of samples A (containing NaCl) after 65 days of curing and characterises the resultant precipitates. This was performed using EDX/SEM combined with the Mineral Liberation Analyser (MLA) automated system. Section 5.4 shows the changes in sulphide distribution within the sample, and section 5.5 studies the leaching extent that occurs over the curing process and introduces a series of dimensionless quantities to estimate the relative proportion

of sulphide grains and precipitates existing at different stages of the process and better describe the process. Part of the results presented in this chapter were published in the journal *Hydrometallurgy* (Salinas-Farran, Batchelor and Neethling, 2022).

5.2. Structural changes

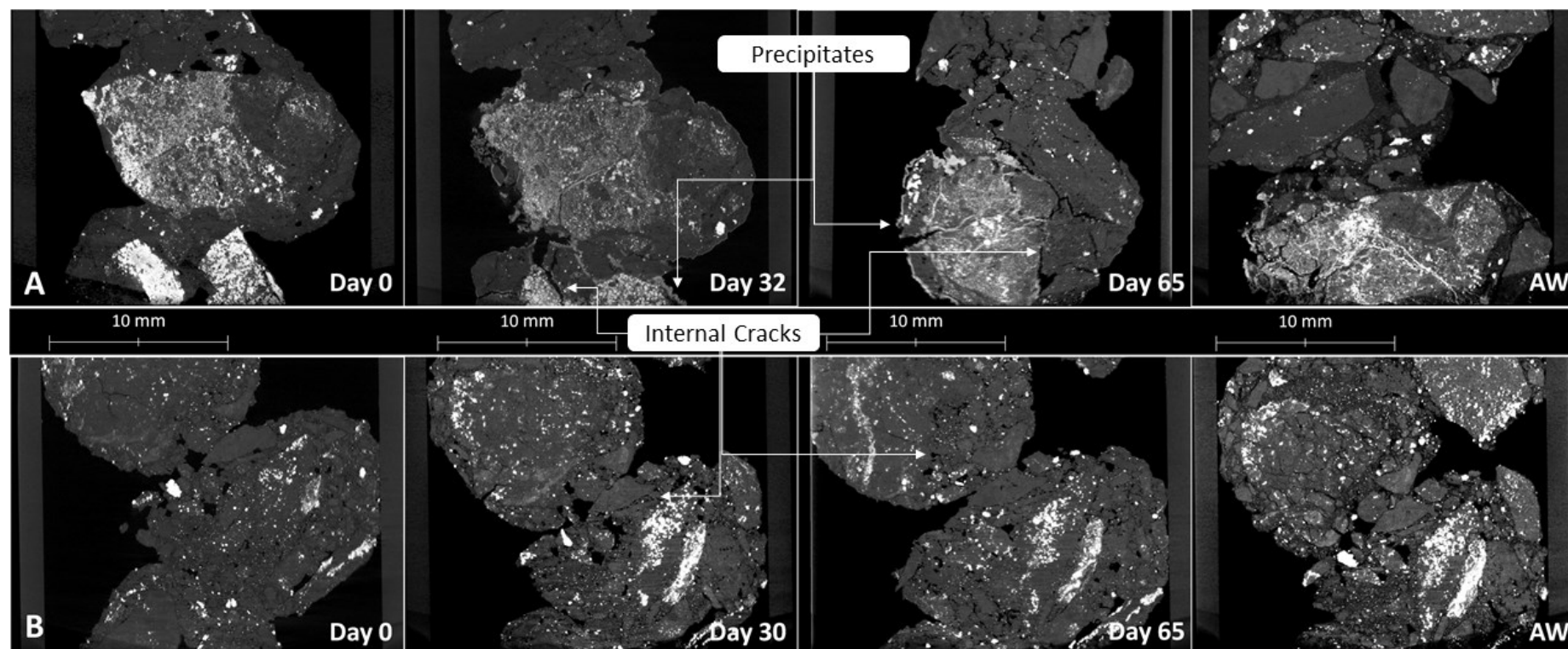


Figure 5.1. Cross-sections of the XMT images obtained for columns of agglomerates of recipes A and B (with and without NaCl, respectively). On top, agglomerates of recipe A at days 0, 32 and 65 of curing and after washing (AW). On the bottom, agglomerates of recipe B at days 0, 30 and 65 of curing and after washing (AW). The XMT data can also be used to assess the evolution of the porosity distribution within the agglomerates. This is important for subsequent leach behaviour as this macroscopic internal porosity provides a path for reactants to enter the agglomerates and dissolved metal species to leave. 3D images of this internal porosity can be obtained using the methodology explained in section 5.2.

Figure 5.2 shows how the internal porosity develops as the curing proceeds. While both agglomerate types develop internal cracks, which significantly increase the mean internal porosity, agglomerates of recipe B present higher porosity at each timestep assessed. The reduced porosity of agglomerates A relative to those of recipe B is mainly due to reprecipitation of the previously dissolved species within the pore spaces due to saturation of the solution. Another interesting point to stress is that agglomerates of recipe A present lower overall porosity at the beginning of the curing stage (i.e. day 0), which may be due to the different agglomeration recipes used or maybe merely random. Given the small number of agglomerates imaged (6 or 7 agglomerate samples), further testing is required to ascertain the source of this dissimilarity.

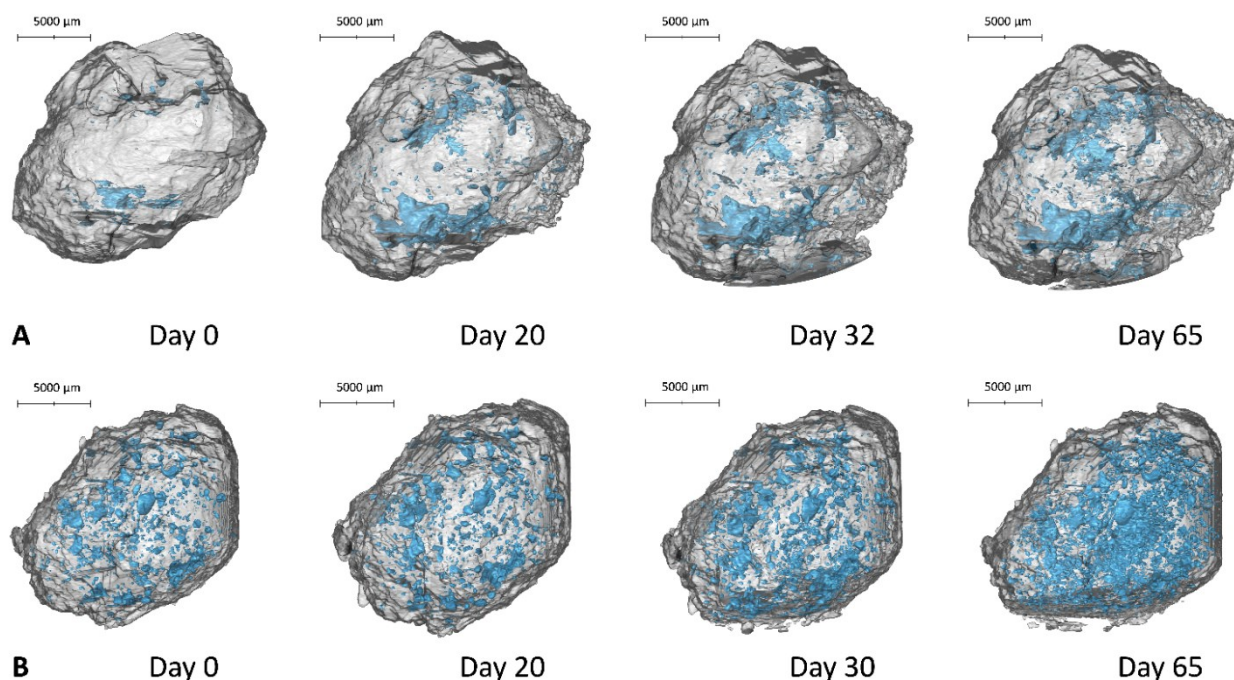


Figure 5.2. 3D rendering of a single agglomerate of recipes A and B at different curing timesteps. The internal porosity of the agglomerates is presented in light blue, whereas the rock matrix in translucent grey.

Another possible explanation for this difference in porosity is the presence of bridges that bind particles over the curing process. These bridges are a product of the dissolution and reprecipitation of species, and they are responsible for providing the agglomerates with the mechanical stability and strength necessary for the subsequent heap leaching stage. Thus, even though the porosity may be lower for samples of recipe A, this might only be a result of a greater number of bridges forming. Although mechanical stability tests, such as compression and soak tests, are essential in order to assess the mechanical stability of agglomerates. Such analysis was out of the scope of this study.

5.3. Energy-dispersive X-rays analysis with Scanning Electron Microscope for mineral identification.

For the purpose of identifying the precipitating species that formed over the 65 days of curing, two unwashed agglomerates of recipe A were sectioned and polished. These sections were selected in order to expose a surface that contained mineralogical information that was representative of what was present in the cured agglomerates. The samples were imaged using EDX/SEM, obtaining a set of Backscatter Electron (BSE) images. Further quantification was achieved using the Mineral Liberation Analyzer (MLA) automated system. Figure 5.3 shows the MLA results obtained with the main mineral components highlighted. From the figure it is possible to identify a set of copper-chloride compounds that have precipitated over both the agglomerate surface and within the internal pores. A close-up view of a region containing large quantities of these compounds are shown in the red rectangle for Figure 5.3B, and in the blue rectangle for Figure 5.3B. Since these are Cu-S-Cl-O complexes of unknown chemical structure, they are named by their mineralogical occurrence.

The elemental composition of each complex, as well as their fraction by weight of the sample, are described in Table 5.1. By analysing the chemical composition of the Cu-S-Cl-O and Cu-S-Cl + Illite complexes, it may be suggested that most copper is in the form of copper sulphate and copper chloride, both compounds being highly soluble in water. This is consistent with what was observed from images acquired after water washing agglomerates, where it is evident that most precipitates formed over the agglomerate surface were removed by the 5-day water wash (section 5.2). There may also be a small fraction of copper as sulphides, though more extensive analyses are required to verify the mineralogical form in which copper is present in the precipitated phase. Overall, these complexes represent a high fraction by weight of the metal containing species within the sample, which is also consistent with the observations from Figure 5.1.

Another interesting result is the presence of a copper-sulphide compound that grows from the chalcopyrite grains as needle-shaped crystals. This compound is probably a product of grain dissolution and instant reprecipitation, suggesting that the precipitation timescales might be different depending on the location of the grains within the agglomerate's structure. Figure 5.4 shows these crystals and the main elemental components.

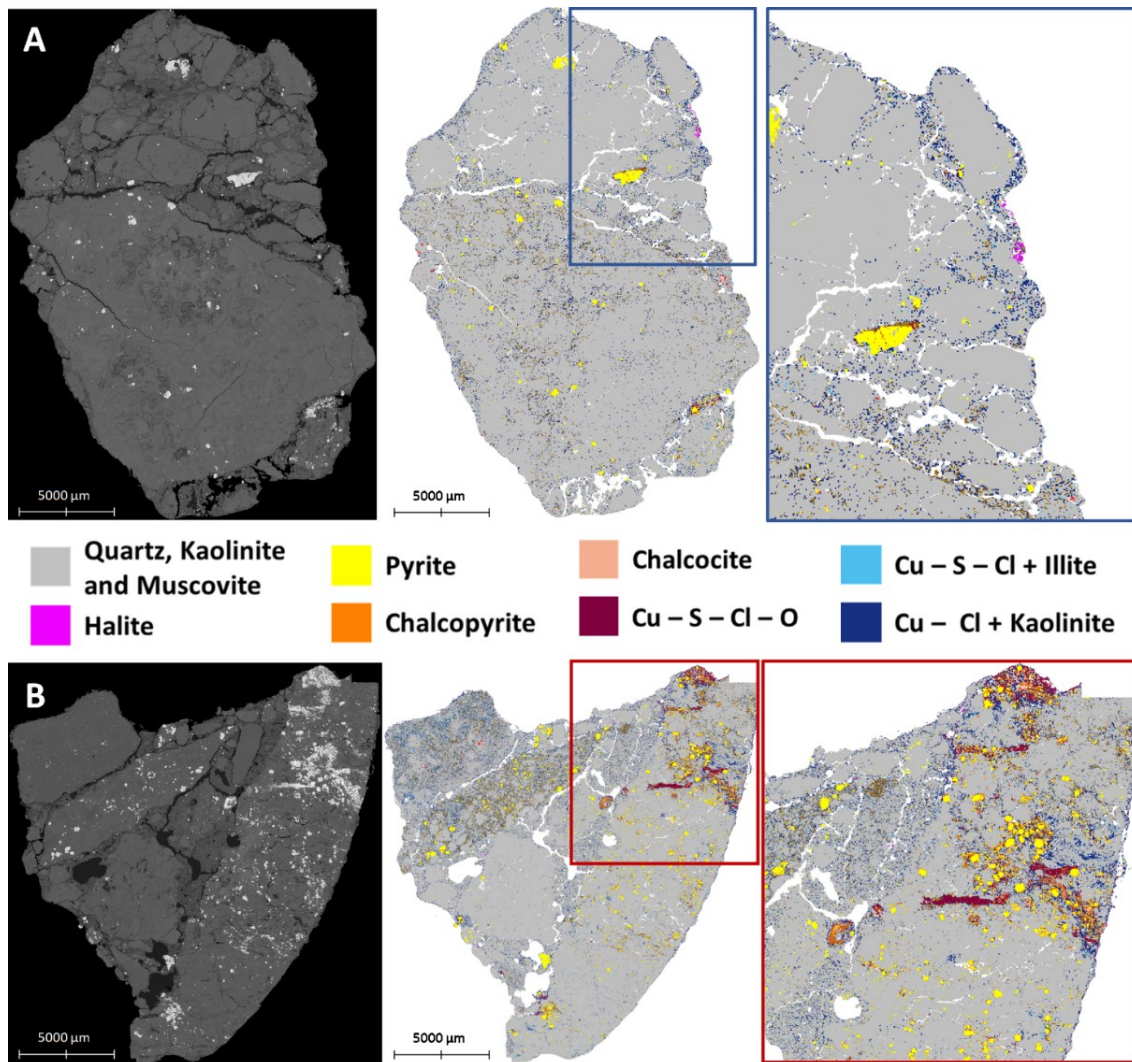


Figure 5.3. MLA results for two agglomerates of recipe A (containing 150 g/t of NaCl) after 65 days of curing. A: Agglomerate with high formation of the Cu – Cl – Kaolinite compound. The BSE image obtained from SEM is shown on the left, whereas the MLA is shown in the middle with a blue box, which is a close-up view of the precipitated material on the agglomerate surface. B: Agglomerate with high formation of the Cu – S – Cl – O complex. The BSE image obtained from SEM is shown on the left, whereas the MLA is shown in the middle with a red box, which is a close-up view of this compound precipitated in the internal pores and close to the agglomerate surface.

Table 5.1. Composition of the copper-chloride complexes formed at day 65 of curing. The fraction by weight of the sample that each of them represents is also presented (this information corresponds to the mineral map presented in Figure 5.3).

	Composition by weight (%) and Molar fraction*							Fraction of the sample by weight (%)
	Cu	S	Cl	O	Si	Al	Fe	
Cu – S – Cl – O	44.6	15.1	10.8	18.3	0.5	0.7	8.1	0.6
	(0.25)	(0.17)	(0.11)	(0.40)	(0.01)	(0.01)	(0.05)	
Cu – S – Cl + Illite	3.1	2.0	1.4	44.6	24.1	24.4	0.4	0.7
	(0.01)	(0.01)	(0.01)	(0.59)	(0.18)	(0.19)	(0.01)	
Cu – Cl + Kaolinite	53.1	-	12.5	19.9	7.0	7.5	-	11.7
	(0.28)	-	(0.12)	(0.42)	(0.08)	(0.10)	-	

* The molar fraction is presented for each element in parenthesis.

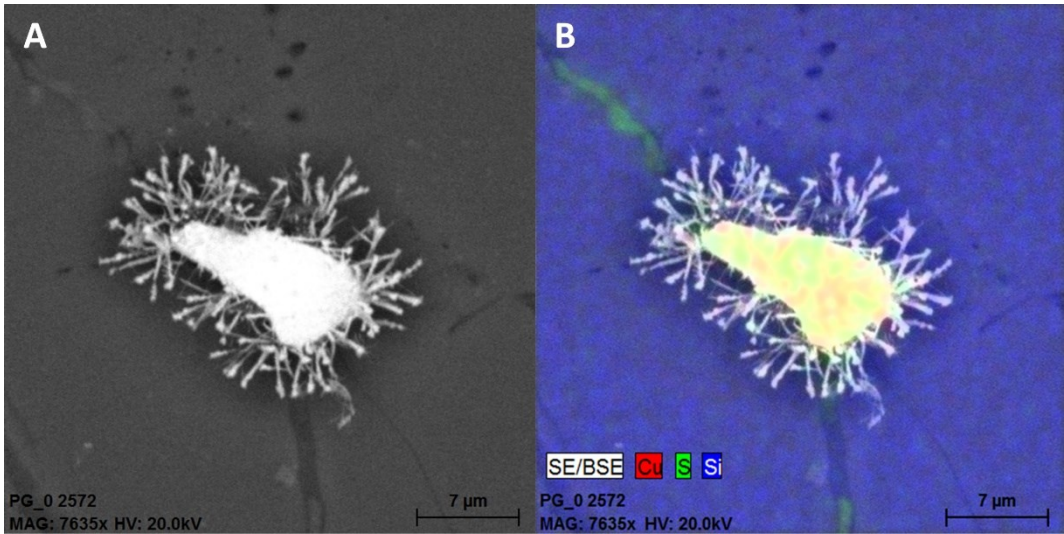


Figure 5.4. Copper-sulphide grain leached and reprecipitated after 65 days or curing. A: grayscale image; and B: elemental composition of the needle-shaped crystals that form as a product of the curing process.

5.4. Sulphide distribution over the curing process

Since the agglomeration solution includes acid, ferric, cupric, and chloride ions, a degree of leaching is expected to occur over the curing process (section 2.2.6.2). The analysis of this leaching is complicated by the fact that all the dissolved metals will remain in the agglomerates as there is no solution flowing through the columns, as would be the case in a more conventional leach test. Metals can only change their mineralogical occurrence and precipitates are expected to form. There is thus no metal extraction during this process and the overall metal grade must remain approximately constant. Overall, it is therefore expected that the metal sulphide grains will shrink, though some of them may appear to grow

as chloride and/or sulphate precipitates form on their surface, while in other regions completely new precipitate grains may form.

Using the segmentation algorithm developed for this thesis, which is outlined in section 4.3, the overall metal containing mineral grain volume can be obtained as a function of the distance to the agglomerate surface at different curing stages for both recipes (Figure 5.5). Since the leaching solution is introduced into the agglomerates during the agglomeration process, leaching is expected to occur everywhere within the agglomerates. On the other hand, water evaporation will occur predominantly from the agglomerate surface, which means that metal concentration in solution will increase towards the agglomerate surface promoting precipitation in these areas.

It is also possible to observe that a period of 20 days was the minimum curing time necessary to obtain an appreciable extent of overall sulphide dissolution for agglomerates of recipe A, whereas for agglomerates of recipe B there is no significant dissolution over the entire 65 days of curing. It should be stressed that Figure 5.5 shows the change in the total volume of metal-containing species. The yellow and red sections correspond to agglomerate regions where the precipitation reactions are mainly occurring, and this precipitate formation is represented as volume growth when a more basic segmentation method is used (as in this case). Yet, in order to quantify the two processes occurring in these regions (i.e. grain dissolution and reprecipitation of species), a more detailed description is required, which can be obtained by assessing the sulphide dissolution extent separately from the precipitation of species.

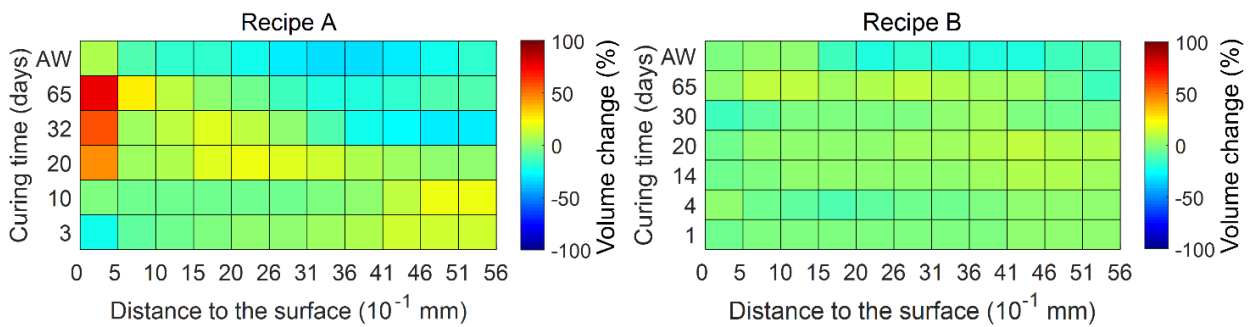


Figure 5.5. Net change in grain volume as a function of distance to the grain surface at different curing times. AW represents the change in grain volume after water washing. All changes are relative to day 0.

5.5. Leaching extent over the curing process

Using a more advanced segmentation methodology (i.e. using all steps developed for the curing process, which are explained in Chapter 4), it is possible to analyse the mean concentration of species. The samples contain different initial sulphide grades due to their natural occurrence. Thus, in order to obtain comparable results, the mean concentration was normalised by dividing the value at each scanning point by the initial sulphide concentration. The normalised concentration can be obtained as follows:

$$C'_i = \frac{C_i}{C_{species_0}} \quad (5.1)$$

where C_i is the concentration of species i (e.g. sulphide grains (MS), precipitates (precip), or the overall metal containing species (species)); and $C_{species_0}$ is the initial concentration of sulphide species.

Figure 5.6 shows the normalised concentration for each sample. As expected, there is a substantial leaching extent occurring for the samples agglomerated using NaCl as an additive (recipe A), whereas agglomerates of recipe B show virtually no leaching occurring after agglomeration (i.e. day 0). Another interesting result is the amount of species that were removed after the water wash, with approximately 50% of the initial metal sulphides being removed from agglomerates of recipe A, and only around 20% of metal sulphides removed from samples of recipe B. Lastly, as it was possible to quantify precipitate formation, the trends show that even though these species form more rapidly in samples without chloride ions (approximately 15% of species are precipitates, which are present throughout the curing process), there is no further formation of these compounds after the first contact with solution, meaning that leaching virtually stopped after that which occurred during the agglomeration. This is not the case for samples where chloride ions are present, as species continue to precipitate even at later stages, reaching a concentration of approximately 48% of the overall sulphide species at day 65 of curing.

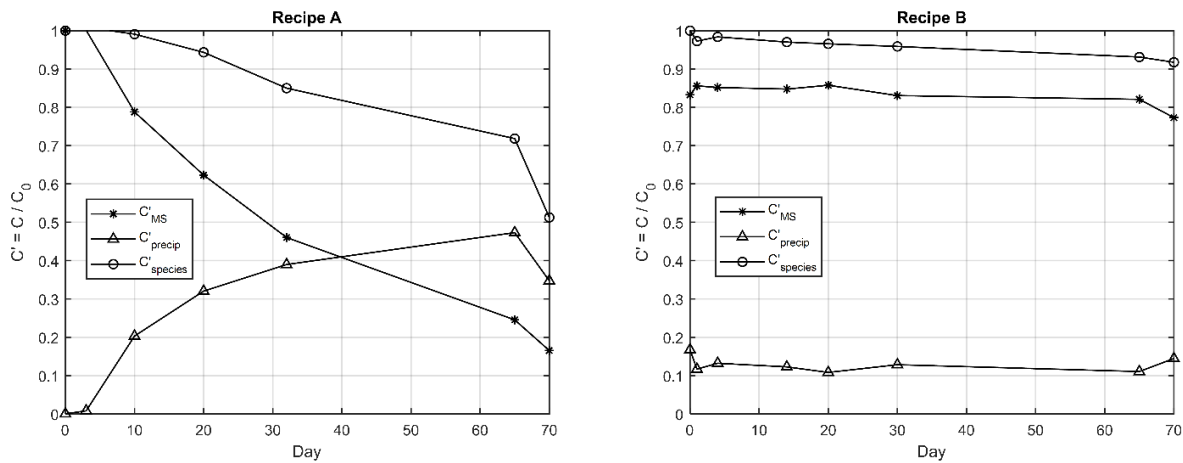


Figure 5.6. Normalised concentration of species at different stages of the curing process, and after water washing the samples.

Since the volume and distance to surface of both sulphide grains and precipitates were successfully quantified and recorded, it is also possible to describe in more detail the spatial distribution of species within the sample. An important point to stress, though, is that this methodology can only quantify volume. Thus, it is convenient to define a dimensionless concentration by considering the density of each component:

$$C_i^* = \frac{C_i}{\rho_i} \quad (5.2)$$

where ρ_i is the mass density of species i (e.g. sulphide grains (MS), precipitates (precip), or the overall sulphide species).

This dimensionless concentration can be obtained directly by using the quantification methodology. It can then be plotted as a function of distance to the nearest surface, giving a better idea of the chemical changes occurring throughout the agglomerate structure. Figure 5.7 shows this plot for the sulphide grains, and Figure 5.8 shows it for the precipitating species.

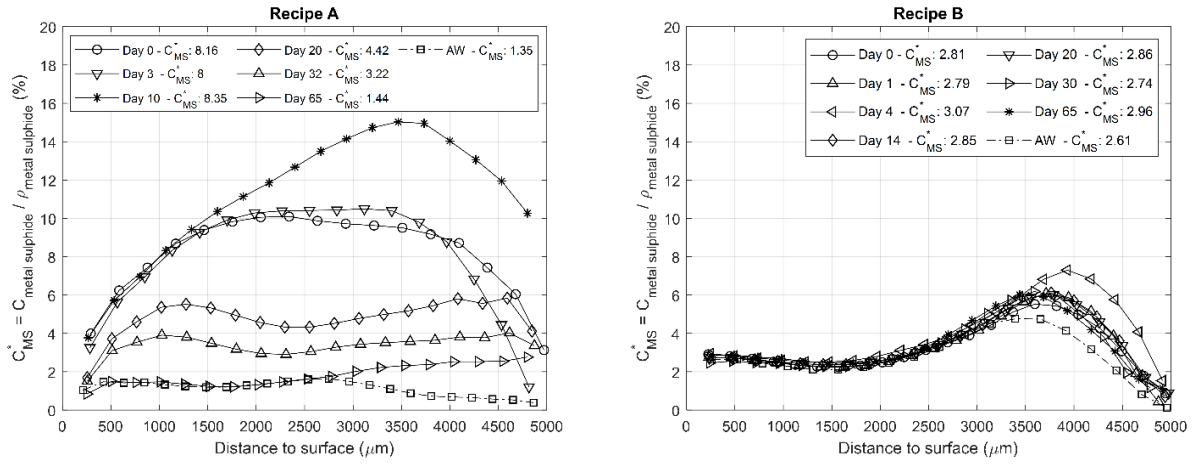


Figure 5.7. Dimensionless concentration of sulphide grains as a function of distance to the nearest surface.

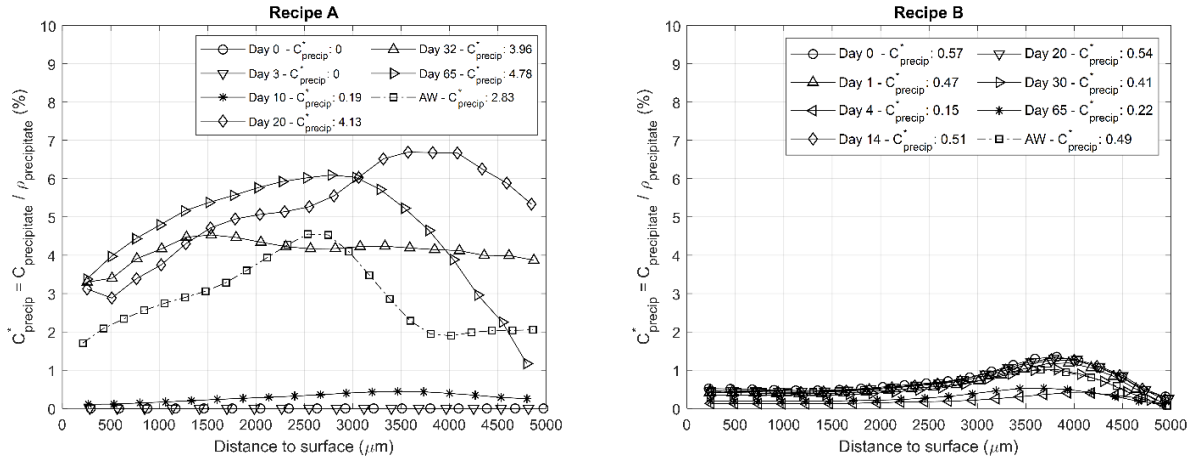


Figure 5.8. Dimensionless concentration of precipitates as a function of distance to the nearest surface.

As there is no clear trend from the figures, it is useful to define another dimensionless quantity that we called the Precipitation Ratio (PR). Considering that precipitates can only form once the initial sulphide grains have been dissolved, this PR can be defined as the amount of precipitates formed at a certain timestep w.r.t the amount of sulphide grains remaining at the point:

$$PR = \frac{C_{precipitate}^*}{C_{Metal\ Sulphide}^*} \quad (5.3)$$

Bearing in mind that the forming precipitates are water-soluble species (Figure 5.3), this PR will be a strong indicator of the proportion of metal species that will be easily leached out when the subsequent leaching process starts.

For instance, a PR of more than 1 will mean that at a certain location and time, there will be more precipitates than sulphide grains within the agglomerate. On the other hand, a PR of values closer to 0 will indicate that there is virtually no leaching occurring over the curing process, and either longer times or additional reagents are necessary to achieve a higher leaching extent over the curing process.

Figure 5.9 shows the PR values as a function of distance to the nearest distance for both sample types. It can be observed that as the agglomerates dried out, the reprecipitation of metal species occurred most strongly close to the agglomerate surface. These results are consistent with what was observed from both the preliminary assessment of structural changes and the MLA analyses (sections 5.2 and 5.3, respectively).

The reason why the precipitation will occur mainly near the agglomerate surface is because the evaporation will occur mainly from near the outer surface, which will induce an outward flow of liquid within the agglomerate and higher concentration of soluble species towards the edge of the agglomerates.

Figure 5.9 also shows that the mean PR value for agglomerates of recipe A at day 20 is approximately 1, so there is virtually the same concentration of remaining sulphide grains as there is of precipitates. This is consistent with the preliminary observations from the more basic analysis in section 3.3, reaffirming that 20 days would be the minimum curing time in the presence of chloride ions to obtain meaningful metal extraction. This is not the case for agglomerates of recipe B, as their PR values never reach values over 0.20, which indicates a very low reprecipitation pattern and, thus, practically no appreciable dissolution extent over the 65 days of curing assessed.

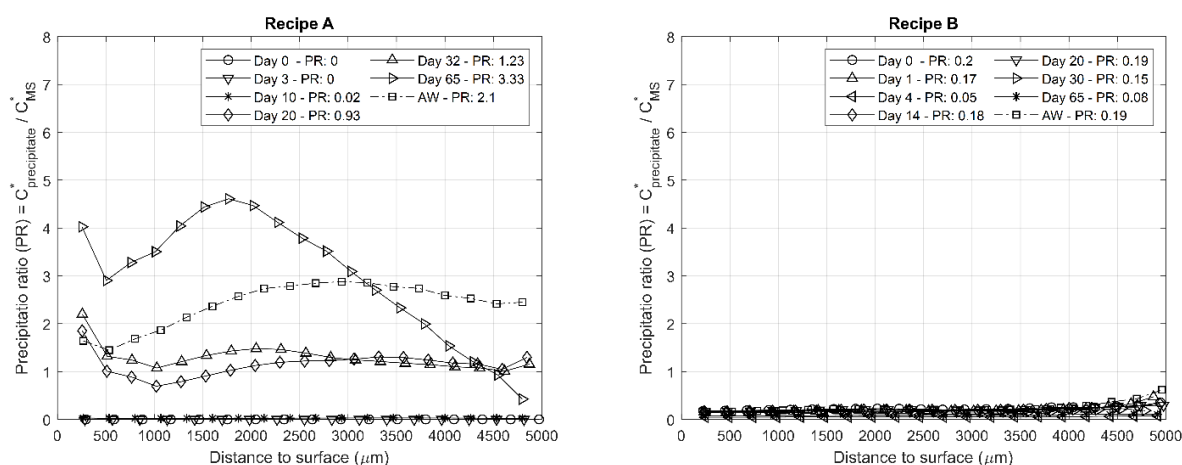


Figure 5.9. Precipitation ratio (PR) as a function of distance to the nearest surface.

5.6. Summary

A study of an extended curing process for copper-sulphide ore agglomerates was successfully performed. This included the development of a methodology for tracking the performance of the agglomerated ores and, in particular, a tool for quantifying grain scale leaching extent over the curing process. Due to the non-destructive and non-invasive nature of XMT scans, it was possible to successfully track the grain scale volume evolution over the curing process, and separately quantify the grain dissolution extent from the precipitation of species.

The study showed that curing mineral samples in the presence of chloride ions made a significant difference to the agglomerate structure and the dissolution rate of the metal sulphides. The assessment of the influence of curing period time on the leach performance showed that for the agglomerates containing NaCl, most of the leaching occurs within the first 20 days of curing, indicating that this may be the appropriate curing length to use. However, the time evolution of other agglomerate properties such as the mechanical stability and strength of the material were not assessed during this study and more further testing is required.

Furthermore, approximately 50% of the precipitates (which are mainly formed by the dissolved metals that reprecipitated as complex species of different mineralogy due to solution saturation) were water washed for samples agglomerated with the addition of chloride ions, whereas only a 20% when using a more typical agglomeration solution (i.e. containing no chloride ions). This result suggests that the precipitating species are water soluble and that a high concentration of chloride ions in the agglomeration solution enhances metal dissolution over the curing process. Lastly, this study shows that extended curing times can result in significant metal leaching, but only for the system containing NaCl.

Chapter 6. Modelling the curing of agglomerated ores

6.1. Introduction

Numerous mathematical models with different degrees of complexity have been published to describe the leaching process both at the micro- and macroscale (Dixon and Petersen, 2003; Leahy, Philip Schwarz and Davidson, 2006; Videla, Lin and Miller, 2007; Moreno-Atanasio, Williams and Jia, 2010; Ferrier *et al.*, 2016; Lin, Barker, *et al.*, 2016; Hoummady *et al.*, 2018). Still, these models mainly describe rock systems and to the author knowledge, no mathematical model that describe either the curing or the leaching of agglomerated ores has been developed to date. A reason for this might be the lack of information that common characterization techniques provide on the degree of change that agglomerates experience at each stage of the process.

With the aim of understanding the coupling between reaction, evaporation, transport, and precipitation of species over the curing process, a model that describes the behaviour of agglomerated ores over curing was developed based on the results obtained in Chapter 5. X-ray Microtomography (XMT or micro CT) was used as a complementary technique to image and describe the process due to its non-destructive and non-invasive nature (section 2.4). In order to fully describe the curing of agglomerated ores, this model considers both the metal dissolution extent, as well as the reprecipitation of species due to water evaporation. This model is able to successfully predict the trends seen in the experiments, with the relative reaction and evaporation rates being controlling factors.

In this chapter, section 6.2 describes the mathematical model and the main considerations and assumptions made, section 6.3 shows the validation of this model by comparing experimental results and simulation results, section 6.4 explains a sensitivity analysis performed to assess the impact of variations in the main non-dimensional numbers formed for this model, and section 6.5 describes the expected impacts of changes in some of the main variables on the curing performance and suggests the most appropriate agglomeration conditions to enhance leaching over the curing process.

6.2. Mathematical Model

A model that describes the curing process for agglomerates ores is derived and presented as a set of partial differential equations. For this purpose, a combination of simultaneous chemical and physical processes is considered to characterise the curing stage. The equations were then solved numerically due to the complexity of the set of partial differential equations that describe the motion of both the internal moisture and the reagents. This section describes the derivation of the governing equations and the methods used for numerically solving them.

6.2.1. Considerations

Over the curing process there are three main processes occurring simultaneously:

- Samples dry out due to water evaporation.
- Dissolution reactions occur due to the addition of leaching reagents.
- Species precipitate due to saturation of the solution.

Since this is a simplified model developed primarily to address the lack of available tools to quantitatively describe the curing of agglomerated ores, quantities will be considered to change spatially only w.r.t radius. While this model is simple, it does not mean that it will not describe the chemical and physical changes occurring over the process, but that a number of common assumptions will be made.

6.2.2. Fluid Motion

In order to describe the water flux within the agglomerates, and considering that this is a not saturated porous system, it is convenient to use Richards' equation (Richardson, 1922; Richards, 1931). This equation is often chosen to physically represent the fluxes in porous systems when the accurate characterization of the soil water dynamics is required (Zha *et al.*, 2019). Richards' equation is widely used in fields such as geology (Yuan and Lu, 2005; Li *et al.*, 2021), hydrology (Pachepsky *et al.*, 2003; Downer and Ogden, 2004; Lee and Abriola, 2015; Zhu *et al.*, 2018; Nimmo *et al.*, 2021), petroleum engineering (Serrano, 2004; Scussiato *et al.*, 2021), and several other systems with similar characteristics to agglomerated ores (Nimmo, 1990; Lee and Abriola, 2015; Broadbridge *et al.*, 2017). Is it highly non-linear and therefore much more complex to solve than the saturated Darcy's equation (H. Darcy, 1865), which is commonly used to describe fluid motion in saturated porous media. It is, thus, necessary to solve Richards' equation for both pressure and saturation. Then, the flux of water is described by the following equation:

$$\mathbf{F} = -\frac{s\phi k}{\mu}\nabla P \quad (6.1)$$

where s : pore saturation

ϕ : porosity

k : is the permeability of the agglomerates (which is a function of pore saturation)

μ : solution viscosity

P : liquid pressure

During the curing process samples dry out and a gradient of liquid pressure over the agglomerate structure will be produced by water evaporation, which can only occur at the outer surface (Figure 6.1). This was observed on the results described in Chapter 5 and, to the author knowledge, is information that has never before been taken into account in the modelling of the curing or the leaching process. Agglomerates will be approximated as spherical; the gradient can be well described by considering the changes in the radial direction:

$$F_r = -\frac{s\phi k}{\mu} \frac{\partial P}{\partial r} \quad (6.2)$$

Furthermore, the evaporation rate at the surface will be given by:

$$F(R) = s\phi v_{evap} \quad (6.3)$$

with v_{evap} the superficial velocity of evaporation and R the agglomerate radius.

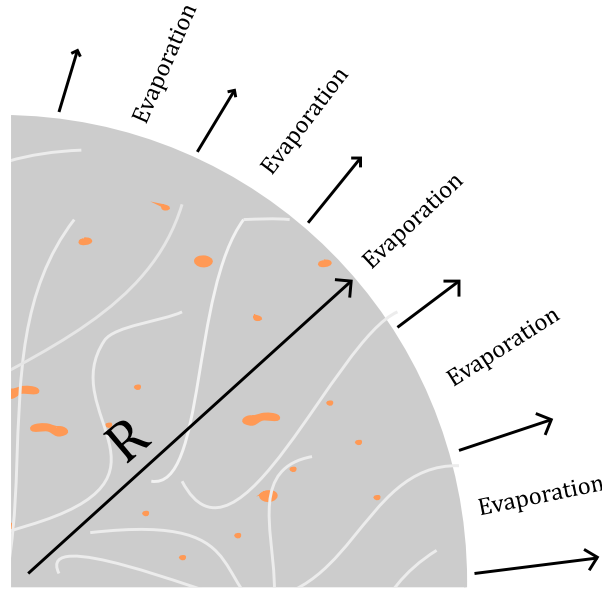


Figure 6.1. Schematic of the transport and evaporation processes occurring over the curing or agglomerated ores.

Since sample saturation will vary spatially and temporally, a continuity equation is necessary to describe the saturation as a function of time:

$$\phi \frac{\partial s}{\partial t} = -\nabla \cdot \mathbf{F} \quad (6.4)$$

And considering only the variation in the radial direction, this can be converted to spherical coordinates, with all fluxes except those in the radial direction set to zero:

$$\phi \frac{\partial s}{\partial t} = -\frac{1}{r^2} \frac{\partial r^2 F_r}{\partial r} \quad (6.5)$$

The pressure within the pores will vary with saturation, thus $P = P(s)$. A function commonly used to describe water retention in fractured/porous rocks is the Van Genuchten function (van Genuchten, 1980). This function relates the capillary pressure to the effective saturation in porous media, and it has been shown to work for a wide range of porous media (de Smedt and Wierenga, 1979; Liu, Ball and Ellis, 1998; Hunt, 2004; Szymkiewicz, 2013; Luo *et al.*, 2019). The relationship is as follows:

$$P = c_{cap} \left(\left(\frac{s - s_r}{1 - s_r} \right)^{\frac{-1}{1-n_1}} - 1 \right)^{n_1} \quad (6.6)$$

where s_r is the water residual saturation, and c_{cap} ¹⁵ (i.e. α^{-1}) and n_1 are empirical parameters that need to be determined for a specific medium.

Meanwhile, permeability of geological materials is often described using the Brook-Corey model (Kewen, 2004; Li, 2010; Yekta *et al.*, 2013; Chen, Zhou and Rahman, 2014; Gershenson *et al.*, 2016; Lian *et al.*, 2016; Hashemi *et al.*, 2021). Brook and Corey (1964) proposed this model that characterises the relative permeability of a fluid in a multi-flow system by considering the residual saturation of each component and the characteristics of the specific medium. For this curing model, the modified power-law relationship (which is commonly referred to as the “modified Brook-Corey relationship”) is used as it also considers the maximum relative permeability for each fluid component:

$$k(s) = k_{max} \left(\frac{s - s_r}{1 - s_r} \right)^{n_2} \quad (6.7)$$

where k_{max} is the maximum relative permeability of solution within the agglomerate’s pores (which can range between 0 and 1) and n_2 is an empirical parameter.

6.2.3. Copper motion

Due to water evaporation occurring over the process, there will be a solution flux directed outwards (i.e. towards the agglomerate surface) and dissolved species motion will be towards the exterior (as shown in Figure 6.1). This assumption is based on the observations and results explained in Chapter 5. These are new findings that were only possible to gather by using a combination of micro-CT (non-destructive characterisation technique) and EDX/SEM imaging (destructive, but more descriptive characterisation technique), and by developing a suitable image processing methodology (as it is explained in Chapter 4). To the author knowledge, this information has never been included in previous curing or leaching models.

¹⁵ C_{cap} is proportional to the surface tension over the pore radius and there is a contact angle dependency.

Then, assuming that the reagent motion is both diffusive and convective, the flux of copper \hat{F}_{Cu} can be described by:

$$\mathbf{F}_{Cu} = \mathbf{F}C_{Cu} - s\phi D_{eff} \frac{\partial C_{Cu}}{\partial r} \quad (6.8)$$

where D_{eff} is the effective diffusivity, which is the apparent diffusivity including the contribution from tortuosity of the pores.

For this case study reactions are assumed to be limited only by copper dissolution and mass transport. The maximum concentration of copper in solution is limited by solution saturation because there is no addition of solution during the curing process. Once the solution reaches the copper saturation concentration, species will begin to reprecipitate in various mineralogical forms (as observed in Chapter 5). We will refer to this new solid phase as “precipitating species” or simply “precipitates”. For the solution there will therefore be copper source terms associated with leaching of mineral grains and sink terms associated with precipitation.

Then, the rate of copper change in solution per time is given by:

$$\frac{\partial C_{Cu}s\phi}{\partial t} = -\nabla \cdot \mathbf{F}_{Cu} + \dot{m}_r - \dot{m}_p \quad (6.9)$$

And since the flux of copper is only a function of radius, equation (6.9) takes the form of:

$$\frac{\partial C_{Cu}}{\partial t} = \frac{1}{s\phi} \left(-\frac{1}{r^2} \frac{\partial(r^2 F_{Cu})}{\partial r} + \dot{m}_r - \dot{m}_p - C_{Cu}\phi \frac{\partial s}{\partial t} \right) \quad (6.10)$$

On the one hand, the dissolution of copper will be described using a typical first order kinetic reaction in order to ease the mathematical solution. Although, higher-order kinetics can be easily included in future and more complex models. It is important to note that dissolution will only occur at the surface of the sulphide grain. Then, it is useful to define the dissolution rate of copper grains (mass per unit volume per time) as follows:

$$\dot{m}_r = f(s) \begin{cases} \beta k_r (\bar{C}_{Cu_{grain}})^{\frac{2}{3}} (C_{sat} - C_{Cu}) & \text{if } C_{Cu} < C_{sat} \\ 0 & \text{otherwise} \end{cases} \quad (6.11)$$

where: $f(s)$ ¹⁶: fraction of the grain surface that is wet

k_r : surface reaction rate (with units of inverse length per time)

¹⁶ At this stage, the actual values for $f(s)$ are not known and it is assumed that $f(s) = 1$ over the entire curing process. This function can be further studied, and its values can easily be implemented in more complex simulations.

β : constant that relates volume and surface (with units of volume over surface)

$\bar{C}_{Cu_{grain}}^{17} = C_{Cu_{grain}}/C_{Cu_{grain_0}}$: proportional to the remaining volume of copper grains

C_{sat} : saturation concentration of copper in solution

The precipitation of copper-containing species is likely to take place when the concentration of copper exceeds the solution saturation (i.e. $C_{Cu} > C_{sat}$). Now, since precipitation will take place within the internal pores, and considering a precipitation rate that is proportional to the excess concentration, C_{Cu} ; the rate of precipitation of copper-containing species per unit volume can be defined as:

$$\dot{m}_p = \begin{cases} s\phi k_p (C_{Cu} - C_{sat}) & \text{if } C_{Cu} > C_{sat} \\ 0 & \text{otherwise} \end{cases} \quad (6.12)$$

with k_p a precipitation rate constant with units of inverse time. Note that as long as this value is large, the maximum concentration will remain close to the saturation concentration.

A symmetry/zero gradient condition is considered at the centre of the agglomerate, so:

$$\left. \frac{\partial C}{\partial r} \right|_{r=0} = 0 \quad (6.13)$$

It is useful to non-dimensionalise equations in order to perform simulations. Firstly, as C_{sat} is the maximum concentration, it would be logical to use this quantity for the dimensionless concentration:

$$C^* = \frac{C_{Cu}}{C_{sat}} \quad (6.14)$$

And the radial distance will be limited by the agglomerate radius, R ; thus, the non-dimensional distance will be given by:

$$r^* = \frac{r}{R} \quad (6.15)$$

Lastly, the dimensionless time is related to the actual time by the relationship:

$$\tau = t\beta k_r \quad (6.16)$$

6.2.4. Summary of equations

The set of equations summarized in Table 6.1 can then be used to model the curing process of agglomerated ores.

¹⁷ The 2/3 power arises because these are surface reactions occurring at the sulphide grain surfaces.

Table 6.1. Set of non-dimensional equations used to describe the curing of agglomerated ores.

Fluid governing equation	$\phi \frac{\partial s}{\partial \tau} = - \frac{1}{r^{*2}} \frac{\partial r^{*2} F^*}{\partial r^*}$
Fluid flux	$F^* = \frac{F}{R\beta k_r} = \frac{s\phi k c_{cap}}{R^2 \mu \beta k_r} \frac{\partial P^*}{\partial r^*}$
Capillary pressure	$P^* = \frac{P}{c_{cap}} = \left(\left(\frac{s - s_r}{1 - s_r} \right)^{\frac{-1}{1-n_1}} - 1 \right)^{n_1}$
Copper governing equation	$\frac{\partial C^*}{\partial \tau} = \frac{1}{s\phi} \left(- \frac{1}{r^{*2}} \frac{\partial (r^{*2} F_{Cu}^*)}{\partial r^*} + \dot{m}_r^* - \dot{m}_p^* - C^* \phi \frac{\partial s}{\partial \tau} \right)$
Copper flux	$F_{Cu}^* = \frac{F_{Cu}}{R\beta k_r C_{sat}} = F^* C^* - \frac{s\phi D_{eff}}{R^2 \beta k_r} \frac{\partial C^*}{\partial r^*}$
Dissolution rate of copper grains	$\dot{m}_r^* = \frac{\dot{m}_r}{\beta k_r C_{sat}} = \begin{cases} \left(\bar{C}_{Cu\ grain} \right)^{\frac{2}{3}} (1 - C^*) & \text{if } C^* < 1 \\ 0 & \text{otherwise} \end{cases}$
Rate of precipitation of species	$\dot{m}_p^* = \frac{\dot{m}_p}{\beta k_r C_{sat}} = \begin{cases} \frac{s\phi k_p}{\beta k_r} (C^* - 1) & \text{if } C^* > 1 \\ 0 & \text{otherwise} \end{cases}$
Boundary conditions	
At the surface	$F^*(r^* = 1) = \frac{s\phi v_{evap}}{R\beta k_r}$
At the centre	$\left. \frac{\partial C^*}{\partial r^*} \right _{r^*=0} = 0$

Dimensionless groups form by using the definitions in Eq. (6.14), (6.15), and (6.16), allowing the number of independent variables to be reduced. One of the most important groups is the one that dictates the relative importance of the diffusive mass transport and the surface reaction rate:

$$\epsilon = \frac{\phi D_{eff}}{R^2 \beta k_r} \quad (6.17)$$

Equation (16) is the inverse of the Damköhler number, which is the ratio between the reaction rate and the mass diffusion rate:

$$Da = \frac{R^2 \beta k_r}{\phi D_{eff}} \quad (6.18)$$

A second dimensionless group of great importance that forms is the one that reflects the relative importance of the precipitation rate and the reaction rate:

$$\kappa_p = \frac{\phi k_p}{\beta k_r} \quad (6.19)$$

A third group, that relates the fluid properties and the agglomerate geometric and material properties:

$$\xi = \frac{\phi k c_{cap}}{R^2 \mu \beta k_r} \quad (6.20)$$

Lastly, the non-dimensional evaporation rate can be expressed as:

$$\lambda = \frac{\phi v_{evap}}{R \beta k_r} \quad (6.21)$$

Then, it is convenient to rewrite the set of equations described in Table 6.1. in terms of the non-dimensional numbers described in equations (6.17) to (6.21) (Table 6.2).

Table 6.2. Set of non-dimensional equations used to describe the curing of agglomerated ores expressed in terms of the non-dimensional groups (6.17) to (6.21).

Fluid governing equation	$\phi \frac{\partial s}{\partial \tau} = - \frac{1}{r^{*2}} \frac{\partial r^{*2} F^*}{\partial r^*}$
Fluid flux	$F^* = s \xi \frac{\partial P^*}{\partial r^*}$
Capillary pressure	$P^* = \left(\left(\frac{s - s_r}{1 - s_r} \right)^{\frac{-1}{1-n_1}} - 1 \right)^{n_1}$
Copper governing equation	$\frac{\partial C^*}{\partial \tau} = \frac{1}{s \phi} \left(- \frac{\partial F_{Cu}^*}{\partial r^*} + \dot{m}_r^* - \dot{m}_p^* - C^* \phi \frac{\partial s}{\partial \tau} \right)$
Copper flux	$F_{Cu}^* = F^* C^* - \epsilon \frac{\partial C^*}{\partial r^*}$
Dissolution rate of copper grains	$\dot{m}_r^* = \begin{cases} \left(\bar{C}_{Cu_{grain}} \right)^{\frac{2}{3}} (1 - C^*) & \text{if } C^* < 1 \\ 0 & \text{otherwise} \end{cases}$
Rate of precipitation of species	$\dot{m}_p^* = \begin{cases} s \kappa_p (C^* - 1) & \text{if } C^* > 1 \\ 0 & \text{otherwise} \end{cases}$
Boundary conditions	
At the surface	$F^*(r^* = 1) = s \lambda$
At the centre	$\left. \frac{\partial C^*}{\partial r^*} \right _{r^*=0} = 0$

6.2.5. Numerical methods

Two different discretization schemes were considered, namely the Forward Time Centred Space (FTCS) scheme and the Crank-Nicolson (CN) scheme. The FTCS is an explicit method, which means that

the new time step values depend only on the current time step values. Therefore, it is easier to implement and quicker per time step but involves strict time step stability requirements. Furthermore, while generally second order accurate in space it is only first order accurate in time (the error associated with the time integration only halves when the resolution doubles).

Considering the arbitrary variable u , the numerical approximations obtained using the FTCS method for the first derivative in time and for the first and second derivatives one spatial dimension, x , are given as follows:

$$\frac{\partial u}{\partial t} \approx \frac{u_i^{n+1} - u_i^n}{\Delta t} \quad (6.22)$$

$$\frac{\partial u}{\partial x} \approx \frac{u_{i+1}^n - u_{i-1}^n}{2\Delta x} \quad (6.23)$$

$$\frac{\partial^2 u}{\partial x^2} \approx \frac{u_{i+1}^n - 2u_i^n + u_{i-1}^n}{\Delta x^2} \quad (6.24)$$

where the superscripts n and $n + 1$ represent the time step and the subscript i and $i \pm 1$ represent the space step. Thus, $t = t_0 + n\Delta t$ and $x = x_0 + i\Delta x$.

Alternatively, the Crank-Nicolson scheme is an implicit method, meaning that each new time step value depends upon both the new and current values. The main advantage of an implicit scheme, though, is that it does not have the strict time step constraints of an explicit scheme and much bigger time steps can be used. Moreover, it is second order accurate in time (i.e. when the time step is halved, the error associated with the time integration drops by a factor of about 4), but each step is slower to solve and it is harder to implement as it requires iteration and/or matrix inversion at each time step.

In this case, the numerical approximations for the arbitrary variable u are obtained by using the average of the spatial derivatives at the current time step and the new time step as follows:

$$\frac{\partial u}{\partial t} \approx \frac{u_i^{n+1} - u_i^n}{\Delta t} \quad (6.25)$$

$$\frac{\partial u}{\partial x} \approx \frac{u_{i+1}^{n+1} - u_{i-1}^{n+1}}{4\Delta x} + \frac{u_{i+1}^n - u_{i-1}^n}{4\Delta x} \quad (6.26)$$

$$\frac{\partial^2 u}{\partial x^2} \approx \frac{u_{i+1}^{n+1} - 2u_i^{n+1} + u_{i-1}^{n+1}}{2\Delta x^2} + \frac{u_{i+1}^n - 2u_i^n + u_{i-1}^n}{2\Delta x^2} \quad (6.27)$$

Any PDE that consider only one spatial dimension, which is the case of this model, can be written in the following form:

$$a_i u_{i+1}^{n+1} + b_i u_{i-1}^{n+1} + c_i u_i^{n+1} = f_i \quad (6.28)$$

where each value from the current time step is treated as constant and will be part of the right-hand side of the equation (f_i). This equation can be written as a matrix, which for the particular case of one spatial dimension is a tri-diagonal matrix, which is readily inverted.

6.2.6. Discretization of the equations

Equations were solved using a finite volume (FV) approximation. A regular mesh was considered for this problem, meaning that each control volume was of the same dimensions. Most equations were resolved using the FTCS scheme for simplicity. The low diffusivity and non-linearity of the mass transport means that a stable explicit time step is both small, resulting in long simulation times, and hard to assess. We therefore use the Crank-Nicolson method to solve the copper transport governing equation. The model was solved using a constant space step, Δr^* , considering that $R^* = 1$:

$$\Delta r^* = \frac{1}{i_{max} - 1} \quad (6.29)$$

the reason why it is necessary to subtract 1 from the number of nodes is because the first node is placed at 0 and the last at R .

The most appropriate time step, $\Delta \tau$, is more complex to determine as it will be a function of the spatial step and will impact the stability of the system (as mentioned in section 6.2.5). For this, the values of the water percolation time, equation (6.30), the diffusion time, equation (6.31), and the evaporation time, equation (6.32), were quantified and the smallest value among them was utilized as the time step. A CFL value of 0.3 was used to ensure numeric stability:

$$\Delta \tau_{water} = \beta k_r CFL \frac{\Delta r^{*2}}{\frac{R^2 k_{max} c_{cap}}{\mu}} \quad (6.30)$$

$$\Delta \tau_{diffusion} = \beta k_r CFL \frac{\Delta r^{*2}}{2R^2 D_{eff}} \quad (6.31)$$

$$\Delta \tau_{evaporation} = \beta k_r CFL \frac{\Delta r^*}{R v_{evap}} \quad (6.32)$$

Then, the discretization of the equations using the FTCS scheme was carried out as follows:

$$s_i = -\Delta \tau \frac{1}{\phi} \frac{1}{\Delta r^{*2}} \frac{F_{i-0.5}^* r_{down}^{*2} - F_{i+0.5}^* r_{up}^{*2}}{\Delta r^*} \quad (6.33)$$

$$F_{i-0.5}^* = -s_{down} \xi \left(\frac{P_i^* - P_{i-1}^*}{\Delta r^*} \right) \quad (6.34)$$

$$F_{i+0.5}^* = -s_{up}\xi \left(\frac{P_{i+1}^* - P_i^*}{\Delta r^*} \right) \quad (6.35)$$

$$P_i^* = \left(\left(\frac{s_i - s_r}{1 - s_r} \right)^{\frac{-1}{1-n_1}} - 1 \right)^{n_1} \quad (6.36)$$

$$\dot{m}_{r_i}^* = \begin{cases} \left(\bar{C}_{Cu\,grain} \right)^{\frac{2}{3}} (1 - C_i^*) & \text{if } C_i^* < 1 \\ 0 & \text{otherwise} \end{cases} \quad (6.37)$$

$$\dot{m}_{p_i}^* = \begin{cases} s_i \kappa_p (C_i^* - 1) & \text{if } C_i^* > 1 \\ 0 & \text{otherwise} \end{cases} \quad (6.38)$$

with $r_{down}^* = \frac{r_{i-1}^* + r_i^*}{2}$, $r_{up}^* = \frac{r_i^* + r_{i+1}^*}{2}$, $s_{down} = \frac{s_{i-1} + s_i}{2}$, and $s_{up} = \frac{s_i + s_{i+1}}{2}$. Then, the boundary conditions at the surface, equation (6.39), and at the centre of the agglomerate, equation (6.40), are given as follows¹⁸:

$$F_{i_{max}+0.5}^* = s_{i_{max}} \lambda \quad (6.39)$$

$$C_0^* = C_1^* \quad (6.40)$$

The discretization for the copper concentration equation is slightly different as this equation was solved using the CN method. Hence, it was solved by matrix inversion, which was implemented in C++ (code available by accessing the link in Appendix B). The coefficients a_i , b_i , c_i , and f_i are given as follows:

$$a_i = -\frac{r_{up}^{*2}}{r_i^{*2} \phi s_i \Delta r^*} \left(\frac{1}{2} F_{i+0.5}^* - \frac{s_{up} \epsilon}{\Delta r^*} \right) \quad (6.41)$$

$$b_i = -\frac{r_{down}^{*2}}{r_i^{*2} \phi s_i \Delta r^*} \left(-\frac{1}{2} F_{i-0.5}^* - \frac{s_{down} \epsilon}{\Delta r^*} \right) \quad (6.42)$$

$$c_i = -\frac{r_{up}^{*2}}{r_i^{*2} \phi s_i \Delta r^*} \left(\frac{1}{2} F_{i+0.5}^* - \frac{s_{up} \epsilon}{\Delta r^*} \right) - \frac{r_{down}^{*2}}{r_i^{*2} \phi s_i \Delta r^*} \left(-\frac{1}{2} F_{i-0.5}^* - \frac{s_{down} \epsilon}{\Delta r^*} \right) - \frac{2}{\Delta \tau} - \frac{\left(\bar{C}_{Cu\,grain} \right)^{\frac{2}{3}} + \kappa_p}{\phi s_i} \quad (6.43)$$

$$f_i = -\frac{C_i^*}{\kappa_p \Delta \tau} - \frac{1}{\phi} \left(1 - \left(\bar{C}_{Cu\,grain} \right)^{\frac{2}{3}} \right) \quad (6.44)$$

6.3. Validation of the model

In order to validate the model, simulations were conducted by considering the overall performance observed from a set of experimental results. Thus, most characteristic parameters were directly obtained from the acquired data set using the image processing methodology explained in (Chapter 4). Although,

¹⁸ As explained in sections 6.2.2 and 6.2.3, the outer surface has a specified evaporative flux, while there is a symmetry/zero gradient condition considered at the centre of the agglomerate.

a number of parameters were estimated by considering typical values of similar mass transport problems, which are summarized in Table 6.3.

Table 6.3. Parameters used for solving the model. All quantities are in standard SI units.

Parameter	μ	c_{cap}	s_r	n_1	n_2	k_{max}	C_{sat}
Unit	m^2s^{-1}	$m^{-1}kgs^{-2}$	—	—	—	m^2	$m^{-3}kg$
Value	10^{-3}	$2.5 \cdot 10^3$	$5 \cdot 10^{-2}$	2	2	10^{-11}	$1.5 \cdot 10^2$

The first 20 days¹⁹ of curing were simulated to assess representativity of the model. Initial simulations were carried out in which it was assumed that all sulphide grains have the same kinetics. In a second set of simulations, this assumption was relaxed, and grains were divided into classes with different kinetics (which would be a more realistic scenario). In both cases all mineral grains were assumed to be evenly distributed throughout the sample (i.e. initial copper concentration is the same at any given point). For the former case, a single reaction rate constant value (i.e. k_r) was considered and the value of this constant was fitted from experimental results.

Kinetics will change with a number of factors including grain size, which is explicitly modelled by considering three different size fractions each with different leaching kinetics (i.e. $k_{r,1}$, $k_{r,2}$, and $k_{r,3}$), as well as with factors such as mineralogy and mineral associations, which will result in a range of surface kinetics for a single particle size. The PSD of the mineral grains in the sample (Figure 4.13) was thus analysed and divided into three equal parts to select three representative particle sizes (in terms of concentration).

The values for $k_{r,i}$ were selected by considering a gamma-type probability density distribution for the quotient between each surface kinetic constant and the average value for its grain category. This approach is based on the work of (Lin, Barker, *et al.*, 2016), in which it was showed that the kinetics of a leaching system can be represented by a distribution of surface kinetics of that system.

A gamma distribution with standard values of $\alpha = 1.8$ and $\beta = 0.4$ (Figure 6.2) and a $k_{mean} = 10^{-6} (m^{-1}s^{-1})$ was considered for the curing process based on experimental results, therefore the surface kinetic constant values selected were $k_{r,1} = 0.5 \cdot 10^{-6} (m^{-1}s^{-1})$, $k_{r,2} = 1.0 \cdot 10^{-6} (m^{-1}s^{-1})$, and $k_{r,3} = 2.0 \cdot 10^{-6} (m^{-1}s^{-1})$. Each grain type was considered to react simultaneously at a constant leaching rate, with the partial contribution of each grain type to the total copper concentration in solution being updated at each step of the simulation.

¹⁹ 20 days would be the minimum curing time required to obtain meaningful results in terms of both grain dissolution and reprecipitation of species.

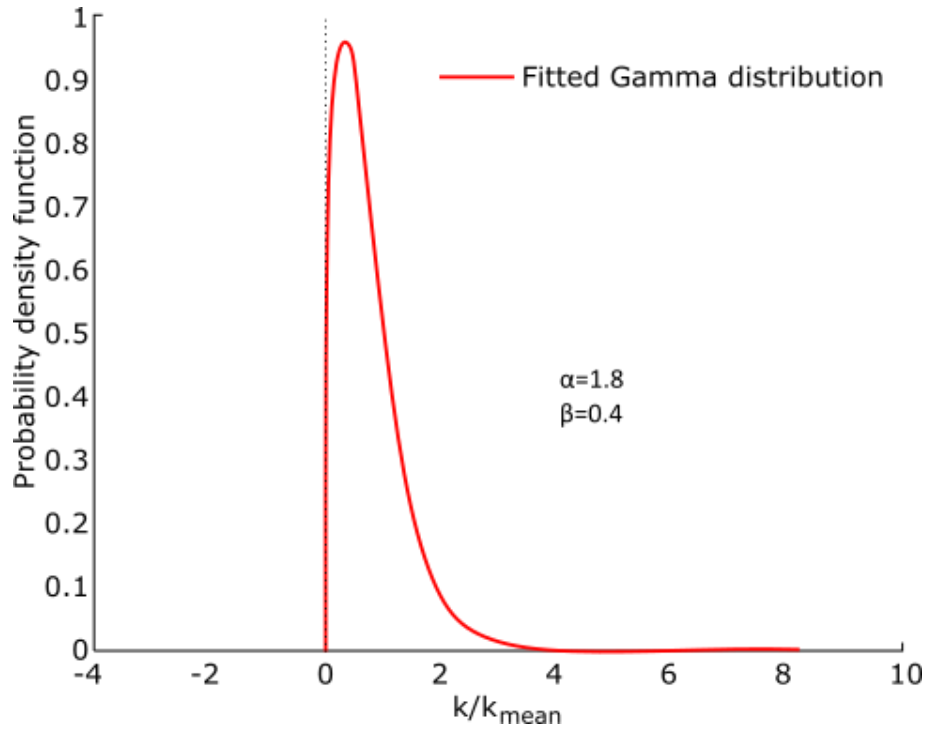


Figure 6.2. Gamma distribution with standard values of $\alpha = 1.8$ and $\beta = 0.4$.

It is worth noting that this methodology for selecting the $k_{r,i}$ values was developed for particulate systems, and it might not be as applicable for agglomerated ores since the transport processes are significantly different and, thus, also the distribution of leaching kinetics (this will be further discussed in Chapter 7). However, it is an appropriate approach at this stage, and it could be easily adjusted in future studies using more detailed information concerning the leaching of agglomerated ores. It is also important to note that choosing only three evenly distributed mineral grain types for these simulations relied merely on a balance between accuracy and computational complexity. It is expected that simulations will converge to the actual experimental values if more mineral grain types are considered, which will incorporate the natural leaching variability in the predicted curing behaviour.

In order to compare simulation and experimental results, it is convenient to present experimental results using the normalised concentration of species ($C'_i = C_i/C_{species_0}$) and the precipitation ratio ($PR = C_{precipitates}/C_{sulphides}$), explained in section 5.5. The concentration of species provides a general idea of the processes occurring within the agglomerate, and the PR value represents both the leaching and precipitation extent at each point in the sample. Figure 6.3 shows the average concentration values for day 20 of curing, while the PR values at each point in the agglomerate structure at the same curing time are displayed in Figure 6.4. Experimental results are on the left-hand side (Figure 6.4A) and simulation results on the right-hand side (Figure 6.4B).

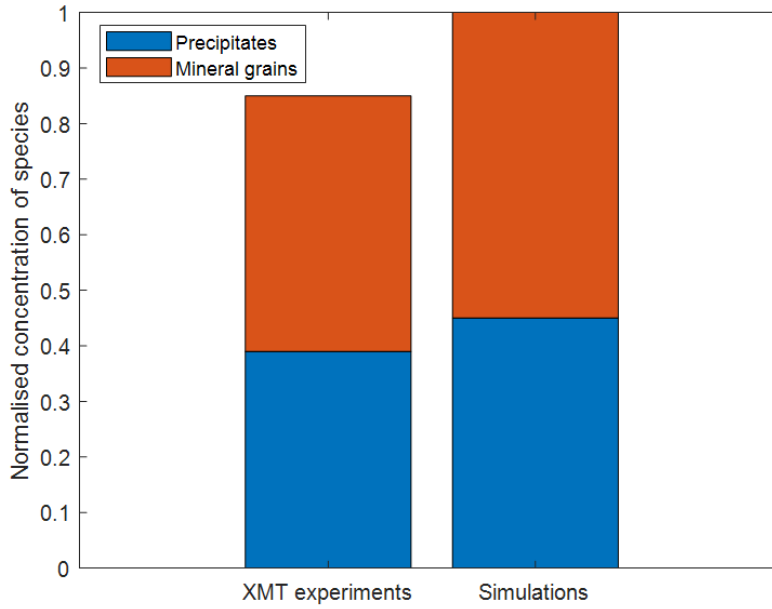


Figure 6.3. Average concentration values of Mineral Grains (blue) and Precipitated Species (orange) for both XMT experiments and Simulations at day 20 of curing.

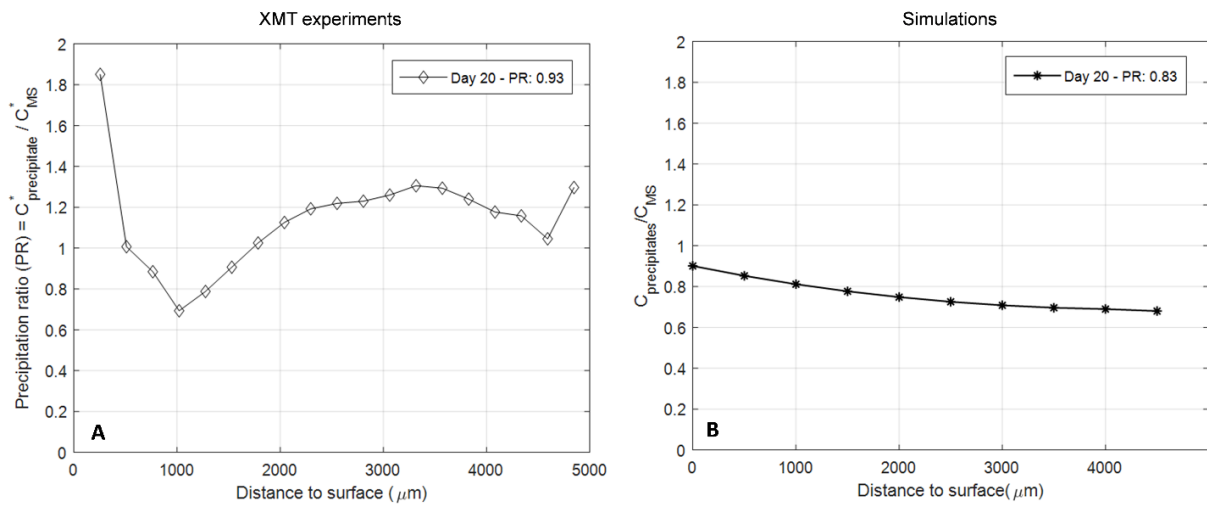


Figure 6.4. Precipitation ratio (ratio between precipitated species and the remaining mineral grains) obtained at day 20 of curing for A: XMT experiments, and B: Simulations.

It can be seen from Figure 6.3 that the proportion of precipitates (in blue) and mineral grains (in orange) at day 20 is virtually identical, with only a slight difference between simulations and experimental results. Some of the discrepancy is caused by the fact that the precipitate and mineral grains fractions do not add up to 1 for the XMT experiments, which is due to minor variations in the imaging and thresholding methods. That is to say that the overall concentration of species appears to be higher at the beginning (i.e. day 0) than at day 20 of the curing process. However, if the ratio between the two fractions is

calculated, very similar results are obtained for the experimental and simulation values (0.93 and 0.83, respectively).

Analysing the more detailed information displayed on Figure 6.4, it can be seen that the calibrated simulations show good agreement with the experimental results in terms of both remaining mineral grains and precipitates. The experimental trends in PR are more variable than the simulated results, but also show higher precipitation near the surface compared to the interior. It is also evident that the simulations slightly diverge from the experimental results. This could be due to the assumption of homogeneous composition of the sample and, even when considering more than one mineral-grain type (i.e. second set of simulations), the natural occurrence of mineral grains within a given sample is not accounted for. Another possible explanation could be the simplicity of the 2D model that does not consider the intrinsic heterogeneities of mineral ores and only considers spheric agglomerates. Nevertheless, trends are similar and can be used to assess the physicochemical changes occurring within the system.

6.4. Sensitivity analysis

6.4.1. Diffusion limited case

Generation and transport of copper will depend only on equation (6.17) and the process can be considered as diffusion limited when $Da \gg 1$ and reaction limited when $Da \ll 1$. Furthermore, this Da does not only affect the transport of species, but also the profile of the precipitate concentration as the transport of species will be towards the agglomerate's surface caused by moisture evaporation (as discussed in section 5.5).

The simulations of Precipitation Ratio at day 20 were carried out by considering Da values ranging from 10^{-6} to 10^{-1} (i.e. from nearly completely reaction limited to nearly completely diffusion limited) are shown in Figure 6.5, and it can be seen that the distribution of PR values throughout the agglomerate is significantly affected by the Da number. The other non-dimensional numbers were fixed, and their values were $\kappa_p = 5 \cdot 10^4$, $\xi = 1.25$, and $\lambda = 5 \cdot 10^{-4}$. The results obtained for higher Da values ($Da \gg 10^{-4}$) are quite far from the experimental results, and curves only start to collapse towards the experimental values for $Da \approx 10^{-5}$. Therefore, it can be speculated that the process is highly reaction limited. Ultimately, the shape of the PR curves only varies slightly for values below 10^{-5} , meaning that a $Da \approx 10^{-5}$ is representative of the transport processes occurring within the agglomerate under the experimental conditions used.

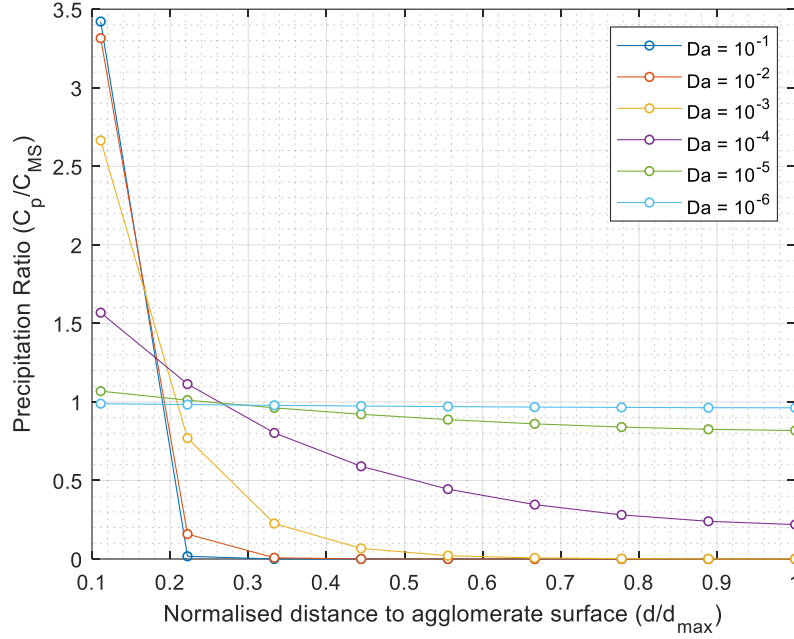


Figure 6.5. Precipitation Ratio as a function of distance to the nearest surface for day 20 of curing obtained from simulations carried out considering Da values from 10^{-6} to 10^{-1} .

6.4.2. Reaction limited case

The rate of precipitation, k_p , is the rate at which the reprecipitation of species will occur when the solution reaches saturation. In parallel, the formation of precipitates will depend on the availability of dissolved species (i.e. the concentration of metals in solution), which will be closely linked to the leaching kinetics. Hence, assessing the proportional effects of dissolution and reprecipitation in the formation of precipitates is also important for fully understand the curing process. This can be assessed by varying the relative rate of precipitation, κ_p , which is the precipitation rate relative to the reaction rate. Higher κ_p values will cause the precipitation process to be limited by the precipitation rate, whereas lower values will indicate that it is dissolution limited.

A set of simulations were, therefore, carried out using κ_p values ranging from 10^4 to 10^8 and the PR values throughout the agglomerate structure were plotted as a function of the distance to the nearest surface (Figure 6.6). The other non-dimensional numbers were fixed, and their values were $\epsilon = 5 \cdot 10^{-1}$, $\xi = 1.25$, and $\lambda = 5 \cdot 10^{-4}$. From the figure it can be seen that the PR profile for processes with a $\kappa_p \gg 10^4$ are quite different to the experimental results (see Figure 6.4). Meanwhile, curves do collapse to the effective values for $\kappa_p \leq 10^4$. Consequently, a $\kappa_p \approx 10^4$ would accurately represent the process under the experimental conditions, and the formation of precipitates would be highly controlled by the leaching kinetics.

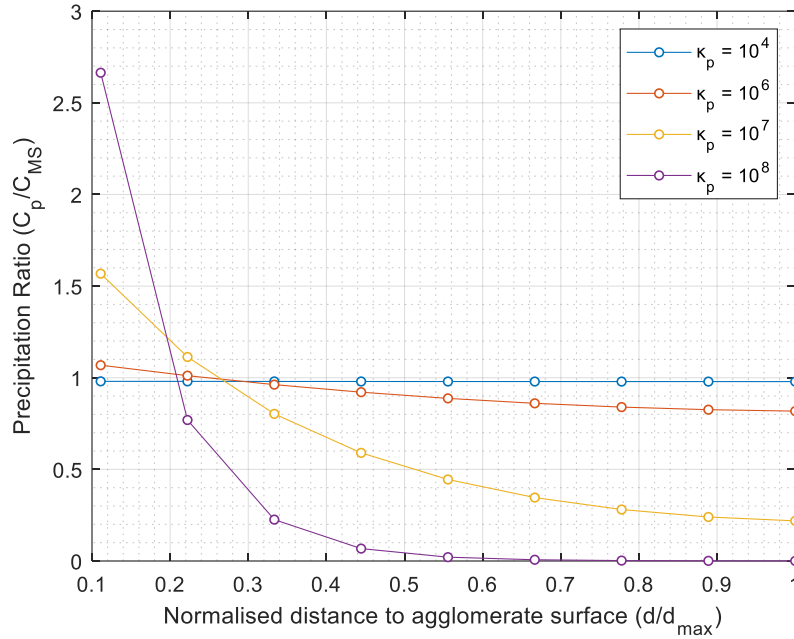


Figure 6.6. Precipitation Ratio as a function of distance to the nearest surface for day 20 of curing obtained from simulations carried out considering Da values from 10^4 to 10^8 .

6.5. Variations in the agglomeration and curing conditions.

One of the main aims of performing simulations is to assess the impact of the different variables on the curing of agglomerated ores avoiding numerous time-consuming experiments and allowing the optimum range of experimental conditions to be determined. In this section, the influence of the evaporation rate and the agglomerate size on the final product is presented and recommendations on the best practices to carry out agglomeration are provided based on the results obtained.

6.5.1. Influence of the evaporation rate

The evaporation rate, v_{evap} , is the volumetric evaporation rate per area of agglomerate surface, and therefore takes the form of a velocity. It is a critical variable in the curing process as the fluid flow will be directed towards the agglomerate surface (Chapter 5) and it will thus induce the outward transport of dissolved species. This can be observed from Figure 5.8 where a higher extent of precipitated species is found closer to the surface of the sample.

The impact of the evaporation rate²⁰ on the dissolution and precipitation of species was assessed for processes whose v_{evap} was a quarter, half, double, and four times the value observed for the experimental conditions used. Figure 6.7 shows the leaching extent at day 20 of curing, where it can be

²⁰ It was estimated that under the experimental conditions $v_{evap} = 10^{-8} \left(\frac{m}{s}\right)$, with an average evaporation time of 10 days.

seen that an increase in the evaporation rate will produce a decrease in the leaching extent. This is because higher leaching extents can be predicted for longer contact times between the agglomeration solution (which contains leaching reagents) and the mineral grains. It is not because evaporation increases the concentration in solution and thus restricts the leaching reach. While dissolution will only take place up till the solution reaches saturation, this is not the case as there is a consistent increase in the leaching extent even at very low evaporation rates.

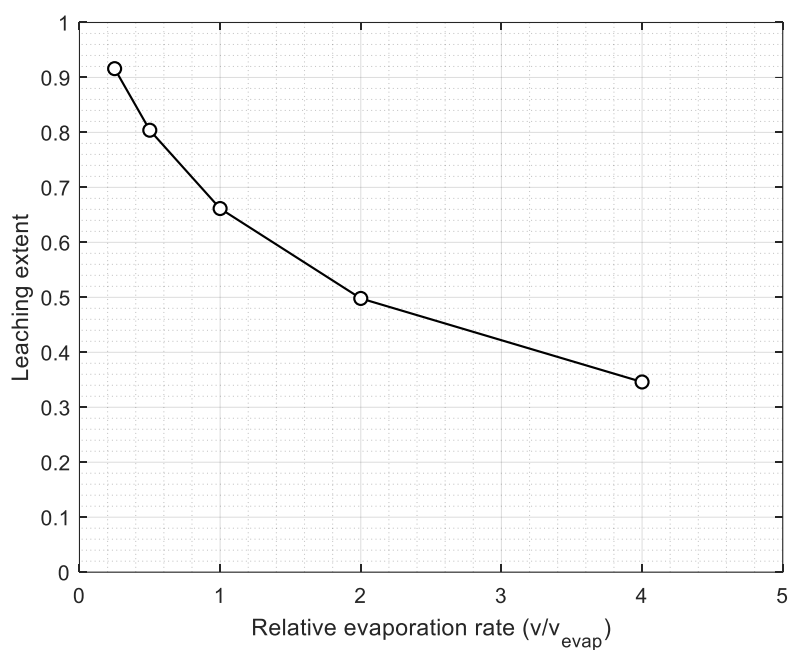


Figure 6.7. Leaching extent for different rates of evaporation at day 20 of curing.

Figure 6.8 shows the evolution of the precipitate formation at different stages of the curing process. It can be seen that a slower evaporation rate will be highly beneficial both for mineral grain dissolution as well as for the generation of precipitates that can be readily extracted in early stages of the leaching process. Although, this does not include the effect that evaporation might have on the stability of the agglomerates, which also needs to be considered

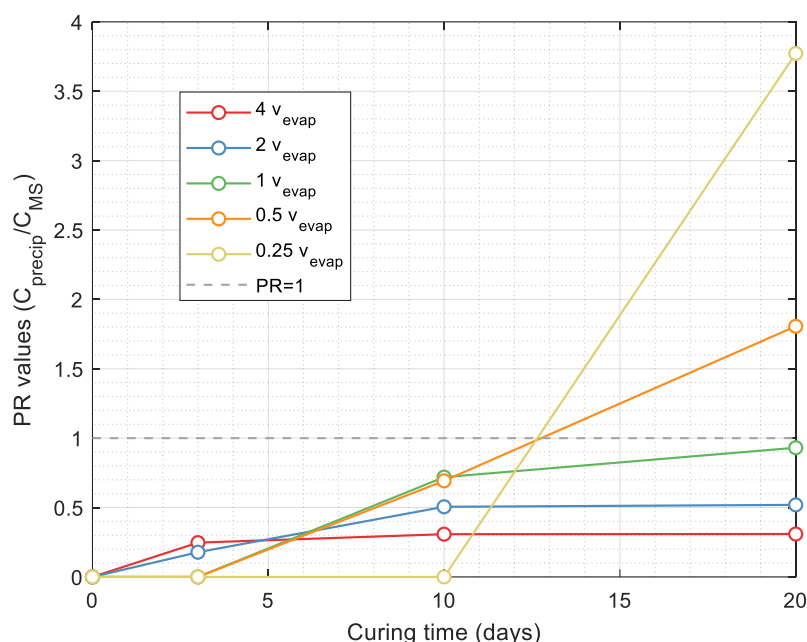


Figure 6.8. Precipitation Ratio at different curing times for different evaporation rates.

A higher leaching extent will generate a greater availability of dissolved species that will reprecipitate when the solution reaches saturation. Thus, a slower evaporation rate will be highly beneficial both for mineral grain dissolution as well as for the generation of precipitates that can be readily extracted in the early stages of the leaching process. Although, this does not include the effect that evaporation might have on the mechanical stability of the agglomerates, which also needs to be considered

6.5.2. Influence of the agglomerate size

The effect of the agglomerate size was also assessed by considering agglomerates of 5, 10, 15, 20, and 40 mm of diameter²¹. The leaching extent at day 20 of curing is presented in Figure 6.9, where it can be seen that a higher extent of grain dissolution may be expected for bigger agglomerates. A possible explanation for this is the decrease in specific surface area with an increase in volume. Since evaporation occurs mainly at the external surface, the evaporation process will take longer for bigger samples. This increases the contact time between the agglomeration solution and the mineral grains, enhancing grain dissolution. This is the opposite of what is expected during the subsequent leaching, which is dependent on the mass transfer of reagents into and copper out of the agglomerate, which should increase for smaller agglomerates.

²¹ The average size considered for of the agglomerates used in the experiments was 10 mm (section 3.4.3.1).

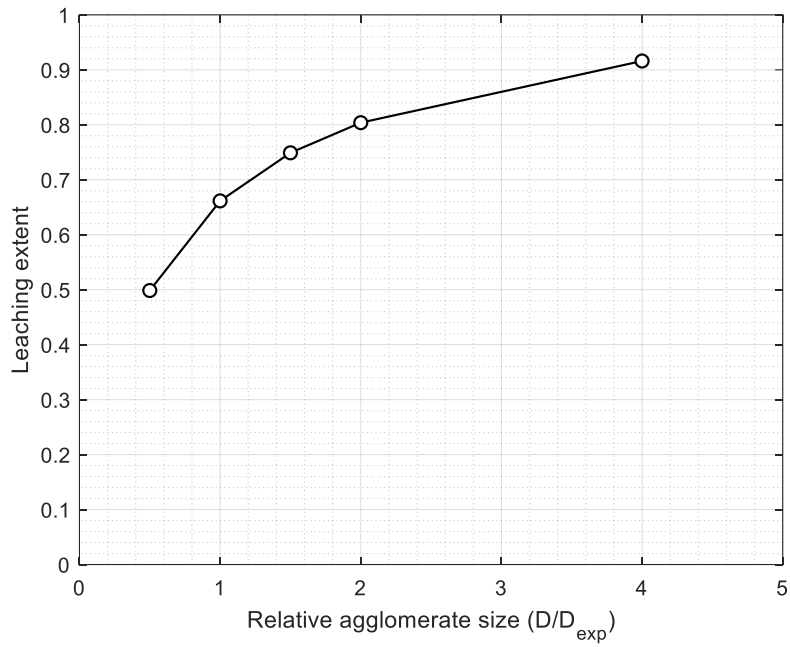


Figure 6.9. Leaching extent for different sizes of agglomerate at day 20 of curing.

Figure 6.10 shows the evolution of the precipitate formation at different stages of the curing process. From the figure it is possible to see that a higher extent of reprecipitated species is expected for bigger agglomerates, which also present the highest leaching extent. This is consistent with the results obtained for slower evaporation rates (section 6.5.1), where higher PR values were also observed when grain dissolution was higher. Consequently, the agglomerate size will directly affect the extent to which grains dissolve and species reprecipitate over the curing process, with bigger agglomerates being suggested for obtaining the highest curing performance. It is important to bear in mind, though, the potential impact on the subsequent leaching and thus the potential for an optimisation of the size to balance curing and leaching performance.

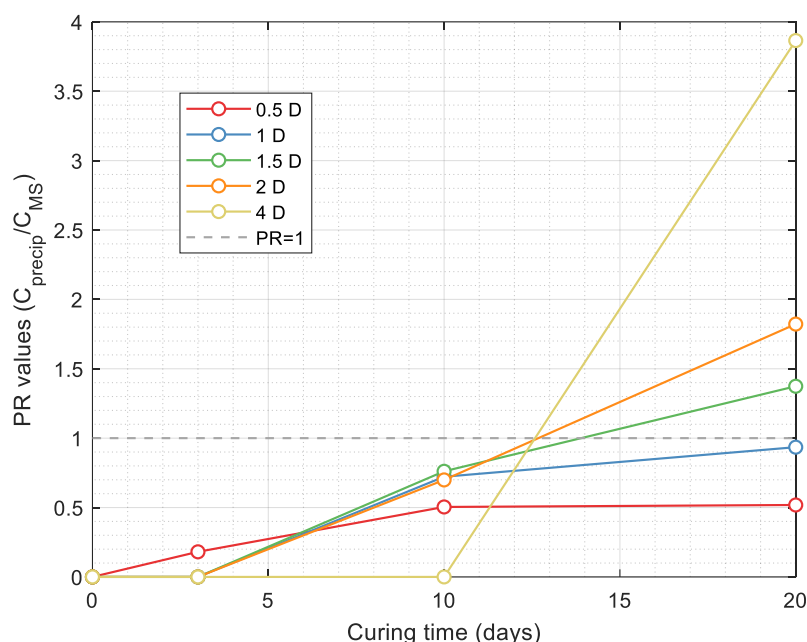


Figure 6.10. Precipitation ratio at different curing times for different agglomerate sizes.

6.6. Final remarks

A model that describes the structural and chemical changes that occur over the curing process within agglomerated ores was presented and described in this chapter. This is based on experimental results obtained from a set of XMT images acquired over the 65 days of the curing process, which were presented in Chapter 5. The model considers an outward flux of liquid produced by evaporative processes, as well as copper dissolution and precipitation due to the presence of leaching reagents added in the agglomeration stage. All leached species will remain within the agglomerates and, due saturation of the solution, these previously dissolved species will begin to reprecipitate in the agglomerate's internal pores. Therefore, the evaporation-reaction couple is considered as the mechanism controlling the overall curing process.

A set of simulations were carried out by considering two different sample types, namely agglomerates with a single type of mineral grain and samples with three different grain classes. In both cases grains were considered to be homogeneously distributed throughout the sample. Results showed that while simulations slightly diverge from the experimental results, which might be due to the simplifying assumptions made for the simulations and the fact that this is only a 2D model (only considers one spatial dimension and one temporal dimension), trends are virtually the same. It was thus demonstrated that this model represents the physicochemical changes occurring within the system and can be used to describe the transport and reprecipitation of species, as well as the structural changes occurring over the curing process.

It was discovered that the copper generation and transport as well as the formation of precipitates are both limited by the leaching reaction rate. Moreover, the evaporation rate and the agglomerate size also play a key role in the process. Longer contact times between the agglomeration solution and the mineral grains can be achieved by lower evaporation rates and by a bigger agglomerate size. This enhances both the leaching extent and the precipitation of species, indicating that these may be the most appropriate conditions to carry out the agglomeration and curing process and to achieve an optimum performance. However, increasing agglomerate size might be detrimental to the subsequent leaching because of the need for transport into and out of the agglomerates.

The aim of this model is to provide mathematical tools to represent the curing process of agglomerated ores, with the additional purpose of reducing the number of time-consuming experiments required to assess the impacts of the different agglomeration and curing variables in the subsequent leaching stage. It is possible to carry out more complex models and simulations in future works using the actual structure of agglomerates as domain. For this purpose, XMT is very helpful due to its 3D voxelized nature that also allows the main components of the sample to be distinguished from each other.

Chapter 7. XMT-based assessments of the leaching of agglomerated ores

7.1. Introduction

Most leaching studies focus mainly on the overall leach behaviour of a particulate system. The PLS is collected at different stages of the process and the concentration of species in the solution is used to calculate the mean recovery of the system. Although, while a common practice, it does not capture the leaching variability that occurs within the system. This variability is affected by several characteristics of the ore, and, at the heap scale, performance is determined by processes that occur at a wide range of length scales (section 2.2.5).

This chapter aims to quantify the mass transport and leaching variability at the particle and grain scale in agglomerated ores over the leaching process and assessing their impact in the overall leach extraction. For this purpose, a set of leaching experiments were carried out over 46 days using two different leach solutions in order to assess the impact of chloride ions on the leaching process, namely solutions A and B (with and without NaCl, respectively). The other components of the leach solution are summarized in Table 3.3. A curing period was performed prior to irrigating the columns with the leach solution as this process significantly improves leaching performance (section 2.2.6.2). The mineral ore was agglomerated using the same solution used for the leaching stage and agglomerates were left to cure for a period of 25 days. This period was selected in accordance with the results obtained in the curing experiments presented in Chapter 5, where it was shown that 20 days should be the minimum curing time in the presence of chloride ions to obtain meaningful results.

Samples were water washed for 5 days prior to starting the leaching (section 3.4.4), removing the reprecipitated species that formed over the 25 days of curing with the main intention of identifying the grain dissolution that takes place over the leaching stage²². The full leaching process was closely monitored using a combination of XMT imaging and ICP measurements of concentrations within the PLS samples, which were collected at the same time-steps that columns were imaged. The imaging and PLS collection schedule are summarized in Table 3.7.

The main advantage of using XMT as a characterisation technique is that the internal changes in the sample can be imaged and analysed without the need for destruction of the sample. This allows the volume of each grain in the sample to be tracked throughout the leaching process using the methodology developed for this thesis and described in Chapter 4. A limitation of this technique, though, is that

²² This washing stage was performed mainly to facilitate image segmentation as sulphide grains and precipitates present extremely similar attenuation values when exposed to an X-ray beam (as discussed in Chapter 4).

different sulphides will present similar attenuation values when exposed to an X-ray beam (section 2.4.2.4). Therefore, it is very hard to quantify the dissolution rate of each component separately. For this reason, the ICP measurements can be used to calibrate the results obtained from the XMT measurements and assess the relationship between the overall sulphide extraction and the effective copper extraction.

In this chapter, section 7.2 describes the relationship between the XMT and ICP measurements, section 7.3 describes the leaching results at the different column scales and their dependency on different characteristics of the ore, section 7.4 details the structural changes occurring over the process, and section 7.5 studies the leaching variability at the sub-particle level and the distribution of kinetics within the sample and its relationship with leaching variability.

7.2. Relationship between image measurement and chemical analysis

It is important to verify that the results obtained using each of the techniques are in accordance with the expected leaching behaviour (i.e. there is a higher leaching extent at the end of the process than at the beginning) and, especially, that these are consistent with each other. Considering that standard studies assess the leaching performance by analysing the concentration of species (and in this case, copper) in solution, the ICP measurements were assessed in the first instance.

7.2.1. Recovery calculations from ICP measurements

Recovery calculations were carried out by considering that a certain degree of leaching had already occurred over the curing stage and that all previously dissolved species were removed by the water wash (as discussed in Chapter 5). Therefore, ICP-MS was used to quantify the copper and iron concentrations in the solutions collected from the water wash stage. These quantities were subtracted from the overall extraction observed over the leaching period, although they were considered in the overall mass balance to avoid underestimating the total metal content in the sample.

Over the water wash period approximately 29.5% of the initial copper was removed from samples of type A, whereas 16.6% was extracted from samples of type B. Subsequently, the leaching recovery was obtained from the ICP measurements, with the results being presented in Figure 7.1. It can be seen from the figure that the ultimate copper recovery for both leaching columns was almost identical, reaching values of 97.6% and 95.4% for samples A and B, respectively. Although, there is a slight difference in the leaching rate over the first 7 days, where the extraction from column A was higher. While extraction for column B was moderately slower at the beginning, the slope of the recovery curve is sustained over time and there is no substantial decrease in the extraction rate. Another interesting result that can be observed from Figure 7.1 is that the ultimate recovery for samples leached with the solution containing NaCl was reached at day 39, meaning that the last 7 days of leaching might not be required.

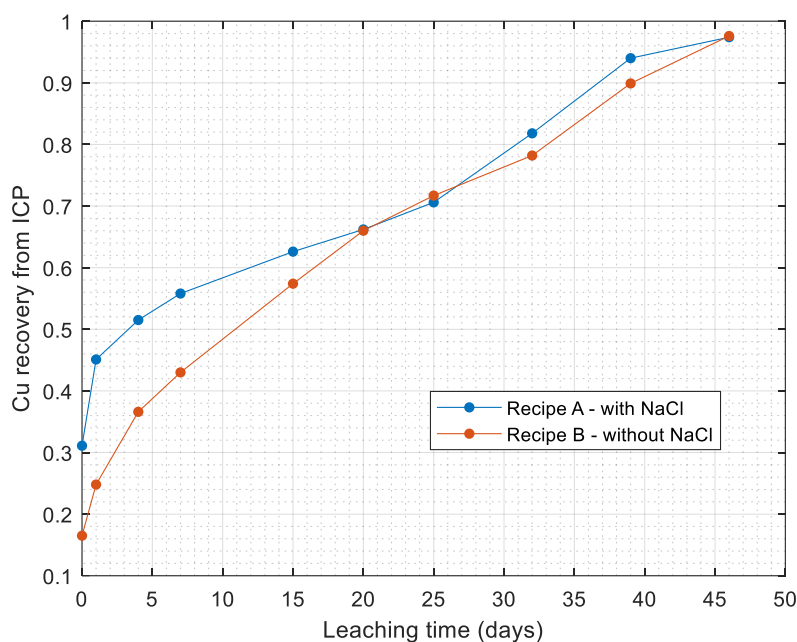


Figure 7.1. Copper recovery obtained from ICP-MS measurements.

It was also possible to estimate the total iron recovery by a similar procedure. The main purpose of analysing the iron extraction extent is to assess the selectivity of the process and for mass balance purposes. 0% and 0.4% of Fe was extracted during the water wash stage from samples A and B, respectively. Thus, after subtracting these quantities from the overall extraction, the iron recovery over the leaching process was calculated and is presented in Figure 7.2. From the figure it can be observed that the iron extraction is virtually the same for both sample types over most of the leaching process, though there is an evident divergence after day 32 of leaching, with a higher ultimate Fe recovery obtained for samples of type B (no chloride ions present). The reason for this will be further investigated in section 7.5.2 by analysing the species remaining in the sample after the leaching process has finished.

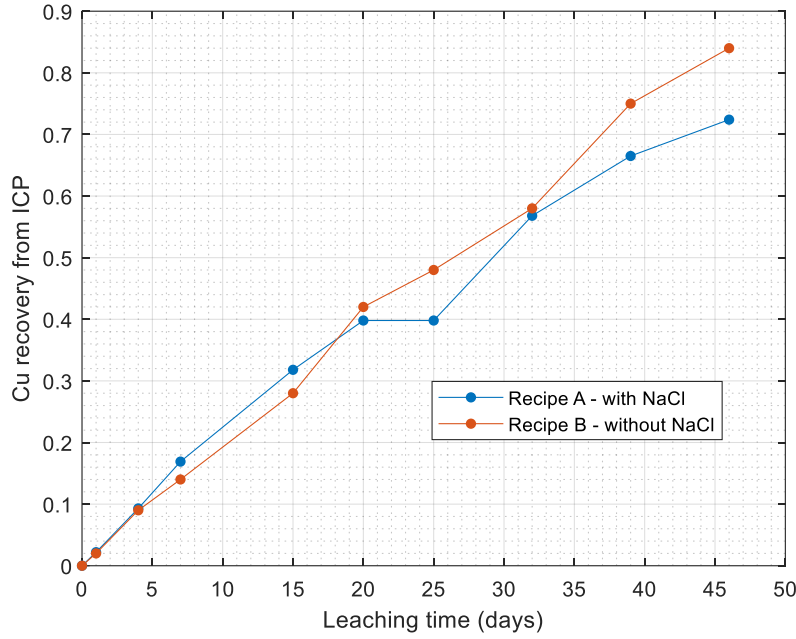


Figure 7.2. Iron recovery obtained from ICP-MS measurements.

7.2.2. Recovery calculations from XMT imaging

Sulphide volume change was quantified by applying only the more basic steps of the methodology explained in Chapter 4, which involved agglomerate segmentation, labelling, and sulphide thresholding. An important, but reasonable, assumption made for this study was that sulphide grade will decrease (or remain the same) as leaching progresses, which will be produced by the selective dissolution of species (i.e. sulphide grains will be leached out, while the rock matrix or gangue will remain almost intact). This assumption was used as a constraint when calibrating the thresholding values when sulphide grains were segmented from the rock matrix.

Three different sections of each column were scanned to assess distribution of leaching recoveries throughout the column (which are shown in Figure 3.5). For this analysis, though, the total sulphide content of column i , $\bar{V}_{sulphide,i}$, $\bar{V}_{MS_{i_t}}$, was quantified by considering the sulphide volume of the n scanned sections for that column:

$$\bar{V}_{MS_{i_t}} = \sum_{j=1}^n V_{MS_{i,j_t}} \quad (7.1)$$

where $V_{MS_{i,j_t}}$ is the total sulphide content of section j of column i at a certain time t . Since for this particular case the number of scanned sections was 3, $n = 3$.

Using the standard definition of leaching recovery at a given time t , R_t :

$$R_t = \frac{V_0 - V_t}{V_0} \quad (7.2)$$

where V_0 is the sulphide volume at the reference time (e.g. before leaching starts, or $t = 0$) and V_t is the volume at the measurement time t .

The overall recovery at time t for column i , \bar{R}_{i_t} , can be calculated using Eq. (7.2) with $V_0 = V_{MSi_0}$ and $V_t = V_{MSi_t}$, such that:

$$\bar{R}_{i_t} = 1 - \frac{V_{MSi_t}}{V_{MSi_0}} \quad (7.3)$$

with V_{MSi_0} and V_{MSi_t} the total sulphide volume of column i at time 0 (i.e. the reference time) and at time t , respectively.

By comparing the overall sulphide content at different stages of the process, it is possible to estimate the evolution of the leaching recovery. Similar procedures for quantifying volume changes from XMT images have been widely used in multiple disciplines and, in particular, in studies in which geological samples are involved (as previously discussed in section 2.4). It is important to stress that this is a fairly basic quantification methodology²³, which only considers the total sulphide volume at each timestep of the process but does not consider grain-scale variations.

Results are presented in Figure 7.3, where it can be seen that the leaching evolution is analogous to the results displayed in Figure 7.1, with the main difference being that results appear to be scaled down with respect to the ICP results. This is because both graphs present different quantities; ICP measurements quantified copper extraction, whereas the XMT assessment quantified overall sulphide extraction. Therefore, since the average recovery at each timestep represents the selective dissolution of copper from the ore, the difference in recovery represents a considerable concentration of non-copper containing sulphides that remain in the sample after all copper has been extracted.

It can also be observed that the curves separate from each other at day 15 and the ultimate copper recovery is noticeably higher for samples of type B, which is the opposite to what was observed in section 7.2.1 where Cu recovery is higher for samples of type A. This might be due to a higher dissolution of sulphides that may not contain copper (i.e. iron sulphides) for leaching B. This lower selectivity is consistent with the higher iron extent observed in Figure 7.2 recovery for samples of this type.

²³ The methodology developed and presented in Chapter 4 also considers a series of steps to track the volume change of each of the hundreds of thousands of grains within the sample. All the steps of this methodology will be used and discussed in section 7.5.

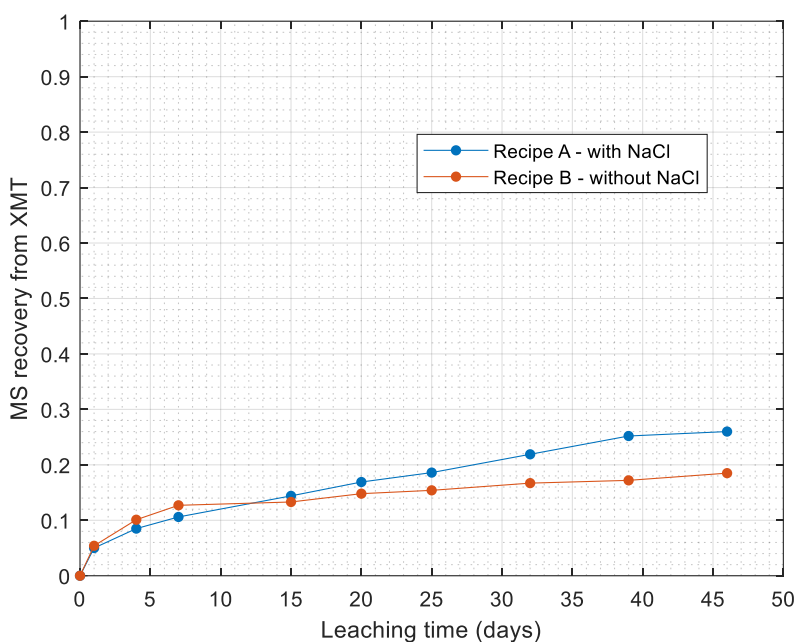


Figure 7.3. Metal sulphide recovery obtained from the XMT image measurements.

7.2.3. Relationship between image measurement and chemical analysis

One of the main purposes of analysing the recoveries obtained from both ICP measurements and XMT measurements was to assess whether the results are consistent with each other. However, there is a slight difference in behaviour, and it is important to make sure that the XMT measurements can accurately represent the copper extraction rate and, more meaningfully, the leaching of agglomerated ores. Therefore, to compare results on a more direct level, sulphide extraction obtained from the XMT measurement was plotted as a function of the copper recovery since the ICP measurements are considered the calibration values (Figure 7.4). The figure shows that results from both assessment methodologies are highly correlated, with a coefficient of determination of $r^2 = 0.9556$. The slope of 0.2615 for the correlation line represents the difference in recovery from both methodologies (one methodology measures copper recovery and the other sulphide recovery), which is consistent with previous observations. Consequently, it is possible to assert that XMT results can be used to represent the copper leaching behaviour.

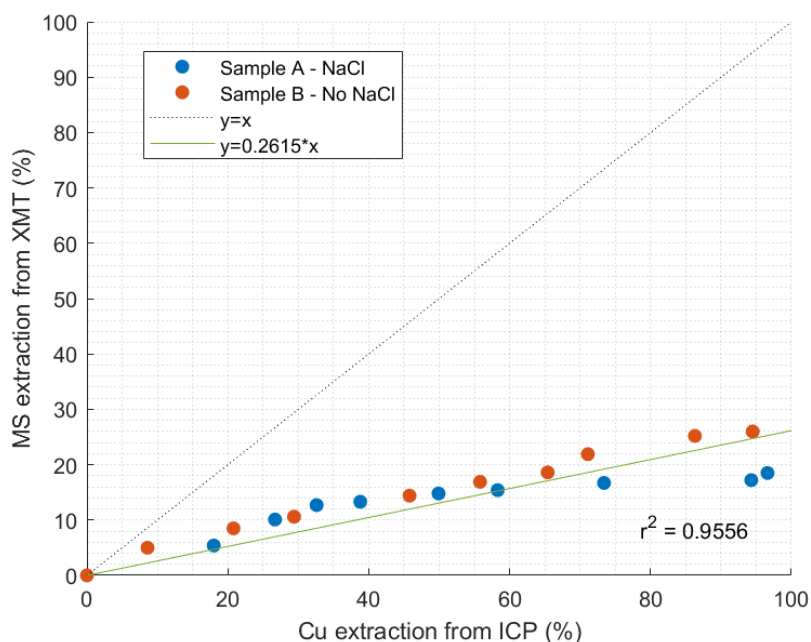


Figure 7.4. Relationship of recovery between image measurement and chemistry measurement from ICP-MS.

7.3. Leaching results at the column scale

7.3.1. Different column scales

A leaching profile will develop throughout the heap. The shape of this profile will depend on numerous variables that affect the leach performance at different scales and locations. Furthermore, most of the macro-scale processes occurring at the heap scale are not present in small column experiments. This thesis, though, is mainly interested in analysing the leaching variability at the inter and intra particle scale, which are processes that can be well reproduced at the small column scale.

Three different sections of each column were scanned (as discussed in the previous section). For this purpose, the sulphide content was quantified at the column, section, and agglomerate scale. The leaching recovery for each section was calculated using an equation analogous to equation (7.3).

It is, then, possible to analyse and compare the leaching variability at the section and agglomerate scale; and assess their relative impact on the overall column performance. Figure 7.5 show these results, where each black dot represents the leach recovery from an individual agglomerate. It can be seen from the figure that there is a slightly higher recovery obtained from the top section. A possible explanation might be that this section was irrigated with fresh and non-loaded leach solution, whereas both the middle and bottom sections were leached with an already partially loaded solution. Although, this might not be the case since the bottom section presents a greater recovery when compared to the middle section and because there is a great variability in recovery obtained from agglomerates located at

different column sections. Therefore, there is no clear trend that can link the leach performance with the relative location of each sample and no clear dependency was found for the overall leach performance on the location of agglomerates within the column. It is, thus, logical to assess the agglomerate’s characteristic features, such as the initial mineral grade or the agglomerate size, to look for a possible correlation with the leach recovery.

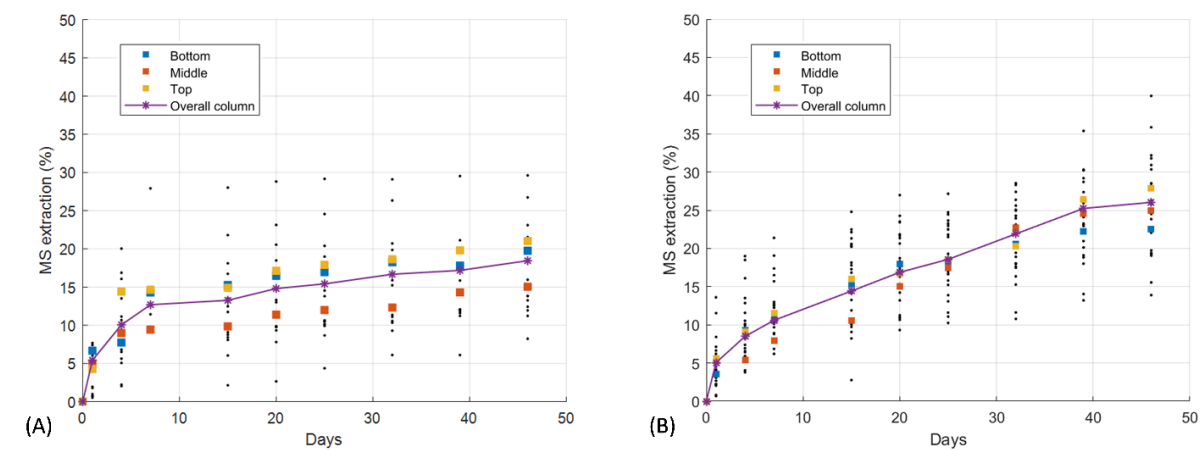


Figure 7.5. Average recovery for the entire column, for the three scanned volumes (top, middle and bottom) within each column and for the individual agglomerates.

7.3.2. Relationship between the agglomerate-scale results and the characteristics of the ore.

The overall recovery obtained for each agglomerate was plotted as a function of its initial mineral content to identify a possible connection with leach recovery. It can be seen from Figure 7.6 that the coefficient of determination, r , is -0.051 and 0.036 for samples A and B, respectively. This value is insufficient to identify a clear trend or dependency of the recovery values on the mineral content.

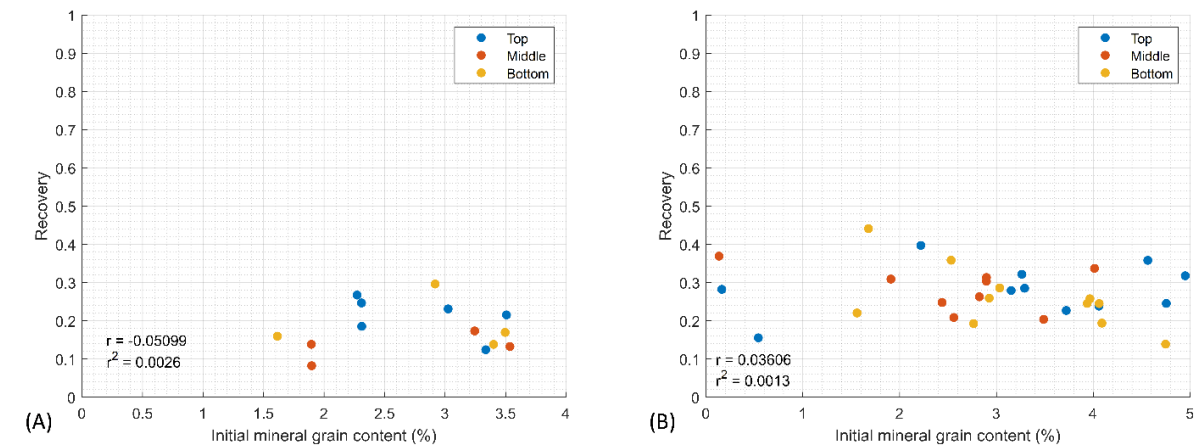


Figure 7.6. Overall recovery for each agglomerate plotted as a function of its initial mineral content. (A) samples of type A with a coefficient of determination of $r = -0.051$, and (B) samples of type B with a coefficient of determination of $r = 0.036$.

In order to analyse the dependency on the agglomerate size, a similar graph was used and the overall recovery for each agglomerate was plotted as a function of the size. Figure 7.7 shows the results, where it can be seen that the coefficient of determination is -0.137 and 0.207 for samples A and B, respectively. While the r values are higher in this case, these correlations are still not significant.

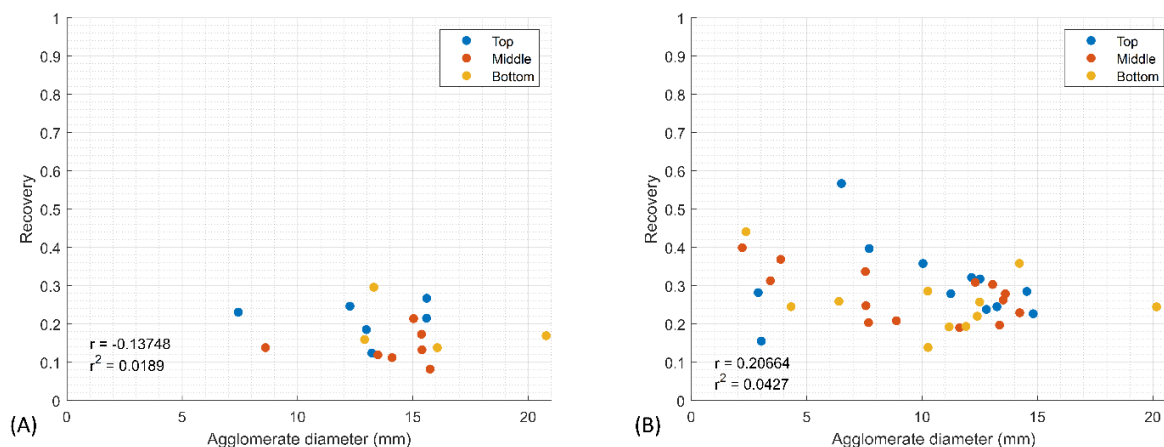


Figure 7.7. Overall recovery for each agglomerate plotted as a function of its initial size. (A) samples of type A with a coefficient of determination of $r = -0.137$, and (B) samples of type B with a coefficient of determination of $r = 0.207$.

The fact that no clear correlation could be established between recovery and both the agglomerate size and initial mineral content does not mean that there is no relationship between leaching variability and the type of mineral that is being leached, but that this might be the wrong process scale to study. For instance, the distribution of grains within the agglomerates (i.e. the local concentration) and the structural changes occurring over the process are not taken into account in this analysis and only macroscopic features of the sample are considered. Therefore, a more direct relationship can be found by analysing and quantifying local variations occurring in the internal structure of the agglomerates.

7.4. Structural changes

A first method for assessing the changes in the internal structure is to analyse the porosity network and how it develops over the leaching period. Porosity is a critical parameter in the leaching process, as it is through these pores that the leach solution flows and reaches the mineral grains to extract the valuable metals from the ore. Different types of porosity can be found throughout a typical packed bed or heap; pores between the agglomerated particles (inter-particle voids), pores already existing within the particles that form the agglomerates (intra-particle voids), and microcracks that develop due to the chemical attack produced during leaching. All of these pore types play a critical role in enabling the contact between solution and the mineral grains and must be considered when assessing the agglomerate quality and performance.

At the column leaching scale, it is not possible to accurately replicate the compaction and mechanical changes occurring within a heap. Compaction will be much more prominent on industrial scale heap leaching operations, though it might be possible to estimate the impact on the porosity caused by the natural compaction processes occurring at the column scale. Under the scanning conditions used, the main limitation is imposed by the image resolution (the linear pixel resolution of the XMT image set was approximately 17 microns) and any pore with an average diameter below about 35 microns cannot be measured (section 2.4.2.5.1). Therefore, only changes in the sample macro-porosity²⁴ at the intra-particle scale were quantified. Heap porosity, microporosity, and microcracks would require experiments and measurements at different scales.

XMT has been used previously as the basis for calculations of porosity changes in the leaching of sulphide ores. (Ram *et al.*, 2020) examined the internal porosity of large sulphide ores, finding a rise of 300 – 17,800% in the overall porosity after a leaching period of 206 – 240 days. This increase in volume of internal voids in solid particles is because the chemical attack will induce microcracks and, therefore, internal breaks in the ore. Yet, the authors studied individual sulphide particles and not ores agglomerated before leaching, for which a different behaviour is expected because the particles themselves can deform, especially when subjected to loads.

(Gao *et al.*, 2021) examined the structural changes occurring within ores agglomerated with and without calcium chloride as a binder and source of Cl⁻ ions. Low-grade chalcopyrite ores were agglomerated manually, and a 5-day curing process was performed in an oven at 50°C prior to leaching tests. The authors reported that porosity increased substantially when a leaching of 8 hours was performed on a single agglomerate sample. However, by only using a single agglomerate for this study authors did not take into account the compaction or compression that typically occurs within packed beds of agglomerated ores. At the same time, typical heap leaching timeframes are much longer (e.g. weeks for on-off heaps or hundreds of days for dump leaching heaps) and the internal porosity of agglomerates will most likely decrease in the long term due to sample compaction produced by the weight of the overlaying particles and the irrigation of the pile. For this reason, one of the aims of this study is extending the knowledge on structural changes occurring within agglomerated ores in longer-term leaching studies.

By applying the pore segmentation methodology explained in section 4.3.2 to the acquired dataset not only was it possible to estimate the volume of internal voids at each scanning point, but also to track and quantify 3D changes in the pore network, which can be linked to variations in the leaching performance at the local and global level.

²⁴ Any internal pore whose mean diameter is above the 35 microns will be considered as macro-porosity, which we will hereafter refer to merely as porosity.

The sample porosity was quantified for two agglomerates from each column that were randomly selected. Figure 7.8 shows the porosity as a function of distance to the nearest surface for different leaching times. The fact that agglomerates of type A present a lower initial porosity (i.e. average porosity at day 0) could be due to the higher amount of precipitates that are expected to form over the curing process, whereas reprecipitation of species will be nearly absent in samples of type B (Chapter 5). However, when these precipitated species are fully dissolved from the internal voids, porosity of both sample types will follow similar tendencies and porosity will decrease to a minimum. It can also be seen that porosity decreases dramatically for both sample types over the first 4 days of leaching and practically reaches its minimum value from day 7, which represents the ultimate porosity value for agglomerates over the remaining leaching days.

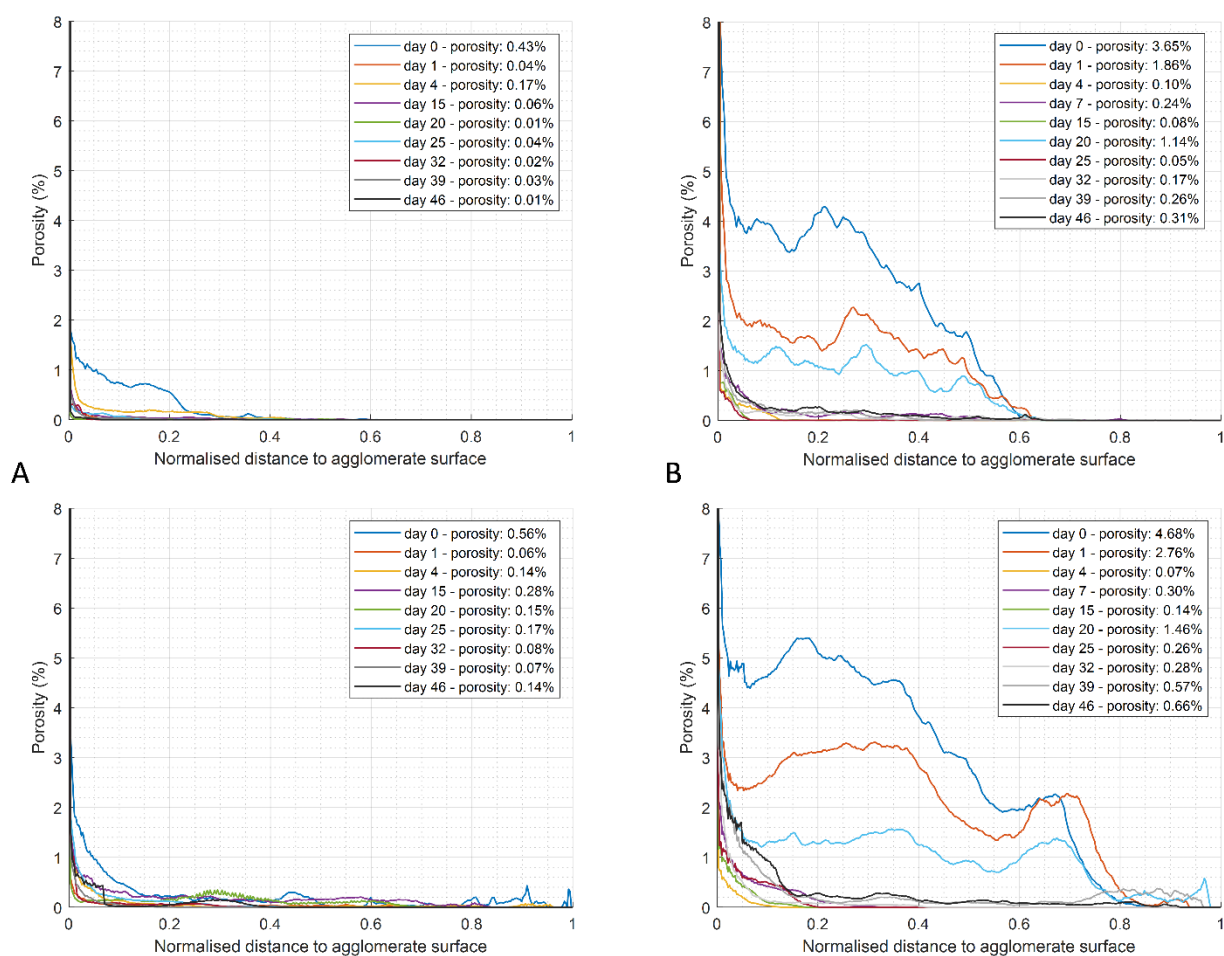


Figure 7.8. Internal porosity distribution as a function of distance to the nearest surface for two randomly selected agglomerates of each recipe type. (A) porosity distribution for agglomerates of recipe A, and (B) porosity distribution for samples of type B.

An important point to stress is that there is no clear relationship between the decrease in porosity and the leaching performance observed in sections 7.2 and 7.3. That is because the extraction curves do not seem to slow down at the same rate that porosity decreases. This result is interesting as it suggests

that it might be the smaller scale of pore network that plays a more important role in the mass transport processes occurring in the agglomerated ores. That is to say that even when the network of pores whose diameter is above the 35 microns changes dramatically and the global internal porosity decreases considerably, this does not necessarily mean that the leaching performance will be reduced. However, due to image resolution the micro porosity and micro cracks in the samples could not be quantified in this study and more detailed information is required to completely describe the relationship between smaller-scale changes in the mechanical structure and the leaching performance.

7.5. Sub-particle level analysis

By using the methodology developed for this thesis, which was explained in Chapter 4, the volume change (and therefore the recovery) at every stage of the process can be quantified for each grain in the sample. The advantage of analysing the leaching behaviour at the grain scale is that the distribution of leach kinetics can be ultimately linked with the overall leaching behaviour. However, since this methodology is based on image quantifications, the size of the measured objects must be taken into consideration.

(Lin *et al.*, 2015) found for a system with a similar image resolution (i.e. pixel size of 17 micron) that to reduce the random component of the uncertainty when measuring volume to less than²⁵ 5%, results must be combined for approximately 600 grains of a volume of 4 voxels, approximately 12 grains of 100 voxels, or one object of 1000 voxels. Consequently, for this assessment to have statistical significance, the results obtained for different grains experiencing a similar leaching history must be combined (as discussed in section 4.4), which is analogous to measuring the same object several times.

A typical porphyry mineral ore will contain a large number of fines that will represent only a small fraction of the total sulphide volume in the sample, whereas a large fraction of the sulphide volume will be contained in a few very big grains. Therefore, it is essential to analyse the size distribution of the mineral grains in the sample to identify the limitations of this methodology.

Approximately a million grains were tracked for each column and the PSD of these mineral grains was plotted by considering not only the cumulative number of particles that correspond to a particular size, but also the cumulative fraction of the total sulphide volume that they represent (Figure 7.9). The figure shows that the mineral grain PSD is fairly similar for both sample types and that more than 85% of grains are of a size equal to or below 100 voxels (equivalent to a diameter of approximately 98 microns), but the relative weight of these grains by volume is less than 10% of the total sulphide volume. Therefore,

²⁵ The fact that an error of 5% is considered for this example relies only on the fact that this is a typical value. Although, equation 4.2 can be used to calculate the number of grains that must be combined to reduce the error by a different quantity.

they will not be tracked in subsequent analysis in order to ease calculations. This consideration may be relaxed in future studies as there are enough of these grains to achieve meaningful results.

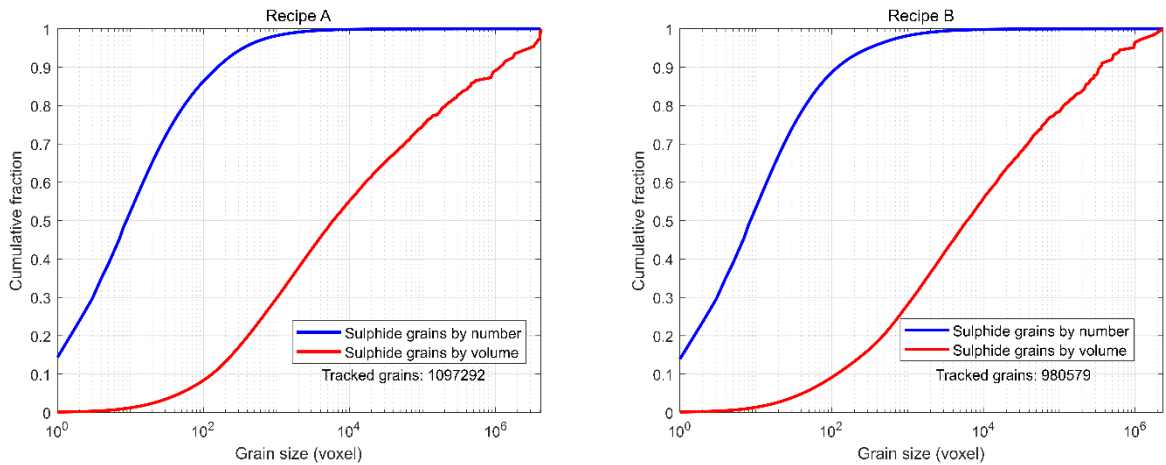


Figure 7.9. Cumulative fraction by volume and particle size distribution (PSD) of the sulphide grains corresponding to leaching agglomerates of samples A and B.

Since the main objective of this section is to analyse the leaching variability occurring at the grain scale, grains of the same size cannot be combined directly. Even though the grains may be similar in size, these may not be experiencing similar leaching conditions or be under similar circumstances, meaning that they will leach at different rates. For instance, grains that are closer to the agglomerate surface are expected to dissolve faster than grains closer to the centre of the sample due to the easier accessibility of solution. Accordingly, the relative position at which grains are located will be just as important as their initial size. Thus, for this assessment to have statistical significance it is essential to combine the results obtained for different grains experiencing similar leaching histories. Two conditions were then considered to group grains into categories, namely their size and distance to surface²⁶ should be approximately equal and that at least 10 grains fall within each category.

7.5.1. Leaching performance by size-distance category

In order to get a first idea about the leaching behaviour of the different grain classes, the average recovery for each size-distance class was quantified, and it is presented in Figure 7.10. There is an obvious difference in the grain dissolution extent experienced by both sample types, which becomes even more pronounced as leaching progresses. It can be seen from Figure 7.10A that there is virtually no recovery from fine grains of sample A (with sodium chloride) over the full duration of the process. This might be because most of the easily leachable minerals have already been leached out over the curing stage and

²⁶ In this case, the distance to the surface is measured as the minimum distance to the nearest accessibility spot for solution, meaning that this could be any pore that is connected to the surface or an outer surface. Therefore, this distance to the surface will represent a proxy to the mass transfer resistance.

the remaining finer grains in sample A may be composed of refractory or highly non-leachable sulphides. It should be noted that these grains are included in the analysis because it was not possible to discriminate between different sulphide types by only using this XMT methodology. Figure 7.10B shows a more predictable leaching evolution and finer grains are dissolved more rapidly than coarser grains. A similar behaviour can be observed for grains closer to the surface, which also leach more quickly.

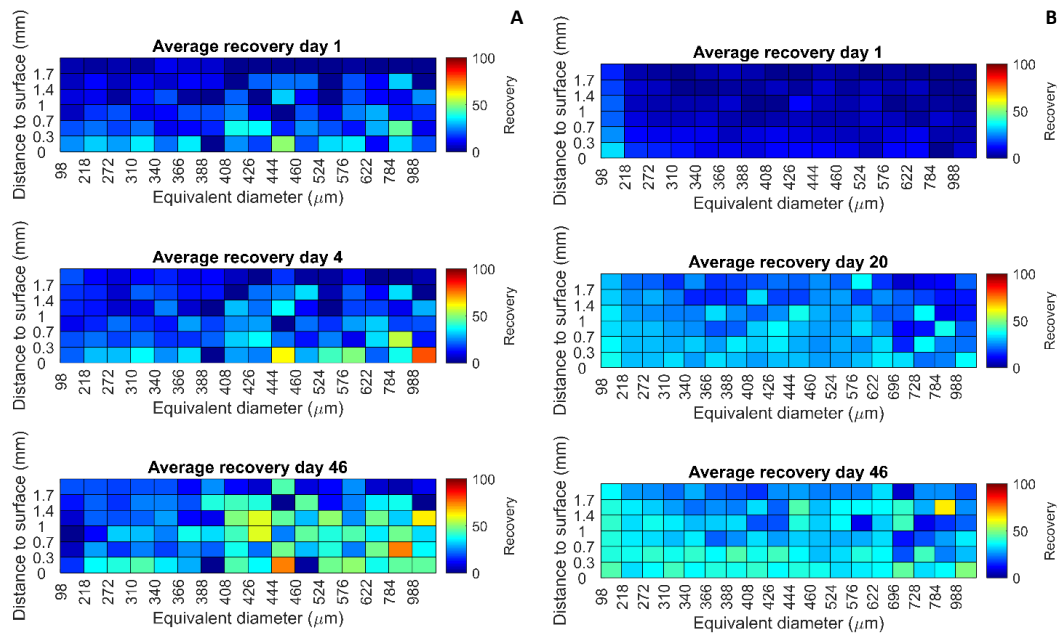


Figure 7.10. Overall change in grain volume for each size-distance category at different leaching times. (A) results obtained for agglomerates of recipe A, and (B) results obtained for agglomerates of recipe B.

Since there is no discrimination between the type of sulphide that is included in this analysis, it is not possible to truly quantify the leaching of the copper-containing species and separate it from the leaching of other non-valuable sulphides. It is thus essential to carry out a more complex analysis that involves the calibration of the results in order to understand the grain-scale performance of each sulphide type.

7.5.2. Calibration of the XMT results using SEM/EDX and mineral mapping.

Up to this point, all grain quantification and analysis has been performed by considering the evolution of all sulphide grains (i.e. copper-containing grains and pyrite²⁷ grains). This is because it is virtually impossible to distinguish between pyrite grains and other copper-containing sulphides by only using the XMT images (previously discussed in section 2.4.2.4).

²⁷ The sulphide grains are assumed to be composed of only copper-containing grains and pyrite, as the sample contains a very low quantity of other sulphide minerals.

In order to address this shortcoming, SEM/EDX analyses were used to complement the information obtained both from the XMT and chemical assessments. The main intention is to characterise the agglomerates and to map the minerals remaining after the 46 days of leaching. Each column was impregnated with resin immediately after the leaching and water washing of the samples. Six discs were obtained by sawing the columns carefully to expose as much of the scanned agglomerates as possible, each of these cross sections corresponding to one of the scanned volumes (described in section 4.2). The glass column was removed, and each disc was mounted in resin cautiously. The samples were analysed using SEM/EDX combined with the TIMA software to produce mineral maps of each sample. It is important to mention that the disc samples corresponding to the top volume of column B was partially destroyed by the sawing process and could not be characterised. However, the other five sections were successfully analysed, and both the SEM/EDX images and the mineralogical maps are shown in Figure 7.11.

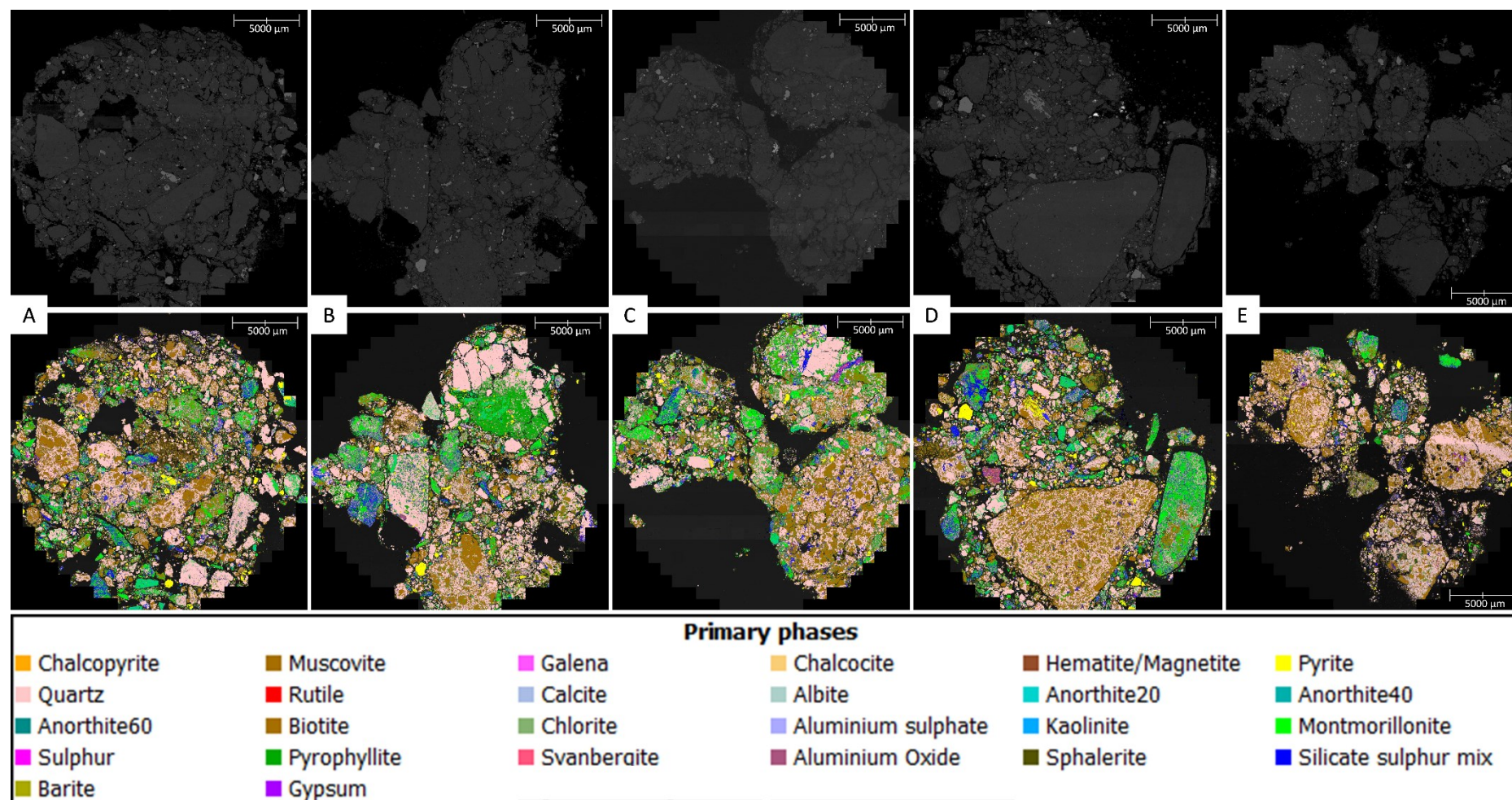


Figure 7.11. EDX/SEM images and mineral map obtained for the five column sections analysed. (A) corresponds to the bottom section of column A, (B) corresponds to the medium section of column A, (C) corresponds to the top section of column A, (D) corresponds to the bottom section of column B, and (E) corresponds to the medium section of column B.

The mineralogical composition of the sample was also quantified, with Table 7.1 summarizing the mineral content of each section for each sample type (i.e. for recipes A and B). It can be seen that the average content of copper-containing species at the end of the leaching process was approximately 0.1 and 0.2 % for samples A and B, respectively. Considering that the initial content of copper-containing species (described in Table 3.1) was of 0.83%, these results are consistent with the chemical analyses presented in section 7.2 where it was shown that approximately 96.5% of the copper was leached out over the process. This result also indicates that the leaching process was extremely effective for both sample types. Another interesting result is that virtually the only sulphide species remaining in the sample is pyrite (which is also the main sulphide component of the ore feed), meaning that virtually all sulphide grains in the sample at day 46 of leaching can be assumed to be pyrite grains. These grains can, thus, be backtracked over the leaching process using the methodology explained in Chapter 4 and this information can be used to calibrate the overall leaching quantifications. By subtracting the contribution of the dissolution of pyrite grains from the overall leaching of sulphide species, the effective leaching of copper sulphide grains can be estimated. It should be noted, though, that for this assessment it is assumed that all the grains that are leached by day 46 are the copper-containing grains. This assumption can be made as the average pyrite content in the samples is approximately 2.66 %, which is virtually identical to the pyrite content of the feed material used for agglomeration and subsequent leaching. Yet, the leaching of both pyrite and copper sulphides must be carefully analysed to confirm this assumption.

Table 7.1. Main mineral species remaining at the end of the leaching process for agglomerates of recipe A and B. Bold indicates the totals for a category of mineral.

Mineral type	Weight (%)				
	Recipe A			Recipe B	
	Top	Middle	Bottom	Middle	Bottom
Copper containing species	0.01	0.01	0.02	0.02	0.01
Chalcopyrite	0.00	0.01	0.01	0.02	0.01
Chalcocite	0.01	0.00	0.01	0.00	0.00
Covellite	0.00	0.00	0.00	0.00	0.00
Pyrite	1.80	2.45	2.97	3.38	2.70
Gangue minerals ^a	98.19	97.54	97.01	96.60	97.29

a. The gangue minerals are muscovite, quartz, montmorillonite, kaolinite, pyrophyllite, and traces of other non-valuable minerals.

7.5.3. Calibration process

All sulphide grains were assigned a unique label considering day 0 as the reference point (see Chapter 4). Therefore, it is possible to use the labels assigned to the grains found at the end of the leaching period (i.e. day 46) to backtrack the pyrite grains, obtaining information about their initial location and their size variation over the process. This information is not only aimed to estimate the pyrite dissolution kinetics, but also to support the assumption that there was virtually no leaching of pyrite grains over the process, considering that virtually all copper-containing grains were completely dissolved by day 46 of leaching (as shown in Table 7.1). A link to access codes “cpy_data_alldays.m”, “obtain_cpy_data.m”, and “py_leach_quantification.m” is provided in Appendix B. These codes were essential for this calibration process.

Pyrite dissolution was first assessed by looking at the evolution of the overall pyrite grade. This was possible by dividing the total pyrite volume in the scanned section i , $\bar{V}_{pyrite,i}$, by the total agglomerate volume in the same section, $\bar{V}_{agglomerate,i}$, as follows:

$$pyrite\ grade\ in\ section\ i = \frac{\bar{V}_{pyrite,i}}{\bar{V}_{agglomerate,i}} \cdot 100\% \quad (7.5)$$

where i represent the top, middle, or bottom section of the column.

The pyrite grade of each section at different stages of the process is shown in Figure 7.12. It can be seen that the initial pyrite content, which is 2.7 % and 2.9 % for samples of type A and B, respectively; is consistent with the pyrite content observed for the agglomeration feed material (2.82% presented in Table 3.1). The fact that there is no dissolution of pyrite over the process is detrimental to the leaching kinetics within a heap, as the pyrite dissolution reactions are exothermic and increase the temperature of the heap, also increasing the leaching kinetics. Although, for the purposes of this thesis this is advantageous as it allows the copper-containing sulphides to be distinguished from other sulphides (mainly composed of pyrite).

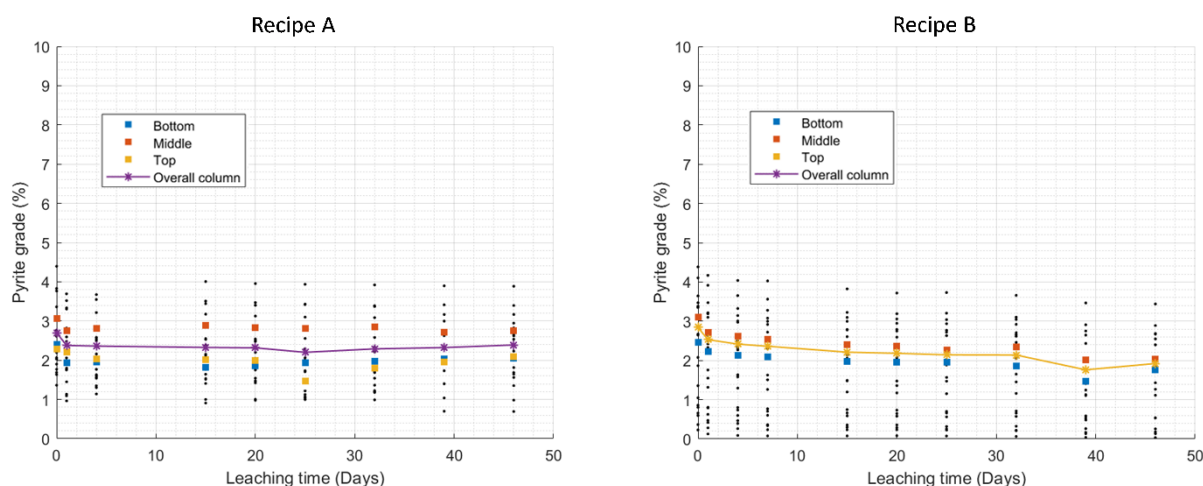


Figure 7.12. Pyrite grade of each column, section, and agglomerate at different stages of the process.

While there is virtually no dissolution of pyrite for samples of type A, there is a certain degree of leaching occurring for samples of type B. This is probably due to the more selective dissolution process that occurs when chloride ions are added to solution. Considering this, the assumption that there is no pyrite dissolution over the process may not be completely correct for samples of type B and can only be used with reasonable accuracy for samples A. This selectivity could be because chloride ions kill the microorganisms that leach the pyrite.

Prior to using this calibration and its assumptions, though, it may be convenient to assess the overall dissolution of copper-containing species as a function of leaching time (Figure 7.13). From the figure it can be seen that there is a consistent decrease in the copper-sulphide grade as the dissolution reactions take place. Therefore, this calibration can be used to describe the leaching kinetics of the copper-containing grains in the next section.

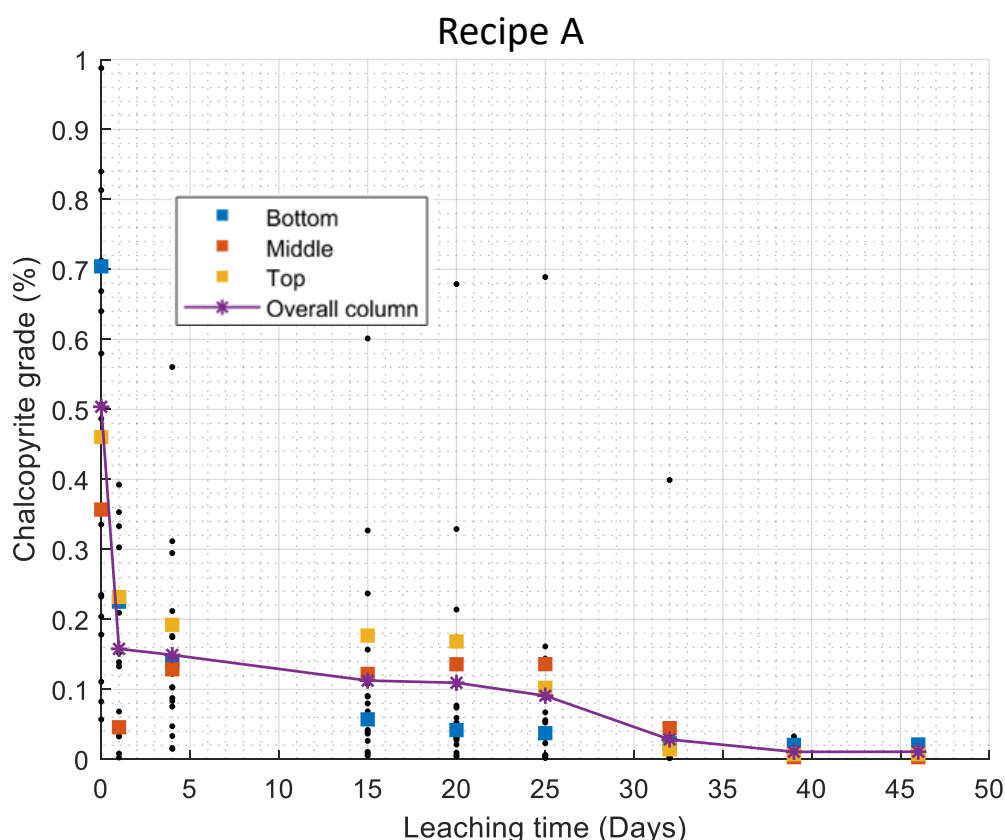


Figure 7.13. Copper-containing species grade of the full column, each section, and each agglomerate at different stages of the process for agglomerates of recipe A.

7.5.4. Distribution of kinetics

The rate at which agglomerates leach depends on the apparent kinetic, which is a complex function of the surface kinetics (and its distribution), the location and size of grains, and their interaction with the mass transport processes within the particle. Thus, by analysing the distribution of kinetics for each grain from a specific size-distance category, a better model for the leaching process can be developed. This methodology is based in the work of (Lin, Neethling, *et al.*, 2016), which was developed to quantify the surface kinetics of metal containing grains. For the case of this thesis, this methodology has been extensively extended to include the calibrated information obtained by combining the SEM/EDX and XMT techniques, which permits to isolate the leaching behaviour of copper containing grains from that of pyrite grains, as well as to account for the significant differences in behaviour between particulate systems and agglomerated ores. A link to access the codes used for this analysis (“surf_kinetics_refined.m”, “leaching_stats_refined.m”, and “pdf_kinetics.m”) is provided in Appendix B The assumption that the surface kinetics are first order is also relaxed.

Another important point to consider is that by the time that agglomerates were irrigated with the leach solution there had been a certain extent of leaching that occurred over the curing process (Chapter 5). Therefore, the distribution of kinetics will be slightly different for different size and distance classes.

This is because the faster leaching components and the smaller grains will be depleted during the curing process.

7.5.4.1. Mathematical description

As the leaching occurs at the surface of the grains and it assumed to be of order n with respect to the concentration, the leaching rate of grain i of volume $V_i(t)$ at the time t can be expressed as:

$$\frac{dV_i(t)}{dt} = -k_i A_i(t) C^n \quad (7.5)$$

where k_i is the surface rate constant of grain i , A_i is its surface area, and C is the concentration of copper in solution. The relationship between the volume of an object and its surface area is given by:

$$A_i(t) = \alpha V_i(t)^{2/3} \quad (7.6)$$

where α is a proportionality constant. Therefore, Eq. (7.6) can be rewritten as:

$$\frac{dV_i(t)}{dt} = -k_i \alpha V_i(t)^{2/3} C^n \quad (7.7)$$

The extent of reaction of grain i can be obtained by integrating equation (7.7) over the leaching time $t < t_f$, with t_f the time at which grain i disappears, and considering its initial volume, $V_i(0)$, and volume at time t , $V_i(t)$; such as:

$$\int_{V_i(0)}^{V_i(t)} \frac{1}{-k_i \alpha V_i(t)^{2/3}} dV = \int_0^t C^n dt, \text{ for } t < t_f \quad (7.8)$$

Obtaining:

$$k_i = \frac{3}{\alpha t \bar{C}} \left(V_i(0)^{1/3} - V_i(t)^{1/3} \right), \text{ for } t < t_f \quad (7.9)$$

where

$$\bar{C} = \frac{\left(\int_0^t C^n dt \right)}{t}, \text{ for } t < t_f \quad (7.10)$$

Equations 7.8 to 7.10 are only valid for times prior to the full dissolution of grain i , or $t < t_f$. For $t \geq t_f$, these equations take the form of:

$$k_i = \frac{3}{\alpha t_f \bar{C}_f} \left(V_i(0)^{1/3} \right), \text{ for } t \geq t_f \quad (7.11)$$

with

$$\overline{C_f} = \frac{\left(\int_0^{t_f} C_f^n dt\right)}{t_f} \quad (7.12)$$

where C_f is the concentration of species produced by the dissolution of grain i at time t_f .

By performing a similar analysis for the grains in the same size-distance category j with the average surface kinetic rate, \bar{k}_j , and corresponding average volume at t , $\bar{V}_{i,j}(t)$:

$$\bar{k}_j = \begin{cases} \frac{3}{\alpha t \bar{C}} \left(\overline{\delta_j(t)^{\frac{1}{3}}} \right) & , for\ t < t_f \\ \frac{3}{\alpha t_f \bar{C}_f} \left(\overline{\delta_j(t)^{\frac{1}{3}}} \right) & , for\ t \geq t_f \end{cases} \quad (7.13)$$

with

$$\overline{\delta_j(t)^{\frac{1}{3}}} = \frac{1}{N} \sum_{i=1}^N \begin{cases} \frac{1}{t} \left(V_{i,j}(0)^{\frac{1}{3}} - V_{i,j}(t)^{\frac{1}{3}} \right) & , if\ t < t_f \\ \frac{1}{t_f} \left(V_{i,j}(0)^{\frac{1}{3}} \right) & , if\ t \geq t_f \end{cases} \quad (7.14)$$

where N is the total number of grains in the category j .

It will be assumed that $\bar{C} \approx \bar{C}_f$. This assumption is more accurate for grains closer to the surface. This assumption could be relaxed in the development of more complex models. The ratio between the surface rate for each grain i in the size-distance category j and the mean surface rate of that category can be thus calculated as:

$$\frac{k_{i,j}}{\bar{k}_j} = \begin{cases} \frac{1}{t} \left(\frac{V_{i,j}(0)^{\frac{1}{3}} - V_{i,j}(t)^{\frac{1}{3}}}{\overline{\delta_j(t)^{\frac{1}{3}}}} \right) & , for\ t < t_f \\ \frac{1}{t_f} \left(\frac{V_{i,j}(0)^{\frac{1}{3}}}{\overline{\delta_j(t)^{\frac{1}{3}}}} \right) & , for\ t \geq t_f \end{cases} \quad (7.15)$$

By dividing the surface kinetic by the average, it is expected that the distance effect is removed, and the distribution curves are expected to be similar. The remaining variability will thus represent the surface kinetics variability, which is essentially independent of the distance to the surface. Besides, there is less variability expected for small grains, as they are expected to be dissolved more rapidly, but there also will be more change over the course of the leaching.

7.5.4.2. Results

The values for equation 7.15 can be calculated from the 4D library obtained for the hundreds of thousand copper sulphide grains analysed for samples of recipe A (the recipe containing chloride ions, for

which there is only copper-sulphide dissolution and virtually no leaching takes place for the pyrite grains). Consequently, the cumulative distribution (CDF) of this ratio was plotted for each distance category at various leaching times, with the grain size represented by a colour palette ranging from darker blue for smaller grains to deep red for coarser ones (Figure 7.14, Figure 7.15, and Figure 7.16). The set of graphs in the figures are presented in such a manner that the leaching time increases from top to bottom and the distance to the surface increases from left to right. The negative values represent a growth in volume, which are most probably caused by errors in the thresholding method used for the segmentation or in the incorrect matching of some grains between time steps.

From **Figure 7.14** it can be seen that at the first day of leaching (day 1), most grains are leaching virtually at the same rate, $\frac{k_{i,j}}{\bar{k}_j} \approx 1$. This is because the actual leaching kinetics of each grain is still evolving and will change as leaching proceeds. Most of the fast-leaching copper sulphides are fully dissolved at the very early days of leaching (between days 4 and 15). The reason for the change over the initial times is the curing process, period during which the first chemical attack occurs easing contact between the leach solution and the mineral grains. At the same time, there is a second group of grains that present very slow surface kinetics. These points represent the slowest-leaching grains, which surface kinetics are slightly greater than 0 and are still developing.

The shape of the curves changes dramatically over the first three weeks of leaching, until there is practically no more change from days 25 till the end of the process (which in this case was day 46). This is because the surface kinetics for most grains have fully developed by this point. Therefore, it can be assumed that the distribution of kinetics for the system can be well represented by analysing only the first 25 days of leaching. It also becomes evident that the distribution of leaching kinetics presents a bi-modal distribution, in which the two main groups include the slow leaching grains, which kinetics have fully developed by day 25 and are visible at the left-hand side of the curves, representing between 25 and 45% of the grains in each category; and the fast-leaching grains, which are fully dissolved within the first two weeks of the process and represent the remaining 55 to 75% of the grains in each category.

Lastly, unlike what was observed by (Lin, 2015) who demonstrated that a single CDF can be used to successfully describe the leaching of particulate systems, a distribution of CDF curves must be considered to represent the leaching of agglomerated ores as the leaching variability is considerably higher. This is most likely caused by the rapid dissolution of grains that occurs at the early stages of the leaching process, which is most probably a consequence of the pre-treatment carried out at the agglomeration and curing stages.

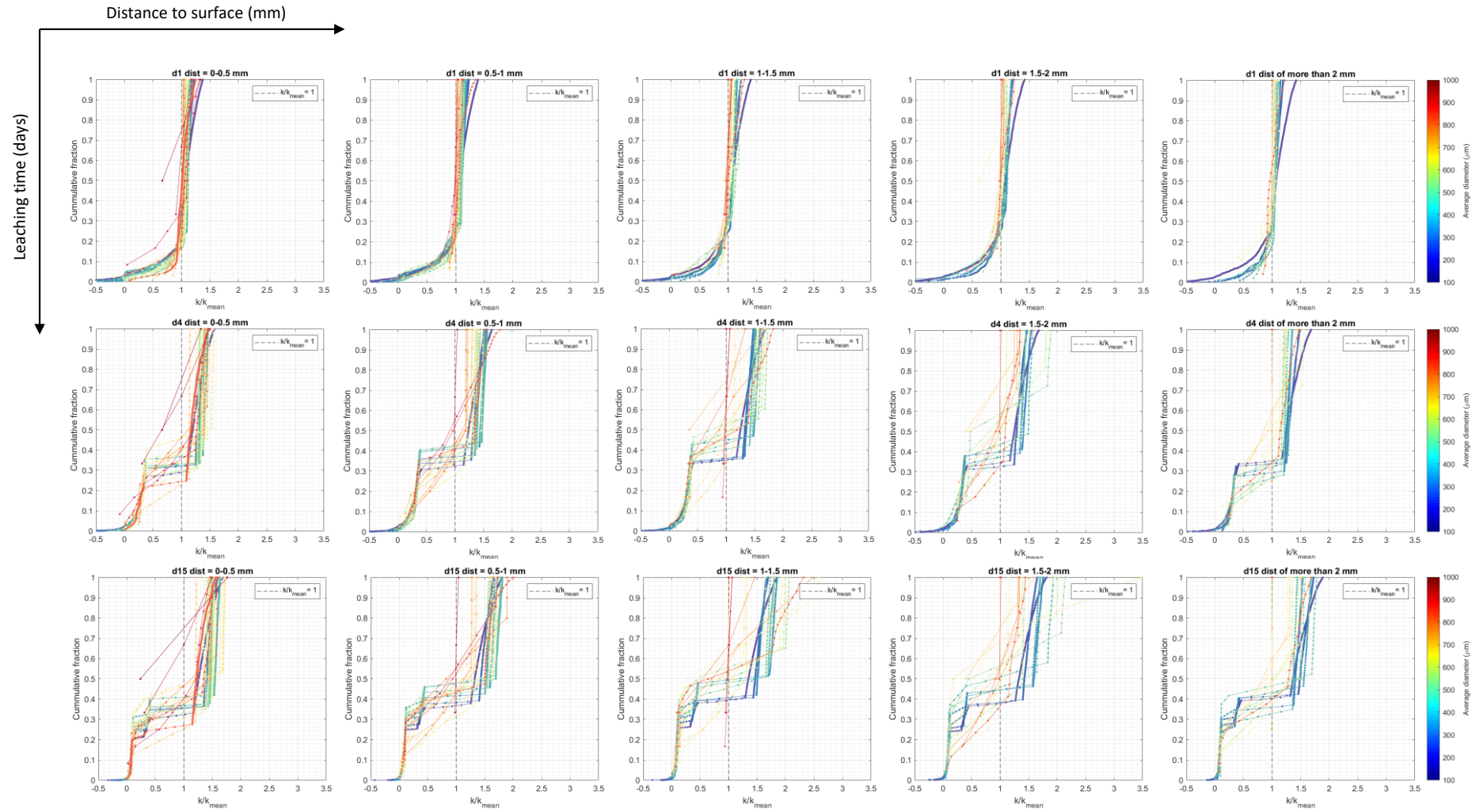


Figure 7.14. Cumulative distribution function of the rate constants for the different size categories and different distance to surface categories. Results obtained for days 1, 4, and 15.

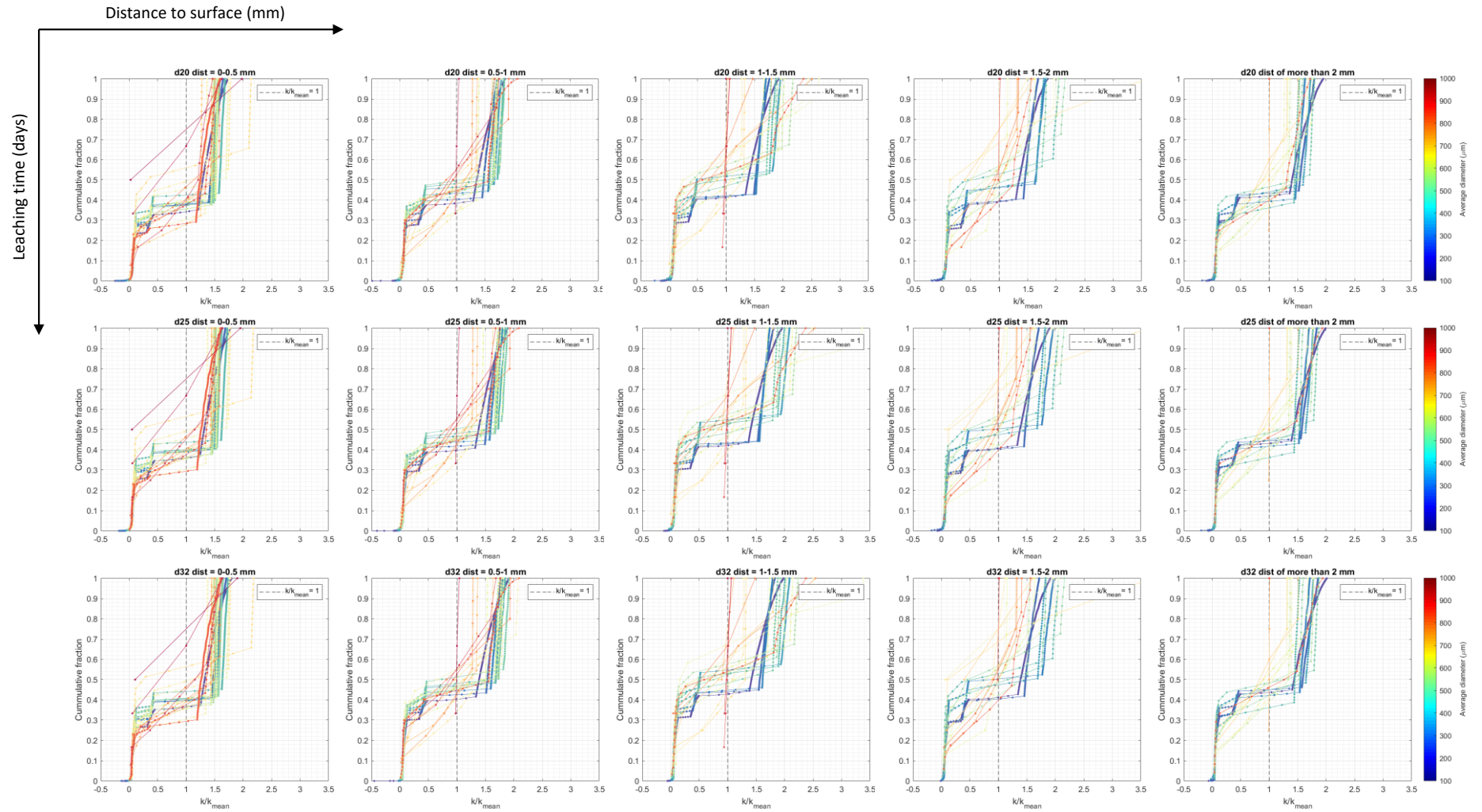


Figure 7.15. Cumulative distribution function of the rate constants for the different size categories and different distance to surface categories. Results obtained for days 20, 25, and 32.

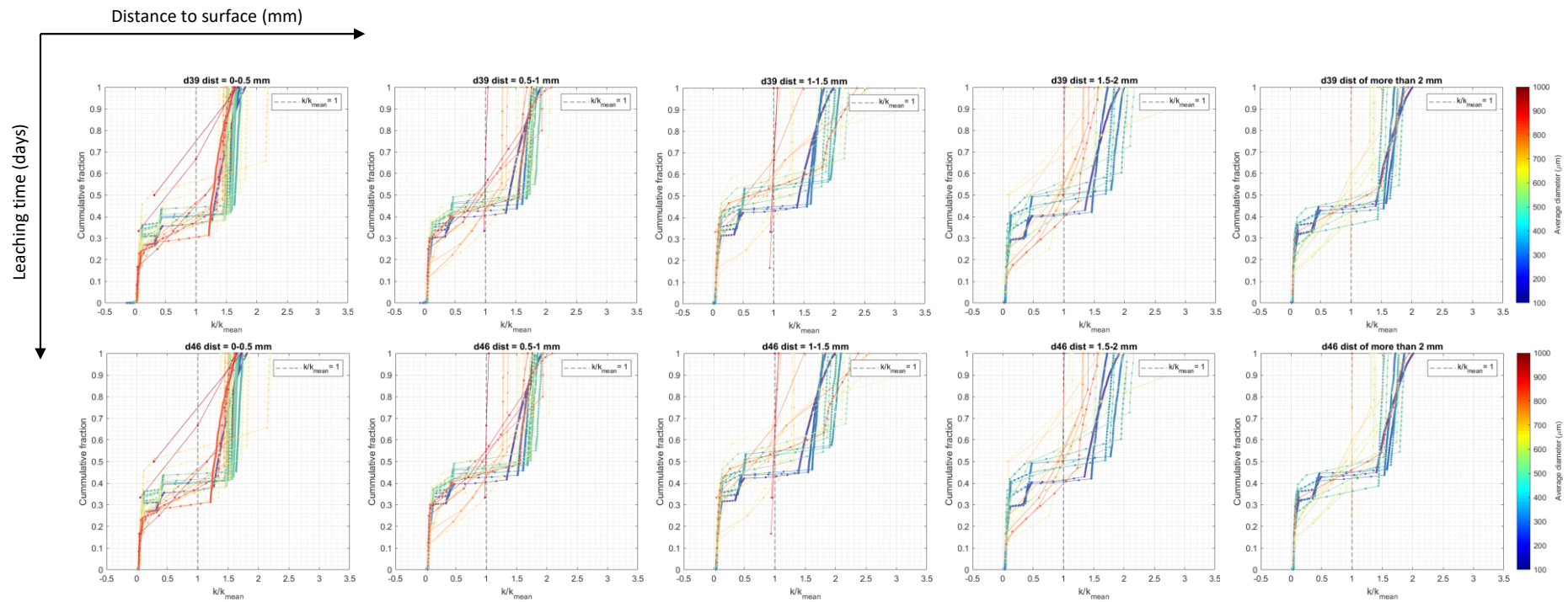


Figure 7.16. Cumulative distribution function of the rate constants for the different size categories and different distance to surface categories. Results obtained for days 39 and 46.

7.6. Summary

A multi-scale image processing methodology to track the structural changes and quantify the leaching variability occurring in the leaching of agglomerated ores was presented in this chapter. Standard chemical analyses of the PLS samples were compared with the XMT results, showing that the XMT measurements successfully describe the process.

Structural changes were analysed by assessing the changes in the internal porosity of the sample, which is produced by the natural compaction occurring over leaching. It was demonstrated that a decrease in the internal macro porosity did not impact the leaching performance at the macro scale. This result suggests that it is the internal micro pores and micro cracks which play a more important role in the mass transport processes and may be influencing the process to a higher extent. Nevertheless, higher resolution assessments are required to verify this assumption, which is out of the scope of this study.

The distribution of surface kinetics was successfully quantified by using the quantification and tracking methodology discussed in Chapter 4. It was found that unlike particulate systems, the leaching of agglomerated ores presents a family of curves that represent the leaching variability of each mineral grain size. Most of the fast-leaching grains, which represent between a 55 and a 75% of grains in each size-distance category, are dissolved within the first two weeks of leaching. There is virtually no more change in the shape of the curves from day 25 till the end of the process, which suggests that it would be possible to describe the full process by only analysing the first three to four weeks of leaching.

Ultimately, the curves presented a bi-modal distribution, in which the slowest-leaching grains (which stand for the remaining 25 to 45% of the grains in each category) represent the first group of kinetics behaviour (i.e. first mode) and the fast-leaching grains represent the second mode. Thus, it was shown that it is of paramount importance to consider a family of curves to represent the leaching variability within a leaching system and not only a limited number of values. By incorporating the relative contribution of the mass transport and surface kinetic effects into particle scale and, ultimately, heap scale leach models, improved predictions and optimisation of leach performance can be made.

Chapter 8. Conclusions

The main objective of this thesis was to study the curing and leaching behaviour of agglomerated ores. This was made possible by using a combination of XMT and SEM/EDX measurements to quantify the variables that influence the process. By developing novel image processing techniques, it was possible to assess both the morphological and mineralogical changes in the samples over time. This information was used as the basis for quantification analyses and to produce a descriptive model for the curing process. Lastly, the leaching variability and the surface kinetics were described in a quantitative way.

The literature review revealed that due to the constantly decreasing copper grade and the necessity for cost-effective processes to produce copper from primary sulphide ores, heap leaching is gaining popularity. Unconventional chemical reagents are added to the leach solution in order to enhance the extraction of metals, with the addition of chloride ions being one of the most frequent choices nowadays. This is due to the faster leaching kinetics that can be achieved especially for chalcopyrite and numerous other advantages.

A standard practice when modelling the leaching process is to include only the input and output of a set of experiments, merely describing the overall behaviour of the system. The leaching process, though, takes place at various scales and both internal changes and the grain-scale processes must be taken into consideration when predicting the behaviour. A common limitation for more detailed modelling, though, is that the conventional characterisation techniques are destructive and can only be carried out once for a given sample. An alternative is X-ray microtomography, which is a non-destructive and non-invasive imaging technique which permits the acquisition of 3D grayscale images of the sample at different timesteps of a continuous process like the curing or leaching processes.

In response to research question number 1 (i.e. how is the agglomerate structure influenced by the parameters chosen for the agglomeration process?), the novel image processing algorithms developed in this work were successfully used to track grains over both the curing and leaching process, taking into account the immense anisometric changes experienced by the agglomerates and the formation and depletion of species. These morphological changes were observed for both sample types (i.e. with and without chloride ions) to a similar degree and the results were inconclusive as to whether the morphological transformations can be coupled to agglomeration conditions. This may be because only two different agglomeration conditions were assessed for this study, thus future work should focus on testing a wider variety of conditions to verify this conclusion.

By carefully thresholding of the sulphide phase, it was possible to quantify the formation of precipitates over the curing process and address research question number 2 (i.e. how much leaching occurs during the curing process and how is this influenced by the agglomeration recipe?). These water-soluble precipitates were dissolved with water, up to 50% of them being removed for samples containing chloride ions and only 20% for the more typical leach conditions. The length of the curing process was thus studied in depth, with the precipitate formation being identified as the basis for an enhanced leaching performance. It was observed that the minimum curing length to obtain significant results was 20 days when using a combination of the more conventional agglomeration solution and chloride ions.

Research question 4 (i.e. can leach and curing performance be accurately modelled and simulated?) was partially answered, as in this thesis only the curing was modelled. Therefore, the hypothesis that the leaching of agglomerates can be modelled cannot be confirmed or rejected. The main reason why leaching was not modelled was time constraints, though very detailed information was gathered, and it can be speculated that the process could be effectively modelled in future work.

On the curing process, a model was successfully produced by considering the evaporation rate as a critical variable to control. This is a model that represents the coupled reaction and evaporation driven mass transfer processes occurring in a curing agglomerate. It includes an outward flux of solution produced by the evaporation of moisture occurring at the agglomerate's surface which drives the convection of species. It was observed that both the copper generation and transport as well as the formation of precipitates are limited by the leaching reaction rate. Simulations were carried out to assess the likely impact of changes in the curing conditions. The results showed that bigger agglomerates and a slower evaporation rate increase the leaching extent over the curing process.

Finally, to address research question 3 (i.e. what are the key factors that impact agglomerate performance during the leaching process?), two sets of agglomerates were cured for 20 days and leached for 46 days using the same recipes assessed for the curing experiments. The process was studied by using a multi-scale image processing methodology. This is an improved version of the previous grain tracking methodology, as it is also able to track agglomerate compaction and porosity changes. It was discovered that the observed decrease in the internal macro porosity (which is any pore with more than 35 microns diameter) had no discernible impact on the leaching performance at the macro scale. Any pore or crack smaller than this size was not considered due to resolution limitations. SEM/EDX combined with the TIMA software was used to characterise the remaining metal-sulphide grains, revealing that virtually all copper was leached out over the 46 days of the process.

Moreover, the leaching involving chloride ions was shown to be more selective and virtually only copper-containing grains were dissolved, with practically no pyrite dissolution. This information was used to calibrate the results and the leaching surface kinetics of the copper-sulphides were quantified at the grain scale. Their distribution over the leaching process was assessed, revealing that the leaching variability presents a family of curves with a bi-modal distribution and not a single distribution curve. Approximately 55-75% of the grains in each size-distance category are leached out within the first two weeks, representing the fast-leaching grains (first mode). The remaining 25-45% take up to 46 days to be leached out and represent the slow-leaching grains (or second mode). Ultimately, this information can be used to improve the simulation of the process and, thus, optimise the parameters to enhance leaching performance.

8.1. Future work

In this thesis a methodology for quantifying and simulating the curing and leaching performance of agglomerated ores was developed and presented. It involved a combination of SEM/EDX images with XMT measurements and novel algorithms to take into account the chemical and morphological changes occurring in the process. This methodology can be used for characterising other chemical and mechanical processes in which there is also significant structural changes over time, as it is not only restricted to mineral systems.

In order to clarify the true impact of agglomeration conditions and parameters chosen for the process on the agglomerate structure, more conditions are required to be tested. This is mostly because, for this thesis, only two conditions were assessed and both sample types experienced similar deformation extents over the process. Hence, no clear trend could be determined by analysing a small number of conditions.

The curing model, which was developed as a mathematical tool to represent the curing process due to the lack of available models, is relatively simplified. Therefore, some assumptions can be relaxed, and the simulations can be performed using the effective 3D structure of the agglomerates as domain to solve the equations over time.

Lastly, mathematical models that describe the leaching of agglomerated ores can be developed by using the information obtained for the agglomerated ore system. The fact that the leaching variability of the system can be represented by a family of bi-modal distributions can be used to perform simulations that represent more closely the true performance of a leaching system at the macro and micro scale. Again, the model can be as complex as appropriate, and the three-dimensional

structure of the agglomerates can be used as domain. By doing this, improved predictions and optimisation of leach performance can be made.

Bibliography.

- Acevedo, F. and Gentina, J. C. (1989) 'Process engineering aspects of the bioleaching of copper ores', *Bioprocess Engineering*, 4(5), pp. 223–229. doi: 10.1007/BF00369176.
- Antonijević, M. M. and Bogdanović, G. D. (2004) 'Investigation of the leaching of chalcopyritic ore in acidic solutions', *Hydrometallurgy*. Elsevier, 73(3–4), pp. 245–256. doi: 10.1016/J.HYDROMET.2003.11.003.
- Appleyard, D. (2017) 'Mind the gap: A bridge between industry and academia', *Renewable Energy Focus*. Elsevier, 18, pp. 36–38. doi: 10.1016/J.REF.2017.02.001.
- Aroca, F., Backit, A. and Jacob, J. (2012) 'CuproChlor®, a hydrometallurgical technology for mineral sulphides leaching', *Proceedings of the 4th International Seminar on Process Hydrometallurgy*, pp. 96–108. Available at: <https://www.scopus.com/inward/record.uri?eid=2-s2.0-84989779380&partnerID=40&md5=275d704df2db91b6f32dddf35cb98817>.
- Batty, J. D. and Rorke, G. V. (2006) 'Development and commercial demonstration of the BioCOP™ thermophile process', *Hydrometallurgy*. Elsevier, 83(1–4), pp. 83–89. doi: 10.1016/J.HYDROMET.2006.03.049.
- Berger, M. J., Hubbell, J. H., Seltzer, S. M., Chang, J., Coursey, J. S., Sukumar, R., Zucker, D. S., Olsen, 2010. XCOM: Photon Cross Sections Database. NIST Standard Reference Database 8 (XGAM)
- Bobadilla-Fazzini, R. A. *et al.* (2017) 'Primary copper sulfides bioleaching vs. chloride leaching: Advantages and drawbacks', *Hydrometallurgy*, 168, pp. 26–31. doi: 10.1016/j.hydromet.2016.08.008.
- Bouffard, S. C. (2005) 'Review of agglomeration practice and fundamentals in heap leaching', *Mineral Processing and Extractive Metallurgy Review*, 26(3–4), pp. 233–294. doi: 10.1080/08827500590944009.
- Brandl, H. (2001) 'Microbial Leaching of Metals', *Biotechnology Set.* (Wiley Online Books), pp. 191–224. doi: <https://doi.org/10.1002/9783527620999.ch8k>.
- Broadbridge, P., Daly, E. and Goard, J. (2017) 'Exact Solutions of the Richards Equation With Nonlinear Plant-Root Extraction'. doi: <https://doi.org/10.1002/2017WR021097>.
- Brooks, R.H., & Corey, A.T. (1964). Hydraulic Properties of Porous Media and Their Relation to Drainage Design. Transactions of the ASABE, 7, 26-0028.
- Burkhardt, D. J. (2003) 'Understanding wash efficiency and chloride transfer in copper solvent extraction', *Jom*, 55(7), pp. 34–37. doi: 10.1007/s11837-003-0122-y.

- Carneiro, M. F. C. and Leão, V. A. (2007) 'The role of sodium chloride on surface properties of chalcopyrite leached with ferric sulphate', *Hydrometallurgy*. Elsevier, 87(3–4), pp. 73–82. doi: 10.1016/J.HYDROMET.2007.01.005.
- Chen, Z., Zhou, F. and Rahman, S. S. (2014) 'Effect of cap rock thickness and permeability on geological storage of CO₂: Laboratory test and numerical simulation', *Energy Exploration and Exploitation*, 32(6), pp. 943–964. doi: 10.1260/0144-5987.32.6.943.
- Chong, S., Hawker, W. and Vaughan, J. (2013) 'Selective reductive leaching of oxidised cobalt containing residue', *Minerals Engineering*. Pergamon, 54, pp. 82–87. doi: 10.1016/J.MINENG.2013.04.004.
- Clark, D. A. and Norris, P. R. (1996) 'Oxidation of mineral sulphides by thermophilic microorganisms', *Minerals Engineering*. Pergamon, 9(11), pp. 1119–1125. doi: 10.1016/0892-6875(96)00106-9.
- Córdoba, E. M. *et al.* (2008a) 'Leaching of chalcopyrite with ferric ion. Part I: General aspects', *Hydrometallurgy*, 93(3–4), pp. 81–87. doi: 10.1016/j.hydromet.2008.04.015.
- Córdoba, E. M. *et al.* (2008b) 'Leaching of chalcopyrite with ferric ion. Part II: Effect of redox potential', *Hydrometallurgy*, 93(3–4), pp. 88–96. doi: 10.1016/j.hydromet.2008.04.016.
- Córdoba, E. M. *et al.* (2009) 'Passivation of chalcopyrite during its chemical leaching with ferric ion at 68 °C', *Minerals Engineering*. Elsevier Ltd, 22(3), pp. 229–235. doi: 10.1016/j.mineng.2008.07.004.
- Darcy, H. (1865) 'Les fontaines publiques de la ville de Dijon : exposition et application des principes à suivre et des formules à [...]', *Gallica*, p. 343.
- Davenport, W. G. *et al.* (2000) *Extractive Metallurgy Of Copper*. 4th Editio, 2000. 4th Editio.
- Davies, E. R. (2018) 'Image filtering and morphology', *Computer Vision*. Elsevier, pp. 39–92. doi: 10.1016/B978-0-12-809284-2.00003-4.
- Dhawan, N. *et al.* (2013) 'Crushed ore agglomeration and its control for heap leach operations', *Minerals Engineering*. Elsevier Ltd, 41, pp. 53–70. doi: 10.1016/j.mineng.2012.08.013.
- Dixon, D. G. . and Petersen, J. (2003) 'Comprehensive modelling study of chalcocite column and heap bioleaching.', VI(February).
- Dixon, D. G., Mayne, D. D. and Baxter, K. G. (2008) 'Galvanox™ - A novel galvanically-assisted atmospheric leaching technology for copper concentrates', *Canadian Metallurgical Quarterly*, 47(3),

pp. 327–336. doi: 10.1179/cm.2008.47.3.327.

Dobson, K. J. *et al.* (2017) 'Insights into ferric leaching of low grade metal sulfide-containing ores in an unsaturated ore bed using X-ray computed tomography', *Minerals*, 7(5), pp. 1–16. doi: 10.3390/min7050085.

Donath, T. (2007) 'Quantitative X-ray Microtomography with Synchrotron Radiation', p. 209.

Downer, C. W. and Ogden, F. L. (2004) 'Appropriate vertical discretization of Richards' equation for two-dimensional watershed-scale modelling', 22(June 2002), pp. 1–22. doi: 10.1002/hyp.1306.

Dreisinger, D. (2006) 'Copper leaching from primary sulfides: Options for biological and chemical extraction of copper', *Hydrometallurgy*, 83(1–4), pp. 10–20. doi: 10.1016/j.hydromet.2006.03.032.

Dyson, N. and Smith, R. M. (1998) *Chromatographic Integration Methods*. The Royal Society of Chemistry (RSC Chromatography Monographs). doi: 10.1039/9781847550514.

Energy and Capital, 2016 - <https://www.energyandcapital.com/articles/copper-investing-2016/76464>

Fagan, M. A. (2013) 'Fundamental Studies of Heap Leaching Hydrology Using Magnetic Resonance Imaging', (April). doi: 10.17863/CAM.6692.

Ferrier, R. J. *et al.* (2016) 'Models for apparent reaction kinetics in heap leaching: A new semi-empirical approach and its comparison to shrinking core and other particle-scale models', *Hydrometallurgy*, 166, pp. 22–33. doi: 10.1016/j.hydromet.2016.08.007.

Fox, T., Crocker, I. and Treatment, R. (2008) 'Image Registration and Fusion Techniques Volume 3 Mechanotransduction'.

Fu, K. *et al.* (2012) 'Comparative study on the passivation layers of copper sulphide minerals during bioleaching', *International Journal of Minerals, Metallurgy, and Materials*, 19(10), pp. 886–892. doi: 10.1007/s12613-012-0643-x.

Gao, X. *et al.* (2021) 'Microstructure evolution of chalcopyrite agglomerates during leaching – A synchrotron-based X-ray CT approach combined with a data-constrained modelling (DCM)', *Hydrometallurgy*. Elsevier B.V., 201(July 2020), p. 105586. doi: 10.1016/j.hydromet.2021.105586.

Garcia, D., Lin, C. L. and Miller, J. D. (2009) 'Quantitative analysis of grain boundary fracture in the breakage of single multiphase particles using X-ray microtomography procedures', *Minerals Engineering*. Elsevier Ltd, 22(3), pp. 236–243. doi: 10.1016/j.mineng.2008.07.005.

- Garvey, C. J. and Hanlon, R. (2002) 'Computed tomography in clinical practice', *BMJ*, 324(7345), pp. 1077 LP – 1080. doi: 10.1136/bmj.324.7345.1077.
- Gay, S. L. and Morrison, R. D. (2006) 'Using Two Dimensional Sectional Distributions to Infer Three Dimensional Volumetric Distributions – Validation using Tomography', 23, pp. 246–253. doi: 10.1002/ppsc.200601056.
- van Genuchten, M. T. (1980) 'A Closed-form Equation for Predicting the Hydraulic Conductivity of Unsaturated Soils', *Soil Science Society of America Journal*, pp. 892–898. doi: 10.2136/sssaj1980.03615995004400050002x.
- Gericke, M., Govender, Y. and Pinches, A. (2010) 'Tank bioleaching of low-grade chalcopyrite concentrates using redox control', *Hydrometallurgy*. Elsevier, 104(3–4), pp. 414–419. doi: 10.1016/J.HYDROMET.2010.02.024.
- Gershenson, N. I. *et al.* (2016) 'Comparison of CO₂ trapping in highly heterogeneous reservoirs with Brooks-Corey and van Genuchten type capillary pressure curves', *Advances in Water Resources*, 96, pp. 225–236. doi: <https://doi.org/10.1016/j.advwatres.2016.07.022>.
- Ghorbani, Y., Becker, M., Mainza, A., *et al.* (2011) 'Large particle effects in chemical/biochemical heap leach processes – A review', *Minerals Engineering*. Pergamon, 24(11), pp. 1172–1184. doi: 10.1016/J.MINENG.2011.04.002.
- Ghorbani, Y., Becker, M., Petersen, J., *et al.* (2011) 'Use of X-ray computed tomography to investigate crack distribution and mineral dissemination in sphalerite ore particles', *Minerals Engineering*. Pergamon, 24(12), pp. 1249–1257. doi: 10.1016/J.MINENG.2011.04.008.
- Ghorbani, Y., Franzidis, J. P. and Petersen, J. (2016) 'Heap leaching technology - Current State, innovations, and future directions: A review', *Mineral Processing and Extractive Metallurgy Review*. Taylor & Francis, 37(2), pp. 73–119. doi: 10.1080/08827508.2015.1115990.
- Gómez, C. *et al.* (1996) 'Electrochemistry of chalcopyrite', *Hydrometallurgy*. Elsevier, 43(1–3), pp. 331–344. doi: 10.1016/0304-386X(96)00010-2.
- Hackl, R. P. *et al.* (1995) 'Passivation of chalcopyrite during oxidative leaching in sulfate media', *Hydrometallurgy*. Elsevier, 39(1–3), pp. 25–48. doi: 10.1016/0304-386X(95)00023-A.
- Hahn, H. K. *et al.* (2005) *A Minimally-Interactive Watershed Algorithm Designed for Efficient CTA Bone Removal, Lecture Notes in Computer Science*.

Haralick, R. M., Sternberg, S. R. and Zhuang, X. (1987) 'Image Analysis Using Mathematical Morphology', *IEEE Transactions on Pattern Analysis and Machine Intelligence*, PAMI-9(4), pp. 532–550. doi: 10.1109/TPAMI.1987.4767941.

Harvey, T. J. and Bath, M. (2007) 'The GeoBiotics GEOCOAT® Technology – Progress and Challenges BT - Biomining', in Rawlings, D. E. and Johnson, D. B. (eds). Berlin, Heidelberg: Springer Berlin Heidelberg, pp. 97–112. doi: 10.1007/978-3-540-34911-2_5.

Hashemi, L., Blunt, M. and Hajibeygi, H. (2021) 'Pore-scale modelling and sensitivity analyses of hydrogen-brine multiphase flow in geological porous media', *Scientific Reports*, 11(1), p. 8348. doi: 10.1038/s41598-021-87490-7.

Hernández, P. C. *et al.* (2019) 'Accelerating copper leaching from sulfide ores in acid-nitrate-chloride media using agglomeration and curing as pretreatment', *Minerals*, 9(4), pp. 1–13. doi: 10.3390/MIN9040250.

Hornak, J. P. (1996) 'Basics of Magnetic Resonance Imaging (MRI).' Rochester, N.Y.: Joseph P. Hornak. Available at: <http://www.cis.rit.edu/htbooks/mri/>.

Hoummady, E. *et al.* (2018) 'An integrated multiscale approach to heap leaching of uranium-ore agglomerates', *Hydrometallurgy*, 178(May), pp. 274–282. doi: 10.1016/j.hydromet.2018.05.011.

Hunt, A. G. (2004) 'Comparing van Genuchten and Percolation Theoretical Formulations of the Hydraulic Properties of Unsaturated Media', *Vadose Zone Journal*. John Wiley & Sons, Ltd, 3(4), pp. 1483–1488. doi: <https://doi.org/10.2136/vzj2004.1483>.

Jämsä-Jounela, S.-L. and Cziprián, Z. (1998) 'Copyright 0 IFAC Automation in Mining, Mineral and Metal Processing, Cologne, Germany, 1998'.

Judy, P. F. (1976) 'The line spread function and modulation transfer function of a computed tomographic scanner', *Medical Physics*. John Wiley & Sons, Ltd, 3(4), pp. 233–236. doi: <https://doi.org/10.1118/1.594283>.

Kappes, D. W. (2002) 'Precious Metal Heap Leach Design and Practice', *Precious Metal Heap Leach Design and Practice*, pp. 1–25. Available at: http://www.kcareno.com/pdfs/mpd_heap_leach_desn_and_practice_07apr02.pdf.

Kapur, J. N., Sahoo, P. K. and Wong, A. K. C. (1985) 'A new method for gray-level picture thresholding using the entropy of the histogram.', *Computer Vision, Graphics, & Image Processing*, 29(3), pp. 273–

285. doi: 10.1016/0734-189X(85)90125-2.

Kareh, K. M. *et al.* (2014) 'Revealing the micromechanisms behind semi-solid metal deformation with time-resolved X-ray tomography', *Nature Communications*. Nature Publishing Group, 5, pp. 1–7. doi: 10.1038/ncomms5464.

Ketcham, R. A. and Carlson, W. D. (2001) 'Acquisition, optimization and interpretation of x-ray computed tomographic imagery: Applications to the geosciences', *Computers and Geosciences*, 27(4), pp. 381–400. doi: 10.1016/S0098-3004(00)00116-3.

Kewen, L. (2004) 'Theoretical Development of the Brooks-Corey Capillary Pressure Model from Fractal Modeling of Porous Media', in.

Kishore, M. S. and Rao, K. V. (2001) 'Robust correlation tracker', 26(June), pp. 227–236.

Klauber, C. (2008) 'A critical review of the surface chemistry of acidic ferric sulphate dissolution of chalcopyrite with regards to hindered dissolution', *International Journal of Mineral Processing*. Elsevier, 86(1–4), pp. 1–17. doi: 10.1016/J.MINPRO.2007.09.003.

Kodali, P. *et al.* (2011) 'Evaluation of stucco binder for agglomeration in the heap leaching of copper ore', *Minerals Engineering*. Elsevier Ltd, 24(8), pp. 886–893. doi: 10.1016/j.mineng.2011.03.024.

Leahy, M. J., Philip Schwarz, M. and Davidson, M. R. (2006) 'An air sparging CFD model for heap bioleaching of chalcocite', *Applied Mathematical Modelling*, 30(11), pp. 1428–1444. doi: 10.1016/j.apm.2006.03.008.

Lee, D. H. and Abriola, L. M. (2015) 'Use of the Richards equation in land surface parameterizations Use of the Richards equation in land surface parameterizations', (June). doi: 10.1029/1999JD900951.

Lehmann, J. and Solomon, D. (2010) *Organic carbon chemistry in soils observed by synchrotron-based spectroscopy*, *Developments in Soil Science*. Elsevier. doi: 10.1016/S0166-2481(10)34010-4.

Levenspiel, O. (1972) *Chemical reaction engineering*, *Chemical Engineering Science*. doi: 10.1016/0009-2509(64)85017-X.

Lewandowski, K. A. and Kawatra, S. K. (2009) 'Polyacrylamide as an agglomeration additive for copper heap leaching', *International Journal of Mineral Processing*. Elsevier B.V., 91(3–4), pp. 88–93. doi: 10.1016/j.minpro.2009.01.004.

Li, K. (2010) 'More general capillary pressure and relative permeability models from fractal geometry.',

Journal of contaminant hydrology. Netherlands, 111(1–4), pp. 13–24. doi: 10.1016/j.jconhyd.2009.10.005.

Li, Z., Özgen-Xian, I. and Maina, F. (2021) 'A mass-conservative predictor-corrector solution to the 1D Richards equation with adaptive time control'. doi: 10.1016/j.jhydrol.2020.125809.

Lian, P. Q. *et al.* (2016) 'Saturation modeling in a carbonate reservoir using capillary pressure based saturation height function: a case study of the SvK reservoir in the Y Field', *Journal of Petroleum Exploration and Production Technology*, 6(1), pp. 73–84. doi: 10.1007/s13202-015-0159-9.

Liddicoat, J. and Dreisinger, D. (2007) 'Chloride leaching of chalcopyrite', *Hydrometallurgy*, 89(3–4), pp. 323–331. doi: 10.1016/j.hydromet.2007.08.004.

Lin, Q. *et al.* (2015) 'Quantifying and minimising systematic and random errors in X-ray micro-tomography based volume measurements', *Computers and Geosciences*. doi: <http://dx.doi.org/10.1016/j.cageo.2014.12.008>.

Lin, Q. (2015) 'Use of X-ray Computed Microtomography to Measure the Leaching Behaviour of Metal Sulphide Ores', (February).

Lin, Q., Barker, D. J., *et al.* (2016) 'Modelling particle scale leach kinetics based on X-ray computed micro-tomography images', *Hydrometallurgy*. The Authors, 162, pp. 25–36. doi: 10.1016/j.hydromet.2016.02.008.

Lin, Q., Neethling, S. J., *et al.* (2016) 'Multi-scale quantification of leaching performance using X-ray tomography', *Hydrometallurgy*. doi: 10.1016/j.hydromet.2016.06.020.

Linge, H. G. (1976) 'A study of chalcopyrite dissolution in acidic ferric nitrate by potentiometric titration', *Hydrometallurgy*. Elsevier, 2(1), pp. 51–64. doi: 10.1016/0304-386X(76)90013-X.

Liu, C., Ball, W. P. and Ellis, J. H. (1998) 'An Analytical Solution to the One-Dimensional Solute Advection-Dispersion Equation in Multi-Layer Porous Media', pp. 25–43.

Lu, J. and Dreisinger, D. (2013) 'Copper leaching from chalcopyrite concentrate in Cu(II)/Fe(III) chloride system', *Minerals Engineering*. Elsevier Ltd, 45, pp. 185–190. doi: 10.1016/j.mineng.2013.03.007.

Lu, J., Dreisinger, D. and West-Sells, P. (2017) 'Acid curing and agglomeration for heap leaching', *Hydrometallurgy*. Elsevier B.V., 167, pp. 30–35. doi: 10.1016/j.hydromet.2016.10.019.

Lu, Z. Y., Jeffrey, M. I. and Lawson, F. (2000a) 'Effect of chloride ions on the dissolution of chalcopyrite

in acidic solutions', *Hydrometallurgy*. doi: 10.1016/S0304-386X(00)00075-X.

Lu, Z. Y., Jeffrey, M. I. and Lawson, F. (2000b) 'Electrochemical study of the effect of chloride ions on the dissolution of chalcopyrite in acidic solutions', *Hydrometallurgy*. doi: 10.1016/S0304-386X(00)00068-2.

Luo, Z. *et al.* (2019) 'Evaluation and application of the modified van Genuchten function for unsaturated porous media', *Journal of Hydrology*. Elsevier, 571(February), pp. 279–287. doi: 10.1016/j.jhydrol.2019.01.051.

Lupo, J. F. (2010) 'Liner system design for heap leach pads', *Geotextiles and Geomembranes*. Elsevier Ltd, 28(2), pp. 163–173. doi: 10.1016/j.geotexmem.2009.10.006.

Mao, L. *et al.* (2019) '3D strain mapping of opaque materials using an improved digital volumetric speckle photography technique with X-ray microtomography', *Applied Sciences (Switzerland)*, 9(7). doi: 10.3390/app9071418.

María, D. and Ruiz, C. (2013) 'Dra. María Cristina Ruiz Departamento de Ingeniería Metalúrgica Universidad de Concepción 2013', p. 200.

Miller, J. D. *et al.* (2009) 'Liberation-limited grade/recovery curves from X-ray micro CT analysis of feed material for the evaluation of separation efficiency', *International Journal of Mineral Processing*. Elsevier B.V., 93(1), pp. 48–53. doi: 10.1016/j.minpro.2009.05.009.

Moreno-Atanasio, R., Williams, R. A. and Jia, X. (2010) 'Combining X-ray microtomography with computer simulation for analysis of granular and porous materials', *Particuology*. Chinese Society of Particuology, 8(2), pp. 81–99. doi: 10.1016/j.partic.2010.01.001.

Nicol, M., Miki, H. and Velásquez-Yévenes, L. (2010) 'The dissolution of chalcopyrite in chloride solutions: Part 3. Mechanisms', *Hydrometallurgy*. Elsevier B.V., 103(1–4), pp. 86–95. doi: 10.1016/j.hydromet.2010.03.003.

Nimmo, J. R. (1990) 'Experimental Testing of Transient Unsaturated Flow Theory at Low Water Content in a Centrifugal Field', 26(9), pp. 1951–1960.

Nimmo, J. R. *et al.* (2021) 'Rapid-Response Unsaturated Zone Hydrology : Small-Scale Data , Small-Scale Theory , Big Problems', 9(March), pp. 1–7. doi: 10.3389/feart.2021.613564.

Norris, P. R. and Owen, J. P. (1993) 'Mineral sulphide oxidation by enrichment cultures of novel thermoacidophilic bacteria', *FEMS Microbiology Reviews*. No longer published by Elsevier, 11(1–3), pp.

51–56. doi: 10.1111/j.1574-6976.1993.tb00266.x.

Ntakamutshi, P. T. *et al.* (2017) 'Agitation and column leaching studies of oxidised copper-cobalt ores under reducing conditions', *Minerals Engineering*. Elsevier, 111(May), pp. 47–54. doi: 10.1016/j.mineng.2017.06.001.

O'Connor, G. M. and Eksteen, J. J. (2020) 'A critical review of the passivation and semiconductor mechanisms of chalcopyrite leaching', *Minerals Engineering*. Elsevier, 154(April), p. 106401. doi: 10.1016/j.mineng.2020.106401.

Ogbonna, N., Petersen, J. and Laurie, H. (2006) 'An agglomerate scale model for the heap bioleaching of chalcocite', *Journal of the Southern African Institute of Mining and Metallurgy*, 106(6), pp. 433–442.

Otsu, N. (1979) 'A threshold selection method from gray-level histograms.', C(1), pp. 62–66. doi: 10.1109/TSMC.1979.4310076.

Oxley, A., Smith, M. E. and Caceres, O. (2016) 'Why heap leach nickel laterites?', *Minerals Engineering*. Pergamon, 88, pp. 53–60. doi: 10.1016/J.MINENG.2015.09.018.

Pachepsky, Y., Timlin, D. and Rawls, W. (2003) 'Generalized Richards ' equation to simulate water transport in unsaturated soils', 272, pp. 3–13.

Parker, A. *et al.* (2003) 'An X-ray photoelectron spectroscopy study of the mechanism of oxidative dissolution of chalcopyrite', *Hydrometallurgy*. Elsevier, 71(1–2), pp. 265–276. doi: 10.1016/S0304-386X(03)00165-8.

Pashminehazar, R., Kharaghani, A. and Tsotsas, E. (2016) 'Three dimensional characterization of morphology and internal structure of soft material agglomerates produced in spray fluidized bed by X-ray tomography', *Powder Technology*. Elsevier B.V., 300, pp. 46–60. doi: 10.1016/j.powtec.2016.03.053.

Peters, E. (1976) 'Direct Leaching of Sulfides: Chemistry and Applications.', *Metall Trans B*, 7 B(4), pp. 505–517. doi: 10.1007/BF02698582.

Petersen, J. (2016) 'Heap leaching as a key technology for recovery of values from low-grade ores – A brief overview', *Hydrometallurgy*. Elsevier B.V., 165, pp. 206–212. doi: 10.1016/j.hydromet.2015.09.001.

Pradhan, N. *et al.* (2008) 'Heap bioleaching of chalcopyrite: A review', *Minerals Engineering*, 21(5), pp. 355–365. doi: 10.1016/j.mineng.2007.10.018.

- Preim, B. and Botha, C. (2014) 'Image Analysis for Medical Visualization', *Visual Computing for Medicine*. Morgan Kaufmann, pp. 111–175. doi: 10.1016/B978-0-12-415873-3.00004-3.
- Purkiss, S. and Anthony, R. (2002) 'Heap leaching base metals from oxide ores.pdf'.
- Quezada, V. *et al.* (2018) 'Effect of curing time on the dissolution of a secondary copper sulphide ore using alternative water resources', *IOP Conference Series: Materials Science and Engineering*, 427(1). doi: 10.1088/1757-899X/427/1/012030.
- Ram, R. *et al.* (2020) 'Study of the leaching and pore evolution in large particles of a sulfide ore', *Hydrometallurgy*. Elsevier, 192(October 2019), p. 105261. doi: 10.1016/j.hydromet.2020.105261.
- Renken, K., Mchaina, D. M. and Yanful, E. (2005) 'Geosynthetics Research and Applications in the Mining and Mineral Processing Environment'.
- Reyes-Leiva, F. (2018) 'Quantification in Minerals Processing Via X-Ray Micro-Tomography'.
- Reyes, F. *et al.* (2017) 'Calibrated X-ray micro-tomography for mineral ore quantification', *Minerals Engineering*, 110(May), pp. 122–130. doi: 10.1016/j.mineng.2017.04.015.
- Reyes, F. *et al.* (2018) 'Quantifying mineral liberation by particle grade and surface exposure using X-ray microCT', *Minerals Engineering*, 125, pp. 75–82. doi: 10.1016/j.mineng.2018.05.028.
- Richards, L. A. (1931) 'Capillary conduction of liquids through porous mediums', *Journal of Applied Physics*, 1(5), pp. 318–333. doi: 10.1063/1.1745010.
- Richardson, L. F. (1922) 'Weather prediction by numerical process', pp. 282–284.
- Rossi, G. (1990) *Biohydrometallurgy*. McGraw-Hill Companies.
- Rubin, G. D. (2014) 'Computed Tomography: Revolutionizing the Practice of Medicine for 40 Years', *Radiology*. Radiological Society of North America, 273(2S), pp. S45–S74. doi: 10.1148/radiol.14141356.
- Salinas-Farran, L., Batchelor, A. and Neethling, S. J. (2022) 'Multimodal assessment of the curing of agglomerated ores in the presence of chloride ions', *Hydrometallurgy*. Elsevier, 207, p. 105776. doi: 10.1016/J.HYDROMET.2021.105776.
- Sandström, Å., Shchukarev, A. and Paul, J. (2005) 'XPS characterisation of chalcopyrite chemically and bio-leached at high and low redox potential', *Minerals Engineering*. Pergamon, 18(5), pp. 505–515. doi: 10.1016/J.MINENG.2004.08.004.

- Schippers, A. *et al.* (2010) 'The biogeochemistry and microbiology of sulfidic mine waste and bioleaching dumps and heaps, and novel Fe(II)-oxidizing bacteria', *Hydrometallurgy*. Elsevier, 104(3–4), pp. 342–350. doi: 10.1016/J.HYDROMET.2010.01.012.
- Scussiato, T. *et al.* (2021) 'Finite element for Richards ' equation in porous rocks'. doi: 10.1088/1755-1315/833/1/012118.
- Serra, J. P. F. (1983) 'Image Analysis and Mathematical Morphology', in.
- Serrano, S. E. (2004) 'Modeling Infiltration with Approximate Solutions to Richard ' s Equation', 9(October), pp. 421–432.
- da Silva, E. A. B. and Mendonca, G. V. (2005) 'Digital Image Processing', *The Electrical Engineering Handbook*. Academic Press, pp. 891–910. doi: 10.1016/B978-012170960-0/50064-5.
- de Smedt, F. and Wierenga, P. J. (1979) 'MASS TRANSFER IN POROUS MEDIA WITH IMMOBILE WATER', 41, pp. 59–67.
- van Staden, P. J. *et al.* (2017) 'Comparative assessment of heap leach production data – 2. Heap leaching kinetics of Kipoi HMS floats material, laboratory vs. commercial scale', *Minerals Engineering*. Pergamon, 101, pp. 58–70. doi: 10.1016/J.MINENG.2016.11.015.
- Stampanoni, M. *et al.* (2009) 'Stripe and ring artifact removal with combined wavelet — Fourier filtering', (June). doi: 10.1364/OE.17.008567.
- Stauber, M. and Müller, R. (2008) 'Micro-Computed Tomography: A Method for the Non-Destructive Evaluation of the Three-Dimensional Structure of Biological Specimens BT - Osteoporosis: Methods and Protocols', in Westendorf, J. J. (ed.). Totowa, NJ: Humana Press, pp. 273–292. doi: 10.1007/978-1-59745-104-8_19.
- Stock, S. R. (1999) 'X-ray microtomography of materials', *International Materials Reviews*, 44(4), pp. 141–164. doi: 10.1179/095066099101528261.
- Swinehart, D. F. (1962) 'The Beer-Lambert Law', *Journal of Chemical Education*. American Chemical Society, 39(7), p. 333. doi: 10.1021/ed039p333.
- Szymkiewicz, A. (2013) *Modelling Water Flow in Unsaturated Porous Media, Modelling Water Flow in Unsaturated Porous Media. Series: GeoPlanet: Earth and Planetary Sciences, ISBN: 978-3-642-23558-0. Springer Berlin Heidelberg (Berlin, Heidelberg), Edited by Adam Szymkiewicz.* doi: 10.1007/978-3-642-23559-7.

- Thennammai, S. *et al.* (2015) 'Object tracking using image processing', 2(4), pp. 67–72.
- Trucco, E. (1995) 'Computer and Robot Vision', *Ai Communications*, 8, pp. 50–51
- Tsai, W. H. (1985) 'Moment-preserving thresholding: a new approach.', *Computer Vision, Graphics, & Image Processing*, 29(3), pp. 377–393. doi: 10.1016/0734-189x(85)90133-1.
- Ulrich, B., Andrade, H. and Gardner, T. (2003) 'Lessons learnt from heap leaching operations in South America-An update', *The Journal of South African Institute of Mining and Metallurgy*, (February), pp. 23–28.
- Velarde, G. (2005) 'Agglomeration control for heap leaching processes', *Mineral Processing and Extractive Metallurgy Review*, 26(3–4), pp. 219–231. doi: 10.1080/08827500590943974.
- Velásquez-Yévenes, L., Nicol, M. and Miki, H. (2010) 'The dissolution of chalcopryite in chloride solutions: Part 1. the effect of solution potential', *Hydrometallurgy*. Elsevier B.V., 103(1–4), pp. 108–113. doi: 10.1016/j.hydromet.2010.03.001.
- Velásquez-Yévenes, L., Torres, D. and Toro, N. (2018) 'Leaching of chalcopryite ore agglomerated with high chloride concentration and high curing periods', *Hydrometallurgy*. doi: 10.1016/j.hydromet.2018.10.004.
- Veloso, T. C. *et al.* (2016) 'Kinetics of chalcopryite leaching in either ferric sulphate or cupric sulphate media in the presence of NaCl', *International Journal of Mineral Processing*. Elsevier B.V., 148, pp. 147–154. doi: 10.1016/j.minpro.2016.01.014.
- Videla, A. R., Lin, C. L. and Miller, J. D. (2007) '3D characterization of individual multiphase particles in packed particle beds by X-ray microtomography (XMT)', *International Journal of Mineral Processing*, 84(1–4), pp. 321–326. doi: 10.1016/j.minpro.2006.07.009.
- Warren, G. W., Wadsworth, M. E. and El-Raghy, S. M. (1982) 'Passive and transpassive anodic behavior of chalcopryite in acid solutions', *Metallurgical Transactions B*, 13(4), pp. 571–579. doi: 10.1007/BF02650014.
- Watling, H. R. (2013) 'Chalcopryite hydrometallurgy at atmospheric pressure: 1. Review of acidic sulfate, sulfate-chloride and sulfate-nitrate process options', *Hydrometallurgy*. Elsevier B.V., 140, pp. 163–180. doi: 10.1016/j.hydromet.2013.09.013.
- Webb, S. (1995) 'A brief history of tomography and CT'.

- Winand, R. (1991) 'Chloride hydrometallurgy', *Hydrometallurgy*, 27(3), pp. 285–316. doi: [https://doi.org/10.1016/0304-386X\(91\)90055-Q](https://doi.org/10.1016/0304-386X(91)90055-Q).
- Yagi, S. and Kunii, D. (1955) 'Studies on combustion of carbon particles in flames and fluidized beds', in *Symposium (International) on Combustion*. doi: 10.1016/S0082-0784(55)80033-1.
- Yagi, S. and Kunii, D. (1961) 'Fluidized-solids reactors with continuous solids feed-I. Residence time of particles in fluidized beds', *Chemical Engineering Science*. doi: 10.1016/0009-2509(61)80043-2.
- Yang, Yi *et al.* (2019) 'Microstructure evolution of low-grade chalcopryite ores in chloride leaching - A synchrotron-based X-ray CT approach combined with a data-constrained modelling (DCM)', *Hydrometallurgy*. Elsevier, 188(April), pp. 1–13. doi: 10.1016/j.hydromet.2019.06.004.
- Yekta, A. E., Stemmelen, D. and Leclerc, S. (2013) 'Numerical and Experimental Study of Water Drop Movement Subjected to an Air Stream in Porous Medium', (1), pp. 1–4.
- Yévenes, L. V., Miki, H. and Nicol, M. (2010) 'The dissolution of chalcopryite in chloride solutions: Part 2: Effect of various parameters on the rate', *Hydrometallurgy*. Elsevier B.V., 103(1–4), pp. 80–85. doi: 10.1016/j.hydromet.2010.03.004.
- Yoo, K. *et al.* (2010) 'Effect of chloride ions on leaching rate of chalcopryite', *Minerals Engineering*. Elsevier Ltd, 23(6), pp. 471–477. doi: 10.1016/j.mineng.2009.11.007.
- Yuan, F. and Lu, Z. (2005) 'Analytical Solutions for Vertical Flow in Unsaturated , Rooted Soils with Variable Surface Fluxes', pp. 1210–1218. doi: 10.2136/vzj2005.0043.
- Zha, Y. *et al.* (2019) 'Review of numerical solution of Richardson–Richards equation for variably saturated flow in soils', *Wiley Interdisciplinary Reviews: Water*, 6(5), pp. 1–23. doi: 10.1002/wat2.1364.
- Zhao, H. *et al.* (2019) 'The dissolution and passivation mechanism of chalcopryite in bioleaching : An overview', *Minerals Engineering*. Elsevier, 136(932), pp. 140–154. doi: 10.1016/j.mineng.2019.03.014.
- Zhao, W. *et al.* (2018) 'Multi-materials beam hardening artifacts correction for computed tomography (CT) based on X-ray spectrum estimation', pp. 1–11. Available at: <http://arxiv.org/abs/1812.02365>.
- Zhu, H. *et al.* (2018) 'Modified Richards ' Equation to Improve Estimates of Soil Moisture in Two-Layered Soils after Infiltration'. doi: 10.3390/w10091174.
- Zitová, B. and Flusser, J. (2003) 'Image registration methods: A survey', *Image and Vision Computing*, 21(11), pp. 977–1000. doi: 10.1016/S0262-8856(03)00137-9.

Appendix A

Publications

The work presented in this thesis has been published in the following Journal article:

- Salinas-Farran, L., Batchelor, A. and Neethling, S. J. (2022) 'Multimodal assessment of the curing of agglomerated ores in the presence of chloride ions', *Hydrometallurgy*. Elsevier, 207, p. 105776. doi: 10.1016/J.HYDROMET.2021.105776.

And the following presentations at international conferences:

- Salinas-Farran, L., & Neethling S. J. Measuring and Modelling Agglomerate Performance using X-ray Micro Tomography. In: 13th International Conference on Process Hydrometallurgy, Santiago, Chile. August 4-6, 2021.
- Salinas-Farran, L., & Neethling S. J. Combining XMT and MLA to describe the structural evolution of agglomerated ores: the impact of chloride ions in the curing process. In: 12th International Conference on Process Hydrometallurgy, Santiago, Chile. October 26-30, 2020.
- Salinas-Farran, L., & Neethling S. J. XMT based assessment of the performance of agglomerated sulphide ores: The impact of long curing times and the addition of chloride ions. In: XXX International Mineral Processing Congress, Cape Town, South Africa. 18-22 October 2020.
- Salinas-Farran, L., & Neethling S. J. Quantifying the effects of mass transport and mineralogy in the curing and leaching of agglomerated ores. In: 15th International Mineral Processing Conference, Santiago, Chile. November 20-22, 2019.

Appendix B

<https://imperiallondon->

my.sharepoint.com/:f:/g/personal/les17_ic_ac_uk/Egz9xOsY3hhKmdBXPTr0E78BaAq058G7e6ZRMslr

QZn_-g